Development and Application of Computational Tools to Analyse Selectivity in Organic Chemistry

Kelvin E. Jackson

April 10, 2016

Contents

Abstract **iv**

1 Introduction **1**

1.1 Computational Chemistry 1
1.2 Quantum Mechanics 2
1.3 Basis sets 3
1.3.1 Slater Type and Gaussian Orbitals 4
1.3.2 Polarisation functions 5
1.3.3 Diffuse basis functions 5
1.3.4 Relativistic effects 6
1.3.5 Summary 7
1.4 Density functional theory 7
1.4.1 Kohn-Sham 8
1.4.2 Exchange-correlation 9
1.4.3 Dispersion 10
1.4.4 Summary 10
1.5 Semi-empirical methods 11
1.6 Molecular mechanics 12
1.7 Coupled cluster theory 13
1.8 Solvation models 14
1.9 The potential energy surface 15
1.10 Transition state theory 17
1.11 Monte Carlo conformational searching 21
1.12 Nucleus independent chemical shifts 23
1.13 Marcus equation 24

2 Mechanism and selectivity in intramolecular Michael additions catalysed by primary amines **27**

2.1 Background 28
2.2 Mechanism 31
2.3 Computational methods 33
2.4 Methylamine catalysis 34

2.4.1 Accounting for diastereoselectivity . . . 34
2.4.2 Density functional comparison: M06-2X vs B3LYP-D3 . . . 40
2.5 Chiral aminocyclohexylthiourea catalysis . . . 42
2.5.1 Flexible catalyst modeling . . . 42
2.5.2 Reaction pathway . . . 43
2.5.3 Explaining enantioselectivity . . . 48
2.6 Chiral 1-(naphthalen-1-yl)etha-1-amine catalysis . . . 50
2.6.1 Conformational considerations . . . 51
2.6.2 Reaction pathway . . . 51
2.6.3 Accounting for enantioselectivity . . . 54
2.7 Conclusions . . . 56

3 Regioselectivity of cyclisations 58
3.1 Background . . . 58
3.1.1 Terminology . . . 58
3.1.2 Origin . . . 60
3.2 Computational methods . . . 60
3.3 5-*endo-trig* in indane synthesis . . . 62
3.3.1 Synthesis . . . 62
3.3.2 Reaction profile . . . 63
3.3.3 NICS analysis: electrocyclic or pseudopericyclic? . . . 65
3.3.4 Substrate manipulation for *endo* ester cyclisation . . . 70
3.3.5 Summary . . . 72
3.4 Varying ring size in *endo*- and *exo-trig* cyclisations . . . 72
3.5 5-*endo-trig* in hypothetical systems . . . 78
3.6 Conclusions . . . 86

4 Stereoelectronic effects in the α-alkylation of bicyclic enamines 88
4.1 Background . . . 88
4.2 Mechanism . . . 90
4.3 Computational methods . . . 91
4.4 Preliminary results and discussion . . . 92
4.5 Development of the model system . . . 96

4.6 Probing the source of asymmetry . . . 100
4.7 Further development of model system . . . 108
4.8 Experimental results . . . 111
4.9 Conclusions . . . 113

5 Thermochemical kinetics of azetidine conformational behaviour 115
5.1 Background . . . 115
5.2 Computational methods . . . 116
5.3 Benchmarking . . . 118
5.4 Ground state conformer analysis . . . 121
5.4.1 *N*-thiopivaloyl-2-methylazetidine . . . 121
5.4.2 *N*-*tert*-butoxythiocarbonyl-2-methylazetidine . . . 123
5.5 Potential energy surface . . . 125
5.6 Rotational TS analysis . . . 127
5.6.1 *N*-pivaloyl-azetidine . . . 127
5.6.2 *N*-*tert*-butoxycarbonyl-azetidine . . . 128
5.6.3 *N*-thiopivaloyl-azetidine . . . 129
5.6.4 *N*-*tert*-butoxythiocarbonyl-azetidine . . . 130
5.6.5 *N*-thiopivaloyl-2-methylazetidine . . . 131
5.6.6 *N*-*tert*-butoxythiocarbonyl-2-methylazetidine . . . 132
5.6.7 Summary and analysis of trends in rotational barriers . . . 133
5.7 Conclusions . . . 135

6 Computational methods development 138
6.1 Magnetic sampling: centroids, vectors and planes . . . 138
6.1.1 Theory . . . 138
6.1.2 Aromatic, antiaromatic and non-aromatic systems . . . 140
6.2 Visualising pyramidalization . . . 145
6.2.1 Theory and implementation . . . 145

Abstract

The work described in this thesis illustrates how a range of computational methods may be applied to explain, both experimentally observed and computationally predicted, selectivity, in the field of Organic Chemistry. We begin with a discussion of the theory behind Computational Chemistry and also background to the ever growing field of organocatalysis, followed by a synopsis on the importance of asymmetry in synthesis.

The second chapter focusses on an asymmetric organocatalysed reaction for the diastereoselective and enantioselective synthesis of the morphan motif (**Figure 0.1**). We look at a range of primary amine organocatalysts in this section, and are able to account for the observed asymmetry that is imparted, both qualitatively and quantitatively. Furthermore, through the course of our investigation, we were able to propose synthetic modifications to an existing organocatalyst used in this reaction, resulting in improvement to the enantioselectivity and atom economy of the reaction.

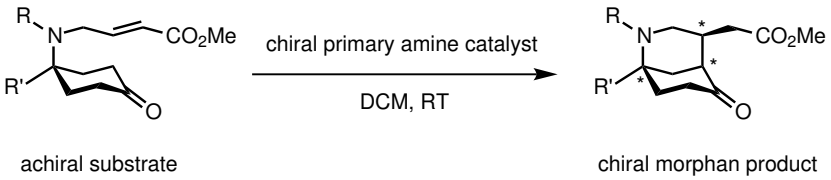

Figure 0.1: Overview of the asymmetric synthesis of the morphan motif.

In chapter three, we examine the various factors influencing ring closing reactions for a range of systems and investigate the origin of the underlying preference for cyclisations to follow Baldwin's rules for selectivity. In order to do this, we use a range of computational techniques, including nucleus independent chemical shift (NICS) analysis to gain a better understanding of the magnetic properties of ring closing transitions structures (TS).

Chapter four contains an in depth look into the stereoelectronic effects altering enantioselectivity in alkylation reactions with bicyclic enamine chiral auxiliaries. In this study, we were able to develop, improve, and implement a new methodology for explaining stereoselective alkylations of tropane-type enamine systems. Our

computationally derived predictions of selectivity made for a number of systems have been subsequently verified with experimental results which were within 5 kJ/mol of our values.

(a) Tropane (6,5) system

(b) Tropane (6,5) system (with geminal methyl groups)

Figure 0.2: General reaction schemes for ethylation of non-racemic tropane-derived enamines. Experimentally derived diastereomeric ratios are shown; the major diastereomer is the result of *Si*-facial electrophilic attack of EtI in both cases.

In chapter five, we use computational analysis to provide insight into the regiodivergent α- and α'-lithiation-electrophile trapping of *N*-thiopivaloyl- and *N*-(*tert*-butoxythiocarbonyl)-α-alkylazetidines. We calculated the magnitudes of rotational barriers for a range of protected azetidine systems and showed that rotamer interconversion could not occur for the aforementioned species at the temperature and on the time scale of the lithiations.

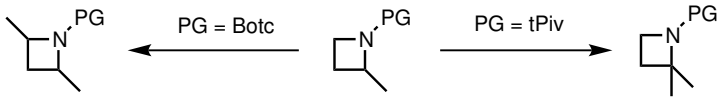

Figure 0.3: Protecting group (PG) dependent regiodivergent methylation reactions; *s*-BuLi/TMEDA/THF, -78 °C then MeI.

In the final chapter, we describe the development of computational tools that have been essential in the other investigations discussed in this thesis. We also look at potential future applications of these programs in the field of Organic Chemistry.

Acknowledgments

Firstly, I would like to thank my DPhil supervisor, Professor Robert Paton, for his constant guidance and mentorship during the years I have spent working in his research group. His apparently limitless patience, and wealth of knowledge in what seems to be all areas of Chemistry, have proven crucial in the generation of new ideas, and the development of the work described in this thesis. Throughout my DPhil he has proven himself to be a truly excellent supervisor, for which I am sincerely grateful.

I would like to thank all members of the Paton Group who have worked in the lab during my time there but especially my fellow DPhil students, Sami Jaffar, Wilian Cortopassi, and Ace Simion, without whom the last couple of years would have been considerably less entertaining. In addition, I would like to acknowledge members of the McGrady Group, with whom we have shared our lab space, in particular Professor John McGrady himself for his fantastic input at our joint group meetings and his many useful suggestions in the past.

In the University of Oxford's Department of Chemistry, I would like to thank Professors David Hodgson, Martin Smith, Darren Dixon, and their respective research groups for collaborative input in much of my research. I would particularly like to thank David for the many useful discussions I have had with him over the years, during both my undergraduate and postgraduate studies. I would also like to thank Adam Gammack, with whom I worked with directly during my study of asymmetric intramolecular Michael additions, and David Robinson, with whom I have discussed numerous programming and Physical Chemistry problems over the years.

Finally, I would like to thank my family, in particular my parents; their unconditional love, support, and encouragement throughout my years studying at Oxford have been invaluable in getting me to where I am today.

Author's declaration

The work presented in this thesis is an account of the work carried out by the author in the Department of Chemistry, University of Oxford, under the supervision of Professor Robert S. Paton. No part of this thesis has previously been submitted for a degree in this University or elsewhere. The work of other authors has been freely drawn and is duly acknowledged in the text. A list of references is given at the end of this thesis.

Publications

Publications describing work in this thesis:

1. "α- and α'-Lithiation-Electrophile trapping of N-thiopivaloyl and N-t-butoxythiocarbonyl α- substituted Azetidines: rationalisation of the regiodivergence using NMR and computation" **Jackson, K. E.**; Mortimer, C. L.; Odell, B.; McKenna, J. M.; Claridge, T. D. W.; Paton, R. S.; Hodgson, D. M. *J. Org. Chem.* **2015**, *80*, 9838–9846, *Featured Article*.

2. "Enantioselective Desymmetrization of Prochiral Cyclohexanones via Organocatalytic Intramolecular Michael Additions to α,β-Unsaturated Esters" Gammack-Yamagata, A. D.; Datta, S.; **Jackson, K. E.**; Stegbauer, L.; Paton, R. S.; Dixon, D. *J. Angew. Chem. Int. Ed.* **2015**, *127*, 4981–4985.

3. "Catalytic Enantioselective Synthesis of Indanes via Cation-Directed 5-Endo-Trig Cyclization" Johnston, C. P.; Kothari, A.; Sergeieva, T.; Okovytyy, S. I.; **Jackson, K. E.**; Paton, R. S.; Smith, M. D. *Nature. Chem.* **2015**, *7*, 171-177.

Other publications

1. "Computational Organic Chemistry" **Jackson, K. E.**; Jaffar, S.; Paton, R. S. *Annu. Rep. Prog. Chem., Sect. B*, **2013**, *109*, 235-255.

Glossary of abbreviations and acronyms

Å	Angstrom (10^{-10} m)
AO	atomic orbital
Ar	aromatic group
B3LYP	Becke exchange with Lee-Yang-Parr correlation
B3LYP-D3	B3LYP with Grimme's D3 dispersion correction
Boc	*tert*-butyloxycarbonyl
Botc	*tert*-butyloxythiocarbonyl
Bu	butyl group
CBS	complete basis set
CBS-QB3	composite *ab initio* method, using B3LYP geometries and frequencies
CCSD	coupled cluster singles doubles method
CCSD(T)	coupled cluster singles doubles with perturbative estimate for connected triples
CGO	compiled graphics objects
CPCM	conductor-like polarisable continuum model
DCM	dichloromethane
DFT	density functional theory
dr	diastereomeric ratio
ECP	effective core potential
ee	enantiomeric excess
Et	ethyl group
EtI	ethyl iodide
GGA	generalised gradient approximation
GIAO	gauge-including atomic orbital
GTO	Gaussian type orbital
HF	Hartree-Fock
IRC	intrinsic reaction coordinate
K	Kelvin
kcal/mol	kilocalories per mole

kJ/mol	kilojoules per mole
LANL	Los Alamos National Laboratory
LSDA	local spin density approximation
M06-2X	Minnesota 06 density functional with 54% HF exchange
MCMM	Monte Carlo multiple minimum
Me	methyl group
MM	molecular mechanics
MO	molecular orbital
MUE	mean unsigned error
n_N	NBO computed occupancy of N lone pair
NBO	natural bond orbital
NICS	nucleus independent chemical shift
NMR	nuclear magnetic resonance
NR	no reaction
PCM	polarisable continuum model
PES	potential energy surface
Ph	phenyl group
Piv	pivaloyl
PM6	semi-empirical method by Stewart
PM6-DH2	semi-empirical PM6 with explicit dispersion and H-bonding correction terms
QM	quantum mechanics
RAMP	(*R*)-1-amino-2-methoxymethylpyrrolidine
RT	room temperature
SAMP	(*S*)-1-amino-2-methoxymethylpyrrolidine
SCRF	self-consistent reaction field
SMD	density based continuum solvation model by Truhlar
STO	Slater type orbital
THF	tetrahydrofuran
tPiv	thiopivaloyl
TS	transition structure
TSEE	total steric exchange energy
TST	transition state theory

UAKS	United Atom Topological Model parameterised for Kohn Sham DFT
UFF	Universal Force Field
wB97XD	dispersion corrected density functional by Head-Gordon
ZPE	zero point energy

1 Introduction

1.1 Computational Chemistry

Computational Chemistry is a multidisciplinary area of research which transcends the borders conventionally separating Mathematics, Physics, Chemistry, and Biology. It makes use of Theoretical Chemistry methods, incorporating them into efficient computer programs, and applies them in the analysis of structures and properties of a variety of chemical systems. In the last two decades, the Nobel Prize in Chemistry was awarded to outstanding chemists in the field of Computational Chemistry. In 1998, Walter Kohn and John A. Pople received the Nobel Prize for their outstanding contributions to the advancement of our understanding of the electronic properties of chemical systems; the former for his fundamental role in the development of density functional theory (DFT) and the latter for his development of computational methods.[1] More recently, in 2013, the award was again given to Computational Chemists: Martin Karplus, Michael Levitt and Arieh Warshel, for "the development of multiscale models for complex chemical systems".[2]

The building blocks for Computational Chemistry were laid close to a century ago, with the development of what are today perceived as fundamental principles in quantum chemistry. Work by Fritz London, Walter Heitler and Erwin Schrödinger in the 1920s, and by Linus Pauling, Henry Eyring and Edgar Wilson in the decades that followed, was essential in this endeavour. With the invention of the first computers in the 1940s, solutions to the complex wave equations for small atomic systems were finally obtainable. In the years proceeding, significant improvements in computer technology resulted in the completion of increasingly more complicated calculations. The first *ab initio* Hartree-Fock electronic structure calculations were performed at MIT in 1950s, with the implementation of a basis set of Slater orbitals in order to simulate simplistic diatomic molecules.[3] In 1964, the Hückel method was utilised in calculations using a linear combination of atomic orbitals, for the determination of electron energies in molecular orbitals of simple conjugated cyclic systems.[4] The 1970s saw the introduction of

a number of efficient *ab initio* computer programs, including Gaussian, which has been expanded and modified significantly since, and has subsequently been used extensively for the work contributing to this thesis.[5]

In recent years, developments in the field of Computational Chemistry have further highlighted the increasingly fundamental role it has in contributing to various fields of Chemistry. Constant improvements to computational processing power combined with advances in quantum chemical techniques have resulted in an ever shifting landscape in this branch of Chemistry, with what-is-feasible, being redefined on a regular basis; calculations aimed at making chemical predications can now be performed on timescales competitive not just with synthesis in academia, but also increasingly with industrial experimental work. Today, it is possible to run highly accurate computational simulations (accurate to < 1 kcal/mol) of chemical systems which were impossible, only a few decades ago. In this thesis, we hope to highlight some of our recent implementations of, and contributions to, the ever expanding field of Computational Chemistry.

1.2 Quantum Mechanics

Quantum mechanics forms the basis upon which all high level calculations, from *ab initio* to DFT, are made.[6] The Schrödinger equation describes the quantum state of a physical system;[7] for our calculations in this thesis, we use the time independent Schrödinger equation,

$$\hat{H}\Psi = E\Psi$$

where Ψ is the wavefunction of the system, E is the energy eigenvalue and $\hat{H}$ is the Hamiltonian operator acting on the wavefunction. Calculating an exact solution to the Schrödinger equation is non-trivial and effectively impossible for all but the most basic, single electron systems, such as the hydrogen atom.

In order for us to use quantum mechanical calculations on chemical systems at a size comparable to those studied in experiment, a number of approximations need

to be made; the most important of these is the Born-Oppenheimer Approximation,[8] which states that due to the much higher mass of the nuclei than electrons (1 amu $>$ 1836 m_e), nuclear motion occurs on a much slower timescale compared to electron motion. This allows us to separate the wave equation into an electronic and a nuclear part:

$$\Psi_{\text{total}} = \Psi_{\text{electronic}} \Psi_{\text{nuclear}}$$

The nuclei in a molecule may be considered to be stationary while the electronic part of the time independent Schrödinger equation is solved in a constant Coulomb potential resulting from the stationary nuclei. Thus, the wavefunction $\Psi_{\text{electronic}}$ is given, which can then be computed quite simply as a function of atomic coordinates, and so yields the concept of a potential energy surface (PES) upon which minima and sadle-points may be located; such positions on the PES can then be connected using knowledge of experimentally observed intermediates, and measured rates and selectivities.[9]

1.3 Basis sets

A basis set is a collection of mathematical functions used to represent atomic orbitals (AOs) irrespective of the quantum chemical method being used.[10] They are typically centred on atomic centres (although this is not essential) and once combined as a sum of linear combinations which are optimized through the course of a calculation, result in the formation of molecular orbitals (MOs). Basis functions do not have the exact same shape as genuine AOs, and so a number are usually summed together to gain an acceptable description of the AO shape. As a general rule, the larger the basis set used, the more accurate the description of the overall molecular wavefunction; in theory, an infinitely large basis set is required but such a calculation would be impossible to run to completion. Mathematical functions which replicate decent wavefunctions efficiently have been the focus of much development; this has utilised the variation principle, which states,"any wavefunction constructed as a linear combination of orthonormal function will have its energy greater than or equal to the lowest energy (E_0) of the system"; using this, the quality of truncated expansions can be judged by evaluating the associated en-

ergy. However, as is so often the case in Computational Chemistry, we must find a balance between accuracy and computational cost. It is required that a chosen basis set is large enough to describe changes in electronic structure that occurs upon bonding; as a consequence of this, they include more flexible representations of the valence orbitals than core orbitals.

1.3.1 Slater Type and Gaussian Orbitals

The most basic, minimal basis sets, which are based upon hydrogenic atomic orbitals, are known as Slater Type Orbitals (STO).[11] Orbitals constructed are of the form e^{-r}, and thus replicate exact eigenfunctions of the Schrödinger equation for a single electron system. In this thesis, we have used the more common, Gaussian Type Orbitals (GTO), which rely on e^{-r^2} Gaussian functions to mimic Slater-type orbitals; the product of a pair of Slater functions can be approximated to any accuracy by a sum of Gaussians - the difficult Slater integrals then become relatively easy contracted Gaussian integrals, which may be solved analytically. GTOs have the advantage that the product of two Gaussian functions centred on different particles can be expressed as another Gaussian function centred between the original centres. The radial component of GTOs differs from that of STOs since they do not have a cusp which is present in STOs. For this reason, to accurately replicate the radial shape of STOs, multiple GTOs are required. Despite the obvious higher computational cost of this, the use of GTOs in Computational Chemistry have become commonplace as a result of their greater accuracy in describing many body systems.

It is a requirement when describing typical organic systems that the basis functions we choose to use allow for core electrons to approach the nucleus and for valence electrons to delocalise. Single-ζ basis sets in which one function is used for every occupied orbital are inadequate in such descriptions, and instead double-ζ basis sets are used where the effective size of the basis set is doubled. Pople introduced an alternative in which a single-ζ representation of the core electrons, with double- or triple-ζ used for the valence electrons; since the majority of chemical reactions studied computationally primarily involve valence electrons, these basis sets pro-

vide an effective and computationally efficient solution. The nomenclature for a typical split-valence double-ζ basis set takes the form X-YZG, in which X defines the number of primitive Gaussians describing each core atomic orbital basis function; Y and Z represent the valence orbitals, and indicate that the first of which is comprised of Y primitive Gaussian functions, and that the other is composed of a linear combination of Z primitive Gaussian functions. The G simply indicates that Gaussian primitives have been used. For larger, triple- or quadruple-ζ basis sets, additional numbers are added after the hyphen. The addition of further basis functions can aid in the description of the electron distribution, by using polarisation functions, and the electron density, by using diffuse functions.

1.3.2 Polarisation functions

Adding polarisation functions allows us to better describe the effects of electron distribution in chemical systems. Polarisation functions are orbitals of higher total orbital angular momentum than those usually occupied in the separated atom. For example, the carbon atom only has s- and p-type occupied orbitals, and if we were to introduce d-type and f-type basis functions to the description, we would consider these to be polarisation functions. The nature of these higher angular momentum orbitals results in a reduced rate of decay upon moving away from the nucleus, allowing for an expanded volume of electron density to be modelled; this is essential when investigating electron rich, or anionic systems.

1.3.3 Diffuse basis functions

Diffuse basis functions are added to a basis set in order to represent broader electron distributions; the basis functions themselves are usually s-type or p-type. These diffuse basis functions have very small exponents and they are especially important when describing electron density in anions and intermolecular complexes, where electron density may be spread over a large region.

1.3.4 Relativistic effects

When dealing with elements from the lower rows of the periodic table, it is necessary that relativistic effects are taken into account. Electron speed in lighter elements is relatively slow but in heavier elements with higher atomic numbers, electrons in orbitals close to the core reach speeds approaching the speed of light, and relativistic effects become non-negligible.[12] This phenomenon is notably responsible for radial contraction of the penetrating s and p shells and the non-penetrating d and f shells becoming more diffuse; it is also results in spin-orbit splitting of p, d and f shells. We can roughly quantify the relativistic effect by looking at the Bohr model for the hydrogen atom, which states that the radius of the first orbital, r_{1s}, is equal to:

$$r_{1s} = \frac{\hbar^2}{me^2} \tag{1}$$

where $\hbar$ is the reduced Planck's constant, m is the electron rest mass and e is the elementary charge. The velocity of an electron in a hydrogen-like 1s orbital is equal to the nuclear charge, Z,

$$v_{1s} = Z \tag{2}$$

According to Einstein's theory,[13] the mass of an electron is described by:

$$m = \frac{m_0}{\sqrt{1 - \frac{v^2}{c^2}}} \tag{3}$$

where m_0 is the mass of an electron at rest, v is the speed of the electron and c is the speed of light. From this analysis, we see that increase in mass will be particularly significant for heavier atoms. Relativistic effects are not taken into account in the previous discussion of the description of atomic and molecular orbitals, however, their effects can not be discarded in chemical systems containing heavy atoms. For this reason, an effective core potential (ECP) is often applied to core orbitals when dealing with such atoms, while valence electrons are described using the Gaussian

functions discussed in section **1.3.1**.

In the commonly used Los Almos National Laboratory (LANL) basis sets, an ECP or pseudopotential, is applied in the handling of elements heavier than neon. The ECP parameters for elements spanning the range sodium to krypton are derived from atomic wavefunctions obtained in high level all-electron non-relativistic Hartree Fock (HF) calculations; for elements in the range rubidium to bismuth, relativistic HF calculations are used.[14]

1.3.5 Summary

In this thesis, we have primarily used Pople split-valence, double- and triple-ζ basis sets with combinations of polarisation and diffuse basis functions. In our description of heavier atoms, we used the LANL2DZ double-ζ basis set which contains an ECP. In all cases, our decision as to which basis set to use was based upon a balance between computational cost, and chemical accuracy.

1.4 Density functional theory

In our study, all high level QM calculations have been performed using DFT.[15] The groundwork for this technique was established by Kohn and Hohenberg in the early 1960s;[16] they proved that the ground state energy of a system could be defined by the electron density distribution which is a function of position, ρ(r) alone, thus reducing the computational demands of many bodied systems. The energy of the molecule is a function of electron density, E(ρ), making this a function of a function, hence the term 'functional' is used to describe this method.[17] The computational cost of DFT based methods scale as between N^3 and N^4, while conventional Hartree-Fock (HF) scales as N^4 and MP2 scales as N^5, where N represents the number of basis functions used. This reduces the computational cost of calculations and enables the study of larger molecular systems. In addition to this, DFT computations converge more quickly with respect to basis-set-size.

1.4.1 Kohn-Sham

Kohn-Sham equations can, in principle, be solved exactly to obtain a description of non-interacting electrons moving in an effective potential.[18] However, various approximations have to be used to describe the interelectronic interaction component. This is because the precise mathematical form of the exchange-correlation functionals is unknown except for the free-electron gas. Therefore, alternative approximations are used to describe interelectronic interactions. The exchange-correlation energy is calculated using an approximate form of the electron density. This is achieved by evaluating the functional derivative of the exchange-correlation energy. Equation 4 shows the ground state electronic energy, E, is the sum of kinetic energy, E_K, the electron nuclear interaction energy, E_V, the Coulomb energy, E_J, and the exchange-correlation energy, E_{XC}.

$$E = E_{\mathrm{K}} + E_{\mathrm{V}} + E_{\mathrm{J}} + E_{\mathrm{XC}} \tag{4}$$

All terms in Equation 4 are dependent on the total electron density, ρ(r) (Equation 5), with the exception of E_K.

$$\rho(r) = \sum_{i=1}^{N} \mid \psi_i(r) \mid^2 \tag{5}$$

In Equation 5, ψ_{i} are Kohn-Sham orbitals and the summation is performed over pairs of electrons. The Kohn-Sham orbitals are single particle wavefunctions and take the form shown in Equation 6.

$$\left(-\frac{\hbar^2}{2m}\nabla^2 + \nu_{eff}(r)\right)\psi_i(r) = \epsilon_i\psi_i(r) \tag{6}$$

In Equation 6, $\nu_{eff}(r)$ is Kohn-Sham potential and ϵ_i is the orbital energy of the corresponding Kohn-Sham orbital.

1.4.2 Exchange-correlation

A variety of functionals are implemented in this thesis, for which exchange-correlation is described in different ways. The dependence of a functional energy on the electron density is expressed as an interaction between the electron density, $\rho(r)$ and the energy density, ϵ_{XC}, which is itself a functional of electron density:

$$E_{XC}[\rho(r)] = \int \rho(r)\epsilon_{XC}[\rho(r)]dr \tag{7}$$

One method by which exchange-correlation is handled is with the local density approximation (LDA) which assumes that energy density is dependent only on the local value of electron density. Empirical constants for this are chosen to fit numerical results from quantum Monte Carlo simulations of uniform electron gases. This method is improved to yield the generalised gradient approximation (GGA) in which energy density is made dependent not only on the local value of electron density, but also on the extent to which the density is changing. B3LYP is a hybrid-GGA, in which a combination of Hartree-Fock exact exchange along with LDA and GGA exchange is incorporated.[19–21] For example, Equation 8 shows the form of the exchange-correlation term in the commonly used B3LYP functional:

$$E_{XC}^{B3LYP} = E_X^{LDA} + a_0(E_X^{HF} - E_X^{LDA}) + a_X(E_X^{GGA} - E_X^{LDA}) + E_C^{GGA} + a_C(E_C^{GGA} - E_C^{LDA}) \tag{8}$$

where $a_0 = 0.2$, $a_x = 0.72$ and $a_c = 0.81$; E_X^{GGA} and E_C^{GGA} are GGAs from the Becke 88 exchange functional[22] and the correlation functional of Lee, Yang, Parr for B3LYP; E_C^{LDA} is the Vosko-Wilk-Nusair LDA to the correlation functional.[23] More recent functionals such as M06-2X, make use of meta-GGAs, which allow energy density to also be dependent on the Laplacian of the electron density which is equivalent to the gradient of the kinetic energy density.[24]

1.4.3 Dispersion

Recently, it has become more common for functionals to contain a London dispersion correction term in order to better describe long-range interactions in chemical systems.[25,26] One of the most popular means by which dispersion is included is through the use of an atom-pairwise London dispersion correction, known as DFT-D, which corrects for the $1/R^6$ dependence of the dispersion interaction energy on the interatomic distances in DFT functionals lacking an appropriate description of long-range dispersion interactions. The wB97XD functional, which is applied in this thesis, uses this type of long-range dispersion correction. Dispersion-corrected DFT is another method by which the effects of dispersion are modelled; functionals such as B3LYP-D3, make use of a preexisting functional but include an add-on energy term for handling of dispersion, which in this case is Grimme's D3 correction.[21] Such dispersion corrections have proven to result in significant improvements to the accuracy of conventional functionals, and the added computational cost of the correction is negligible.[27]

1.4.4 Summary

In this thesis, a number of different density functionals were used, depending on the chemical system being investigated in each case. The hybrid meta-GGA functional, M06-2X, which contains a local spin kinetic energy density term in the exchange-correlation functional, has been shown to be effective at modelling thermochemical and kinetic parameters, particularly when non-local dispersion interactions are important; it was used for the entirety of our investigation into the mechanism and selectivity of intramolecular Michael additions. This functional, along with the dispersion corrected range-separated hybrid functional, wB97XD, were used in our study of regioselective cyclisations. In our investigation into stereoelectronic effects of α-alkylation of bicyclic enamines, previous work indicated that the B3LYP functional was effective at describing such systems. We also employed the dispersion-corrected DFT method, B3LYP-D3, in our later study of this system. After an extensive benchmarking study, we opted to once again use the M06-2X functional for our research into thermochemical kinetics of azetidine

conformational behaviour.

1.5 Semi-empirical methods

Semi-empirical methods are based on Hartree-Fock but include a number of approximations and include parameters taken from empirical data. As a result of this, they are significantly faster than full QM methods, allowing them to be applied when studying larger chemical systems or in conformational searching techniques where many molecules need to be screened in a short space of time. Furthermore, due to its parameterisation, electron correlation effects can be captured by this technique (unlike in pure Hartree-Fock).[28]

Severe reductions in the number of basis functions considered in many semi-empirical models results in an overall reduction to system size; treatment is restricted to valence electrons only, with electrons in the core orbitals being ignored. In addition to this, the basis set is further restricted to a minimal valence representation only: for main group elements, a single s-type function is used along with a set of p-type functions, while for transition metals, a set of d-type functions is also added. Elements in the second period, for instance, would be represented using just 2s, $2p_x$, $2p_y$ and $2p_z$, orbitals, and for a first-row transition metal, $3d_{xy}$, $3d_{yz}$, $3d_{zx}$, $3d_{x^2-y^2}$, $3d_{z^2}$, 4s, $4p_x$, $4p_y$ and $4p_z$, orbitals would be used in their representation. Hydrogen is represented by a single 1s function. All semi empirical calculations in this thesis are performed on molecules containing only elements from the first, second and third periods of the periodic table.

The main approximation used to reduce overall computational costs, is that there is no overlap between atomic orbitals residing on different atomic centres, that is to say,

$$\int \psi_a \psi_b d\tau = 0$$

where ψ_a and ψ_b are orbitals not on the same atom. This is known as the Neglect of Diatomic Differential Overlap approximation and it restricts the number of

electron-electron interaction terms from N^4 down to N^2, where N is the total number of basis functions. Further approximations may be made in the interest of providing a framework for the introduction of empirical parameters, and to simplify the overall calculation. Parameterisation is performed through the reproduction of a wide range of experimental data, which includes: equilibrium geometries, ionisation potentials, dipole moments and heats of formation.[29]

In this thesis, we use the augmented PM6 Hamiltonian, PM6-DH2. The PM6 model was parameterised using 80 elements and has proven to be one of the most accurate semi-empirical methods across a range of investigations.[30] The DH2 component is an added correction to handle dispersion and hydrogen-bonding interactions.[31]

1.6 Molecular mechanics

Molecular mechanics (MM) employs a classical mechanics description of molecular structure and bonding and is not dissimilar to simple ball-and-spring models.[32] The atoms in a molecule are described as a collection of single particles, each with a predefined radius, charge, and sometimes polarisability, held together by elastic and simple harmonic forces. In the most simple force fields, force constants are chosen to fit either an experimentally or theoretically determined stretching constant, about a reference equilibrium bond length. In addition, angle-bending and dihedral rotational terms are included along with classical electrostatic and approximate van der Waals forces to generate a molecular force field. This is summarised in Equation 9, which shows all the energy contributions that make up the E^{strain} of a system; it defines the potential energy as a function of the internal coordinates of the molecule, and can therefore be used to optimise the structures.[28]

$$E^{\text{strain}} = \sum_{A}^{bonds} E_A^{stretch} + \sum_{A}^{bond\ angles} E_A^{bend} + \sum_{A}^{torsion\ angles} E_A^{torsion} + \sum_{A}\sum_{B}^{non-bonded\ atoms} E_{AB}^{non-bonded} \tag{9}$$

The advantage of using MM methods over other more sophisticated QM ones is the speed afforded by their simplicity. With the exception of very small systems, the computational cost of these calculations primarily stems from the non-bonded term, which is comprised of van der Waals and Coulombic interactions; these scale with the square of the number of atoms in a system but at longer range the magnitude of interactions drops off and scaling becomes effectively linear if these terms are neglected. Due to the high speed at which these calculations may be performed, MM calculations have proven invaluable in techniques like conformational analysis where the relative energy of many structures (E_{rel}) needs to be assessed. However, because the overall energy of systems calculated with MM is the summation of contributions arising from distortions within the structures, the E_{rel} may only be used for the comparison of structures with the same bonding and atomic configuration (i.e. for conformational analysis).

1.7 Coupled cluster theory

Broadly speaking, coupled cluster theory is a mathematical technique used to describe many-bodied systems. In the field of Computational Chemistry, it allows for the Schrödinger equations to be solved in post-Hartree-Fock *ab initio* methods. It utilises the HF wavefunction with an additional operator which produces a linear combination of excited determinants; this enables a full configuration interaction wavefunction to be described.[6,33] The result is an exact wavefunction found in the basis set approximation, and it allows electron correlation to be estimated much more accurately than in the methods discussed previously. The coupled-cluster wavefunction may be written as,

$$\Psi_{CC} = e^{T}\psi_0$$

Where Ψ_{CC} is the couple cluster wavefunction, T is the cluster operator, and ψ_0 is the ground state wavefunction. The cluster operator used in coupled-cluster theory takes the form,

$$T = T_1 + T_2 + T_3 + ...$$

where T_1 is the operator for all single excitation, T_2 the operator for double excitations, and so on. The exponential operator, e^{T} can be represented as a Taylor series. For a system in which we only consider the T_1 and T_2 cluster operators of T, we can write,

$$e^{\mathrm{T}} = 1 + T + \frac{1}{2!}T^2 + ... = 1 + T_1 + T_2 + \frac{1}{2}T_1^2 + T_1T_2 + \frac{1}{2}T_2^2 + ...$$

Since the number of molecular orbitals and the number of excitations is finite, this series must also be finite. However, these calculations are highly demanding in terms of computational resources, and calculations on systems of more than a dozen electrons are often considered to be computationally unfeasible. For this reason, the cluster operator often only includes singles and doubles (CCSD), as this yields a method that is computationally affordable for many organic systems. The computational demands of this technique are still significant, scaling with N^6; despite this however, the high degree of accuracy shown in describing small organic systems makes this a powerful technique for Computational Chemists. The involvement of perturbative triple excitations in the CCSD(T) method has resulted in it being frequently used as the Computational Chemistry "gold standard", yielding energies which deviate only by $\sim$ 1 kcal/mol from those obtained experimentally provided a large enough basis set is used.[34]

1.8 Solvation models

Solvation in synthetic chemistry can often play a crucial role in reactions. Computationally, we can model explicit solvation by explicitly including solvent molecules within the systems which we are optimising. However, modelling solvation in this way can prove to be computationally expensive with quantum mechanical techniques and conformational issues are bound to arise in the absence of a proper sampling methodology. For this reason, it is often more appropriate for computational chemists to use implicit solvation models.

One type of implicit solvation model applies a homogenous dielectric field across an entire system, effectively averaging the effect of the solvent across the whole

molecular system of interest. This is referred to as a continuum model, the most frequently used of which is the self-consistent reaction field (SCRF) method, where a cavity is defined in which the system being solvated is placed. Terms for cavitation, electrostatic and non-electrostatic interactions contribute towards the total solvation energy ($\Delta G_{solvation}$), which is defined as,

$$\Delta G_{solvation} = \Delta G_{cavity} + \Delta G_{dispersion} + \Delta G_{repulsion} + \Delta G_{electrostatic} \tag{10}$$

where ΔG_{cavity} is the free energy cost of creating the cavity, $\Delta G_{dispersion}$ is the dispersive interaction between solvent and solute, $\Delta G_{repulsion}$ is the repulsive interaction between solvent and solute, and $\Delta G_{electrostatic}$ is the electrostatic interaction between solvent and solute. The field generated by the solute effectively polarises the solute electron density, as does the field generated by the solvent to the solute. Numerous variations of these continuum models exist; in this thesis, we will primarily be dealing with the conductor-like polarisable continuum model (CPCM),[35,36] where the solvent is treated as a conductor and impacts upon the polarisation charge of area between the solute and solvent, and density based solvation model (SMD).[37]

1.9 The potential energy surface

Understanding the form of the potential energy surface (PES) of chemical systems is of great importance to Computational Chemists. The PES itself is multidimensional and is a function of 3N-6 dimensions, where N is the number of atoms in the system of interest. When mapping out a PES, we are interested in locating ground state and transition state structures; locating these stationary points is done through the use of geometry optimisation. In order find a ground state structure, we first use chemical intuition to manually generate a guess geometry, which consists of an array of coordinates we wish to optimise. We then apply a criteria for what constitutes a completed optimisation - the more strict the criteria, the more accurate the optimisation will be in mapping a point on the PES. Finding transition structures (TS) is more complicated than locating ground states, since we need the single coordinate for which the associated force constant is negative.

The direction of the search is obtained by calculating the gradient of the energy and the initial Hessian, a matrix of second derivatives of the energy with respect to the nuclear coordinates. TS geometry optimisations are much more sensitive to the initial guess geometry provided for the calculation than for the location of ground states.

For the work in this thesis, all ground state and TSs discussed were located using Gaussian 09[5] with the use of the Berny algorithm.[38] In order for this technique to work, an accurate initial guess is required; one method through which we can generate accurate guess geometries is by running a PES scan, which uses varied fixed geometries across a range of bond distances, angles or dihedral angles. Confirmation that stationary points located are either minima or TSs is performed through analysis of the harmonic vibrational frequencies. An optimised geometry may be classified as a minima if it has all real vibrational frequencies, and the location of a TS is established by the presence of a single imaginary frequency resulting from a negative force constant.

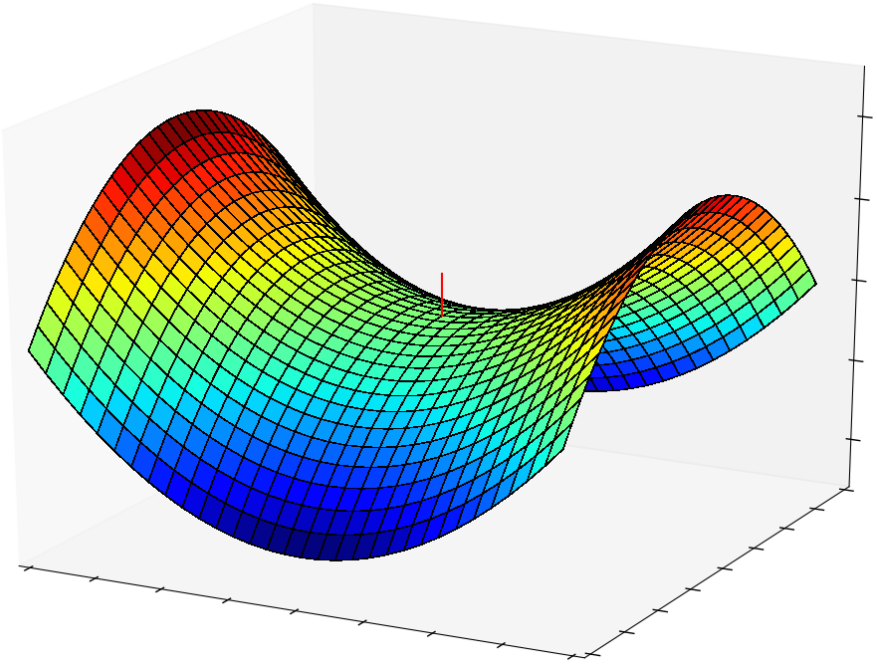

Figure 1.1: Illustration showing the location of the saddle point (indicated by the red line) on a fictitious potential energy surface plot. This image was generated using *Matplotlib*.[39]

1.10 Transition state theory

Transition state theory (TST), also known as activated complex theory, can be used to explain the rates of chemical reactions; it assumes a quasi-equilibrium (where intermediate steps are all close to equilibrium) between reactants and activated transition state complexes. The rate of reactions may be investigated through the examination of activated complexes which lie close to the saddle point on a PES. The activated complexes may change into products; the rate of this conversion may be calculated using kinetic theory.

TST can be used by computational chemists to link computed chemical structures to experimental results, and in the construction of a PES for a reaction, allowing multiple ground state structures to be connected via TSs. **Figure 1.2** shows a simple reaction profile for the bimolecular reaction between A and B to make AB_{prod}. We see that the two ground states are linked *via* the saddle point and

TS, $AB^{\ddagger}$, which may be described by it's Gibbs free energy of activation, $\Delta G^{\ddagger}$, the stability difference between the TS and the preceding ground state. The Gibbs free energy of the reaction is defined as the difference between the reactants and product of the reaction, ΔG_{rxn}.

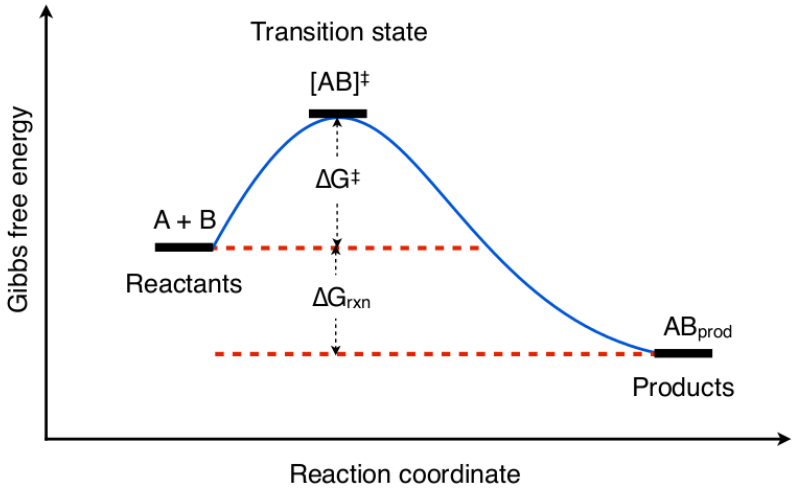

$$\text{Reaction: } A + B \xrightarrow{AB^{\ddagger}} AB_{prod}$$

Figure 1.2: Hypothetical bimolecular reaction profile depicting the reaction between reactants A and B to form AB_{prod} *via* the $AB^{\ddagger}$ activated transition state complex; $\Delta G^{\ddagger}$ is the Gibbs free energy of activation.

The most basic equation for understanding kinetics is the Arrhenius equation, which gives us the rate constant k,

$$k = Ae^{\frac{-E_a}{RT}} \tag{11}$$

where A is the pre-exponential factor, E_a is the activation energy, R is the universal gas constant and T is the absolute temperature. We can manipulate Equation 11 to describe E_a,

$$E_a = RT^2 \frac{d(Lnk)}{dT} \tag{12}$$

We may also apply the Eyring equation to calculate the reaction rate constant

for reactions following TST. For this, we make the assumption that no recrossing is involved from reactants to product, that is to say the TS always results in the product and does not revert back to the reactants. The Eyring equation may be written,

$$k = \frac{K_B T}{h} e^{\frac{-\Delta G^{\ddagger}}{RT}} \tag{13}$$

where K_B is the Boltzmann constant, $\Delta G^{\ddagger}$ is the Gibbs free energy of activation and h is Plank's constant. The Boltzmann distribution states that different energy states will be populated according to $e^{\frac{-\Delta G}{k_B T}}$, where k_B is the Boltzmann constant; if we have a system for which numerous non-degenerate conformers may exist, we can evaluate their relative populations using,

$$\frac{P_1}{P_n} = \frac{e^{\frac{-\Delta G_i}{k_B T}}}{\sum_{i=1}^{n} e^{\frac{-\Delta G_n}{k_B T}}} \tag{14}$$

In Equation 14, we compare the P_1, the population of "conformer 1" compared to the populations of all other conformers, P_n. We can compare the $\Delta G^{\ddagger}$ of different TSs to obtain $\Delta\Delta G^{\ddagger}$ values which may then be used with this equation; this allows for the extraction of computational predictions for diastereomeric and enantiomeric excesses (dr and ee), which allow computational chemists to link their results with those of experimentalists. Since the relationship between the rate constant and calculated selectivities with the Gibbs free energy is exponential, minor errors in computed energies result in major errors in the former.

Using Gibbs free energies of activation $\Delta G^{\ddagger}$, we may compare different TSs to obtain $\Delta\Delta G^{\ddagger}$ values, with which we can use this equation to determine the selectivities of various reactions, yielding computational predictions for diastereomeric and enantiomeric excesses (dr and ee). **Figure 1.3** illustrates the effect minor errors when calculating energy have on the computationally predicted ee when replicating various experimentally derived ees. We see that the effects of error in calculated energies has the most pronounced effect when the selectivity of the modelled system is low; the error is less upon handling systems which are expected to exhibit high degrees of selectivity.

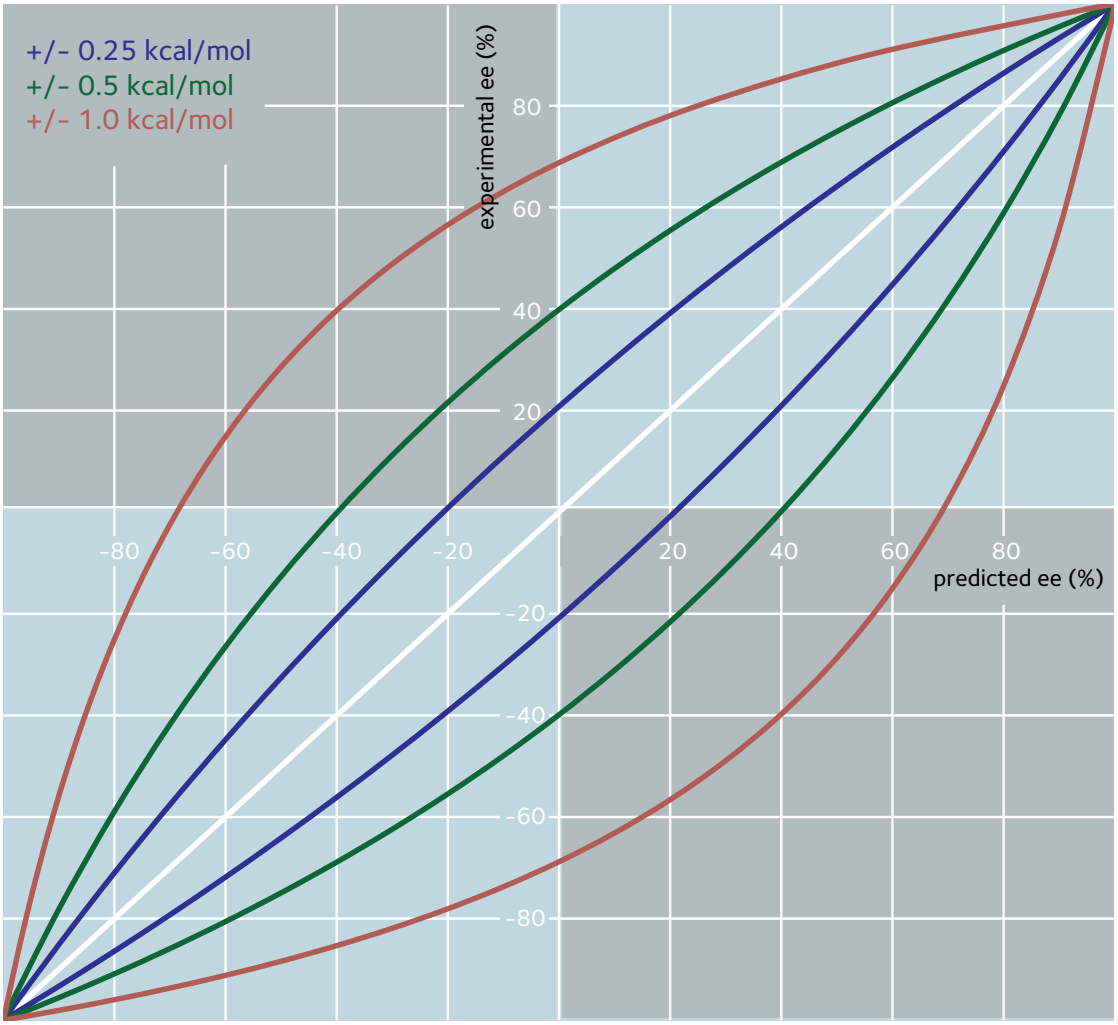

Figure 1.3: Plot showing the effect small errors in energy make to the predicted ee for a system when trying to replicate various experimentally determined ees.

1.11 Monte Carlo conformational searching

The basics for Monte Carlo conformational searching were outlined in Still's seminal paper in 1989, where he describes a random searching method to obtain low-energy conformations of organic molecules using internal coordinates.[40] The technique biases in favour of the more stable regions of the conformational space by selecting starting geometries from previously saved low-energy conformers as the simulation progresses. The inclination of this searching technique to gravitate towards certain regions of conformational space at the expense of others is reduced through the uniform usage of stored structures as input geometries and by using a varying number of torsional rotations in each step. This protocol is termed Monte Carlo Multiple Minimum (MCMM) conformational searching, a summary of which is outlined in **Figure 1.4**. "Test 1" is a constraint test used to: eliminate optimised structures which have energies outside of the selected energetic upper bound relative to the global minimum, determine whether structures have inverted chiral centres, and to eliminate structures with interatomic distances or torsion angles which do not match the explicit user defined distances and torsions set by the user. "Test 2" is another constraint test and is applied to structures prior to optimisation in order to eliminate systems with high-energy nonbonded contacts.

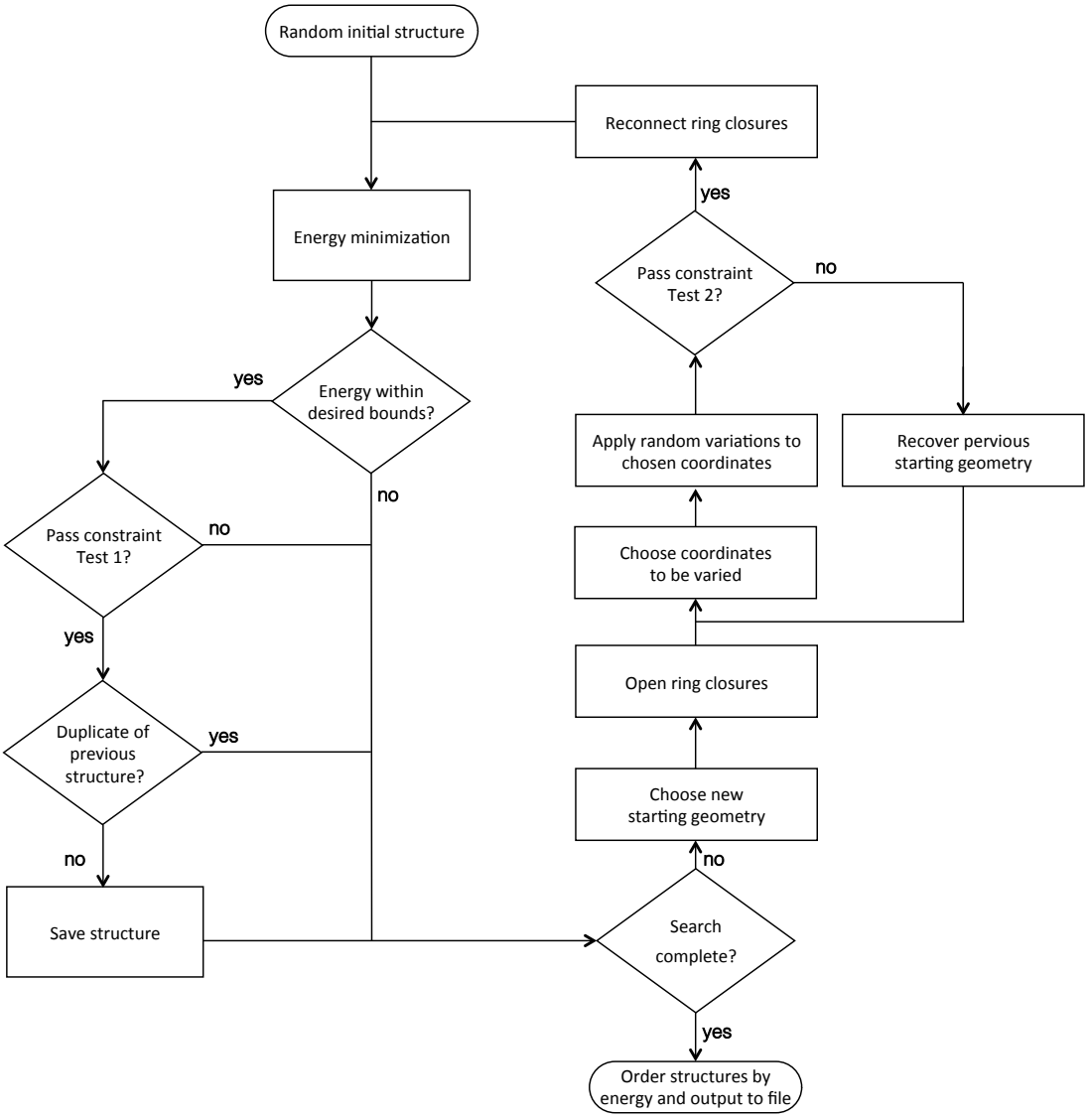

Figure 1.4: A flowchart describing the original MCMM protocol outlined by Still.[40]

Our Monte Carlo Multiple Minimum (MCMM) searching protocol, termed *Full Monte*[41] has been automated through *Python*[42] scripts and proceeds as follows; firstly, a core TS is defined for the step (or steps) of interest in the reaction; this is usually a truncated form of the full chemical system. This approach is similar to that proposed by Prof. KN Houk at the University of California, Los Angeles, for the design of theoretical enzymes or "theozymes".[43] Unfortunately, there are few easy ways to locate a core TS. We use chemical intuition and interpolate from our knowledge of optimised geometries of the reactive species and product(s) to create a candidate structure. We use DFT[15] to perform constrained geometry optimisations[44] followed by full saddle point (i.e. TS) optimisations. This core TS is then functionalised with the full catalyst structure we wish to study. Keeping key bond distances and angles fixed in the core TS, we then use our in-house Monte Carlo conformational searching program in conjugation with low-level semi-empirical or molecular mechanics (MM)[32] optimisations to randomly sample dihedral angles in the TS. Due to the approximate nature of the low-level methods used at this stage in the sampling, it is not sufficient to simply rely on the lowest energy structure generated at this stage; instead, an energy limit is specified, structures below which are reoptimized using a high-level method such as DFT. This approach is outlined in **Figure 1.5**.

1.12 Nucleus independent chemical shifts

Nucleus independent chemical shifts (NICS) allow computational chemists to assess the magnetic environment at any point in space, in or around a chemical system. The technique works by calculating the absolute magnetic shielding at a location, through the use of the gauge invariant chemical shift (GIAO) method,[45] where wavefunctions in the presence of a uniform external magnetic field are determined by self-consistent field (SCF) perturbation theory, and which allows for the computation of magnetic susceptibilities. Schleyer first proposed the use of such calculations in the assessment of the aromatic nature of chemical systems.[46] Since then, NICS analysis has found use in evaluating aromaticity, antiaromaticity and non-aromaticity in structures containing ring systems;[47] more recently, it has

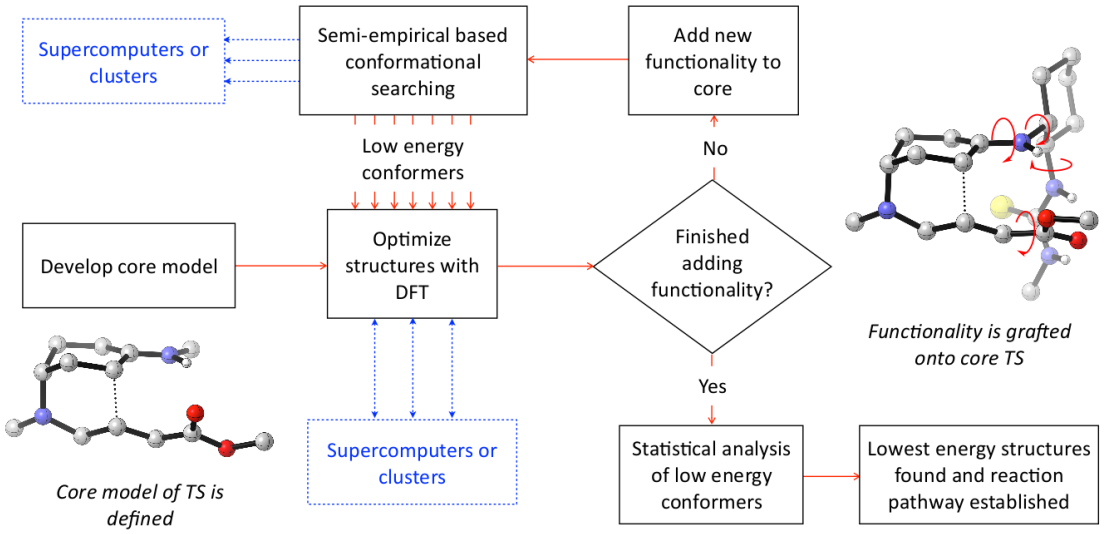

Figure 1.5: An illustration of our approach used for MCMM conformational searching. In this example case, rotatable bonds altered during conformational analysis are shown in red.

been shown that NICS calculations along vectors passing through the centroid of organic[48] and inorganic[49] ring systems can reveal information about the aromatic properties of molecules, intermediates, ions and transition structures.[50–52]

1.13 Marcus equation

Marcus theory was developed to explain the rates in electron transfer reactions (i.e. the rate of intermolecular transfer of an electron from one chemical species to another) but has since found wide spread application in other areas of chemistry.[7,53] The theory itself was initially constructed to investigate outer sphere electron transfer reactions where two chemical species change in their charge due to an electron moving between them, but where no significant structural changes occur (e.g. M^{+}/M^{2+}, where M is a metal). It was, however, later expanded to include inner sphere electron transfer contributions where changes to distances or geometries in solvation, or coordination shells of the chemical species, is also accounted for (e.g. M-O distances in $M(H_2O)_6^{+}$ and $M(H_2O)_6^{2+}$).

Figure 1.6 shows a hypothetical PES for a charge transfer reaction, with reactants and products represented by two parabolas. The two ground states have different equilibrium positions, represented by their differing positions along the reaction coordinate and the energy difference between reactants and products, ΔE_{rxn}, is represented by the different energy minima of the parabolas. λ represents the reorganisation energy of the reaction, which is the change resulting from molecular rearrangement which happens as the charge is distributed throughout the donor-acceptor complex. Marcus made the assumption that the form of the two parabolas for such a system was identical, and therefore it was possible to solve the point of crossing between the parabolas, from which the activation energy, and subsequently the rate constant, could be derived simply from the thermodynamic parameters of the system.

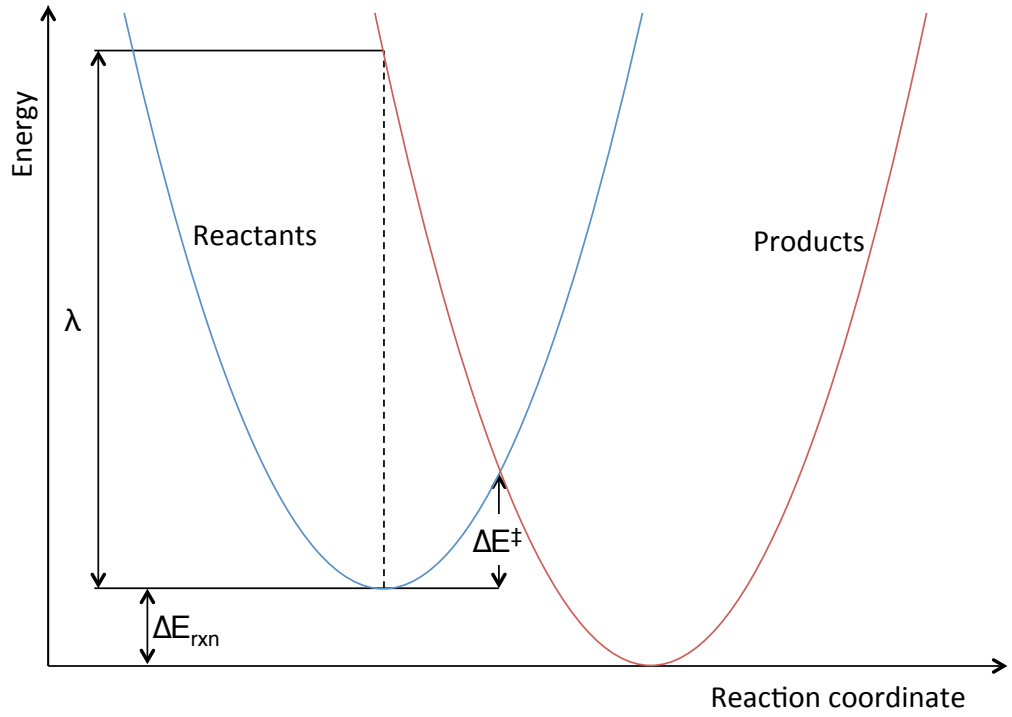

Figure 1.6: An illustration of the PES for reactants and products for a hypothetical reaction. λ is the reorganisation energy, $\Delta E^{\ddagger}$ is the energy of activation and ΔE_{rxn} is the energy change between reactants and products of the reaction.

In this thesis, we use intrinsic reaction barriers (E_0) calculated using the Mar-

cus equation (Equation 15) in order to effectively remove the thermodynamic bias of systems, and reveal the innate stereoelectronics of each reaction more accurately.[54]

$$E_0 = \frac{E^{\ddagger} - \frac{E_{rxn}}{2} + \sqrt{E^{\ddagger 2} - E^{\ddagger} E_{rxn}}}{2} \tag{15}$$

$E^{\ddagger}$ is the activation energy and E_{rxn} is the energy of the reaction, which is the difference in energy between the reactants and products of the reaction.[54]

2 Mechanism and selectivity in intramolecular Michael additions catalysed by primary amines

The morphan motif is an ubiquitous structural feature in numerous biologically important alkaloid natural products (**Figure 2.1**) and is found in over 300 known natural products.[55–57] In addition to this, it is also found in medically relevant compounds, including cytotoxic drug aspernomine, immunosuppressant FR901483 and opioid analgesic morphine.[58] Despite the high frequency with which this core subunit occurs in organic synthesis, methods towards asymmetric synthesis of the six membered nitrogen containing ring are lacking; existing methods using radical induced cyclization[59] or organocatalysis,[60] have resulted in poor yields and modest levels of asymmetry.

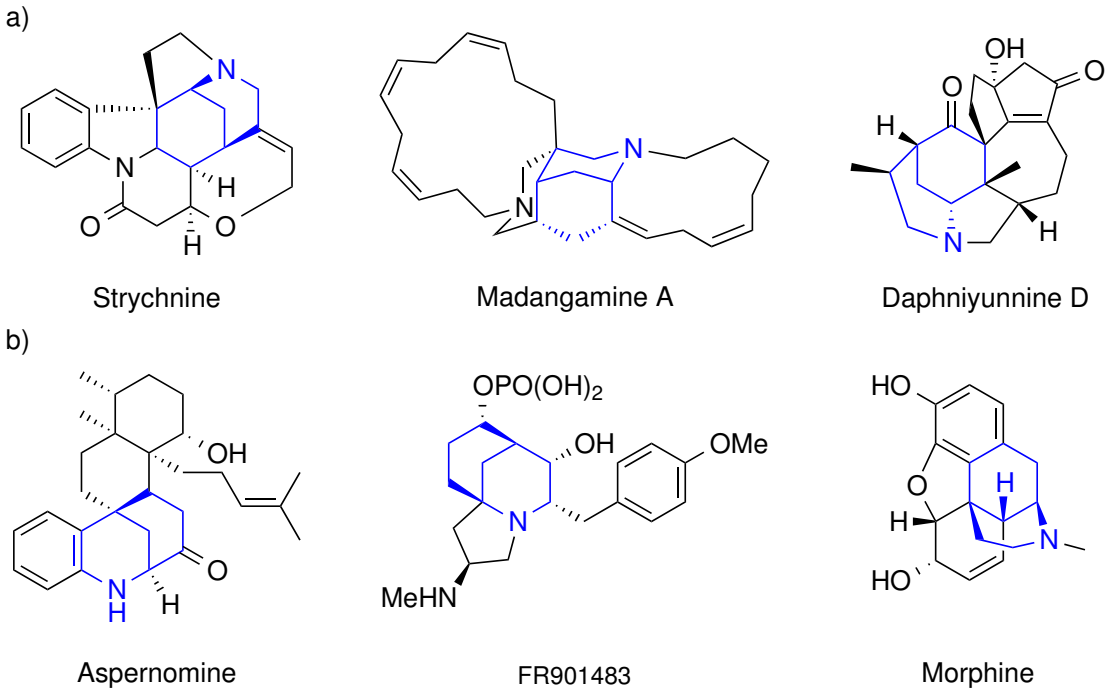

Figure 2.1: Examples of the morphan structural motif in a) alkaloid natural products, and b) bioactive drug molecules.

Recently, Prof. Dixon and coworkers uncovered a reaction which results in high degrees of stereoinduction. The reaction in question was discovered unexpectedly during purification of a ruthenium catalysed cross metathesis product using QuadraSil AP, a propylamine-functionalised silica gel scavenger. Further investigation using other primary amines as catalysts showed that the diastereomeric preference of the reaction was always replicated (>98:2 dr); secondary amines were unsuccessful in eliciting reactivity. Experimentation with chiral primary amine catalysts revealed that a high degree of enantioselectivity could also be imparted in this reaction (up to 97% ee). Through our collaboration with the Dixon Group, we were able to rationalise both the observed diastereoselectivity and enantioselectivity of the system; this resulted in the design and development of a new primary amine catalyst which replicated the previous highest ee but with a higher atom economy.

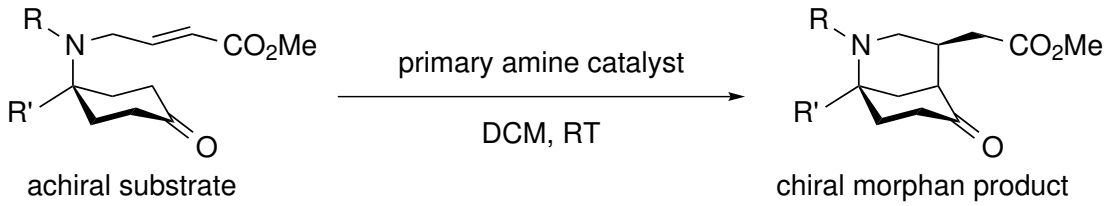

Figure 2.2: Simplified reaction profile for asymmetric synthesis discovered in the Dixon group.

2.1 Background

Large, flexible organic molecules have become commonplace in catalysis[61–63] but detailed insights into the mechanism by which they operate often remain elusive. Such molecules are termed organocatalysts, and they have a wide range of synthetic applications in asymmetric catalysis. Knowledge of how they operate and, in particular, impart selectivity would be invaluable to the development of improved catalyst structures; at present, this is often performed in an *ad hoc* trial-and-improvement manner.

Computation has a valuable role to play in this endeavour since the geometries of transition structures (TSs) can be studied to gain insight into mechanism in

a way not often possible experimentally.[64] Calculations with density functional theory (DFT) were important in the development of small molecule organocatalysts[65] and we hope that we may be able to achieve the same for much larger and more challenging catalyst structures. However, the high degree of conformational flexibility combined with the large number of atoms in the systems of interest presents a considerable computational challenge. At the heart of this challenge is the location and analysis of multiple transition state conformations on a timescale compatible with an on going synthetic project, with sufficient accuracy to generate reliable predictions. This involves a trade-off between precision and speed, which we have addressed through the development of computational protocols that combine calculations at different levels of theory with Monte Carlo[66] searching algorithms.

In recent years, the use of amine organocatalysts has become widespread as a powerful means of imparting asymmetric control in organic synthesis. However, the origins of this branch of catalysis can be traced back to work from the 1970s, when Eder, Sauer and Wiechert found that L-proline, along with a number of other natural amino acids, were able to induce enantioselectivity in the Michael addition of vinyl ketones to cyclic 1,3-diketones to form bicyclic compounds.[67] Around the same time, Hajos and Parrish independently discovered that incorporation of L-proline in the aldolization step for the synthesis of the Wieland-Miescher ketone resulted in a high degree of stereoselectivity.[68]

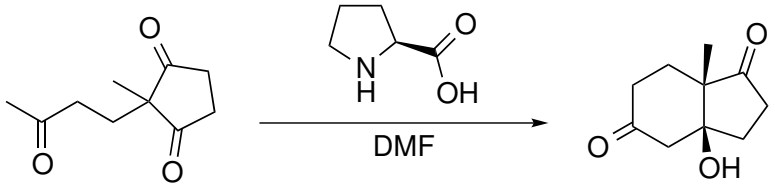

Figure 2.3: Synthesis of asymmetric bicyclic diketone (Weiland-Miescher ketone) discovered by Hajos and Parrish and by Eder, Sauer and Wiechert.

It took almost 30 years before such organocatalysis in asymmetric synthesis reemerged,[62] with work by List, Lerner and Barbas in 2000 showing L-proline and its derivatives to be effective catalysts in enantioselective intermolecular aldol reactions.[69] This work went on to become the subject of computational study,

through which the mechanism was found to proceed *via* an enamine intermediate and concerted C-C bond formation with H transfer from the carboxyl group to the carbonyl,[70,71] rather than *via* the previously accepted mechanism by Agami, involving the use of a second molecule of proline in the rate limiting step of the reaction.[72] This has led to the widespread adoption of the so-called Houk-List model for stereocontrol.

In recent years, other small organic molecules have drawn the attention of synthetic chemists as potential organocatalysts in asymmetric synthesis. Catalysts popularised by Jacobsen and Schreiner, containing the thiourea functional group have shown promise in a range of reactions,[73,74] and computational studies have followed.[75] Enantioselective intermolecular Michael reactions between nitroolefins and acetylacetone using asymmetric thiourea catalysts have been investigated computationally by Papai *et al.*[76] Their study highlights the role of the thiourea moiety, particularly in imparting selectivity by coordinating to, and activating the olefin through an H-bonding interaction with the nitro group. Thiourea containing catalysts have also shown promise in activating carbonyl containing compounds.[77]

The reaction found by Dixon and coworkers, shown in **Figure 2.2**, is another contemporary example of a thiourea containing organocatalyst being used to impart asymmetry in synthesis. The reaction proceeds with a range of R and R' (**Table 2.1**) suggesting a high degree of substrate scope, and a number of products with the morphan motif were synthisised using Jacobsen's thiourea catalyst at a high degree of enantioselectivity and near exclusive diastereomeric ratio of >98:2 dr, which is the upper limit of product assignment through standard H^1 NMR spectroscopy. The catalysts for which the reaction has been shown to work (with and without enantioselectivity) span a range of primary amines; secondary amines and zwitterionic catalysts were shown to be ineffective with no reaction taking place (**Table 2.2**). Our computational analysis of this system provided in depth chemical insight into the reaction's stereocontrol and we were able to propose the design of a new organocatalyst, which was then synthesised and tested experimentally; the new catalyst matched the highest ees and drs observed with previously tested catalysts but with a more efficient atom economy.

Table 2.1: Selected experimental examples showing the scope of desymmetrization using Jacobsen's thiourea catalyst under optimised conditions. *Work carried out by Adam Gammack Yamagata under the supervision of Prof. Darren Dixon.*

	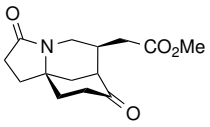	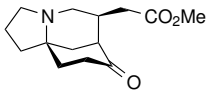	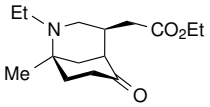
time [h]	40	36	96
yield [%]	88	83	83
ee [%]	93	94	96
	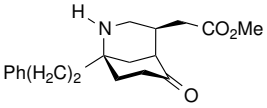	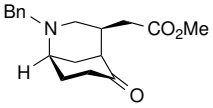	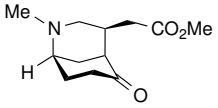
time [h]	96	96	96
yield [%]	92	90	84
ee [%]	84	97	96

2.2 Mechanism

In order to ascertain the origin of enantio- and diastereoselectivity in this reaction, we first need to understand the mechanism by which this reaction proceeds (**Figure 2.2**). There is support in the literature for the order by which similar amine catalysed reactions take place,[62,78,79] and a plausible mechanistic proposal is outlined in **Figure 2.4**. The reaction begins with a condensation addition of the primary amine catalyst to the carbonyl of the substrate **2.4.01** to form imine **2.4.02**. This imine can then tautomerize to the enamine **2.4.03**. Once formed, the enamine can undergo an intramolecular Michael addition with the α,β-unsaturated ester to generate the morphan motif **2.4.04**; at this stage, the stereochemistry at three stereocenters is fixed, and there are two sets of diastereomeric enantiomers possible. A second tautomerization of the substrate-catalyst zwitterionic species reforms the ester **2.4.05** and the catalytic species is then regenerated by hydrolysis, leaving the morphan containing product **2.4.06**.

Table 2.2: Experimental results for various catalysts performing the aforementioned desymmetrization to form the first entry in **Table 2.1**. All reactions were carried out at 45°C with 20 mol% of both catalyst and benzoic acid. *Work carried out by Adam Gammack Yamagata under the supervision of Prof. Darren Dixon.*

	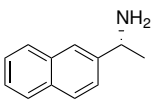	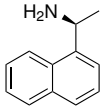	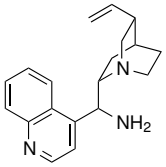	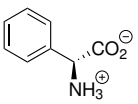	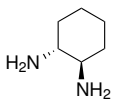
time	5 days	8 days	7 days	NR	24 h
yield [%]	72	74	69	-	82
dr	98:2	>98:2	>98:2	-	>98:2
ee [%]	63	69	31	-	63
		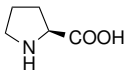	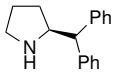	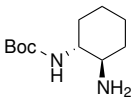	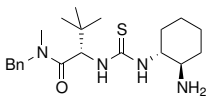
time	NR	NR	NR	22 h	26 h
yield [%]	-	-	-	87	86
dr	-	-	-	>98:2	>98:2
ee [%]	-	-	-	64	90

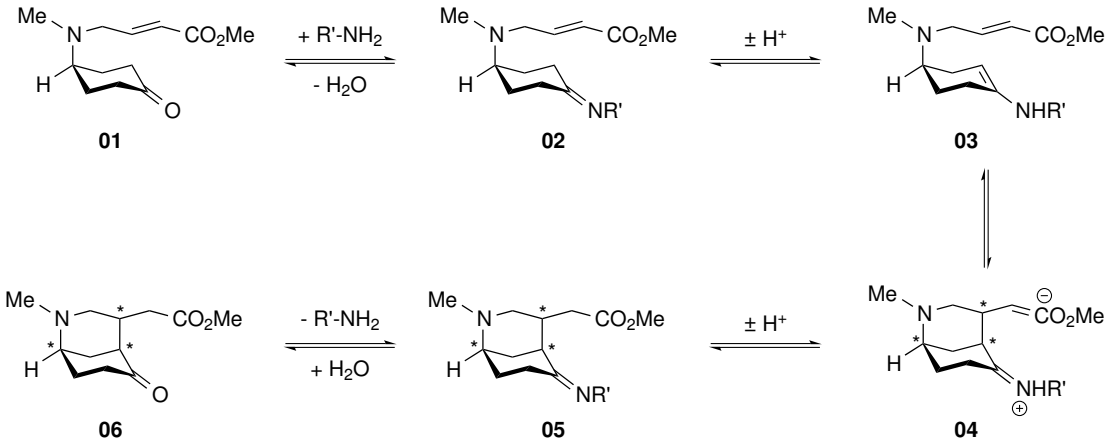

Figure 2.4: Pathway for the reaction; all intermediates and products may be considered racemic where stereochemistry is possible. * indicates the presence of a stereocenter; R' may be chiral or achiral.

2.3 Computational methods

DFT calculations in this section were performed using Gaussian 09[5] using the hybrid meta-generalized gradient approximation functional, M06-2X.[24] This density functional includes a local spin kinetic energy density term in the exchange-correlation functional and has been shown to be effective at modelling thermochemical and kinetic parameters, especially when non-local dispersion interactions are important. Initial geometry optimisations were performed using the Pople 6-31G(d) basis set before key ground states and TSs were then reoptimised using the valence triple-ζ polarised 6-311+G(d,p) basis set.[80,81] Solvent was modelled using an implicit description of dichloromethane (DCM) using a conductor-like polarisation continuum solvation model (CPCM);[36,82] solute cavities were defined by UFF atomic radii.[83] Gibbs free energies were evaluated at the reaction temperature of 45 °C and vibrational entropy contributions towards this value were computed using a free-rotor approximation for low frequency modes. We used a smooth damping function centred about a frequency of 100 cm^{-1} to switch between the harmonic approximation for vibrations above this value and the free-rotor approximations below.[84,85] Translational entropies were calculated using the conventional standards state of 1 mol/l in solution solution for all species *via* the Sackur-Tetrode expression, however, the lack of any associative or dissociative steps in our calculated mechanism means that his has no effect on our results. We computed vibrational frequencies for all stationary points to confirm them as either minima or TSs, based on whether they had zero or a single imaginary frequency respectively. Intrinsic reaction coordinate (IRC) calculations were used to confirm the connection of TSs with the appropriate ground state species on either side of the barrier on the potential energy surface (PES).[86,87]

To cope with the conformational issues associated with computing the lowest energy pathway for flexible organocatalysts, we used a locally modified form of Still's Monte Carlo Multiple Minimum (MCMM) conformational search,[40] using a semi-empirical PM6-DH2 Hamiltonian[31] (with transferable corrections for dispersion and hydrogen-bonding) run through Mopac.[88] When searching for lowest energy TSs, we froze the coordinates of the "core" geometry previously established with

methylamine while conformations of the flexible catalyst were sampled. Conformations within 20 kJ/mol of the global minimum located at the PM6-DH2 level of theory were subsequently reoptimised to minima or saddle points as appropriate at the M06-2X/6-31G(d) level of theory. The lowest energy structures were then reoptimized again using the computationally intensive M06-2X/6-311+G(d,p) with implicit CPCM solvation with DCM.

2.4 Methylamine catalysis

Achiral n-propylamine is able to act as a catalyst for this reaction, resulting in formation of the *endo*-diastereomer (dr of >98:2) and in racemic form. To eliminate additional conformational issues and in the interest of computational simplicity, we used methylamine as an appropriate computational model for n-propylamine in our study; we postulated that the electronics of our chosen catalyst would be almost identical at N and the difference in sterics between the methyl and n-propyl groups would be minimal. Understanding the form of the potential energy surface (PES) with this simplified system would be useful as a starting point when studying more complex catalytic systems.

2.4.1 Accounting for diastereoselectivity

After locating all the stationary points thought to be relevant to this reaction using M06-2X/6-31G(d), we recalculated using the M06-2X/6-311+G(d,p) level of theory with a continuum description of dichloromethane solvent to study the mechanism of the cyclization catalysed by the achiral primary amine; the resulting free energy profile is shown in **Figure 2.5**. We used the M06-2X functional with Pople basis sets as previous studies has shown it to be effective in modelling similar reactions[89] and other organocatalysis studies.[90] In determining which stationary points would be relevant to our system, we looked at other similar reactions which had previously been studied computationally, such as the Michael additions between aldehydes and nitroalkenes reported by Papai and Pihko.[91]

We found condensation of the ketoester substrate **2.5.01** with methylamine to be

marginally endergonic (by 2.4 kcal/mol) upon formation of ketimine **2.5.02**. Of the two possible enamine conformations, it is the *s-cis* enamine **2.5.03**, with the methyl group eclipsing the C=C bond, which is the most stable; the *s-trans* enamine **2.5.04** is less stable by 2.9 kcal/mol. We were not concerned with computing the activation barriers for these steps since relative stereochemistry is not set at this stage with respect to the morphan product. However, previous studies suggest the presence of an acid co-catalyst will accelerate condensation and imine:enamine tautomerization steps.[92]

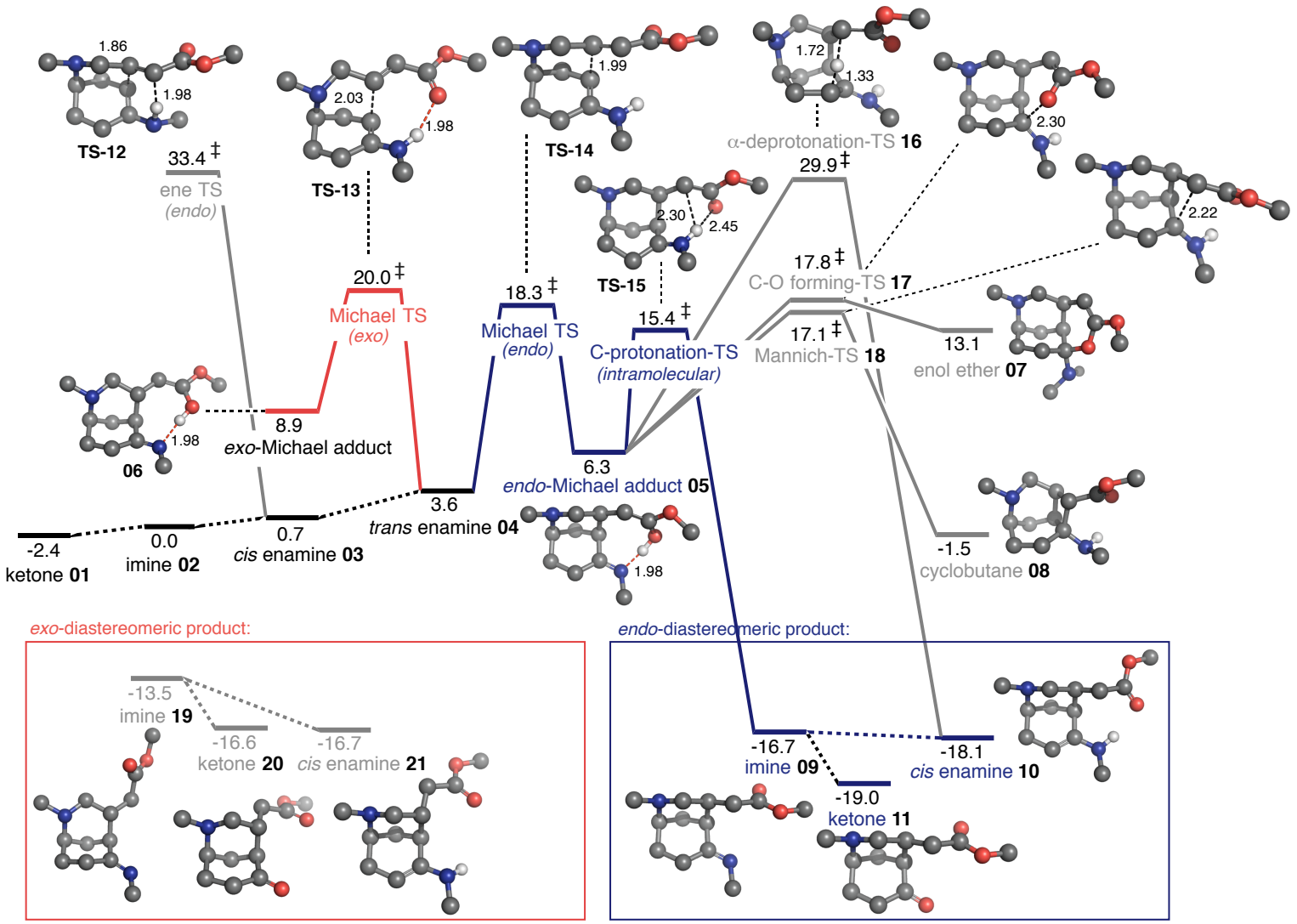

Figure 2.5: Free energy profile for cyclization of ketone starting material catalysed by methlyamine at the CPCM-M06-2X/6-311+G(d,p) level of theory (G_{rel} values in kcal/mol at 45°C, 1 mol/L).

We explored competing pathways leading to C-C bond formation for both (*s-cis* and *s-trans*) enamine configurations. For *s-cis* enamine **2.5.03**, we found the only plausible intramolecular reaction to be an "ene-like" process (via **TS 2.5.12**), in which C-C formation and N-H$\cdots$Cα proton transfer occur simultaneously to form the *endo*-adduct. We can, however, confidently assert that, with a computed activation barrier upwards of 30 kcal/mol, this reaction is energetically unfeasible under the reaction conditions. Conversely, the *s-trans* enamine **2.5.04** was shown to have much lower barriers towards C-C bond formation, largely due to the favourable orientation of the N-H bond towards the developing oxyanionic group of the ester. A Curtin-Hammett scenario[93] emerges in which cyclization occurs exclusively through the thermodynamically less favourable, but considerably more reactive *s-trans* enamine. It is therefore not immediately clear how this leads to near complete diastereoselectivity.

Formation of the *endo*-Michael adduct **2.5.05** proceeds *via* selectivity-determining **TS 2.5.14**. Conjugate addition of the enamine to the β-carbon in this TS occurs with a perfectly staggered conformation (**Figure 2.6**) about the forming C-C bond and has an activation barrier of 14.7 kcal/mol relative to enamine **2.5.04**. IRC calculations confirm that this TS leads to full N-H proton transfer to the oxygen atom of the ester-enolate in intermediate **2.5.05**, which is stabilized by an intramolecular enolic OH$\cdots$N hydrogen bond. The most energetically favourable path available to this intermediate is an irreversible imine-assisted tautomerization*via* **TS 2.5.15**, with a barrier of 9.1 kcal/mol, forming the *endo*-ester Michael adduct **2.5.09**. In the absence of assistance from the imine group, the tautomerization would be thermally disallowed by Woodward-Hoffmann rules as a suprafacial sigmatropic 1,3 shift (the thermally allowed antarafacial equivalent is geometrically impossible),[94] and so this step is not pericyclic.

The labile N-H proton of the primary amine organocatalyst is readily transferred to the ester-enolate upon conjugate addition. For the major *endo*-diastereomer, α-protonation at C is rapid and forms the stable product irreversibly. Importantly, an external proton source is not required to achieve this step. It is also important to note that this mechanistic scenario differs from that encountered in the Michael additions of pyrrolidine-enamines to nitro-olefins; with no comparable

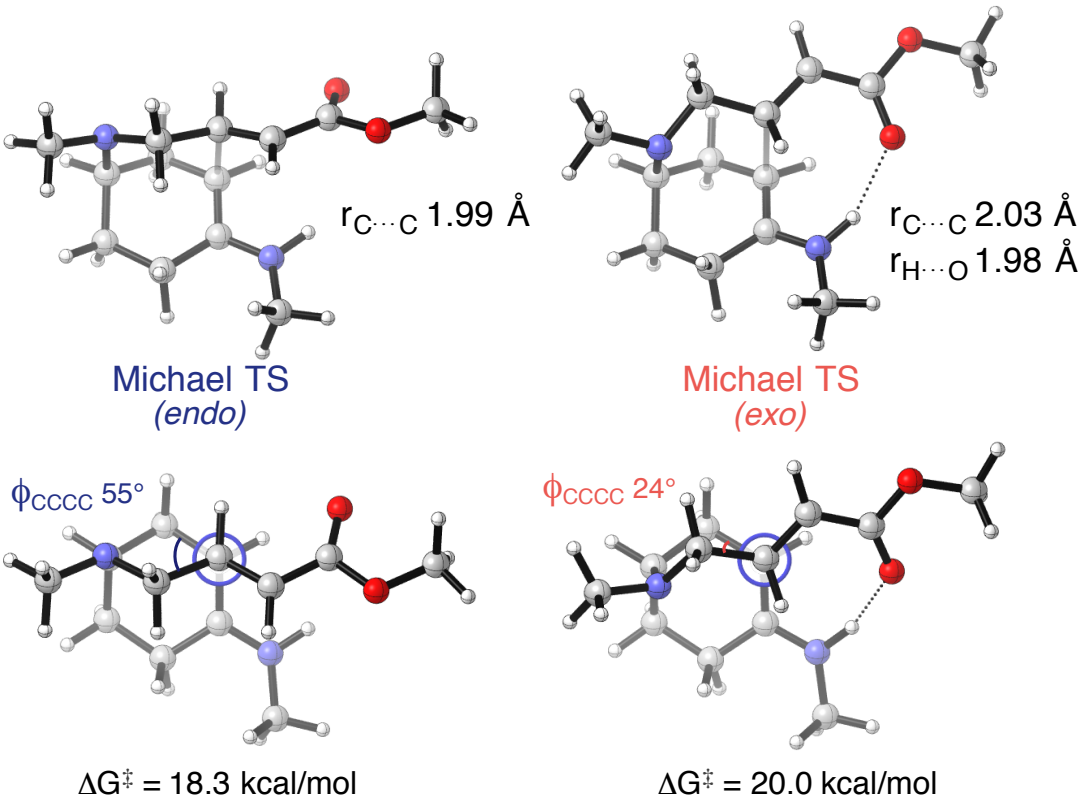

Figure 2.6: Analysis of the competing diastereomic Michael TSs (CPCM-M06-2X/6-311+G(d,p)) for the formation of the *exo*- and *endo*-Michael adducts.

labile N-H proton, protonolysis by an acidic co-catalyst following conjugate addition is turnover-limiting.[91] In the case for organocatalysts containing an internal carboxylic acid, or where strongly acidic additives are used, C-C bond formation has been found as rate limiting in conjugate additions of aldehyde-derived enamine to nitroolefins.[95] The iminium species from primary enamines has an acidic N-H proton upon conjugate addition, which is transferred to the Michael-adduct, making this C-C bond formation irreversible and hence diastereoselectivity determining. Interestingly, initial calculations of the *endo* pathway with the smaller 6-31G(d) basis set yielded a slightly different Michael addition step (**TS 2.5.14**) for which the Michael adduct was the zwitterionic iminium-enolate species. The following C-protonation step (**TS 2.5.15**) was the same for both the 6-31G(d) and 6-311+G(d,p) basis sets.

Another route we postulated for intramolecular proton transfer from *endo*-Michael adduct **2.5.05** is *via* deprotonation α to the imine. This α-deprotonation step shown in **TS 2.5.16** is computed to proceed with a barrier of 23.6 kcal/mol and it is therefore an improbable route to *endo*-diastereomeric product **2.5.10** under the reaction conditions.

We were able to find TSs and intermediates corresponding to the formation of two cyclic intermediates, 6-membered enol ether **2.5.07** and cyclobutane **2.5.08**, both of which have been observed experimentally in Michael additions of pyrrolidine-enamines to nitro-olefins.[96–98] In this case, however, we see that they are both kinetically disfavoured with respect to internal proton-transfer (**TS 2.5.15**) and are therefore not formed. The cyclobutane containing species **2.5.08**, however, is predicted to be thermodynamically more stable than the reactant enamine **2.5.04** by 5.1 kcal/mol and therefore may exist as a potential off-cycle intermediate in the reaction. Conversely, the cyclic enol ether lies much higher in free energy and we do not expect it to play any significant role in this reaction.

The *exo*-reaction pathway, *via* **TS 2.5.13**, which has a higher activation barrier than **TS 2.5.14** of 16.4 kcal/mol, is kinetically disfavoured relative to the *endo*-pathway. Although the N-H proton is able to stabilise the developing oxyanion, eclipsing interactions occur about the forming C-C bond (**Figure 2.6**), which result from adopting a boat-like conformation necessary to maintain the NH$\cdots$O interaction. No other conformation of this *exo*-TS was found. Also important is the fact that, unlike the *endo*-diastereomer, there is no analogous intramolecular mechanism leading to protonation of the ester α-carbon (due to ester group pointing away from the iminium) and so the most likely fate of unstable *exo*-adduct **2.5.06** is a retro-Michael ring opening back to the more stable starting enamine. We are therefore able to conclude that the exclusive favourability of the *endo*-diasteromer results from the irreversible, stepwise, C-C bond formation, followed by intramolecular proton transfer, in which selectivity determining **TS 2.5.14** is perfectly staggered about the forming bond. The C-C bond forming step leading to the minor, *exo*-diastereomer is kinetically disfavoured and the analogous intramolecular proton transfer required to form the stable product is not geometrically possible, making this path readily reversible.

Upon formation, *endo*-adduct **2.5.09** is sufficiently stable such that the retro-Michael reaction is highly improbable, as it would proceed with a barrier of 35 kcal/mol. The relative stability of product enamine **2.5.10** with respect to **2.5.09** (1.4 kcal/mol lower in free energy) is such that, if tautomerization is rapid with respect to hydrolysis, it would be an observable intermediate. Hydrolysis to afford ketone **2.5.11** and regenerate the amine catalyst is also computed to be exergonic, although these steps were not explicitly calculated.

2.4.2 Density functional comparison: M06-2X vs B3LYP-D3

In order to test the validity of our results obtained using the M06-2X density functional, we recalculated all stationary points located on the potential energy surface in **Figure 2.5** using the B3LYP-D3[19–21] level of theory, using the same 6-311+G(d,p) basis set and implicit treatment of solvation by dichloromethane. Both methods capture dispersion effects, albeit in different ways. The recomputed free energy profile is shown in **Figure 2.7**. The geometries of all stationary points are not substantially altered between M06-2X and B3LYP-D3, and the relative energetics from both approaches lead to identical mechanistic conclusions. The *endo*-Michael pathway is once again kinetically favoured and irreversible, while the *exo* is reversible. Alternative cyclization pathways, forming 6-membered enol ether and 4-membered cyclobutane intermediates are viable but still disfavoured relative to proton transfer which again irreversibly forms the *endo*-Michael adduct. This agreement of the mechanistic pathway from another density functional gives us confidence that our conclusions drawn from the previous study are robust with regard to the use of different model chemistries.

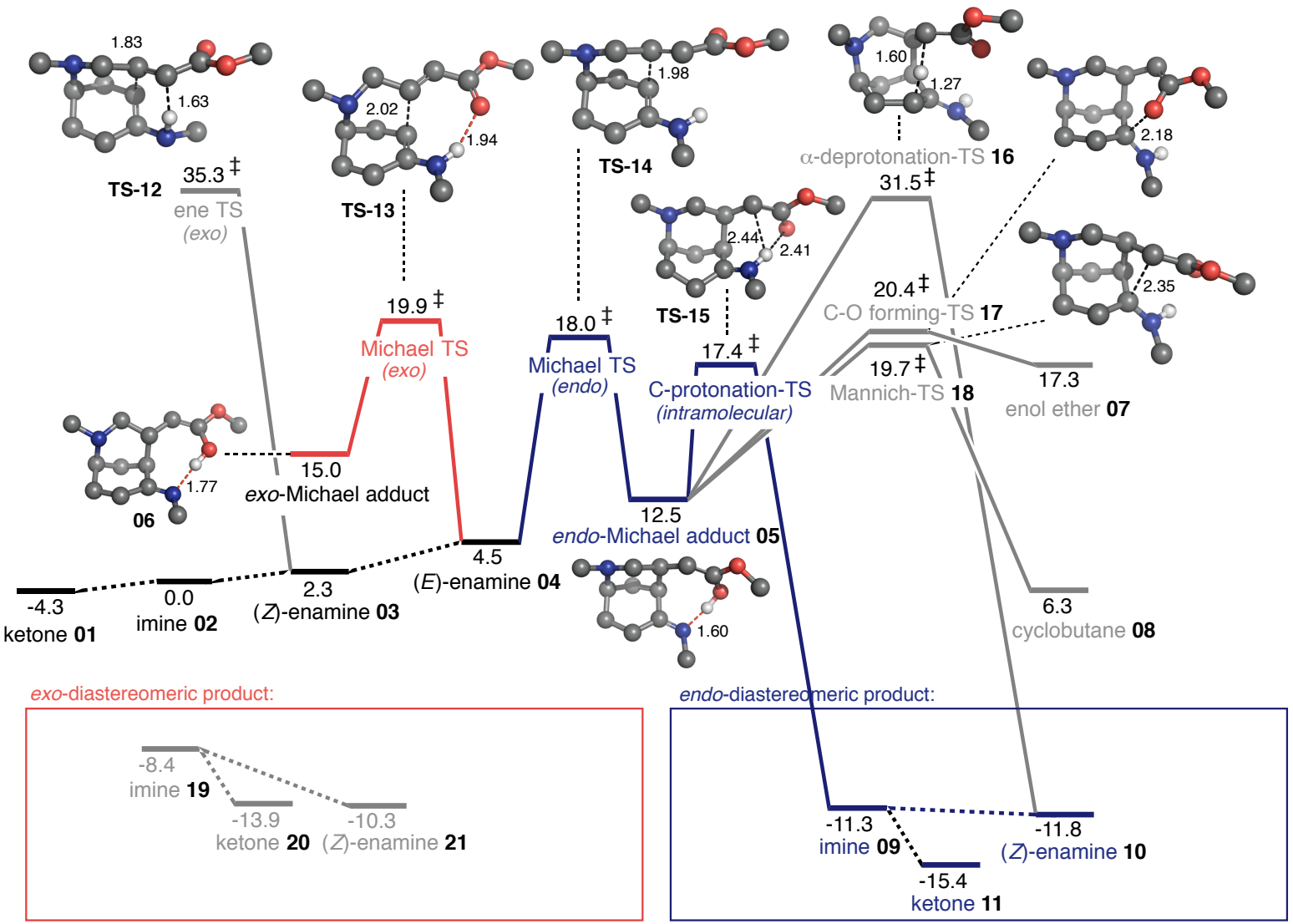

Figure 2.7: Free energy profile for cyclization of ketone starting material catalysed by methlyamine at the CPCM-B3LYP/6-311+G(d,p) level of theory (G_{rel} values in kcal/mol at 45°C, 1 mol/L).

2.5 Chiral aminocyclohexylthiourea catalysis

Experimentally, it was shown that the primary amine thiourea catalyst, **k** in **Table 2.2** (**Figure 2.8a**), resulted in a high degree of enantiocontrol (upwards of 90%, $\Delta\Delta G$ >5.8 kcal/mol at 45°C).[99] From examining this catalyst it seemed that the part most likely to be responsible for imparting catalytic activity upon condensation of the primary amine was the thiourea functionality. Therefore, it seemed sensible to assume that a truncated version of the catalyst would be appropriate for the study of stereoselective intramolecular conjugate addition, and the catalyst shown in **Figure 2.8b** was used in our calculations.

(a) Jacobsen's thiourea catalyst. **(b)** Our truncated thiourea catalyst.

Figure 2.8: Primary amine catalysts containing thiourea functionality

2.5.1 Flexible catalyst modeling

Even with our truncated catalyst, issues arising from the many conformations of the flexible catalyst had to be considered. We needed to ensure that the stationary points we used to construct our reaction schemes were of the most stable conformations in each case in order for us to make accurate stereochemical predictions on the progress of the reaction. In order to ensure this was the case, we employed Monte Carlo searching on key TSs and ground state structures, using our in-house protocol termed *Full Monte*, more details for which are outlined in the section **1.11**. The key assumption in this method is that each intermediate is in thermal equilibrium, and so the most stable conformation will dominate the Boltzmann population.

Erring on the side of caution, the number of steps we chose to run our MCMM search for was of a similar order of magnitude to the total number of possible conformers for the molecule. Assuming 3 minima will be found upon rotation about

each sp^3 hybridized bond, we approximated there should be 3^n possible conformers for each system. Based on this assumption, there should be 81 possible conformers for **TS 2.9a** and 2187 possible conformers for **2.9b**. In reality, however, the true number of computationally isolatable conformers is not this easily defined; bonds with sp^2 character may have only 2 stable rotamers and intramolecular forces may add stability to sterically disfavoured dihedral angles.

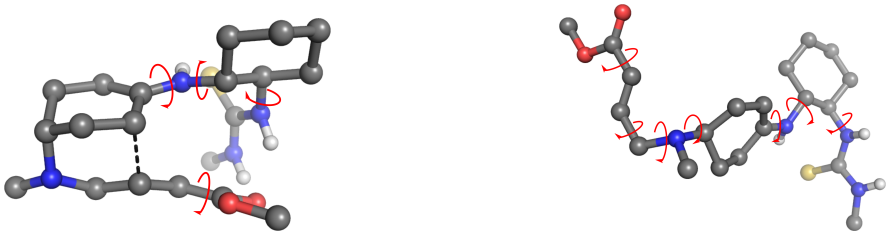

(a) TS with 4 rotatable bonds. **(b)** Ground state with 7 rotatable bonds.

Figure 2.9: Illustrations of rotatable bonds in the aminocyclohexylthiourea catalysed system.

Following an initial benchmarking study, we concluded that 1000 steps was sufficient for our MCMM searches and 4.8 kcal/mol (20 kJ/mol) was a suitable energy threshold (range above the lowest energy conformer) for structures generated by *Full Monte*, optimized using the semi-empirical PM6-DH2 method,[31,100] as subsequent DFT optimization of the low-level results would be unlikely to yield a lower energy, most stable, conformer from outside of this range.

2.5.2 Reaction pathway

There are four stereochemically different morphan-motif containing products which may be formed as products of this reaction, shown in **Figure 2.10**. Products **2.10a** and **2.10c**, and products **2.10b** and **2.10d**, are enantiomeric. In section **2.4** we looked at the formation of racemic forms of the *exo*- and *endo*-products of this reaction, and the overwhelming preference of this reaction to form the *endo*-diastereomer. In the presence of a chiral primary amine catalyst, it is now possible to distinguish between the two enantiomers of the *exo*- and *endo*-products, and, for reasons previously discussed, we would expect the major enantiomer to

come from the latter pair of enantiomers. Despite this, we investigated all C-C bond forming TSs (**Figure 2.13**) which would result in the four possible Michael adducts and, as was the case with methylamine catalysis, formation of the *exo*-adducts (**Figure 2.11**) was found to be disfavoured relative to the *endo*-adducts (**Figure 2.12**).

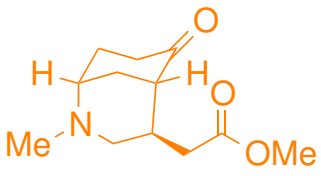

(a) (*R*)-*exo*-product

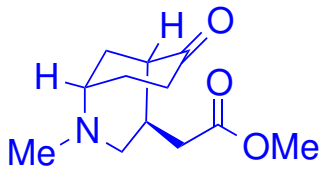

(b) (*S*)-*endo*-product

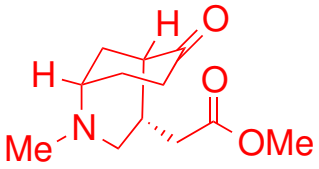

(c) (*S*)-*exo*-product

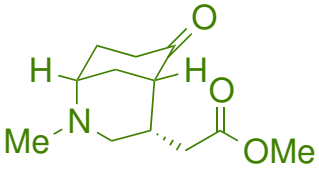

(d) (*R*)-*endo*-product

Figure 2.10: Four stereochemically different potential products.

We investigated the two mechanistic pathways leading to the two enantiomers of the favoured *endo*-diastereomer (**Figure 2.11**). We located all stationary points along the pathway to formation of the two enantiomeric *endo*-amido-ester products, initially using MCMM searching with PM6-DH2, followed by M06-2X/6-31G(d) reoptimisation and then further optimisation with M06-2X/6-311+G(d,p) and implicit modelling of the DCM solvent using CPCM. With a thiourea present in the catalyst, the mechanism proceeds in a stepwise manner: cyclization of the enamine substrates (**2.11.01** and **2.11.02**) proceeds *via* C-C bond formation through a Michael addition (**TS 2.11.05** and **TS 2.11.10**), followed by intramolecular proton transfer to the ester α-carbon (**TS 2.11.07** and **TS 2.11.12**). As was the case in the methylamine study, the formation of the *endo*-Michael-adduct is moderately endergonic and reversible. The stereodetermining step is predicted to be the irreversible proton-transfer from thiourea to the ester enolate, which, with a free energy difference $\Delta\Delta G^{\ddagger}$ of 2.4 kcal/mol leads to a computed ee of 96%. Experimentally, the same truncated thiourea catalyst shown in **Figure 2.8** was synthesised and led to formation of this enantiomer with an ee of 96%. We ruled

out interference by intermolecular protonation as the entropic cost alone (ca. 12 kcal/mol) associated with a bimolecular process makes this uncompetitive in our system. The protonation step is crucially very different to that in the methylamine catalysed system as the proton comes from the catalyst, and not the iminium functional group.

In addition to our study of the formation of the favoured *endo*-products, we also looked at the pathways leading to the enantiomers of the disfavoured *exo*-product (**Figure 2.12**). We located all the stationary points for the chemically most plausible pathways for the two enantiomeric *exo*-ester products using M06-2X/6-31G(d) and pleasingly, both the route to the (*R*)- and (*S*)-*exo*-esters were shown to proceed with significantly higher barriers than those for either *endo*-enantiomer when calculated at this level of theory. For this reason, we did not reoptimize the full *exo* pathway shown in **Figure 2.12** using the same higher level of theory applied in the previous *endo* case (**Figure 2.11**).

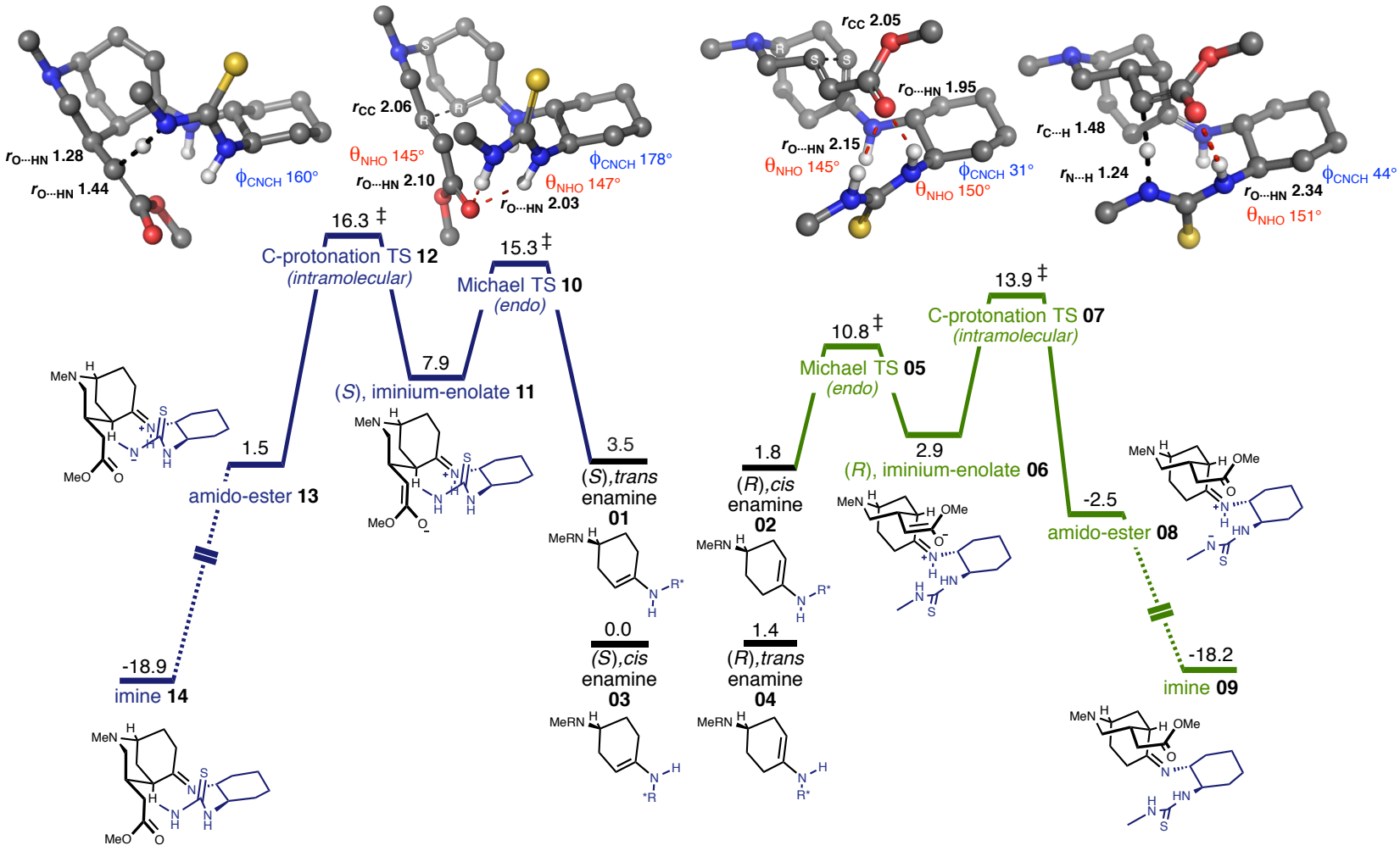

Figure 2.11: Free energy profile for *endo*-cyclization of ketone starting material catalysed by aminocyclohexylthiourea at the CPCM-M06-2X/6-311+G(d,p) level of theory (G_{rel} values in kcal/mol at 45°C, 1 mol/L).

Similarities can be seen between this *exo* mechanistic pathway and the one calculated with the methylamine catalyst; formation of the Michael-adduct proceeds with a similar activation barrier and is once again highly endergonic. It is therefore expected to be readily reversible as was the case in the methylamine catalysed system. With the thiourea group on the catalyst, intramolecular protonation is now geometrically possible, unlike in the methylamine catalysed system. Protonation of the (*S*), iminium-enolate **2.12.04** proceeds with a high barrier (**TS 2.12.09**) and the formation of the (*S*), amido-ester **2.12.05** is highly endergonic and reversible. Protonation of (*R*), iminium-enolate **2.12.06** proceeds with a very high barrier (**TS 2.12.11**) relative to the starting enamine and is energetically unfeasible under the reaction conditions. No intermediate amido-ester **2.12.07** is expected to be formed in the reaction.

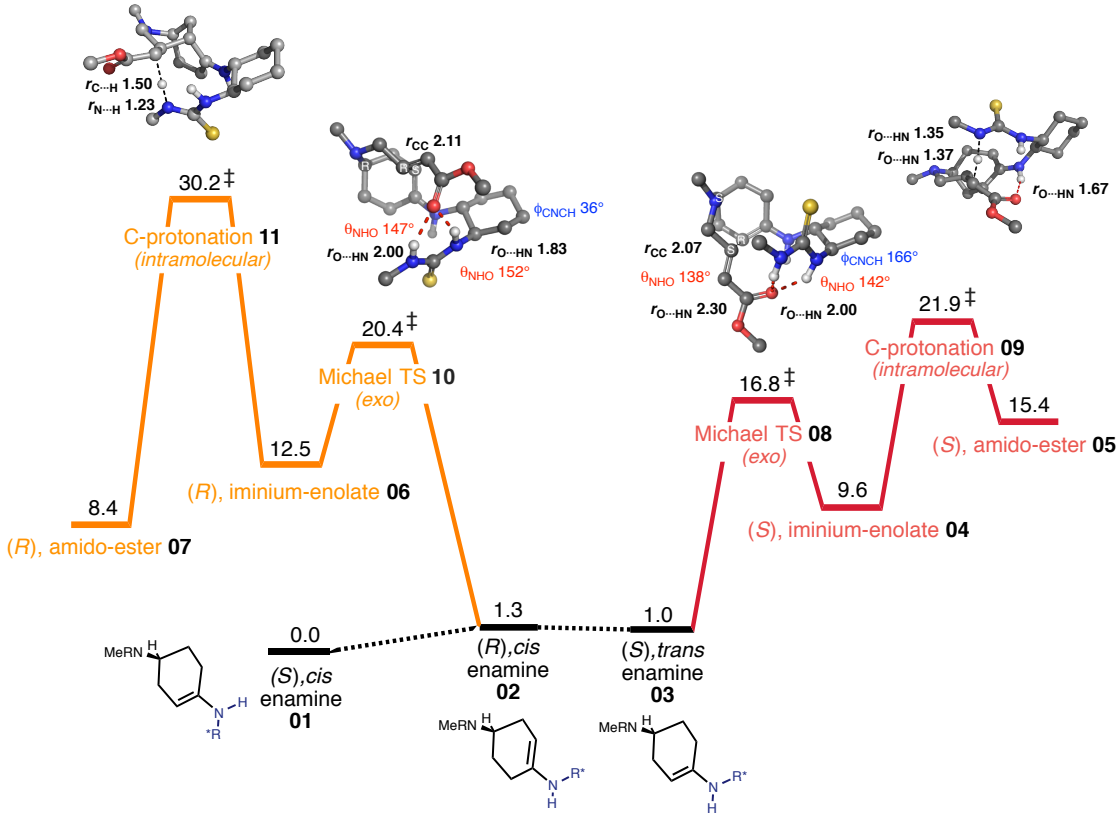

Figure 2.12: Free energy profile for *exo*-cyclization of ketone starting material catalysed by aminocyclohexylthiourea at the CPCM-M06-2X/6-31G(d) level of theory (G_{rel} values in kcal/mol at 45°C, 1 mol/L).

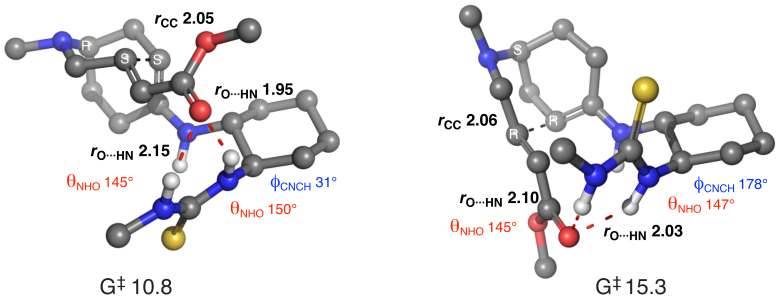

(a) *Endo*-diastereomers

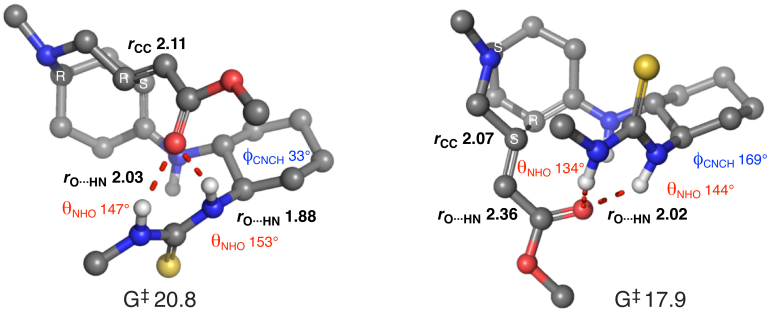

(b) *Exo*-diastereomers

Figure 2.13: CPCM-M06-2X/6-311+G(d,p) diastereomeric TSs for the formation of pairs of *endo*- and *exo*-enantiomers. Distances shown are in Å.

2.5.3 Explaining enantioselectivity

Both Michael addition C-C bond forming TSs for the *endo*- and *exo*-Michael adduct receive a stabilising hydrogen-bonding interaction between the developing negative charge on the ester/enolate and thiourea group and therefore it can not be used to explain the energetic preference between these 4 TSs (**Figure 2.13**). The difference in stability between the *endo*- and *exo*-diastereomers can be attributed to the sterically disfavoured boat ring conformation (**Figure 2.6**) which forms in the latter; the origin of enantioselectivity is less obvious. The enamine configuration differs between the two pathways, being *s-cis* for the major and *s-trans* for the minor enantiomers, however, in the achiral methylamine catalysed system, we computed the latter of these enamine configurations to be the more stable and so this geometric difference is unlikely to account for the preference for the former. We discovered that to explain the origins of stereoinduction, we needed to look more closely at the conformation of the cyclohexylthiourea, which we found to

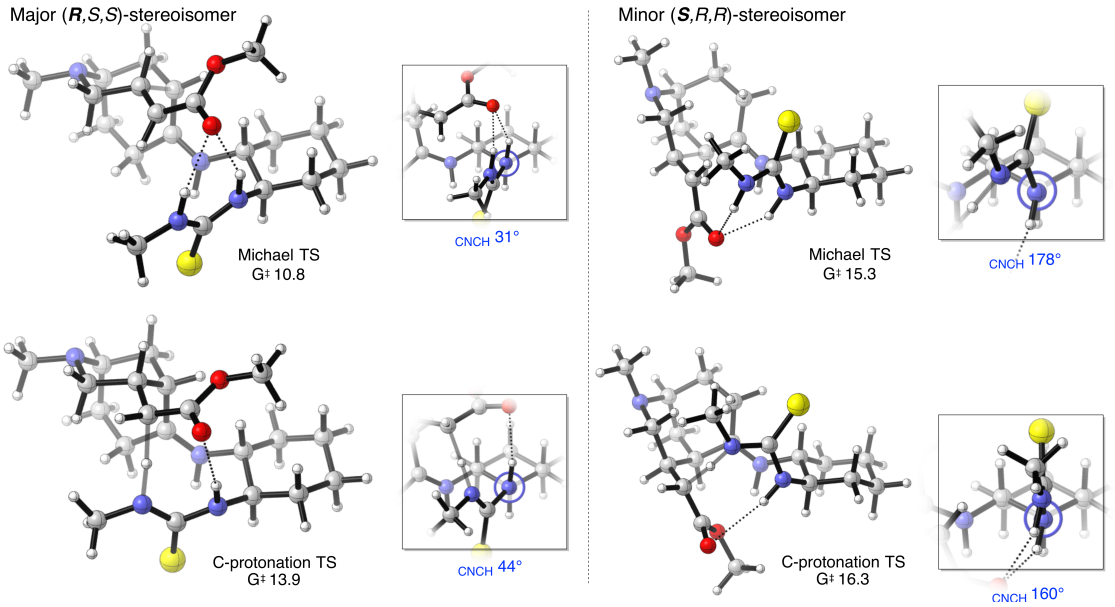

Figure 2.14: CPCM-M06-2X/6-311+G(d,p) transition structures leading to the major and minor enantiomers of the *endo*-Michael adducts with graphical Newman projections of the cyclohexylthiourea CNCH dihedral.

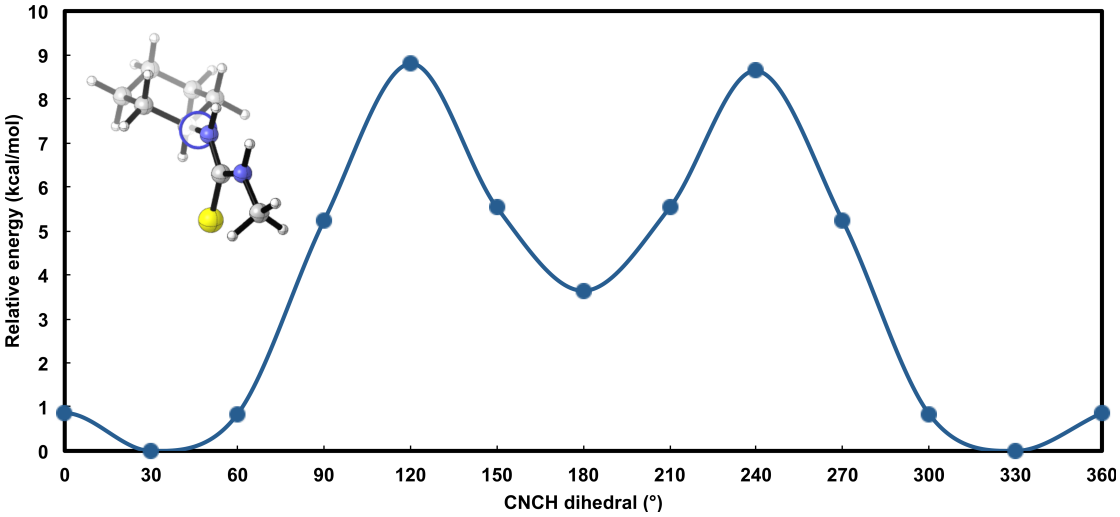

Figure 2.15: Restricted coordinate dihedral scan using M06-2X/6-311+G(d,p) for cyclohexylthiourea.

have a 4 kcal/mol preference for the cyclohexyl C-H to lie nearly syn-coplanar to the N-C(=S) bond. The conformational energy profile for (S=)C-N-C-H dihedral rotation is shown in **Figure 2.15**. Upon forming the major enantiomer, both **TS**

2.11.05 and **TS 2.11.07** adopt conformations in which this dihedral preference is satisfied, effectively minimising allylic 1,3 strain. In the case of the minor enantiomer both **TS 2.11.10** and **TS 2.11.12** do not adopt a conformation in which this is minimised (these interactions are shown more clearly in **Figure 2.14**).

It is possible that the major enantiomer forms *via* a *trans* enamine configuration (**2.16**); however, in the resulting structures no hydrogen-bonding interactions would be possible between the ester/enolate group and the thiourea and the pathway is disfavoured by 6.3 kcal/mol relative to **TS 2.11.07**. This *trans* **TS 2.16b** is less stable than proton transfer in **TS 2.11.09** and so it does not make an energetically feasible pathway. This alternative pathway is similar to that computed for the methylamine catalysed system and has a similar activation barrier (as it does not have a hydrogen-bonding interaction).

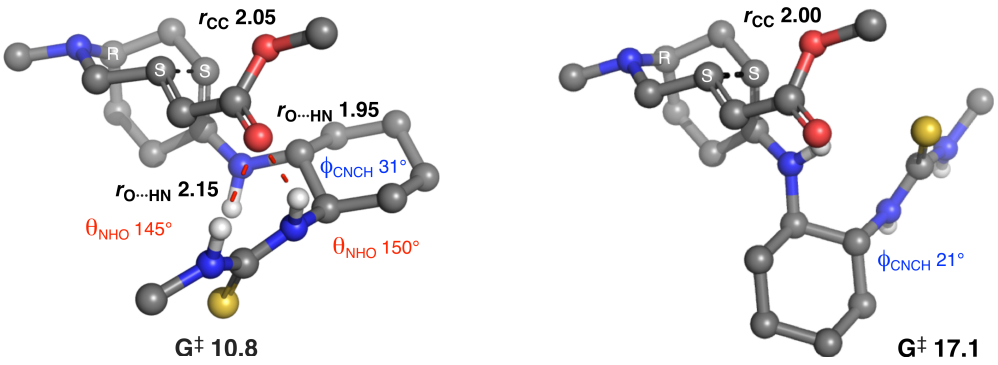

(a) *cis* enamine **(b)** *trans* enamine

Figure 2.16: CPCM-M06-2X/6-311+G(d,p) TSs leading to the major enantiomer. Hydrogen bonding between thiourea and Michael acceptor is only possible *via* an *cis* enamine configuration and not in the *trans* enamine configuration.

2.6 Chiral 1-(naphthalen-1-yl)etha-1-amine catalysis

The chiral 1-(naphthalen-1-yl)etha-1-amine catalyst illustrated in **Figure 2.17**, was shown experimentally to produce the same major enantiomer as the aminocyclohexylthiourea catalyst, albeit with a lower ee of 69% (**Table 2.2**, catalyst **a**). As with all other primary amine catalysts studied, it resulted in a high dr of >98:2. Unlike in the previous catalytic system studied, this catalyst has no hydrogen-

bonding capabilities. It is probable, therefore, that the enantioselectivity imparted is a result of the asymmetric steric environment created by the catalyst.

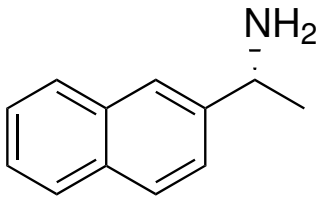

Figure 2.17: (R), 1-(naphthalen-1-yl)etha-1-amine catalyst.

2.6.1 Conformational considerations

In order to ensure that we were studying the lowest energy conformers at each point on our reaction profile, we again needed to employ MCMM searching. This naphthalene containing primary amine catalyst has the same number of asymmetric freely rotatable bonds as the thiourea catalyst examined previously. The lack of any strongly polar functional groups in the catalyst meant that structures with significantly different geometries had comparable energies (i.e. a flatter PES). For this reason, we uncovered significantly more PM6-DH2 optimized conformers during our MCMM scan which were below our energy threshold of 4.8 kcal/mol and more structures needed to be reoptimized with DFT in the second stage of our MCMM searching protocol. **Figure 2.18** shows two structures generated during one such MCMM search for the lowest energy form of a single TS enantiomer; the core TSs of the two structures have been superimposed but large geometric differences between the structures are evident, despite the energy difference of 0.6 kcal/mol given by PM6-DH2.

2.6.2 Reaction pathway

As discussed in the previous section, there are four stereochemically different morphan-motif containing products which may be formed as products of this reaction (**Figure 2.10**). This 1-(naphthalen-1-yl)etha-1-amine catalysed system is more similar to the methylamine case than the aminocyclohexylthiourea, as it too

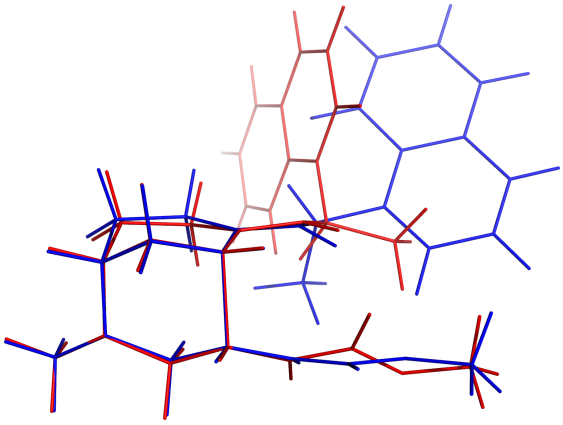

Figure 2.18: Example of two PM6-DH2 optimized structures produced during MCMM searching, with an energy difference of 0.6 kcal/mol. The morphan structural motifs are superimposed.

is unable to protonate the enolate species formed upon Michael addition cyclization. In order to form the ester product of this reaction, we must once again look to the iminium functional group for protonation of the enolate species formed upon cyclization. For this reason, we only need to consider the *s-trans* enamine for the reaction as cyclization of the *s-cis* stereoisomer would have an unsurmountable geometric barrier to protonation of the enolate species. Furthermore, the *s-trans* receives stabilisation of the developing oxyanionic group on the ester from the favourable orientation of the N-H bond of the enamine towards this charge buildup (hydrogen bond); such TS stabilisation is not possible in the *s-cis* enamine case.

When explaining the origins of the overwhelming diastereoselective preference for the *endo* adduct, we can employ similar arguments used in the methylamine study. Upon cyclization of the *s-trans* enamine to form the enol product, the nitrogen of the imine is needed to facilitate tautomerization to the ester product. As shown in section **2.4**, the *exo* intermediate following cyclization cannot tautomerize to form the ester product, as the α-carbon is too far from the iminium for an imine-assisted tautomerization. Therefore, any *exo*-Michael adduct formed is done so reversibly. **Figure 2.19** shows *exo*-Michael adduct formation to be reasonably exergonic, as it was in the methylamine study, and we can be confident that this intermediate will not accumulate to the point at which intermolecular tautomerization becomes

viable. Despite the hydrogen bonding interaction between the developing oxyanion on the ester/enolate group and the enamine in the *exo* cyclization, **TS 2.19.05** and **TS 2.19.07** remain high in energy because of the necessity that they adopt a boat conformation as in (**Figure 2.6**).

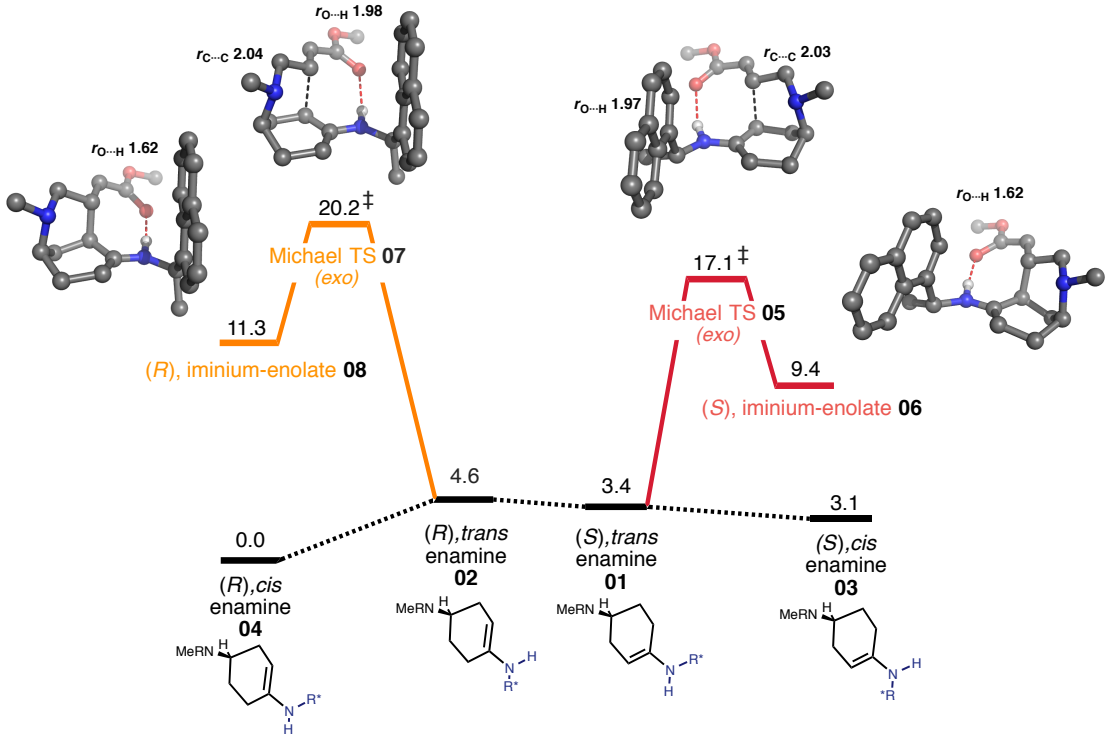

Figure 2.19: Free energy profile for *exo* cyclization of ketone starting material catalysed by (*R*), 1-(naphthalen-1-yl)etha-1-amine at the CPCM-M06-2X/6-311+G(d,p) level of theory (G_{rel} values in kcal/mol at 45°C, 1 mol/L).

The enantioselective bias of the (*R*), 1-(naphthalen-1-yl)etha-1-amine catalysed *endo*-cyclization reaction is not as significant as with for the aminocyclohexylthiourea catalyst (69 vs 90% ee, **Table 2.2**).

Figure 2.20 shows our calculated reaction pathway for the favoured *endo* diastereomer. We predict the cyclization step to be enantioselectivity determining, contrary to in the previous aminocyclohexylthiourea catalysed system where selectivity was driven by intramolecular protonation by the thiourea to form the amido-ester species. We calculate imine-assisted tautomerization of the Michael adduct (**TS 2.20.07** and **TS 2.20.11**) to take place with a significantly lower bar-

rier than the corresponding Michael cyclizations; for this reason, we expect it to be facile, and not play a selectivity-determining role. The sense of enantioselectivity in this reaction is reproduced by our calculated $\Delta\Delta G^{\ddagger}$ between the lowest energy conformers of the TSs for Michael cyclization, **TS 2.20.05** and **TS 2.20.09**, of 1.4 kcal/mol. This predicts a 81% ee at 45°C, which is larger than the 69% ee observed experimentally. The quantitative difference between experimental and calculated enantioselectivity is 0.3 kcal/mol, well within the error margin for the M062X density functional.[101] Our computed $\Delta\Delta G^{\ddagger}$ between selectivity controlling TSs for this system is lower than that for the thiourea, agreeing with the selectivity ranking observed experimentally.

Interestingly, applying a Boltzmann weighting across other fully optimised TS conformers close in energy to **TS 2.20.05** and **TS 2.20.09** also uncovered through our MCMM searching, yields a better match with the experimentally observed ee; incorporation of all conformers which have stabilities within 4 kcal/mol of the cyclisation TS for the major enantiomer yields an ee of 73% at 45°C.

2.6.3 Accounting for enantioselectivity

It is not immediately obvious how differences in noncovalent interactions causes the energetic difference between **TS 2.20.05** and **TS 2.20.09**. However, upon closer inspection of the favoured conformers of the two TSs of interest, there is a geometric similarity between the structures, with the tertiary H on the catalyst sitting trans across the enamine. This preference is driven by a reduction in the 1,4 steric clash between hydrogens on the cyclohexyl ring and, H, the smallest substituent on the tertiary carbon of the catalyst. In the case of the (*S*) conformer, this eclipsing interaction is accompanied by a significantly closer 1,4 H-H interaction with the naphthylene. Using NBO steric calculations,[102] we can quantify the steric congestion caused by the three highlighted interactions shown in **Figure 2.21** and we see that for the (*S*) TS, the steric penalty for these aforementioned interactions is 1.7 kcal/mol higher than in the (*R*) system.

Figure 2.22 shows the superposition of the mirror inverted form of the (*S*) Michael-TS over the analogous (*R*) system; this representation allows us to better

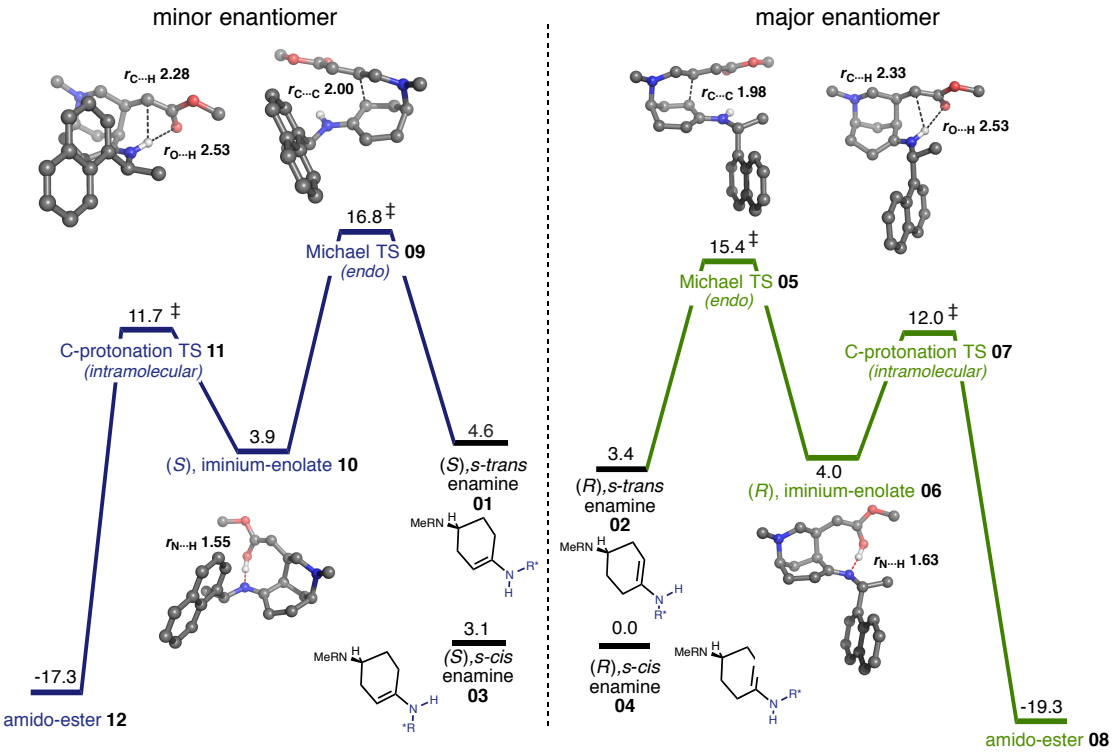

Figure 2.20: Free energy profile for *endo* cyclization of ketone starting material catalysed by (*R*), 1-(naphthalen-1-yl)etha-1-amine at the CPCM-M06-2X/6-311+G(d,p) level of theory (G_{rel} values in kcal/mol at 45°C, 1 mol/L).

visually compare the enantioselectivity determining diastereomeric TSs of this reaction. It is apparent that the core TSs are remarkably similar, and there is a great deal of overlap between these parts of the structures. The interatomic distances between the methoxy O of the ester and the nearest C-H groups on the catalyst are similar and have near identical interaction energies according to NBO steric and perturbation analysis, despite their differing levels of hybridisation. In both cases the naphthylene group points away from the system in order to minimise steric repulsion.

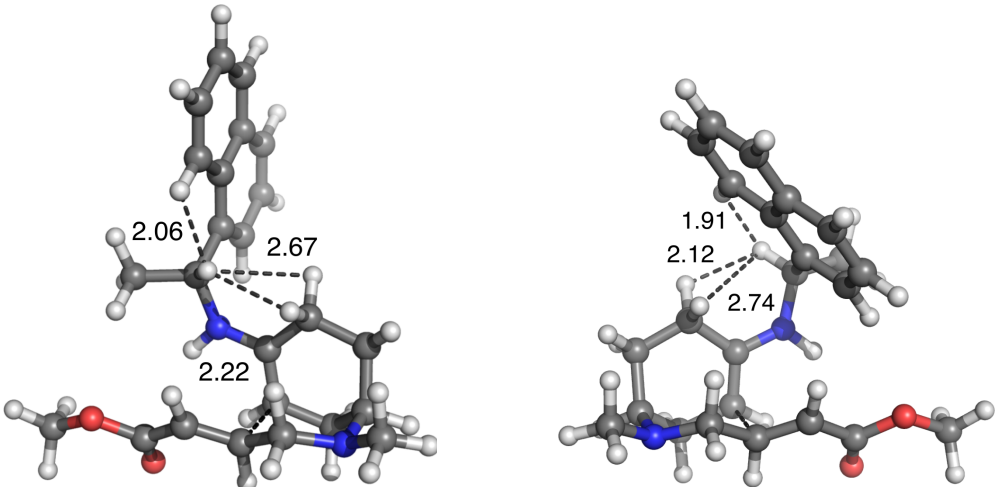

(a) (R)-TS, ΔE_{steric} = 5.9 kcal/mol **(b)** (S)-TS, ΔE_{steric} = 7.6 kcal/mol

Figure 2.21: Optimized TSs for (R) and (S) Michael adduct formation. Key interatomic distances are given in Å.

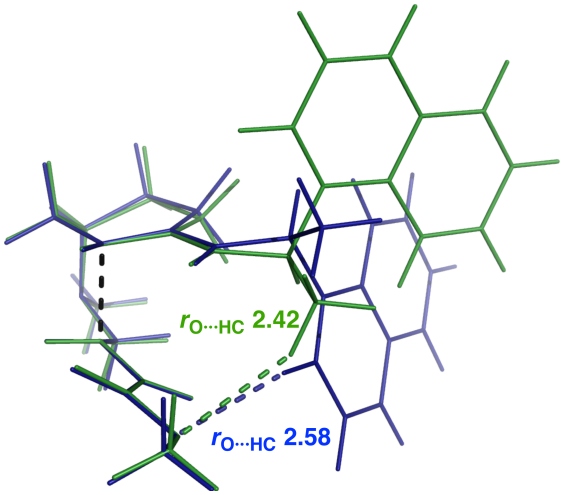

Figure 2.22: Superposition of R (green) and mirror inverted S (blue) Michael TSs; interatomic distances are highlighted and given in Å.

2.7 Conclusions

In this investigation, we were able to show that, by using a combination of computational techniques, we can explain the origin of both diastero- and enatioselectivity for cyclization of an unsaturated ester-ketone substrate with a range of primary amine catalysts. After rationalising diastereoselectivity in the achiral

methylamine reaction, we showed how various chiral primary amine catalysts imparted stereoselectivity in different ways, to differing extents, and *via* different reaction pathways. Through our computations, we dismissed off-cycle intermediates thought to be important in similar reactions, and discovered the conformational importance of the C-C bond forming TS. For two chiral catalysts, we implemented exhaustive MCMM conformational searching followed by full DFT optimisations, in order to compute the lowest energy reaction pathways in each case. Examining a catalyst with a strong intramolecular hydrogen-bonding interaction (section **2.5**) and another with purely steric interactions (section **2.6**), presented us with different challenges in each case. We were ultimately able to show that these catalysts impart an asymmetric bias by mechanisms with unique selectivity determining steps. Our calculations not only predicted the correct sense of selectivity observed experimentally; the relative magnitude of our predictions were also in agreement.

In addition to providing an account of the source, direction and magnitude of selectivity, we were able to make practically useful predictions which led to the synthesis of a more compact and yet equally enantioselective catalyst (**Figure 2.8**).[99]

3 Regioselectivity of cyclisations

Since their inception in the 1970s, Baldwin's rules for the relative favourabilities of alicyclic ring forming reactions have provided near-foolproof guidelines for Organic chemists.[103–106] Although not infallible, they apply to the majority of cases, and exceptions to these rules are rare;[107] when anomalies are uncovered, they are the source of much scientific interest, and explaining the origin of their atypical behaviour often requires in depth and involved chemical analysis.[48]

3.1 Background

In the 1976, Prof. Jack Baldwin published his seminal paper on "Baldwin's Rules",[103] a set of qualitative guidelines for relative favourabilities of ring closing reactions of alicyclic compounds; to date, this paper has been cited over 2000 times, and remains one of the most influential Organic Chemistry papers of all time. Following initial publication, Baldwin expanded these rules to incorporate additional cyclisations, most notably for enolates in 1977,[106] and aldols in 1982.[108] The rules themselves (**Figure 3.1**) are formulated from a combination of observation and stereoelectronic reasoning, and are a reflection of the relative rates at which different ring closures occur; a reaction that is classified as disfavoured has a slow enough rate of reaction that it is unable to compete with an alternative, faster, favoured reaction. The rules were not intended for application beyond the second row elements of the periodic table. Baldwin also states that his rules may not be applied to concerted electrocyclic processes.[103]

3.1.1 Terminology

The terminology laid out by Baldwin to describe cyclisation reactions has since become a staple in the vocabulary of chemists worldwide. The prefixes, *endo* and *exo*, refer to the location of the bond being broken upon formation of the cyclic system. If the bond being broken is inside the forming ring (endocyclic), the process is *endo*; if the bond is outside of the ring (exocyclic), the process is

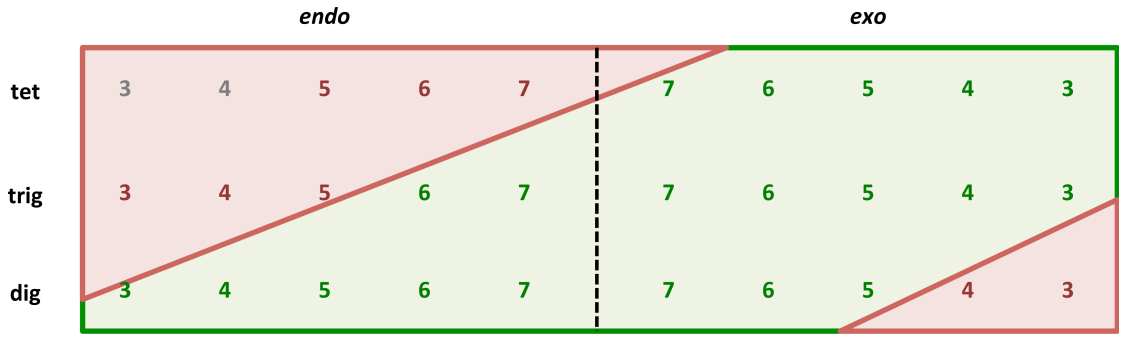

Figure 3.1: Baldwin's rules.

exo (**Figure 3.2**). Numerical prefixes refer to the size of the ring being formed. Suffixes refer to the geometry of the carbon undergoing nucleophilic attack: *tet* for tetrahedral sp^3, *trig* for trigonal sp^2, and *dig* for digonal sp hybridised carbon (**Figure 3.3**).

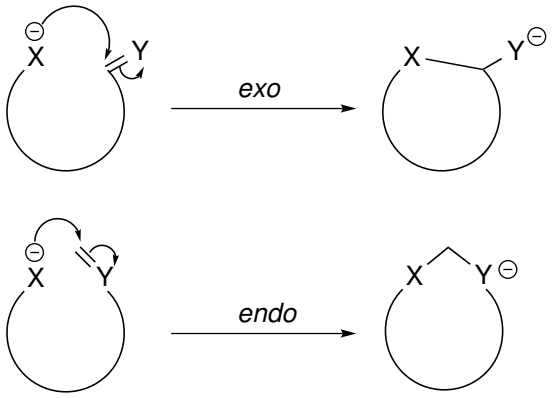

Figure 3.2: Generic representation of *endo* and *exo* cyclisation reactions.

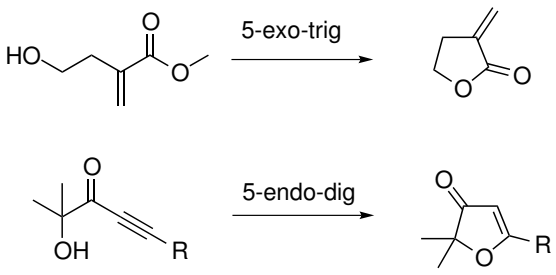

Figure 3.3: Examples of the usage of Baldwin's rules terminology.

3.1.2 Origin

Baldwin's rules are largely driven by the ideal orbital angle for nucleophilic attack. For *exo-tet* cyclisations, the Walden inversion taking place results in the ideal angle of attack being 180° (**Figure 3.4**);[109] *exo-trig* cyclisations favour the Bürgi-Dunitz trajectory of 105° ± 5° (**Figure 3.5**) while *endo-dig* reactions prefer attack at 120°.

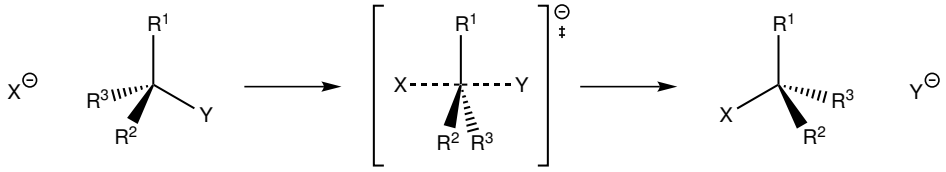

Figure 3.4: Generic example of the Walden inversion. The X-C-Y angle in the TS is 180°.

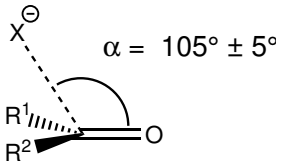

Figure 3.5: Illustration of the origin of the Bürgi-Dunitz trajectory for addition to a carbonyl.

3.2 Computational methods

In this section, we performed all DFT calculations using Gaussian 09.[5] We primarily used two functionals: the hybrid meta-generalized gradient approximation functional, M06-2X,[24] and the dispersion corrected range-separated hybrid functional, wB97XD.[110] The M06-2X level of theory has been shown to result in good thermochemical kinetics in agreement with experimental values obtained for conjugate additions and closely-related reactions.[111,112] The wB97XD functional is a long-range corrected hybrid density functional with damped atom to atom dispersion corrections, and it has been shown to be effective at describing thermochemistry, kinetics and non-covalent interaction; studies in which it has been used include

those of aromatic systems, where results were compared with those obtained using CCSD(T) complete basis set (CBS) calculations.[113] We used a variety of Pople basis sets in our description of all elements present in our calculations, and in our Nucleus Independent Chemical Shift (NICS) analysis.[80,81] In cases where we modelled the effects of solvation, we implemented the conductor-like polarisable continuum model (CPCM).[36,82] We confirmed the presence of stationary points along our calculated potential energy surfaces as being either minima or transition structures (TS) by the presence of zero or a single imaginary vibrational frequency. Free energies were evaluated at 25 °C using harmonic vibrational frequencies. The connection of saddle points to minima, necessary for our construction of potential energy surfaces (PES), was confirmed through the use of intrinsic reaction coordinate (IRC) calculations.[86,87] NICS calculations[46,114] were evaluated at the ring centre of the cyclic TSs, NICS(0), as a probe of aromaticity using London orbitals (Gauge-including Atomic Orbitals, GIAOs)[115–117] with the B3LYP functional[19,20] and the 6-31++G(d,p) Pople basis set. The out-of-plane component of the chemical shielding, $NICS(0)_{zz}$[118,119] was obtained by decomposition along the unit vector normal to the plane of the ring, as defined by least-squares fitting from the coordinates of the five ring atoms, since this component is not contaminated by contributions from in-plane components to the shielding.[54] The distance dependence of the out-of-plane $NICS_{zz}$ component was analysed along the plane's normal vector (NICS-scan)[50] to give a further indication of aromaticity. We computed dissected localised molecular orbital (LMO) contributions to the shielding values, $NICS(0)_{MOzz}$, through the natural chemical shielding (NCS) approach implemented in NBO version 6.0.[102] Ring planes were defined by minimising the sum of squared perpendicular distances for the five carbon atoms in the ring. We automated the process of positioning Gaussian 09 "ghost atoms" for use in these calculations by using in-house software (for further details, see section 6.1).

3.3 5-*endo-trig* in indane synthesis

3.3.1 Synthesis

Recently, an enantioselective cation directed 5-*endo-trig* cyclisation was uncovered by Prof. Smith and coworkers, for the synthesis of the functionalised indane motif.[48] The reaction, summarised in **Figure 3.6**, proceeds with a range of different substrates and electrophiles. The reaction is of synthetic importance since the indane structure is a constituent of many natural product families and a key component of clinically important and biologically active molecules; despite this, however, there have been relatively few catalytic enantioselective methods for their synthesis to date.[120–129] These strategies have typically invoked the use of 5-*exo-trig* Michael additions to generate such carbocycles, using chiral imidazolidinones,[124] cyclic isothioureas,[125] *N*-heterocyclic carbenes,[125–128] or proline derivatives.[129] To date, the 5-*endo-trig* cyclisation has been overlooked for the synthesis of such structures, presumably because it is expected to be stereoelectronically disfavoured by Baldwin's rules.

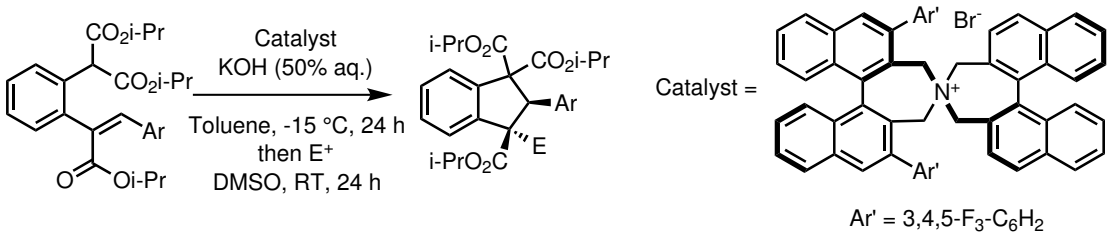

Figure 3.6: An example of enantioselective synthesis of pentasubstituted indanes from malonate substrate; the reaction was shown to work with a variety of "Ar" and "E^+" substituents.[48]

Interestingly, a similar reaction in which ester rather than malonate functionality was used, was shown to proceed exclusively to the 5-*exo-trig* substrate (**Figure 3.7**). The origin of this chemoselectivity difference between these two reactions is explained in further detail below.

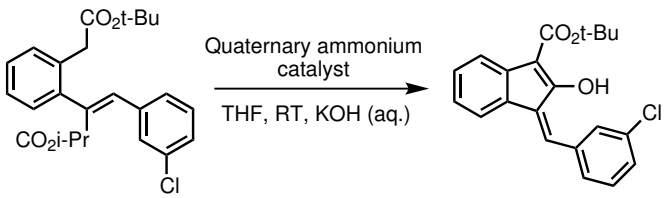

Figure 3.7: Cyclisation of an ester substrate leads exclusively to the 5-*exo-trig* cyclisation.

3.3.2 Reaction profile

We conducted preliminary calculations to locate the key stationary points for the construction of reaction profiles for 5-*exo-trig* and 5-*endo-trig* cyclisations of our model ester and malonate systems using the wB97XD density functional and a 6-31+G(d,p) basis set. We implemented MCMM searching with the semi-empirical dispersion corrected PM6-DH2 functional to locate the lowest energy conformer of these structures before reoptimising using DFT. For the sake of conformational simplicity, we substituted isopropyl and tertiary butyl with methyl functionality. In collaboration with Tetiana Sergeieva and Prof. Sergiy Okovytyy from Dnipropetrovsk National University, the systems were calculated using the M062X density functional and a 6-311++G(d,p) basis set with a CPCM description of solvation. The ester reaction profile is shown in **Figure 3.8**. From this scheme, the origin of the preference for the reaction to proceed *via* a 5-*exo-trig* mechanism is clear; the *exo* pathway is kinetically favoured, relative to the *endo* with a relative free energy difference between the two barriers (**TS 3.8.02** and **TS 3.8.05**) of 9.6 kcal/mol. The barrier for the *endo* cyclisation of 21.6 kcal/mol is not expected to be surmountable under the reaction conditions.

The computed reaction profile for the cyclisation of the malonate substrate is shown in **Figure 3.9**. The scheme shows the kinetic and thermodynamic preference of this reaction to proceed *via* the 5-*endo-trig* cyclisation; the reaction occurs readily under the reaction conditions, and irreversibly. Conversely, the *exo* pathway is seen to progress with a significantly higher barrier of 21.6 kcal/mol (**TS 3.9.02**) to the high energy 5-*exo*-adduct, **3.9.02**. With a free energy difference between the TSs for *exo* and *endo* cyclisations of 8.7 kcal/mol, we can predict that

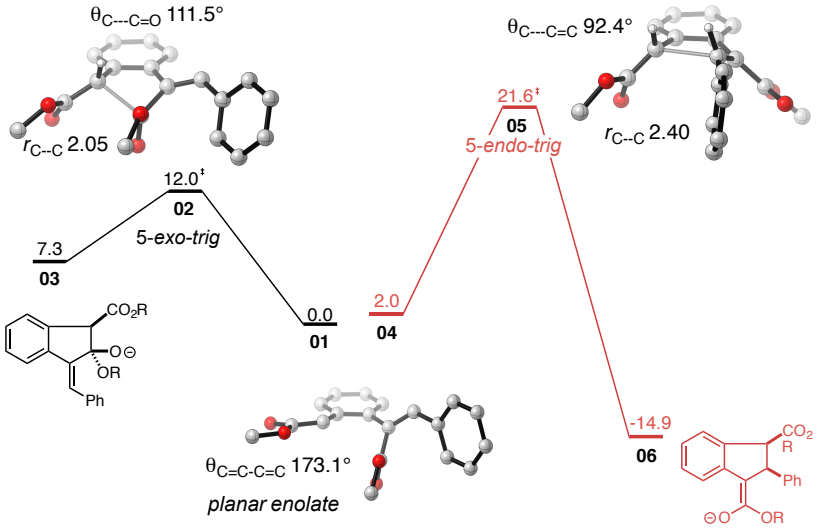

Figure 3.8: Cyclisation of an ester substrate leads exclusively to the 5-*exo-trig* cyclisation; $\Delta G^{\ddagger}$ are in kcal/mol. *Calculations by Tetiana Sergeieva and Prof. Sergiy Okovytyy.*

there will be exclusive preference for the formation of enolate **3.9.06**.

Interestingly, the thermodynamics for *endo* cyclisation to form the *endo*-adduct in both the ester and malonate cases (**3.8.06** and **3.9.06**) are similarly exergonic. A minor difference exists in the obtuse trajectory of attack between **TS 3.8.05** and **TS 3.9.05** for *endo* attack in each case, of 92.4° and 96.5° for those TSs respectively, which is unlikely to account for the 8.7 kcal/mol difference in 5-*endo-trig* barriers. The starting enolate shown in **Figure 3.8** is virtually planar, with a dihedral angle between the C-C double bond of the enolate and the aromatic ring of 173.1°. The origin of planarity here is likely delocalisation of the negative charge about the π-system of the substrate; this planarity, and therefore conjugation, must be interrupted by out-of-plane rotation of both enolate and enoate groups in order to reach the *endo* cyclisation TS in this case. Conversely, for the *exo* pathway, the out-of-plane enolate rotation required to reach the geometry of **TS 3.8.02** is less by 20°; in addition, bond formation is more advanced in the *exo*-TS, further highlighting the favourability of this pathway. The loss of delocalisation in **TS 3.8.05**, which is regained in **3.8.06**, is a significant contributor to the large rise in activation barrier for the ester versus malonate *endo* cyclisations.

In the case of the malonate substrate cyclisation, there is a far greater geometric predisposition of the starting enolate towards the cyclisation TSs than in the ester substrate, with an out-of-plane rotation of the enolate of 130.6° as determined by the C-C double bond of the enolate and the aromatic ring. This is a significant contributing factor towards the lower barrier to formation of the *endo* cyclised product, **TS 3.9.06**, with a change in dihedral angle upon going to **TS 3.9.05** of less than 15°.

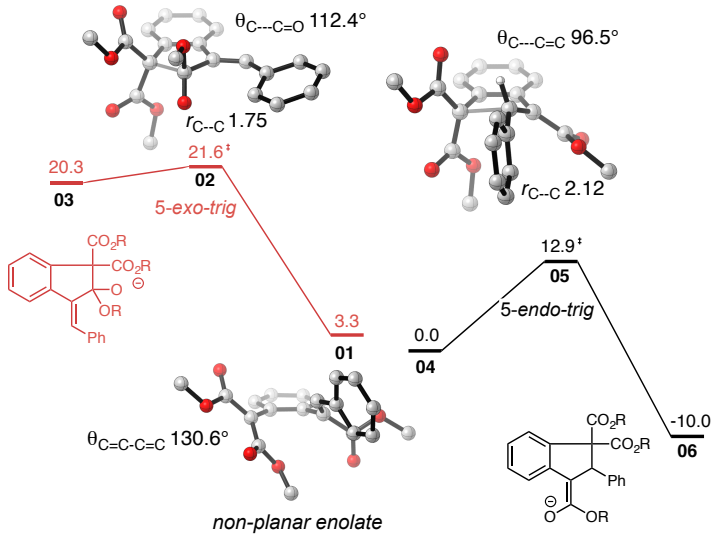

Figure 3.9: Cyclisation of an ester substrate leads exclusively to the 5-*exo-trig* cyclisation; $\Delta G^{\ddagger}$ are in kcal/mol. *Calculations by Tetiana Sergeieva and Prof. Sergiy Okovytyy.*

The significantly higher barrier for the malonate *exo* cyclisation when compared to that in the ester system can largely be attributed to the greater steric penalty upon formation of a C-C bond between two quaternary centres, as opposed to the quaternary-tertiary C-C bond formed in the ester system.

3.3.3 NICS analysis: electrocyclic or pseudopericyclic?

In order to better assess the nature of the TSs by which the 5-*endo-trig* ring closure occurs, and to more conclusively determine whether these reactions were formally pericyclic, we resorted to calculations of TSs and their magnetic properties. The cyclisations in question could conceivably be described as either electrocyclic or

pseudopericyclic processes. It had previously been reported that TSs of electrocyclic ring closures may adopt a planar geometry, blocking overlap of the σ- and π-orbitals, in what is described as a pseudopericyclic orbital topology.[130–133] An example of a reaction which has been classified as pseudopericyclic is that for the 6π-electrocyclic ring closure in the formation of azatrienes.[134,135] The defining characteristics of pseudopericyclic reactions are low or nonexistent barriers, planar TS geometries, such as those found for the 5-membered ring closures of conjugated nitrile ylides[136] and iminodiazomethanes,[137] and cyclic reactions that are allowed irrespective of the number of atoms.[138]

As a means of comparison for this study, we first optimised the pericyclic TSs for three hypothetical examples of 5-membered anionic cyclisations, shown in **Figure 3.10**. The first of these, **TS 3.10.01**, is for a 5-*endo*-*trig* cyclisation stabilised by a 5-centre, 6-electron σ-aromatic orbital array involving the lone pair at the nucleophilic carbon atom, the adjacent π-bond, and the forming σ_{CC} bridge. **TS 3.10.02** is recognised formally as a 6-π aromatic TS, consistend with the electrocyclic ring closure of a pentadienyl anion, and the large activation barrier is indicative of this pericyclic nature. **TS 3.10.03** is similar to **TS 3.10.02**, but with an attached neighbouring aromatic ring, making it more similar to the systems of synthetic interest. The assessment of TS aromaticity is a common method by which reactions may be categorised as either pericyclic or pseudopericyclic. Therefore, we computed NICS values along the axis running through the ring centre of each TS, perpendicular to the plane of the ring. We only considered the component of the NICS value along this calculated axis, since the isotropic NICS value is contaminated by contributions from in-plane, perpendicular, tensor components unrelated to aromaticity. The typical forms of the plotted values, illustrated in **Figure 3.11**, show the expected behaviour due to in-plane aromaticity in each TS. We note that all species have negative $NICS_{zz}$ values close to the ring centre, ranging from around -25 ppm to -35 ppm, while σ-aromaticity results in greatest shielding in the plane of the ring, and π-aromaticity results in the greatest shielding around 1 Å above and below the plane of the forming carbocycle - this is symptomatic of the topology of the π-electron cloud surrounding these systems.

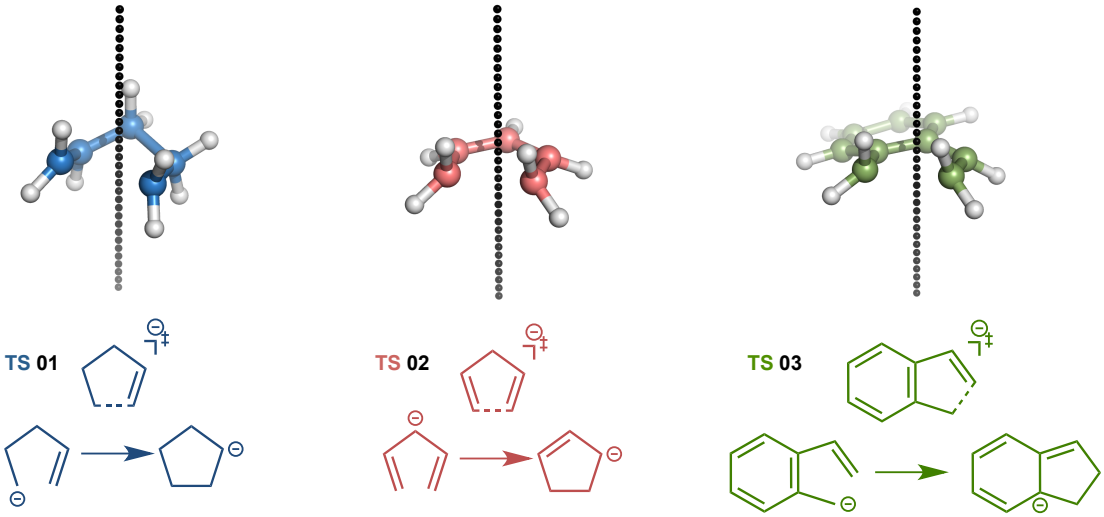

Figure 3.10: CPCM-M062X/6-311++G(d,p) optimised transition structures for the cyclisation of various 5-membered rings; black spheres represent the location of "ghost atoms".

We used our results from this study into hypothetical 6-electron 5-membered anionic cyclisations as a means to assess the pericyclic character of the 5-*endo-trig* cyclisation TSs for the ester and malonate systems discussed previously, based on the computed similarities in their magnetic properties. The computed magnetic properties for **TS 3.9.05** and **TS 3.8.05** (**TS 3.12.01** and **TS 3.12.02**) are shown in **Figure 3.12**. The magnetic properties for **TS 3.12.01** can clearly be seen to be different from those computed in **Figure 3.11**, since the $NICS_{zz}$ values in and close-to the plane of the ring is positive and those in the previous example were negative. The positive value is indicative of decreased effective nuclear shielding, resulting from two occupied MOs lying in or close to the plane of the ring i.e. the forming C-C σ-bond and developing carbanion. Upon closer inspection of the localised orbital contributions to the $NICS_{zz}$ values, we see that the negative contributions > 1.5 Å away from the centroid of the ring are not associated with the orbitals involved with changes in bonding in the TS, but due to contamination by the oxygen atoms on the ester groups oriented perpendicular to the plane of the ring, above and below the plane. Based on this analysis, we may conclude that there is no pericyclic character evident in the 5-*endo-trig* closure *via* **TS 3.12.01**. In addition, **TS 3.12.01** does not posses a planar ring geometry associated with

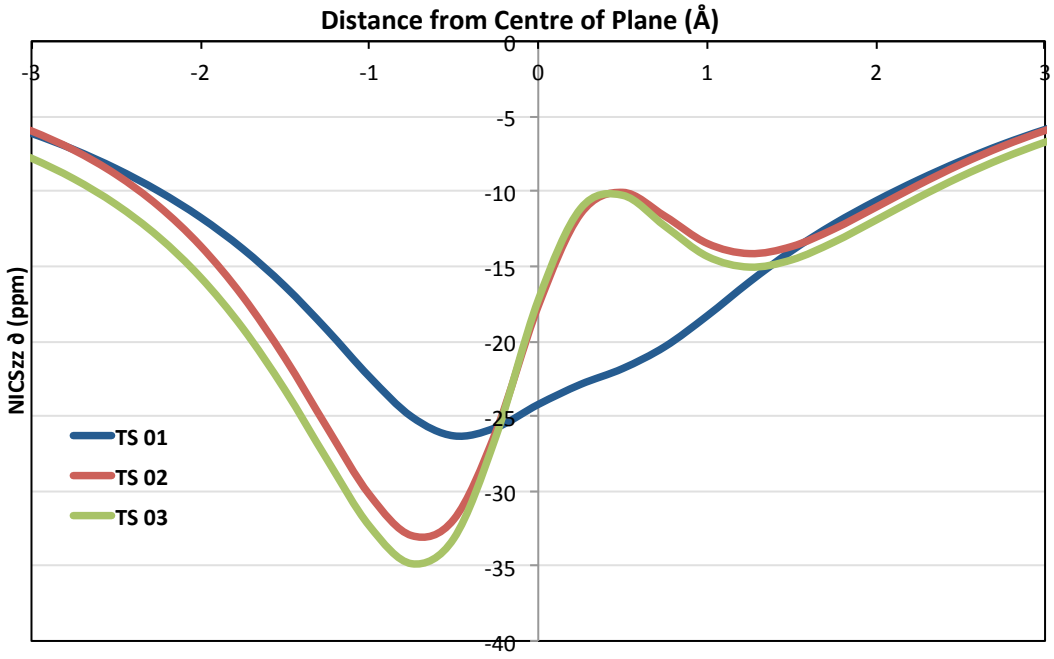

Figure 3.11: $NICS_{zz}$ component along the axis running through the ring centre (shown as black spheres in **Figure 3.10**, perpendicular to the ring plane).

pseudopericyclic TSs; it can therefore be best described as a 5-*endo*-*trig* nucleophilic cyclisation. Such a mechanistic possibility has previously been suggested by Huisgen for 1,5-electrocyclisation.[139]

Our computed magnetic properties of **TS 3.12.02** show significantly greater π-aromaticity than was observed in **TS 3.12.01** (**Figure 3.13**). Although not of the same magnitude of **TS 3.10.02** and **TS 3.10.03**, the $NICS_{zz}$ values between 1 Å and 1.5 Å above and below the plane of the ring are around -10 ppm, arising due to contributions from the carbanionic lone pair (-2.2 ppm), the C=C bond (3.1 ppm), and the aromatic C=C bond (3.1 ppm), which make up the 6π system of the 5-centre TS. We may therefore describe the cyclisation of the ester species through **TS 3.12.02** as having electrocyclic character.

The greater participation of the π-system in the *endo* ester cyclisation **TS 3.12.02** (**TS 3.8.05**) is also reflected in the dihedral angle between the enolate and benzene

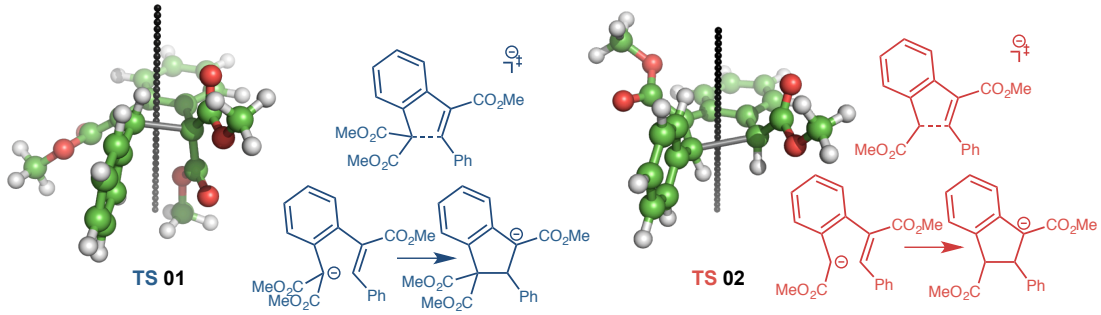

Figure 3.12: CPCM-M062X/6-311++G(d,p) optimised transition structures for 5-*endo-trig* cyclisations of ester and malonate substrates; black spheres represent the location of "ghost atoms".

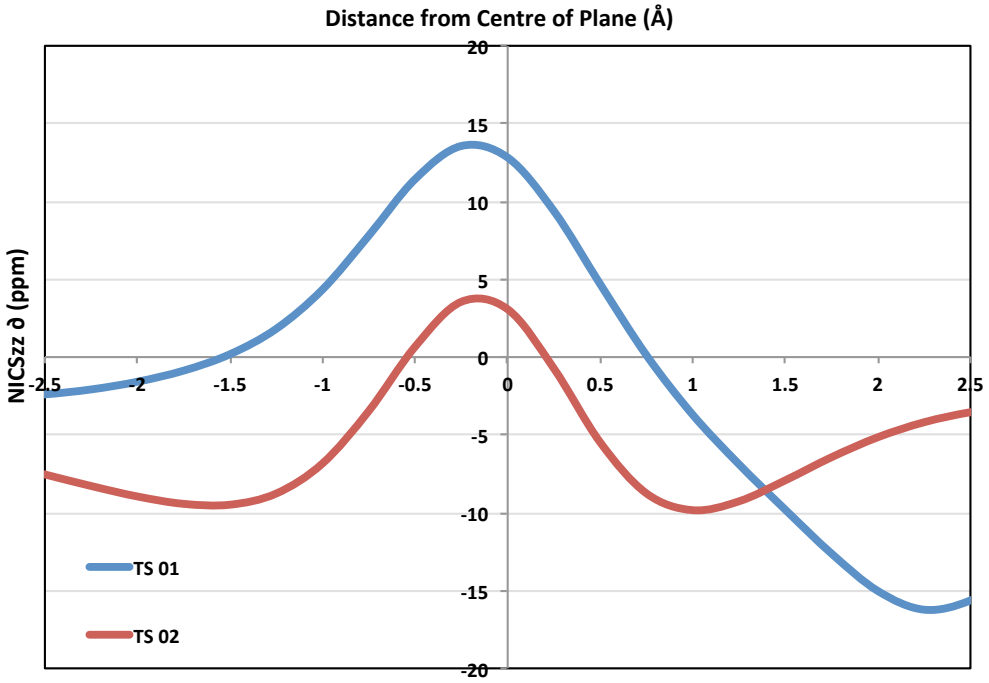

Figure 3.13: $NICS_{zz}$ component along the axis running through the ring centre (shown as black spheres in **Figure 3.12**, perpendicular to the ring plane.

of 54°. Conversely, the analogous angle in the *endo* malonate cyclisation **TS 3.9.05** is 89°, indicating virtually no participation of the π-system across the ester/enolate functionality.

3.3.4 Substrate manipulation for *endo* ester cyclisation

In a follow up study, we looked at whether stabilisation of the negative charge in the anionic substrate could result in a reversal of the regioselectivity determined by kinetics in the ester system, to make the 5-*endo-trig* cyclisation favoured. It could be argued that the better stabilisation of negative charge in the malonate system partially results in the *endo* cyclisation being favoured; we also postulated that functionalisation in the *ortho* position with sterically bulky groups could force the ester group to sit more out of the plane of the forming ring, thus bringing it geometrically closer to the TS for *endo* ring closure in a similar manner to in the malonate system. For these reasons, we opted to look at the effect that substitution of the aromatic would have on the cyclisation, in the *ortho* and *para* positions relative to the point of nucleophilic attack (**Figure 3.14** and **Figure 3.15**).

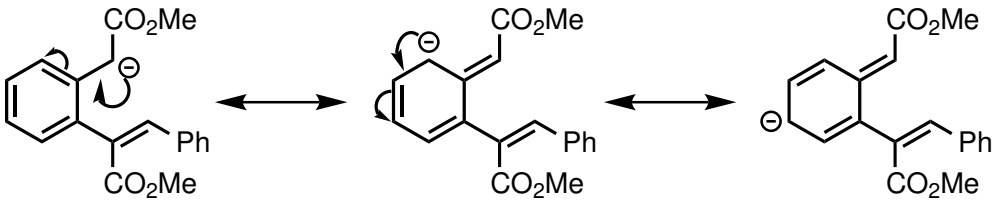

Figure 3.14: Mesomeric resonance forms of the uncyclised ester substrate with the negative charge delocalised *ortho* and *para*, relative to the nucleophilic carbon.

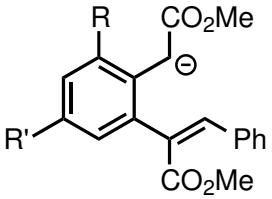

Figure 3.15: Generic functionalised form of the ester substrate under investigation in this section.

The systems we investigated are shown in **Table 3.1**. From looking at our data, a number of trends are immediately obvious; the unsubstituted system **01** in **Table 3.1** serves as a benchmark in this study. System **02** has methyl substitution *ortho* to the nucleophilic carbon; its proximity to the ester group forces the ester out

Table 3.1: Computed $\Delta\Delta G^{\ddagger}$ values for the favourability of *exo* cyclisation versus *endo* in kcal/mol; calculations were performed at the M06-2X/6-31+G(d) level of theory. The location of R and R' is indicated in **Figure 3.15**.

System	R (*Ortho*)	R' (*Para*)	$\Delta\Delta G^{\ddagger}$ (exo)
01	H	H	-8.3
02	Me	H	-4.1
03	*t*-Bu	H	-4.4
04	$SiMe_3$	H	-6.4
05	CN	H	-4.2
06	CN	CN	-4.3
07	CO_2Me (*cis*)	H	-7.5
08	COH (*cis*)	H	-5.5
09	NO_2	H	-5.1
10	H	NO_2	-7.1
11	NO_2	NO_2	-5.2
12	C_2H	H	-4.8

of the plane of the forming ring, thus reducing the magnitude of the $\Delta\Delta G^{\ddagger}$ for this system. Similar effects are seen in systems **03** and **04**, with the introduction of sterically bulkier groups in the same position. The effect is less pronounced however, presumably because of the greater electron inducing effect of these groups through the σ-framework, which prevents delocalisation of the negative charge across the benzene aromatic part of the molecule. Introduction of strongly electron withdrawing groups to the *ortho* position in systems **05**, **07**, **08**, **09** and **12**, results in a significant narrowing of the gap between *endo* and *exo* TSs, with a reduction in the magnitude of $\Delta\Delta G^{\ddagger}$ to nearly half that of the unsubstituted system **01**. Interestingly, introduction of a second electron withdrawing group in the *para* position in system **06** and **11** results in a reduction of the magnitude of the $\Delta\Delta G^{\ddagger}$. The reason for this is unclear, but it would seem that if the negative charge is delocalised to too great an extent across the benzene aromatic, *exo* cyclisation preference is encouraged. Substitution in just the *para* position in system **10** is seen to result in a small narrowing of the free energy gap between *endo* and *exo*

cyclisation TSs resulting from greater stabilisation of the negative charge across the benzene aromatic, in the absence of any geometric interference with the ester *via* steric interaction.

3.3.5 Summary

In this subsection, we were able to show the thermodynamic and kinetic rationale behind the preferential 5-*endo-trig* over 5-*exo-trig* cyclisation of the malonate substrate. Using our DFT calculations, we constructed reaction profiles for the reactions of the ester and malonate substrates, and were able to explain the regiodivergence between these systems upon cyclisation. Our NICS analysis allowed us to assess the nature of the TSs by which the *endo* and *exo* cyclisations took place, and we were able to conclude that for the formally Baldwin-disallowed cyclisation to take place in the malonate system, the TS had virtually no participation of the π-system suggesting that the cyclisation is not pericyclic in nature, while the *exo* cyclisation of the ester substrate showed some electrocyclic character in the TS.

Manipulation of the ester substrate revealed that substitution of the aromatic ring *ortho* to the deprotonated ester with sterically bulky groups reduces the Gibbs free energy gap between the TSs, thus reducing the favourability of the *exo* over *endo* cyclisation. Substitution by electron withdrawing groups in the *ortho* and *para* positions also resulted in a reduction in this free energy gap. However, we were unable to find a substitution pattern that reversed the inherent *exo* favourability of this system.

3.4 Varying ring size in *endo*- and *exo-trig* cyclisations

In a study intended to probe the origin of ring size upon *endo* or *exo* preference for trigonal cyclisation, we investigated the effect of varying ring size in model reactions, from four to seven. We also computed the effect of different second row nucleophiles, and we simulated cyclisations with carbon, nitrogen and oxygen (**Figure 3.16**). In addition to calculating the energetic activation barriers for ring

closure ($E^{\ddagger}$), we also calculated the intrinsic reaction barriers using Marcus theory (E_0),[140] and the reaction energy (E_{rxn}). In the interest of making comparisons with analogous systems in the absence of ring strain, we also calculated these values for bimolecular systems with carbon, nitrogen and oxygen for the pseudo-*endo*/*exo* reactions, undergoing conjugated nucleophilic attack, and attack at the carbonyl, respectively (**Figure 3.17**). We conducted this study using the wB97XD density functional and the 6-311++G(d,p) basis set. Solvation effects were accounted for through the use of CPCM solvation with tetrahydrofuran (THF); we decided to incorporate solvation by a polar solvent such as THF in our calculations because the systems being investigated have large charge separations, both in the ground states and saddle points.

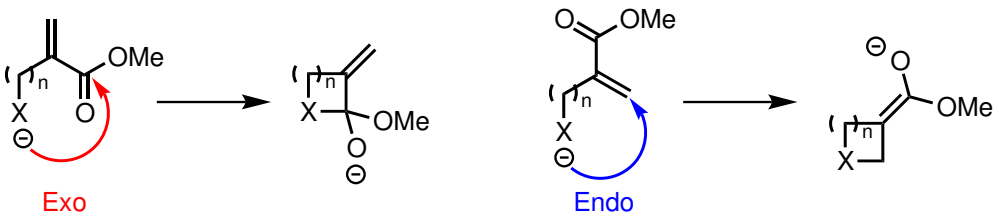

Figure 3.16: Cartoon representations of the cyclisations investigated in this study; X = C, N, O and n = 4, 5, 6, 7.

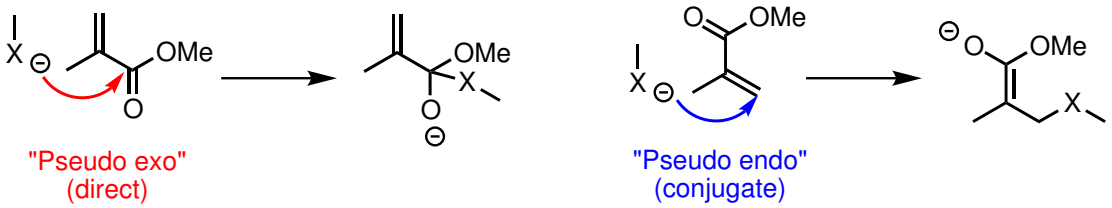

Figure 3.17: Cartoon representations of acyclic pseudo-*endo*/*exo* reactions investigated for comparison to cyclisation reactions; X = C, N, O.

Figure 3.19 shows our analysis of the E_{rxn} values for these systems; our results reveal that the *endo* cyclisations are favoured by thermodynamics in nearly all cases, resulting in the more stable product (4-*endo*-*trig* with nucleophilic oxygen is the exception). We presume the origin of this effect is the greater steric penalty from forming a new X-C bond to a quaternary carbon centre. The thermodynamic preference of this type of cyclisation is also shown in the pseudo-*endo* cyclisations.

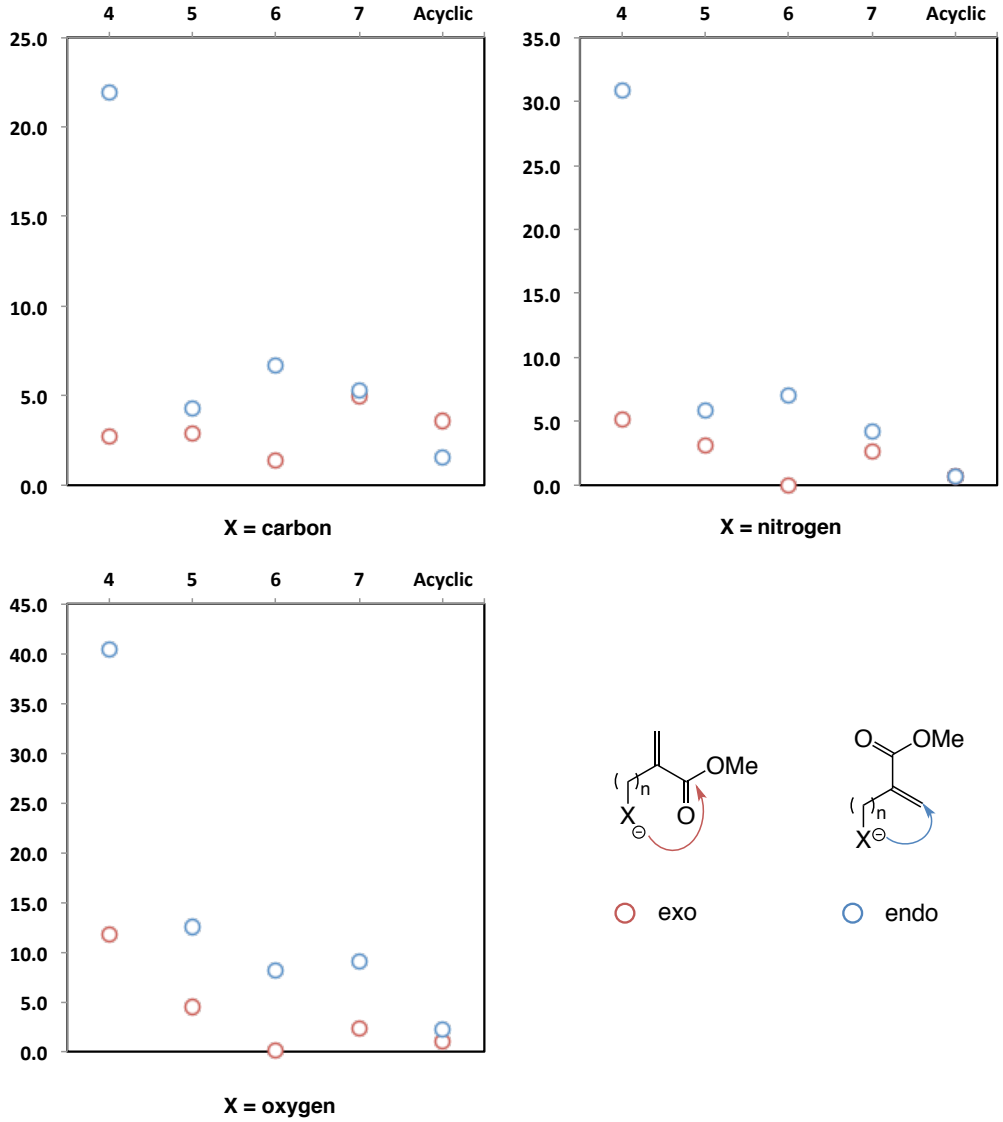

Figure 3.18: Graphs showing the effect of varying ring size (x axis) on activation energy ($E^{\ddagger}$) in kcal/mol (y axis).

These results imply that *endo* cyclisations lead to the thermodynamic product in these systems. With the exception of the 4-*endo-trig* with nucleophilic oxygen cyclisation, we calculate all reactions to be exergonic.

Our analysis of activation barriers (**Figure 3.18**) revealed that 4-*endo-trig* cyclisations were universally disfavoured across all three systems when compared to

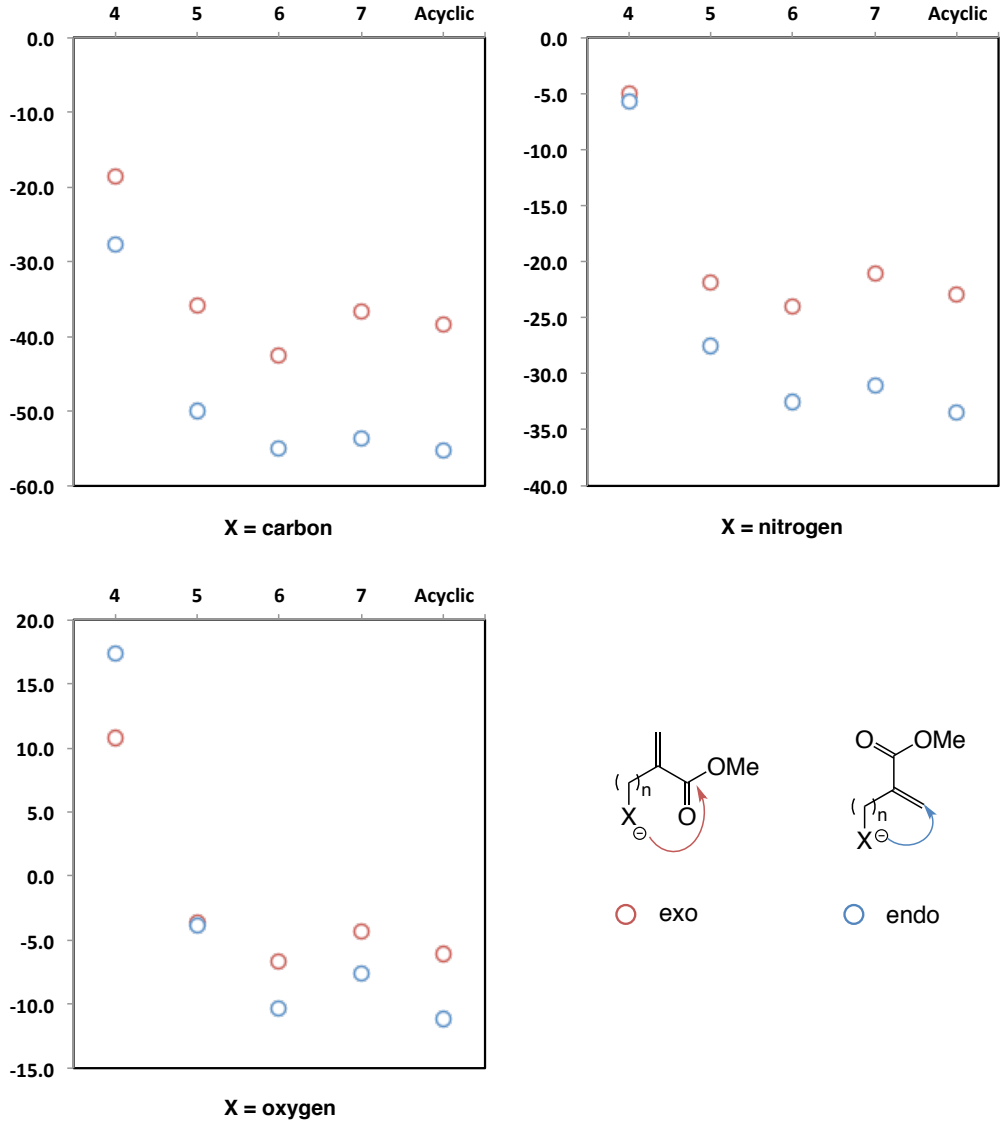

Figure 3.19: Graphs showing the effect of varying ring size (x axis) on energy of reaction (E_{rxn}) in kcal/mol (y axis).

analogous 4-*exo*-*trig* reactions by a $\Delta\Delta E^{\ddagger}$ of $>$ 19 kcal/mol. Upon increasing the ring size to five, we see that the preference for *exo* cyclisation is maintained, but the margin by which it is favoured reduces significantly; this is particularly noticeable in the nucleophilic carbon system, where the TS stability difference is just 1.3 kcal/mol. We also see a general decrease in the amount by which *exo* cyclisations

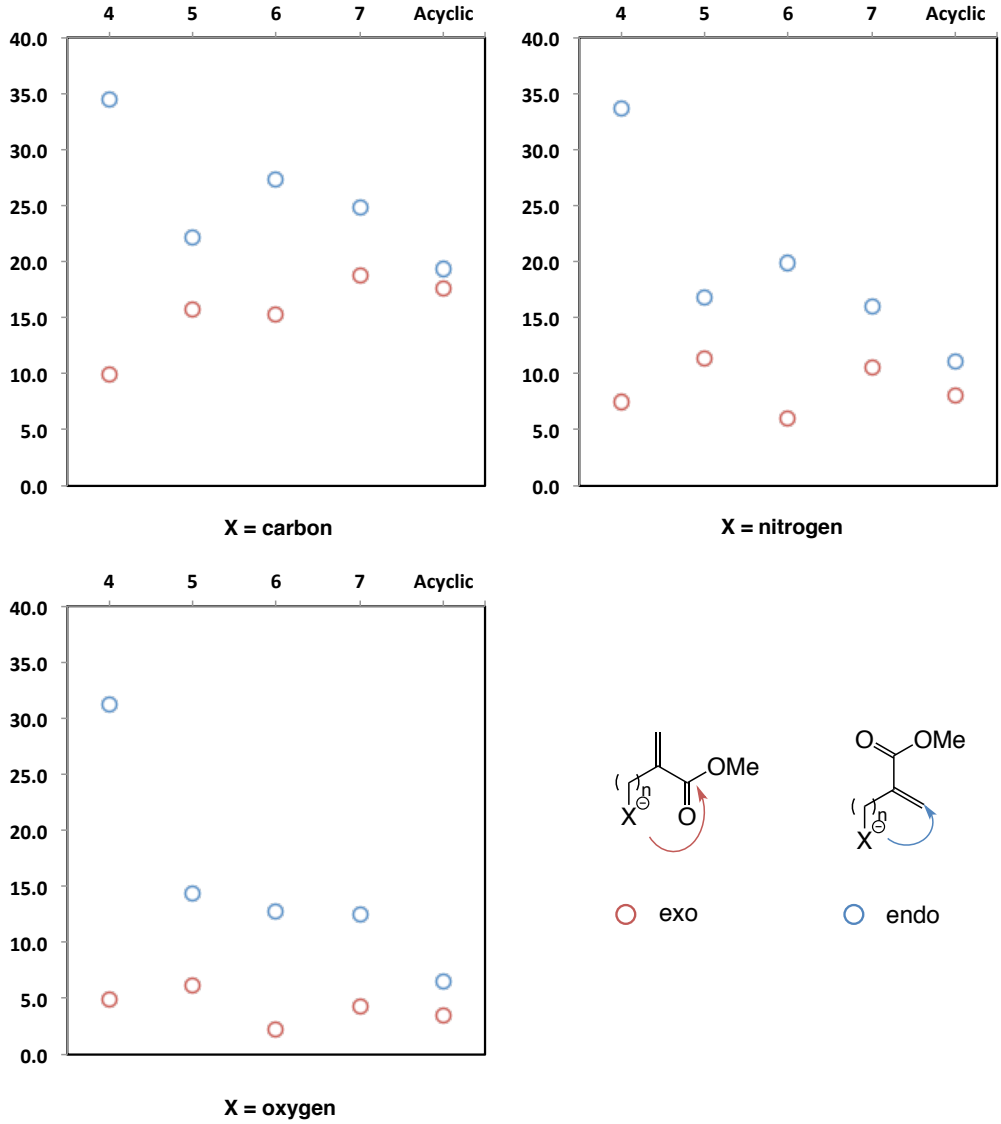

Figure 3.20: Graphs showing the effect of varying ring size (x axis) on intrinsic reaction barrier energies (E_0) in kcal/mol (y axis).

are preferred when changing the nucleophile from oxygen to nitrogen to carbon. Interestingly, upon increasing the ring size again, to six, the *exo* preference increases across all systems. However, the gap between the $\Delta E^{\ddagger}$ for *endo*/*exo* cyclisation narrows once again upon increasing the ring size to seven. It would seem that the differences in activation barriers in these systems are governed by ring strain, and

limitations on the angles of trajectory accessible in C-X bond formation; analysis of the pseudo-cyclisations reveals that the activation barriers for these reactions are low (< 4 kcal/mol), with little discrepancy between the pseudo-*endo*/*exo* systems, particularly for nucleophilic nitrogen and oxygen systems. From this analysis, we can infer that *exo* regioselectivity in these cyclisations is under kinetic rather than thermodynamic control. There is a marked decrease in the magnitude of activation barriers in all three systems for *endo* cyclisations upon going from the four membered system to the larger ring sizes and this is likely an important factor in explaining the Baldwin's rules preference for *endo-trig* cyclisations for the larger systems.

Our intrinsic reaction barriers, determined using Marcus theory, effectively remove the thermodynamic bias of systems, and reveals the innate stereoelectronics of each reaction more accurately.[54] Similarly to the $E^{\ddagger}$, they show that the *exo* cyclisations are universally favoured across all systems (**Figure 3.20**). The largest intrinsic barrier differences occur for the four membered ring closures and also for the six membered ring cyclisations. Five and seven membered ring cyclisations are both favoured over six membered ring closures; this trend is similar to that observed in the $\Delta E^{\ddagger}$ values. The intrinsic barrier for the acyclic pseudo-*endo*/*exo* reactions were the closest in energy.

Our results from this study indicate that the *exo-trig* cyclisations are always favoured by kinetics. The magnitude of this preference changes dramatically with ring size, with the greatest difference in TS stabilities occurring in the four membered ring closure, followed by the six (except for X = oxygen), then the five, and finally the seven. Thermodynamically, *endo-trig* cyclisations are always favoured relative to their *exo* analogues; the origin for this preference is presumably down to sterics, and the favourability of forming a X-C bond to a secondary rather than a quaternary carbon centre. In addition to this, 1,2-addition breaks conjugation in the system, which is disfavoured, but the resulting intermediate is a delocalised enolate, which is thermodynamically more stable than the intermediate formed from direct addition in the *exo* cyclisation. Baldwin's rules state that all *exo-trig* cyclisations are favourable for ring sizes ranging from four to seven; *endo-trig* cyclisations for six and seven membered rings are also described as favourable. From

this study, we may conclude that when *endo* ring closure is favoured, the reaction is likely under thermodynamic control. We have also shown that the hypothetical 5-*endo-trig* cyclisation with nucleophilic carbon should be competitive with its *exo* analogue.

3.5 5-*endo-trig* in hypothetical systems

Another study we conducted looked into the effect of heteroatom introduction, and the addition of functionality α and β to the nucleophile, on 5-*endo*/*exo-trig* cyclisations. Our aim was to determine whether appropriate modifications to the five membered system could result in *endo* over *exo* preference during ring closure, similar to that in the case described in section 3.3. Similarly to in our previous study into variation of ring size and nucleophile heteroatom (section 3.4), we calculated the energetic activation barriers for ring closure ($E^{\ddagger}$), the intrinsic reaction barriers using the Marcus equation (E_0),[140] and the reaction energy (E_{rxn}). In addition to this, we measured the X—C bond distances for the forming single bond (X is the nucleophilic centre), along with the X—C=Y bond angle (where Y is oxygen or carbon), in the TS for *endo* and *exo* cyclisations. We carried out this part of our investigation using the wB97XD density functional and the 6-311++G(d,p) basis set. Solvation effects were accounted for through the use of CPCM solvation with tetrahydrofuran (THF); we once again incorporated solvation by a polar solvent like THF in our calculations because the systems being investigated have significant charge separations, both in the ground states and saddle points.

Table 3.2 summarises the results for the 23 hypothetical systems we investigated using our described protocol. Our selection of systems spans a wide range of "hard" and "soft" nucleophiles, adjusted by addition of functionality α and β to the nucleophilic centre - the introduction of electron withdrawing groups makes the nucleophile "softer" relative to the unfunctionalised system while electron donating groups have the opposite effect. We also investigated the effects of altering the trajectory for these five membered ring cyclisations through the introduction of heteroatoms S and Si to the forming ring.

In the majority of systems, the *endo* ring closure resulted in the thermodynamic

product; the two exceptions were systems **05** and **18**. In system **05**, this thermodynamic preference for the *exo* cyclisation is minor, with a $\Delta\Delta E_{rxn}$ of only 0.8 kcal/mol, but in system **18**, this thermodynamic preference for the *exo* product is much larger, with $\Delta\Delta E_{rxn}$ of 8.9 kcal/mol. The difference in intrinsic barriers for *endo* and *exo* cyclisations of system **05** ($\Delta\Delta E_0$) of 11 kcal/mol is similar to the $\Delta\Delta E^{\ddagger}$ of 10.6 kcal/mol; this is the result of the slim thermodynamic difference between the regiodivergent cyclisations.

The trend observed when switching between second row elements as the nucleophile (systems **01** to **03**), is discussed to some extent in section 3.4: the trend is for the favourability of *exo* cyclisation to increase with increasing atomic number. Here we look in greater detail at the geometry of the TSs involved; the bond distances decrease in the *exo* and *endo* cyclisations, indicating that the TSs are becoming later with increasing atomic number. This trend is intuitive, as electronegativity correlates with atomic number in this series, and greater electronegativity results in better stabilisation of negative charge and therefore greater overall stability in the acyclic substrate. This observation is reinforced by the results for other nucleophilic oxygen systems where electron withdrawing groups have been introduced β to the oxygen; in systems **15** and **16** we see that the introduction of cyano groups to stabilise the negative charge has a similar effect on the lateness of the TSs, with O—C bond distances decreasing with progressive addition of this functionality. In agreement with this explanation for factors determining the lateness of TSs, we see a minor increase in the TS O—C bond distance for *exo* cyclisation of system **08** with the introduction of geminal methyl groups in the β position, which act as hyperconjugatively electron donating groups, making the nucleophile "harder", with less well delocalised negative charge. Interestingly, the introduction of $SiMe_2$ to the system in the same position in **05**, results in a decrease in O—C bond distance, implying that this actually makes the TS earlier, despite the greater electron donating properties of this functionality relative the that in system **08**. The most likely reason for this is the greater Si-O compared to C-O bond distance in the acyclic starting materials of 1.59 Å and 1.35 Å respectively; the longer bond distance in system **05** allows for the nucleophilic oxygen to sit closer to the carbon with less geometric strain being incurred by the forming five membered ring sys-

tem, thus making an earlier TS energetically more feasible. Similar effects are seen with carbon as a nucleophile, in system **04**, where the increased Si-C bond length also results in earlier TSs as determined by the C—X bond distances. Introduction of sulphur to the ring, however, does not have the same effect, with the lateness of TSs remaining virtually the same in system **06** when compared to **01**.

Table 3.2: Activation barriers for ring closure ($E^{\ddagger}$), intrinsic reaction barriers (E_0), reaction energies (E_{rxn}), X—C bond distances and X—C=Y bond angles for 5-*endo*/*exo*-*trig* cyclisation TSs; calculations were performed at the wB97XD/6-311++G(d,p) level of theory with THF solvation simulated using CPCM. Illustrations of the TSs for the various systems are shown above the tabulated data.

	5-*endo*-*trig*	**5-*exo*-*trig***	**5-*endo*-*trig***	**5-*exo*-*trig***
System	**01** 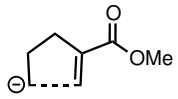	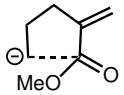	**02** 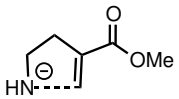	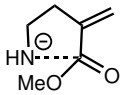
(X—C=Y)°	83.1	114.8	89.5	109.8
(X—C)Å	2.82	2.78	2.39	2.55
$\Delta E^{\ddagger}$	4.3	2.9	5.9	3.1
ΔE_{rxn}	-49.9	-35.7	-27.5	-21.8
ΔE_0	22.2	15.7	16.8	11.4
System	**03** 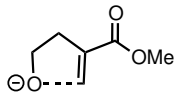	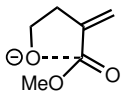	**04** 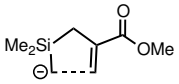	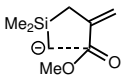
(X—C=Y)°	94.9	107.3	94.2	107.5
(X—C)Å	2.05	2.14	2.53	2.50
$\Delta E^{\ddagger}$	12.5	4.5	10.4	5.5
ΔE_{rxn}	-3.8	-3.6	-29.4	-18.9
ΔE_0	14.4	6.1	22.7	13.3
System	**05** 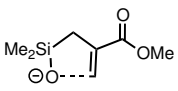	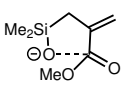	**06** 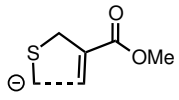	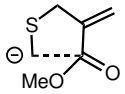
(X—C=Y)°	102.4	108.1	86.9	109.8
(X—C)Å	1.94	1.81	2.83	2.75
$\Delta E^{\ddagger}$	22.6	12.0	1.2	0.7
ΔE_{rxn}	11.4	10.6	-37.9	-27.2
ΔE_0	16.4	5.4	13.6	9.4
System	**07** 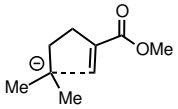	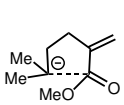	**08** 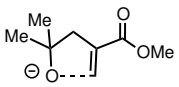	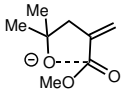
(X—C=Y)°	83.3	115.2	94.6	106.7
(X—C)Å	2.87	2.96	2.06	2.08
$\Delta E^{\ddagger}$	2.1	0.5	12.0	-0.1
ΔE_{rxn}	-56.9	-39.1	-5.9	-5.1
ΔE_0	20.9	12.3	14.8	-

	5-*endo-trig*	5-*exo-trig*	5-*endo-trig*	5-*exo-trig*
System	**09** 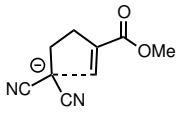	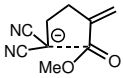	**10** 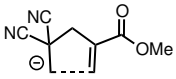	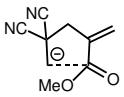
(X—C=Y)°	96.5	108.4	82.5	113.1
(X—C)Å	2.06	1.84	2.62	2.48
$\Delta E^{\ddagger}$	19.7	18.9	3.5	0.1
ΔE_{rxn}	8.9	18.9	-43.1	-23.3
ΔE_0	14.9	5.1	18.8	6.5
System	**11** 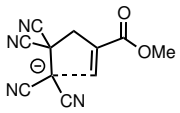	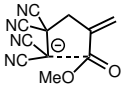	**12** 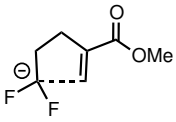	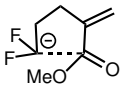
(X—C=Y)°	98.0	-	88.4	114.5
(X—C)Å	2.02	-	2.48	2.48
$\Delta E^{\ddagger}$	21.4	-	9.7	4.0
ΔE_{rxn}	14.6	Does not cyclise	-42.0	-24.5
ΔE_0	13.1	-	26.5	13.5
System	**13** 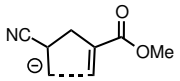	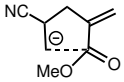	**14** 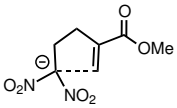	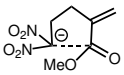
(X—C=Y)°	82.5	113.8	97.5	115.2
(X—C)Å	2.65	2.61	1.94	1.88
$\Delta E^{\ddagger}$	5.5	0.7	27.2	30.0
ΔE_{rxn}	-44.9	-29.5	17.4	29.6
ΔE_0	22.2	9.9	17.5	9.3
System	**15** 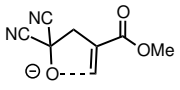	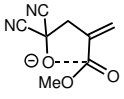	**16** 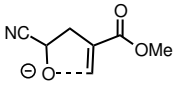	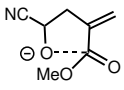
(X—C=Y)°	97.7	-	95.9	107.6
(X—C)Å	1.90	-	1.98	1.88
$\Delta E^{\ddagger}$	15.4	-	6.6	8.8
ΔE_{rxn}	11.6	Does not cyclise	4.8	7.6
ΔE_0	8.6	-	3.8	4.1

	5-*endo-trig*	**5-*exo-trig***	**5-*endo-trig***	**5-*exo-trig***
System	**17** 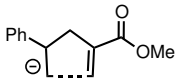	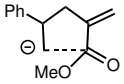	**18** 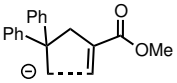	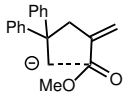
(X—C=Y)°	84.5	115.2	85.2	-
(X—C)Å	2.75	2.66	2.69	-
$\Delta E^{\ddagger}$	3.2	0.7	3.7	Barrier too low, no TS
ΔE_{rxn}	-50.2	-34.0	-23.3	-32.2
ΔE_0	20.7	11.3	12.6	-
System	**19** 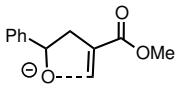	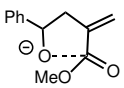	**20** 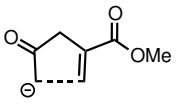	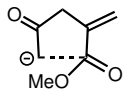
(X—C=Y)°	94.6	-	89.3	111.0
(X—C)Å	2.04	-	2.23	2.12
$\Delta E^{\ddagger}$	12.7	No TS located	23.7	18.9
ΔE_{rxn}	-2.1	0.4	-10.8	3.3
ΔE_0	13.7	-	28.8	17.2
System	**21** 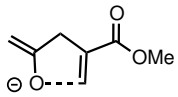	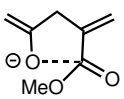	**22** 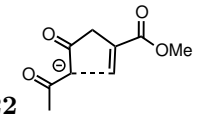	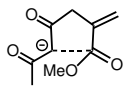
(X—C=Y)°	96.6	-	91.7	112.7
(X—C)Å	1.91	-	2.15	1.98
$\Delta E^{\ddagger}$	18.9	Does not cyclise	27.5	24.3
ΔE_{rxn}	9.9	-	4.0	17.5
ΔE_0	13.5	-	25.4	14.2
System	**23** 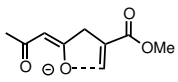	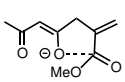		
(X—C=Y)°	98.1	-		
(X—C)Å	1.83	-		
$\Delta E^{\ddagger}$	22.3	Does not cyclise		
ΔE_{rxn}	17.9	-		
ΔE_0	11.6	-		

We found that we were able to significantly alter the nature of TSs for systems in which a carbon centre was acting as the nucleophile. We achieved this by adding a range of functional groups to the α and β positions of these systems. The addition of mesomerically electron withdrawing groups to the α position in systems **11** and **14** yielded a reversal of the expected 5-*exo*-*trig* cyclisation preference, with the *endo* TS leading to the kinetic and thermodynamic product in these reactions. System **09** also would be expected to yield the *endo* product because of the highly reversible nature of the *exo* pathway. It may seem that the origin of this effect is the disfavourability of the formation of a quaternary to quaternary C-C bond in the *exo* product, however, we see that α substitution with inductively electron withdrawing geminal fluorine results in the *exo* pathway being favoured, with the overall reaction being exergonic with a ΔE_{rxn} of -24.5 kcal/mol. Therefore, it seems likely that the mesomeric electron withdrawl in systems **11** and **14** has a role to play here; the ability of the cyano and nitro to delocalise electron density out of the plane of the forming ring in the TS results in reduced electrocyclic character in the TSs, making them similar to the malonate substituted indane reaction discussed in section 3.3. Substitution with electron inducing methyl groups in system **07** resulted in a lengthening of C—C bond distances in the TS, as well as an increase in C—C-Y bond angle, both indicative of a latening of the TS. This was accompanied by a decrease in $\Delta E^{\ddagger}$ values for both cyclisations, along with an increase in exothermicity. Interestingly, substitution at the α position with electron withdrawing groups raises the activation barriers of both *endo* and *exo* cyclisations, while substitution with electron inducing methyl groups has the opposite effect.

Substitution in the β position tends to result in a reduction of the $\Delta E^{\ddagger}$ for both *endo* and *exo* cyclisations, with the $\Delta\Delta E^{\ddagger}$ in favour of *exo* selectivity increasing relative to that for the unfunctionalised system **01**. The introduction of a single β cyano group in system **13** reduces the barrier to *exo* cyclisation to 0.7 kcal/mol and introduction of a second cyano group reduces it further, to 0.1 kcal/mol in system *10*. The $\Delta E^{\ddagger}$ value for *endo* cyclisation in system **10** is reduced to 3.5 kcal/mol (4.3 kcal/mol in unfunctionalised system **01**) however, the *endo* cyclisation for system **13** is instead raised to 5.5 kcal/mol. Electron withdrawing groups in the

β position are unable to withdraw electron density mesomerically, but electron withdrawal through the σ framework may play a role here.

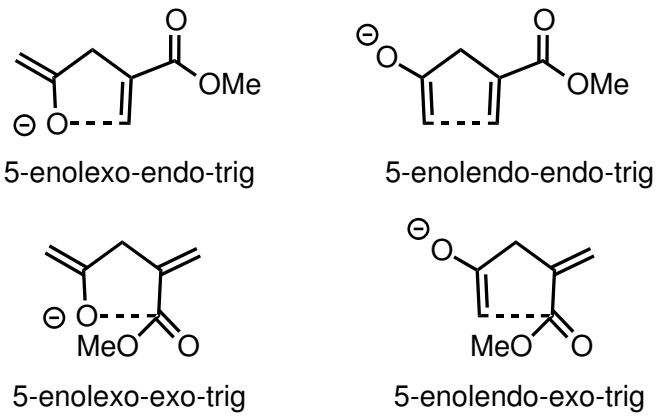

Figure 3.21: Illustration of 5-*enolendo-endo/exo-trig* and 5-*enolexo-endo/exo-trig* cyclisations.

Systems **20** to **23**, are examples of 5-*enolendo-endo/exo-trig* and 5-*enolexo-endo/exo-trig* cyclisations (**Figure 3.21**). 5-*enolexo-endo-trig* cyclisations have previously been reported in the synthesis of Spirotryptostatin B,[141] although they are generally thought to be disfavoured relative to the *exo* equivalent ring closure. Comparing systems **20** and **21**, we see that cyclisation via the *enolexo* pathway results in a more stable than the *enolendo* route to the *endo* product. The 5-*enolendo-exo-trig* cyclisation shown in system **20** proceeds with a similar barrier to the 5-*enolexo-endo-trig* ring closure in system **21**, with both proceeding with a $\Delta E^{\ddagger}$ of 18.9 kcal/mol. It is the latter, however, that yields the thermodynamic product, and our calculated ΔE_0 values further support the bias for this product formation. Comparison of systems **22** and **23** also reveals that the 5-*enolexo-endo-trig* is favoured, this time both thermodynamically, and kinetically.

It would seem that there are a number of routes that could be explored in future when trying to make 5-*endo-trig* cyclisations favourable compared to 5-*exo-trig*. Increasing the "hardness" of nucleophiles reduces the barrier to *endo* ring closure, however, it also has a similar effect on the *exo* cyclisations. In cases where the reaction barriers are lowered sufficiently, it may be possible to run reactions under thermodynamic control to yield the *endo* product. Introduction of mesomerically

electron withdrawing groups α to the nucleophile significantly destabilises the *exo* product, and subsequently the *exo* TS for cyclisation; we saw in systems **09**, **11** and **14**, that this results in the *endo* product being favoured. Finally, in cyclisations of nucleophilic enols, we saw that 5-*enolexo*-*endo*-*trig* could be favoured thermodynamically in system **21**, and kinetically too in system **23**.

3.6 Conclusions

In this section, we looked at the various factors controlling regioselectivity in a range of cyclisation reactions. Analysis of these factors relied on us using a variety of computational techniques, including the development of novel software for performing NICS calculations to assess the magnetic properties of cyclisation TSs. For the 5-*endo*-*trig* cyclisations in the formation of the functionalised indane motif, we were able to show that the origin of this formally disallowed ring closure, relative to what is usually the kinetically favoured *exo* cyclisation, lay in the inherent geometric bias of the uncyclised malonate species, combined with a lack of electrocyclic character in the *endo* TS resulting from out of the plane delocalisation of negative charge across the geminal ester functional groups. We computed the effects of modifying the stereoelectronic properties of the system using various substitution patterns across the benzene aromatic of the forming indane in the ester substrate; through doing so, we showed that the addition of steric bulk in the *ortho* position relative to the ester group resulted in decrease *exo* cyclisation bias in this system. We also showed that electron withdrawal resulted in a reduction in this kinetic regioselective preference.

In our followup study, we probed the origin of the *endo*- versus *exo*-*trig* cyclisations across a range of ring sizes, with nucleophilic carbon, nitrogen and oxygen. We were able to show that the four membered ring cyclisation to form an *endo*-product is unlikely to ever be possible, with the activation barriers for these ring closures being disfavoured by > 19 kcal/mol. The *endo* cyclisations lead to the thermodynamic product in nearly all of the systems we investigated, while the *exo* ring closure is always kinetically favoured. Interestingly, our calculations indicate that the *endo* five membered ring cyclisations should be competitive with *exo* cy-

clisations, to the same or greater extent as in the six membered ring systems. The $\Delta\Delta E^{\ddagger}$ between *endo* and *exo* cyclisation was smallest for seven membered ring formation, across all systems. Our acyclic equivalent systems showed that there is little difference between conjugated addition, or direct attack at the carbonyl, suggesting that the majority of selectivity encountered in these systems is the direct result of geometric constraints upon nucleophilic attack trajectories.

Finally, our study into hypothetical five membered ring *endo*- and *exo*-cyclisations revealed that a number of functional group modifications could result in a reversal of the *exo* kinetic bias, and also the *endo* thermodynamic product preference. We showed that geminal α substitution with mesomerically electron withdrawing groups was an effective way to impart *endo* selectivity in ring closure, with the reaction becoming kinetically favoured *via* a significant reduction in the stability of both the *exo* cyclisation TS, and the cyclised *exo* product.

4 Stereoelectronic effects in the α-alkylation of bicyclic enamines

4.1 Background

The introduction of chiral enantioenriched α-alkyl-substituted aldehydes in synthesis is an invaluable tool for Organic Chemists. In the past, a number of methods involving chiral auxiliaries have been used for such asymmetric inductions but each is not without its specific drawbacks. One of the most common techniques used to generate enantioenriched α-alkyl-substituted aldehydes is through the use of Enders' lithiated SAMP/RAMP hydrazones but the requirement for low temperature (usually -80 to -120 °C) and the need for ozonolysis for auxiliary cleavage can cause problems.[142,143] Higher oxidation level alkylations are also known with Evans' oxazolidinone[144] or Myers' pseudoephedrine[145] auxiliaries but once again further manipulation is required in the removal of these auxiliaries through reduction.[146]

Catalytic α-alkylation of aldehydes using enamines has attracted much attention in recent years and has even been described as the 'Holy Grail' for organocatalytic chemists.[147] This task has proved to be a challenge because of the numerous side reactions which may occur in such a reaction mixture including Cannizzaro and Tishchenko reactions of the aldehydes, and N- and O-alkylation of the catalysts.[78] MacMillan's work on asymmetric one-electron mediated organic transformations using photoredox-organocatalysis provides a smart route to performing such catalysis, however, this method requires a radical stabilising electron withdrawing group on the alkyl substituent, thus greatly reducing the generality of this technique.[148]

Prof. Hodgson (University of Oxford) and coworkers previously reported asymmetric induction in the reactions of chiral, non-racemic tropane- and homotropane-derived enamines, with alkyl iodide electrophiles.[149] Experimentally, it was shown that two bicyclic secondary amines differing by a single methylene group (**Figure 4.1**) gave the opposite sense of asymmetric induction upon alkylation with EtI.

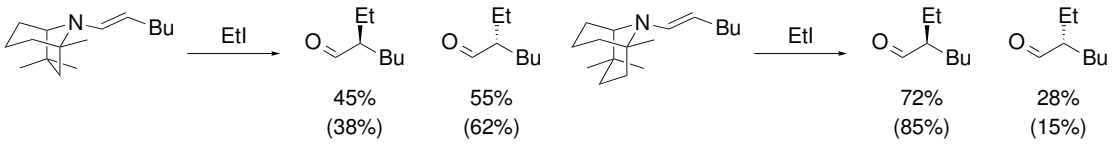

(a) Tropane (6,5) system **(b)** Homotropane (6,6) system

Figure 4.1: General reaction schemes for ethylation of non-racemic tropane-derived enamines carried out in the Hodgson group. Experimentally determined enantiomer percentages are shown under the products and the computationally derived values for the model system are in brackets.

Prof. Paton was able to successfully provide an explanation for the origin of the asymmetry in these systems using computation at the B3LYP/6-31G(d) level of theory (to simplify the systems for calculations, the butyl group on the substrate was simplified to a methyl group); the same methodology had been previously employed by Prof. Houk in a study of related acyclic systems.[150] Intrigued by the possibility of further structural modifications to the amine auxiliary, we have investigated the potential for other enamines to undergo enantioselective alkylation. In the process, we have further developed the computational model in the pursuit of creating a more accurate account of the asymmetric bias of these systems. Our work has since been supported by a series of new experimental results from the Hodgson group, a summary of which are shown in **Figure 4.2** (at the time of writing, these results are unpublished).

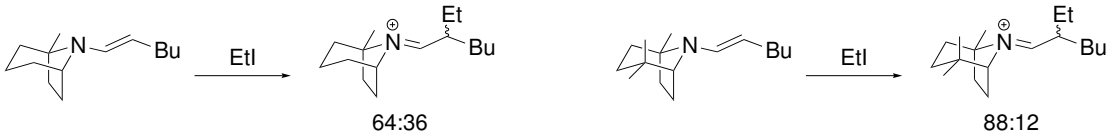

(a) Tropane (6,5) system **(b)** Tropane (6,5) system (with geminal methyl groups)

Figure 4.2: General reaction schemes for ethylation of non-racemic tropane-derived enamines carried out in the Hodgson group in 2014/15 by Ben Le Neve-Foster.[151] Experimentally derived diastereomeric ratios (dr) are shown; the major diastereomer is predicted to be the result of *Si*-facial electrophilic attack of EtI in both cases although this has yet to be determined experimentally.

4.2 Mechanism

In this investigation, we focus primarily on a single step: that in which alkylation occurs *via* irreversible electrophilic attack of EtI to the enamine substrate, forming an iminium salt; this TS is selectivity determining for the reaction. However, there are multiple experimental steps in the full reaction procedure which leads to the generation of a functionalised aldehyde. **Figure 4.3** shows a breakdown of the synthetic steps involved in the generation of a chiral α-alkylated aldehyde; in this case, a tropane-type auxiliary is synthesised.

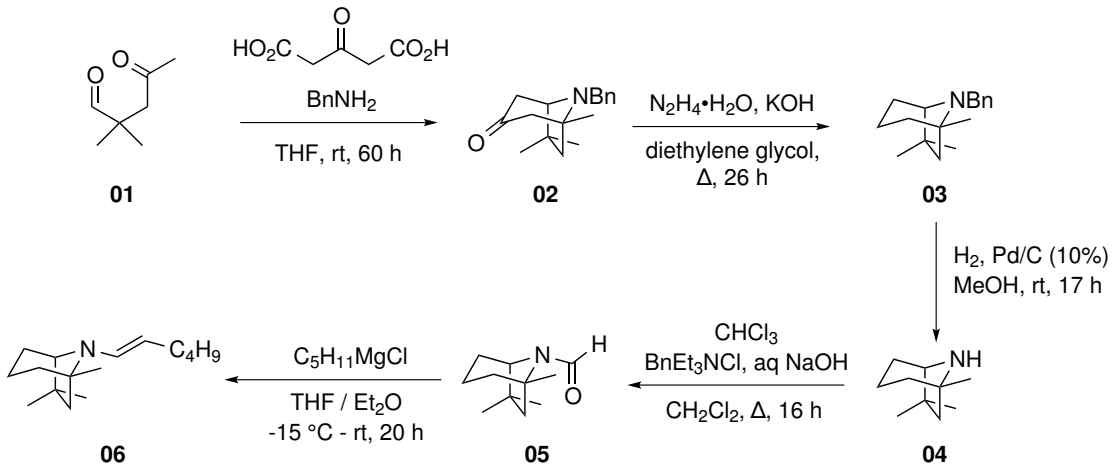

Figure 4.3: Synthesis of a tropane-derived enamine.[149]

The Synthetic Chemistry begins with a Robinson-type tropane synthon invoking reaction of dicarbonyl species **4.3.01** with 1,3-acetonedicarboxylic acid and benzylamine *via* decarboxylation and dehydration respectively to form structure **4.3.01**, which now contains the tropane structural motif. This is then modified *via* a Wolff-Kishner reduction to eliminate the carbonyl to give **4.3.03**,[152] followed by hydrogenolysis to generate **4.3.04**.[153] Synthesis of formamide **4.3.05** is then carried out through a procedure developed by Blum and Nyberg.[154] In a variant of the Bouveault aldehyde synthesis involving non aqueous work-up,[155] Grignard addition of $C_5H_{11}MgCl$ yields the desired tropane-derived hydrolytically unstable enamine **4.3.06**. This species then undergoes asymmetric alkylation through reaction with EtI.

4.3 Computational methods

All calculations in this section were performed using DFT which was implemented using Gaussian 09.[5] For the majority of this work, the B3LYP functional[19,20] was used, largely because of its proven success in the modelling of other similar systems previously.[149,150] However, for our most recent calculations in this study, we also incorporated Grimme's DFT-D3 dispersion correction in order to better handle dispersion effects in our systems of interest.[21] In all our calculations, we used the Pople 6-31G(d) basis set in our description of all elements with the exception of iodine for which we used the Hay-Wadt LANL2DZ effective core potential (ECP), which gives an accurate account of orbital relativistic contraction.[14] In order to account for the effects of the solvent used in the experiment (acetonitrile), we used the implicit CPCM method, which takes into account the solvent bulk dielectric constant. The handling of solvation in this system is particularly important since the reaction generates an iminium iodide ion pair; solvation by the highly polar solvent in this case significantly stabilises charge separation in this system relative to the gas phase. Solute cavities were defined by UFF atomic radii, as is the default in Gaussian 09.[83] Gibbs free energies were evaluated at the reaction temperature of 65 °C and vibrational entropy contributions towards this value were computed using a free-rotor approximation for low frequency modes. We used a smooth damping function centred about a frequency of 100 cm^{-1} to switch between the harmonic approximation for vibrations above this value and the free-rotor approximations below.[84,85] Translational entropies were calculated using the conventional standard state of 1 mol/l in solution for all species *via* the Sackur-Tetrode expression, however, the lack of any associative or dissociative steps in our calculated mechanism means that his has no effect on our results. We computed vibrational frequencies for all stationary points to confirm them as either minima or TSs, based on whether they had zero or a single imaginary frequency respectively.

4.4 Preliminary results and discussion

We began our investigation by looking into how a pattern of structural modifications affected the extent to which tropane-type chiral auxiliaries impart selectivity in the previously discussed alkylation reactions with EtI. We based our initial methodology on that used in previous investigations of similar systems;[149,150] we used B3LYP/6-31G(d) (LANL2DZ for iodine) with CPCM handling of solvation by acetonitrile. In our model, we studied the difference in stabilities of four alkylation TSs - two conformers for each of *Re*- and *Si*-face addition. A depiction of all plausible conformations for alkylation TSs is shown in **Figure 4.4**; positions 'a' and 'b' (for the methyl group of EtI) correspond to the conformers considered to be the most stable in previous investigations. Position 'c' was ruled out because of the assumed steric penalty resulting from methyl proximity to the tropane ring. The geometry across the enamine with respect to the bicyclic system was considered fixed in the *s-trans* conformation to avoid the steric clashing between the methyl group α to N and the enamine; this steric interaction is depicted in **Figure 4.5**.

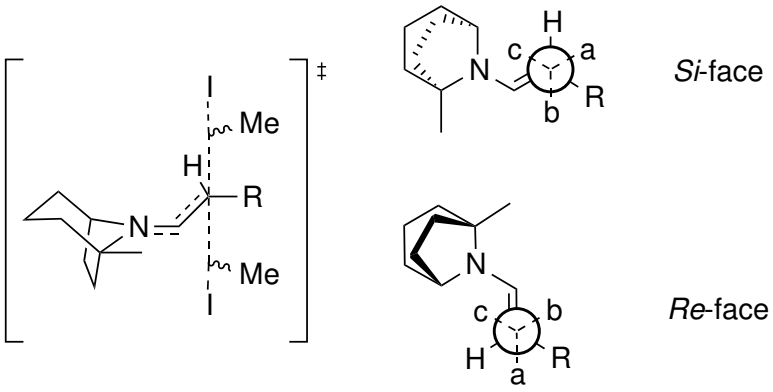

Figure 4.4: Illustration of *Si*- (top) and *Re*-face (bottom) alkylation TSs with EtI; the three plausible orientations which the methyl group may adopt are marked on the Newman projections as a, b and c; R = Me (R = Bu in experiment).

Having chosen an appropriate model, we started our investigation by looking at the effect tropane ring size has on the level of computed enantioinduction introduced upon alkylation with EtI; previous studies had shown a significant change both in magnitude and direction of enantioselectivity upon varying ring size by a single

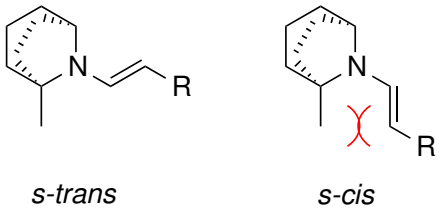

Figure 4.5: Illustration of the origin of the enamine *s-trans* preference in a singly methylated tropane enamine; steric interaction shown in red.

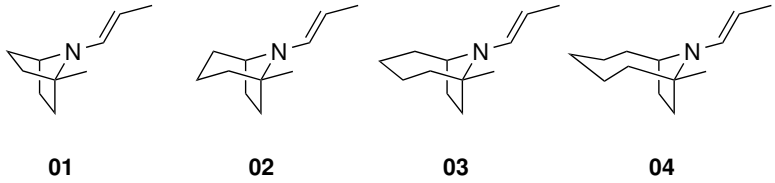

Figure 4.6: Depiction of tropane-type enamine ring size variation.

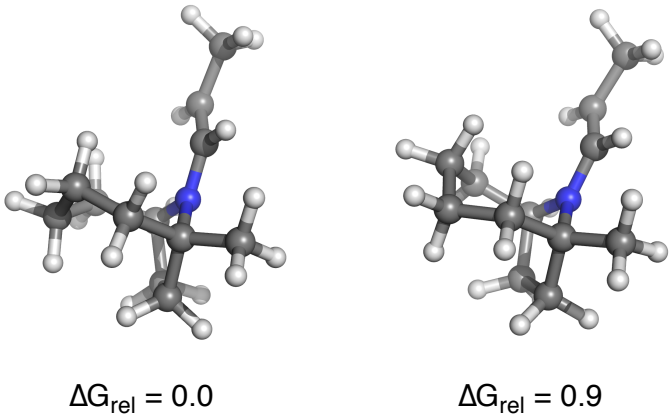

Figure 4.7: Optimised conformer comparison for seven membered ring tropane-type enamine **4.6.03**.

methylene (**Figure 4.1**).[149] Starting with the basic singly methylated tropane-motif **4.6.02**, we varied the size of the six membered ring, in the range five to eight (**Figure 4.6**). Five membered tropane-type enamine ring system **4.6.01** is C_s symmetric, making it unable to impart asymmetry to the alkylation as *Si*- and *Re*-face TSs are mirror images of one another and therefore have identical stabilities. The simulation of rings composed of upwards of six atoms is often fraught with conformational challenges resulting from multiple distinct conformers,

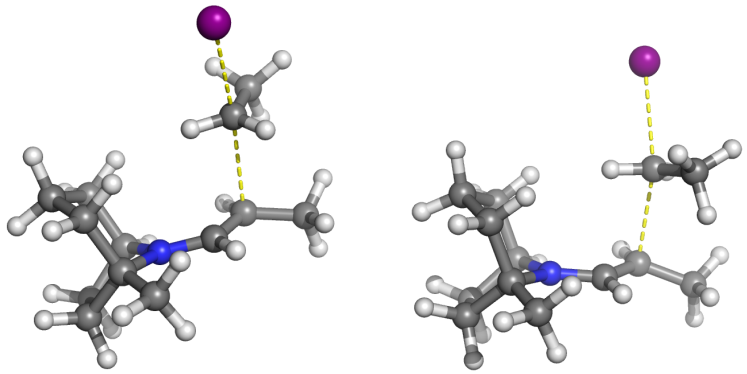

Si-face conformer 'a' TS;
$\Delta G^{\ddagger}$ = 108.9 kJ/mol

Si-face conformer 'b' TS;
$\Delta G^{\ddagger}$ = 109.1 kJ/mol

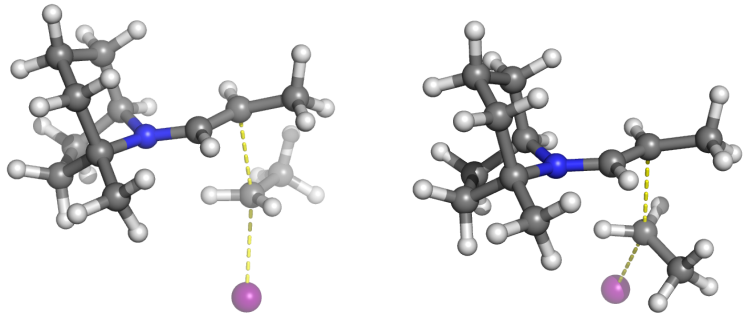

Re-face conformer 'a' TS;
$\Delta G^{\ddagger}$ = 107.4 kJ/mol

Re-face conformer 'b' TS;
$\Delta G^{\ddagger}$ = 106.4 kJ/mol

Figure 4.8: Four fully optimised alkylation TS conformers for the methylated tropane system; $\Delta G^{\ddagger}$ values are relative to the separated most stable conformer of the methylated tropane-enamine and EtI.

which often have similar stabilities. The seven membered ring system **4.6.03** in particular presented us with issues over subtle differences in conformational stability; we found two distinct ground state conformations for this system with similar stabilities (**Figure 4.7**), both of which would need to be considered in our study of alkylation TSs. Based on our TS conformational analysis earlier (**Figure 4.4**), there are eight TSs which need to be considered for enamine **4.6.03**. Fortunately, eight membered ring system **4.6.04** proved to be simpler to model, with a single crown conformation proving to be the only stable conformer needing consideration.

With ring and TS conformers both under consideration, we computed all 16 TSs

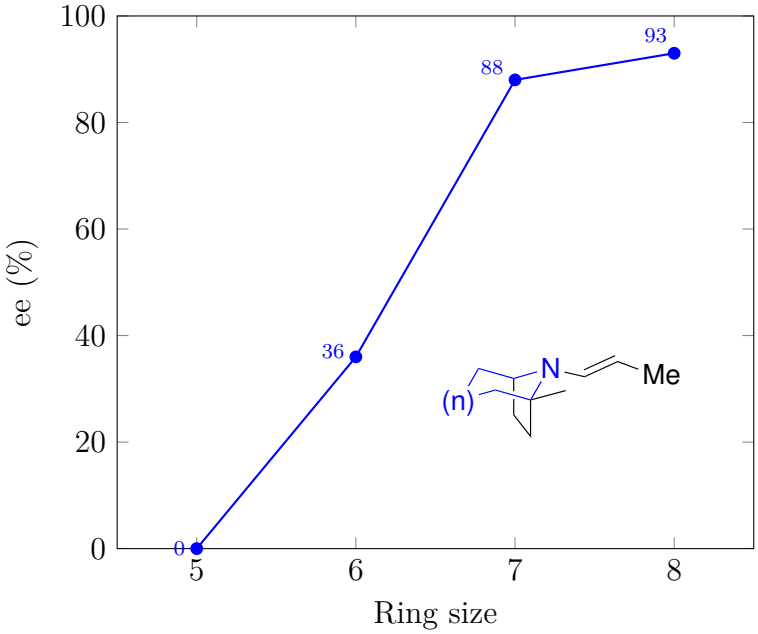

Figure 4.9: Plot of the relationship between calculated ees and ring size in tropane-type systems (**Figure 4.6**) at 65 °C; 16 fully optimised TSs are used in this plot. The ee favours *Re*-face addition.

for alkylation (four TSs for six and eight membered rings; eight TSs for seven membered ring). We did not compute TSs for the C_s symmetric five membered ring system as it is incapable of imparting asymmetry. Using a Boltzmann distribution in the handling of the stabilities of all the TSs found for each of our computed systems, we were able to calculate predicted ees at the reaction temperature of 65 °C. **Figure 4.8** shows the four TSs under consideration for the standard (six-membered ring) tropane enamine, as an illustrative example of the TSs used in the determination of ee for a system; the relative stabilities of the two *Si*- and *Re*-face TSs are handled using a Boltzmann distribution to produce *Si*:*Re* ratio of 32:68, and an ee prediction of 36%, in favour of the *R* intermediate and product for our computational system.

Figure 4.9 shows the effect of varying the size of a single ring on the tropane enamine system on enantioselective alkylation with EtI. The general trend observed is for the level of asymmetry in the alkylation to increase as ring size is increased. This observation is intuitive, as increasing ring size creates a greater

degree of asymmetry in the tropane-type system, thus we might expect the level of imparted enantioselectivity to also be greater.

Previous studies of this asymmetric alkylation reaction had been conducted with tropane and homotropane derivatives containing geminal methyl groups β to N (**Figure 4.1**).[149] From a synthetic point of view, the inclusion of geminal methyl groups at this position in the chiral auxiliary is relatively facile; they are introduced through inclusion in the starting materials and do not generate an additional stereocenter in the bicyclic amine. With this in mind, we investigated the effect of including geminal methyl groups in analogous positions on the variable ring sizes used in our previously investigated system. Our results from the 20 alkylation TSs (four from the five, six and eight membered ring systems; eight from the seven membered ring system) are summarised in **Figure 4.10**. Once again, we see that increasing ring size increases the level of imparted asymmetry in the reaction. We also see that the inclusion of geminal methyl groups to the system further forces the enantioselective bias of the reaction, with the introduction of each additional methylene group resulting in significantly higher ee. Interestingly, in the first system of the series (comprised of two five membered rings), we see a modest level of enantioinduction resulting from the presence of the geminal methyl groups, of 42% ee; as noted earlier, no selectivity can be imparted in the analogous system without geminal methylation, since the two five-membered ring-containing auxiliary is achiral.

4.5 Development of the model system

In the interest of bettering our computational representation of the way in which this system undergoes alkylation with EtI, we optimised TSs with the more sterically encumbered, conformer 'c' (**Figure 4.11**). To our surprise, the relative stability of these TSs were comparable to those for conformers 'a' and 'b', which had only been used in our investigation up until now; in some cases, conformer 'c' was found to be the most stable conformer for alkylation.

Figure 4.11 shows the key interactions at a TS for conformer 'c', *Re*-face alkylation of a tropane enamine system. Using NBO steric and second order perturbation

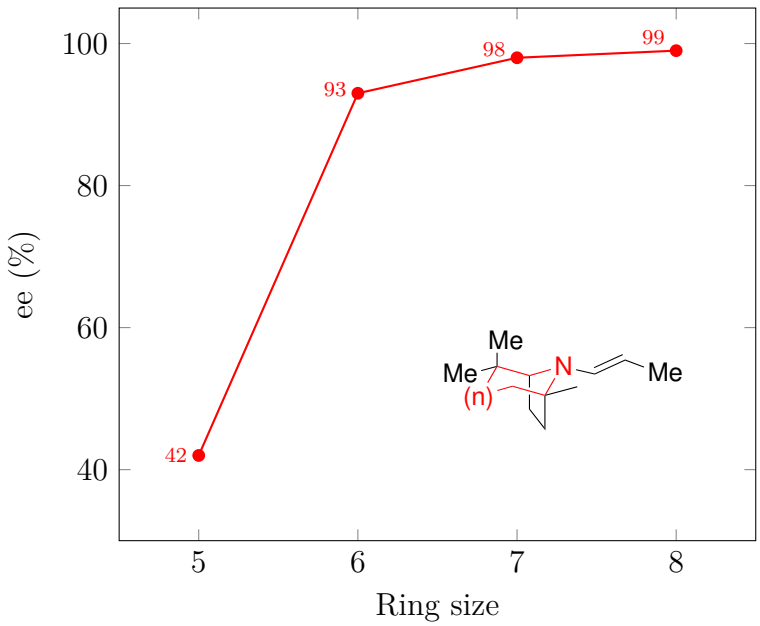

Figure 4.10: Plot of the relationship between calculated ees and ring size in tropane-type systems with geminal methyl groups β to N at 65 °C; data from 20 fully optimised TSs are used in this plot. The ee favours *Re*-face addition.

theory analysis, we were able to quantify some of the key stabilising and destabilising interactions in this particular TS, and rationalise what might otherwise appear to be chemically unintuitive; we computed the stabilising interaction between the N lone pair and the C-H σ^* (shown in blue, **Figure 4.11**) to account for 14 kJ/mol of stability. This is offset by a combination of the two C-H σ to C-H σ steric interactions (shown in red), which account for 2.4 kJ/mol of instability. However, there is also the steric repulsion between the N lone pair with the C-H σ of the ethyl, which destabilises the system by 10.4 kJ/mol, yielding a net stabilising interaction of 1.2 kJ/mol. This analysis goes some way towards explaining the increased stability of conformer 'c' but does not fully explain the marked preference seen for this conformation when compared to its conformer 'a' and 'b' analogues.

The inclusion of TSs for conformer 'c' in our previous study alters our calculated predictions for levels of asymmetric induction; however, it does not change the general trends observed upon ring expansion, and for the introduction of geminal

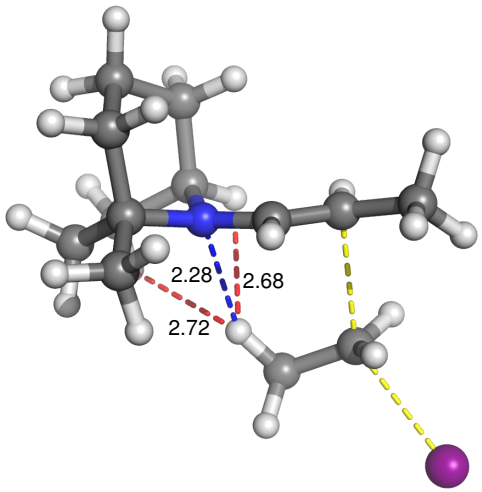

Figure 4.11: Conformer 'c' TS for alkylation on the *Re*-face of the tropane enamine system; the blue line shows the interaction between the N lone pair and H of the methyl group; red lines indicate H-H steric interactions; yellow lines indicate bonds being formed and broken in the TS; distances shown are in Å.

methyl groups. The compilation of the results shown in **Figure 4.12** compares our computed ees for each of the two series studied against the results from the previous investigation. It is clear that the inclusion of conformer 'c' in this investigation further increases the *Re*-face bias for all systems where selectivity is observed (see also **Table 4.1**); the origin of this becomes clear when we look more closely at the free energies of the conformer 'c' TSs, relative to the other conformers (**Table 4.2**). We notice that for the *Re*-face addition, the 'c' conformer is predominantly the most stable conformer for each system. Conversely, the *Si*-face 'c' conformer is frequently close to, or less stable than (particularly for the non gem-dimethyl systems), the other conformers for this face. Therefore, the overall effect on the asymmetric induction for each system after inclusion of conformer 'c' is an increased preference for *Re*-face alkylation (**Figure 4.12**). The most likely explanation for this effect is that conformer 'c' suffers the most from steric interactions between the ethyl group and axial/pseudoaxial H or axial methyl groups on the adjacent ring in the *Si*-face TSs; these interactions increase as the ring is expanded. For *Re*-face addition, the ring in closest proximity to the ethyl group remains the same size, and steric clashing with the pseudoaxial C-H bonds on the five membered ring remain minimal. This is given further credence by the increase

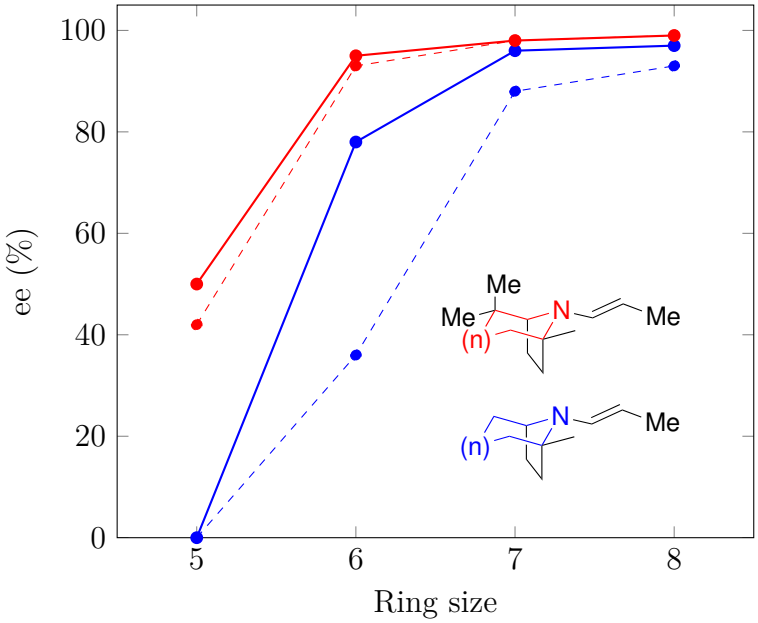

Figure 4.12: Plot of the relationship between calculated ees and ring size in two different tropane-type systems (with and without geminal methyl groups β to N) at 65 °C; dashed lines represent results from the previous study; solid lines represent ees calculated using conformers 'a', 'b' and 'c'. The ee favours *Re*-face addition.

in conformer 'c' *Si*-face TS values upon ring expansion; this is not observed for the *Re*-face analogues.

Table 4.1: Ees calculated using a Boltzmann distribution of all TS conformers for each system studied compared with ring size.

System	Ring size			
	5	6	7	8
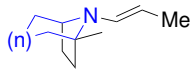	0%	78%	96%	97%
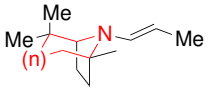	50%	95%	98%	99%

Table 4.2: ΔG values for TSs of all three conformers on both *Re*- and *Si*-faces for each tropane-type system investigated in kJ/mol; values are relative to the separated starting materials. All calculations were performed at the B3LYP/6-31G(d) level of theory (LANL2DZ for I) in CPCM acetonitrile solvation.

Face	Conformer ΔG‡			System	Face	Conformer ΔG‡			System
	a	b	c			a	b	c	
Si	-	-	-	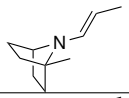	*Si*	112.8	111.2	111.8	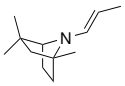
Re	-	-	-		*Re*	110.8	108.5	107.8	
Si	108.9	109.1	110.4	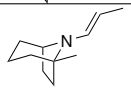	*Si*	110.5	108.8	112.2	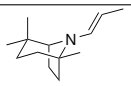
Re	107.4	106.4	101.3		*Re*	100.6	100.4	99.2	
Si	112.1	110.1	116.6	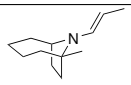	*Si*	114.8	115.7	115.2	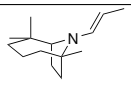
Re	103.2	102.9	98.1		*Re*	103.6	101.5	100.6	
Si	113.9	110.6	117.5	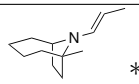	*Si*	113.5	117.2	117.8	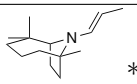
Re	103.8	106.3	100.5 *		*Re*	104.0	102.9	102.8 *	
Si	115.5	114.1	123.6	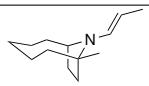	*Si*	120.2	122.2	126.8	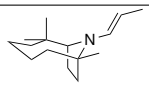
Re	105.7	105.1	103.0		*Re*	107.8	106.0	107.6	

* Second, less favourable conformer of the seven membered ring containing system.

4.6 Probing the source of asymmetry

So far, we have been able to correlate the extent of enantioinduction in our systems to the degree of asymmetry in the tropane-type enamine system. However, in order to understand how asymmetry is induced in this reaction, we need to have

a better understanding of the various factors which act to stabilise or destabilise the alkylation TSs. We observe that increasing the size of one of the rings relative to the other, increases the steric bulk on one side of the system, making alkylation upon that face more hindered and therefore less favourable; the same explanation may be used to account for the difference in ees between the systems with and without geminal methyl groups β to N, as these too are a source of increased steric bulk. It should be possible to give this hypothesis partial quantitative backing by comparing the Total Steric Exchange Energy (TSEE) of the TSs for *Re*- and *Si*-face alkylation. TSEEs are the summation of all NBO calculated steric (filled-filled orbital) interactions in a system; comparison of TSEEs between systems can provide us with a general quantitative insight into the relative steric strains of various systems. In order to make our assessment of the TSEEs for a set of TSs in a particular system more physically correct, we calculated Boltzmann weighting coefficients for alkylation on each face; these differ from the coefficients used to determine ee, which were derived from an amalgamation of TSs for alkylation on both faces for each system.

Table 4.3: *Re*-face TS bias based on Boltzmann weighted TSEEs in kJ/mol for variable ring sizes in the range of 5 to 8; all values are given relative to the *Si*-face TSs. Positive values indicate the *Re*-face is disfavoured while negative values indicated favourable *Re*-face addition.

System	Ring size			
	5	6	7	8
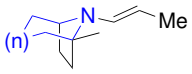	-	11.9	5.7	3.4
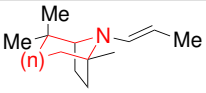	-14.5	-7.8	-5.6	-2.8

The scaled TSEEs for our systems calculated in the previous section are shown in **Table 4.3**. The results for the system without geminal methyl groups (blue) match the expected trend upon ring expansion, with the difference in TSEE between the two faces decreasing as the methylene spacers are introduced; however, the magnitude of the values suggests that the *Re*-face would be disfavoured by sterics.

The magnitude for the systems with geminal methyl groups (red) indicates that the *Re*-face should be favoured by sterics across all ring sizes, in agreement with the stabilities of our fully optimised TS. Although these values lead to the correct sense of stereoinduction, their increase with ring expansion is contrary to the expected trend. From this study, we see that the origin of asymmetric induction can not be explained simply using these calculations. In order to better understand these systems, we must also investigate the electronic factors governing selectivity, and develop our methods for gauging steric interactions.

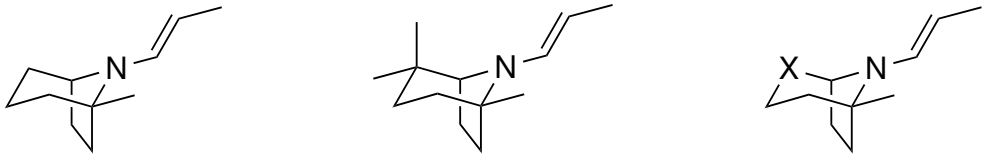

(a) Original tropane system

(b) Tropane with geminal methyl groups β to N

(c) Tropane system with generic heteroatom functionality

Figure 4.13: Illustrations of the two tropane systems investigated in the previous section and the new generic tropane system.

In a study aimed at uncovering the origin of increased stereoselective bias following introduction of geminal methyl groups, we investigated the effect of introducing heteroatom functionality to the six membered ring of the tropane system, β to N (in the same location geminal methyl groups were previously introduced; see **Figure 4.13**). The majority of the functionality we introduced to this system was hypothetical from the point of view of a synthetic chemist; our aim was to compute the stabilities of the same TSs as before, but in the presence of drastically different sterics and electronics, and to ultimately judge their effect on selectivity. Fully optimised alkylation TSs and the predicted ees are shown in **Table 4.4**.

Using chemical intuition, we can make a number of interesting observations from the data in **Table 4.4**. We see that axial inclusion of sterically bulky groups such as SiH_3, Br and Cl, results in a marked increase in the *Si*-face TS free energies, and an overall increase in the calculated ee; this is consistent with our steric based explanation for the increase in ee upon introduction of geminal methyl groups to

the basic tropane system, **4.13a**. Interestingly, we observed a reduction in *Re*-face selectivity in the geminal F system. Closer inspection of the *Si*-face TSs revealed what appeared to be attractive rather than steric interactions between C-H σ^* of EtI and F lone pair orbitals; this stabilising effect was particularly pronounced in conformers 'a' and 'b' for *Si*-face addition, where the interaction is between the more polarised sp^3 hybridised C-H bonds, and this is reflected in the relative stabilities of these TSs. Similar interactions were seen in the analogous conformers in the geminal CF_3 system; no TS could be located for *Si*-face conformer 'c' addition.

In the systems where a heteroatom was introduced to the six-membered ring, we saw a number of different effects on the calculated ee. Introduction of more electronegative atoms such as N and O resulted in a dramatic shift from *Re*- to *Si*-face selectivity (**03** and **06**). Upon closer inspection of the structures, the origin of this effect appears to be a H-bonding type interaction between the C-H groups on the ethyl fragment and the heteroatom lone pair when alkylation is taking place on the *Si*-face. When less polar, more polarisable, S is introduced in system **04**, the same attractive interaction does not take place and selectivity switches back to the *Re*-face. SiH_2 acts in a similar manner to CH_2 in the original tropane system. However, Si-H bonds are longer than C-H bonds, and act as a greater steric deterrent to *Si*-face attack, resulting in slightly higher *Re*-face selectivity for this system (**05**).

Table 4.4: ΔG values for TSs of all three conformers on both *Re*- and *Si*-faces for tropane-type enamine systems in kJ/mol; values are relative to the separated starting materials. Ees are for *Re*-face alkylation, and were calculated using a Boltzmann distribution at 65 °C (negative ees indicate an overall *Si*-face preference). All calculations were performed at the B3LYP/6-31G(d) level of theory (LANL2DZ for I) in CPCM acetonitrile solvation.

	Face	Conformer ΔG			System	ee (%)		Face	Conformer ΔG			System	ee (%)
		a	b	c					a	b	c		
01	*Si*	108.9	109.1	110.4	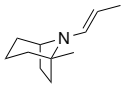	78	**02**	*Si*	110.5	108.8	112.2	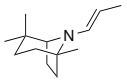	95
	Re	107.4	106.4	101.3				*Re*	100.6	100.4	99.2		
03	*Si*	110.2	109.9	112.9	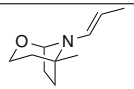	-23	**04**	*Si*	117.4	114.7	122.3	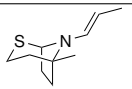	51
	Re	117.4	116.4	109.3				*Re*	116.6	115.3	111.5		
05	*Si*	117.0	108.1	115.3	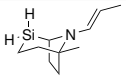	84	**06**	*Si*	102.7	102.3	106.3	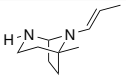	-33
	Re	104.2	104.4	103.6				*Re*	109.9	108.8	102.6		
07	*Si*	114.5	114.7	-	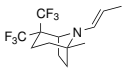	69	**08**	*Si*	108.7	106.5	111.5	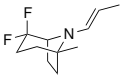	19
	Re	111.5	110.3	111.4				*Re*	110.8	109.7	104.8		
09	*Si*	116.7	116.5	118.9	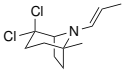	83	**10**	*Si*	119.1	116.1	121.2	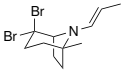	83
	Re	111.8	110.2	109.8				*Re*	112.4	111.9	110.3		
11	*Si*	120.3	119.6	123.4	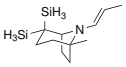	99	**12**	*Si*	106.3	106.4	105.5	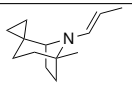	52
	Re	108.7	107.7	105.2				*Re*	102.7	102.6	103.5		

Perhaps the most interesting individual result from this data set is that for the cyclopropyl substituted system (**12**). We might expect this aliphatic functional group to act in a similar manner to geminal methyl groups, increasing steric hinderance of the *Si*-face alkylation TSs and thus raising our calculated ee; however, the opposite is observed, with a lower predicted ee than that for original tropane system (**01**). The origin of this effect must lie in the electronics of the system; the cyclopropyl functional group can act as a strong electron inducing group through a σ bond framework,[156] however, it is not immediately obvious how this might influence selectivity in this system.

This data set's greatest value is in its range of calculated ees, resulting from a variety of different systems. In order to further analyse this information, we needed to better quantify the steric and electronic properties of each of the variable functional groups. One method we used to evaluate the electronic influence of these groups on the enamine/iminium was to set up a series of isodesmic reactions, assessing the stability added to a system when positioned β to a carbonyl functional group in a six membered ring system, compared to the analogous alkyl system (**Figure 4.14**). We chose to use six membered rings for this study to match the ring size on to which functionality was added in the tropane-type systems previously; a carbonyl group was chosen because of its orbital similarity and isoelectronic properties with the iminium functionality in the TSs for alkylation.

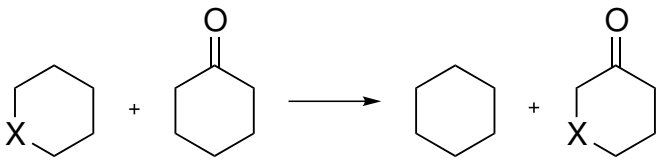

Figure 4.14: Illustration of generic isodesmic reaction scheme used in the evaluation of electronic stability of various functional groups positioned β to the carbonyl.

We calculated our stabilisation energy (E_{stab}) values as the summation of reactant energies in **Figure 4.14**, subtracted from the summation of product energies; the more negative the E_{stab}, the more stability results from having the 'X' functionality β to the carbonyl; all optimisations were performed at the B3LYP/6-311G(d,p) level of theory. A summary of our results is shown in **Table 4.5**; a plot of this data set revealed little discernible correlation between E_{stab} and ee, with an R^2

value of 0.28. This suggests that the ability of the various functional groups to stabilise neighbouring π-systems does not play a significantly dominant role in the determination of ee.

Table 4.5: Stabilisation energies (kJ/mol) calculated from the isodesmic reaction shown in **Figure 4.14**, with various 'X' functionality and the respective ees (%) for alkylation on the *Re*-face in the tropane-type systems (**Figure 4.13**).

X	$C(SiH_3)_2$	CMe_2	SiH_2	CCl_2	CBr_2	CH_2
$\mathbf{E_{stab}}$	0.6	-3.2	-11.1	11.5	11.2	0.0
ee	99	95	84	83	83	78
X	$C(CF_3)_2$	C_3H_4	S	CF_2	O	NH
$\mathbf{E_{stab}}$	4.5	0.7	7.9	9.1	13.7	9.0
ee	69	52	51	19	-23	-33

Table 4.6: Fractional volumes of heteroatom containing tropane-type enamine systems (compared to X=CH_2) with various 'X' functionality and the respective ees (%) for alkylation on the *Re*-face in the tropane-type systems (**Figure 4.13**).

X	$C(SiH_3)_2$	CMe_2	SiH_2	CCl_2	CBr_2	CH_2
Volume	1.33	1.16	1.17	1.20	1.34	1.00
ee	99	95	84	83	83	78
X	$C(CF_3)_2$	C_3H_4	S	CF_2	O	NH
Volume	1.24	1.04	1.01	0.94	0.95	0.93
ee	69	52	51	19	-23	-33

In another study, we aimed to quantify the steric size of the functional groups used in our investigation of heteroatom effects; we calculated the volumes of the tropane-type enamine systems using the Gaussian keyword "volume", which requests that molecular volume be calculated, defined as the volume inside a contour of 0.001 electrons/Bohr^3 density; additionally, we specified the keyword "tight", which requests that an increased density of points is used for more accurate integration in the calculation of these values. In a separate benchmarking study we constructed hypothetical systems consisting of the dimethylated forms of the various heteroatoms and functional groups; we chose methyl groups in the interest of

keeping the system size small whilst maintaining a similar chemical environment to that in the tropane-type systems. We observed that using the larger basis sets, 6-311G(d) and 6-311G(d,p), resulted in little deviation of the computed volumes of the systems, with ∼6 % total MUE in both cases when compared to calculations performed with the smaller 6-31G(d) basis set. In our tropane-type enamine investigation, we used the B3LYP/6-31G(d) level of theory; since the calculated volumes of these systems are somewhat difficult to interpret physically, we assessed these values as a fraction of the basic system, **4.13a** (**Table 4.6**).

Analysis of the results in **Table 4.6** reveals a reasonable correlation between the relative volume of the 'X' functionality and the magnitude of the computed ee, suggesting that greater steric volume on one of the rings destabilises addition on that face, thus increasing the selectivity of the alkylation; **Figure 4.15** illustrates the relationship between the two variables, the R^2 value for which is 0.72. The observed correlation is in keeping with our initial hypothesis: that steric bulk is a significant contributing factor towards determining the extent of selectivity in these reactions.

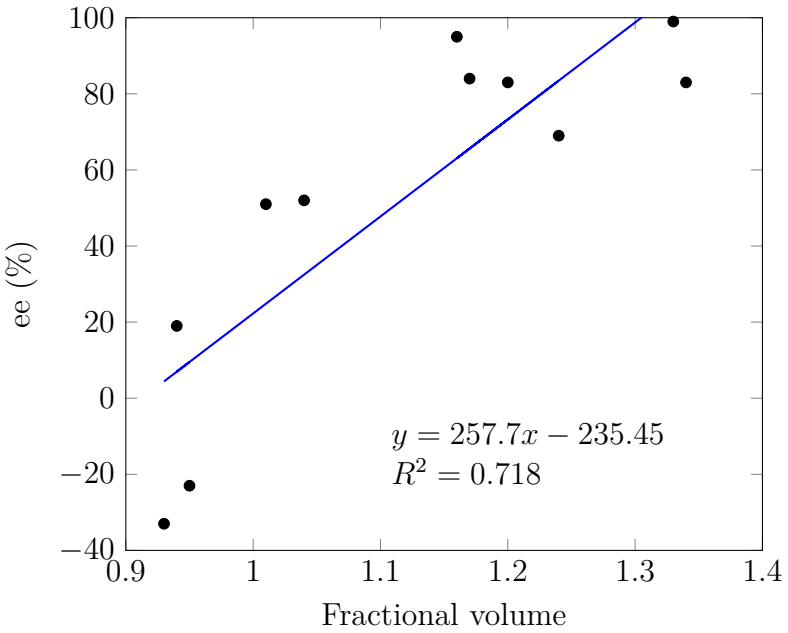

Figure 4.15: Plot of the relationship between calculated ee for alkylation (at 65 °C) and the fractional volumes of tropane-type enamines.

From our exploration of the factors affecting selectivity in the alkylation of tropane-type enamine systems, we can conclude that steric effects are largely responsible for the differing selectivity observed with various systems. Our calculated TSEEs correlated with the correct sense of stereoinduction geminally methylated systems but they did not fit the trend with increasing ring size. Conversely, with the unmethylated system, the wrong sense of stereoinduction was predicted by the TSEEs but the trend with increasing ring size was reflected. The volumetric study with the heteroatom containing systems provided the greatest support for the hypothesis that selectivity is governed by sterics. Although it is likely that electronic effects also play a role in determining selectivity, we must assume that their effects are more subtle; our E_{stab} values calculated from our isodesmic study did not show a good correlation with ee.

4.7 Further development of model system

We began our investigation into tropane-type systems as chiral auxiliaries for enantioselective enamine alkylation in late 2012; since then, the availability of computational resources has increased, and the techniques used to analyse chemical systems have also improved. In the interest of updating this study for future publication alongside more recent experimental results from the Hodgson Group (see section 4.8), we reran some of the experimentally reproducible systems using the more modern functionals, wB97XD[110] and M062X;[24] we reran our previous B3LYP calculations with the incorporation of Grimme's dispersion correction, B3LYP-D3[19–21] (**Table 4.7**).

Interestingly, the computed ees with the dispersion corrected functionals were all higher than those previously calculated using B3LYP. Part of the origin of this increased prediction of selectivity appears to be the increased stability of the conformer 'c' for *Re*-face addition, which we previously showed benefitted from a H-bonding type interaction between the ethyl group and the N of the enamine in the TS (see section 4.7); it is likely that inclusion of dispersion correction in these calculations offers greater computed stability for these sorts of non-bonded interactions, resulting in their increased calculated relative stability. We opted

to use the B3LYP-D3 method for future calculations as it yielded similar results to other functionals, and it has been shown to be effective in previous selectivity determining studies.[157,158]

Table 4.7: Comparison of ΔG values for alkylation TS of the basic tropane enamine system, **4.13a**, across a range of dispersion corrected functionals, with the predicted ee for the reaction; stabilities are relative to the separated tropane enamine and ethyl iodide; calculations were performed with implicit CPCM modelling of acetonitrile solvation and a 6-31G(d) basis set (LANL2DZ for I).

Face	Conformer	B3LYP	B3LYP-D3	wB97XD	M062X
	a	108.0	72.2	99.6	107.3
Si	b	107.6	71.8	98.2	107.6
	c	108.6	77.6	99.2	109.5
	a	106.2	74.4	95.5	106.0
Re	b	105.0	70.5	93.9	103.2
	c	99.4	63.1	85.9	98.0
ee		78%	84%	95%	87%

Following recent computational investigation into the effect of pyramidalisation and rotation about cyclic N containing systems,[159] we decided to investigate the relative stabilities of the four possible conformations for the tropane enamine system (two enamine geometries with pyramidalisation in two directions). Our previous assumption was that the s-*cis* conformation about the enamine would be disfavoured due to steric clashing with the bridgehead methyl group on the tropane (**Figure 4.5**); we previously modelled both pyramidal conformations of the s-*trans* enamine and calculated our relative TS free energies based on the more stable of the two. Surprisingly, we discovered that the stability of one conformer with the s-*cis* geometry was only 10.1 kJ/mol higher in energy than the most stable s-*trans* conformer, and more stable than the less stable s-*trans* conformer. We ran dihedral scans on the system, and were able to locate two TSs for rotation of the enamine (**Figure 4.16**). In theory, there could be four rotational TSs for this system, however, the two TSs in which the lone pair on N is *cis* to the C-H of the enamine would suffer from significantly greater steric strain due to the close

proximity of the C=C of the enamine and the adjacent heterocycle when in that orientation. The free energies of the two rotational TSs in **Figure 4.16** are almost equivalent, and both are easily surmountable under the reaction conditions, allowing for facile conformational switching between the s-*trans* and s-*cis* forms of the enamine. Therefore, we hypothesised that the alkylation TSs of the s-*cis* conformers might be thermodynamically competitive with the s-*trans* alkylation TS - these are the only TSs we have calculated and discussed up to this point.

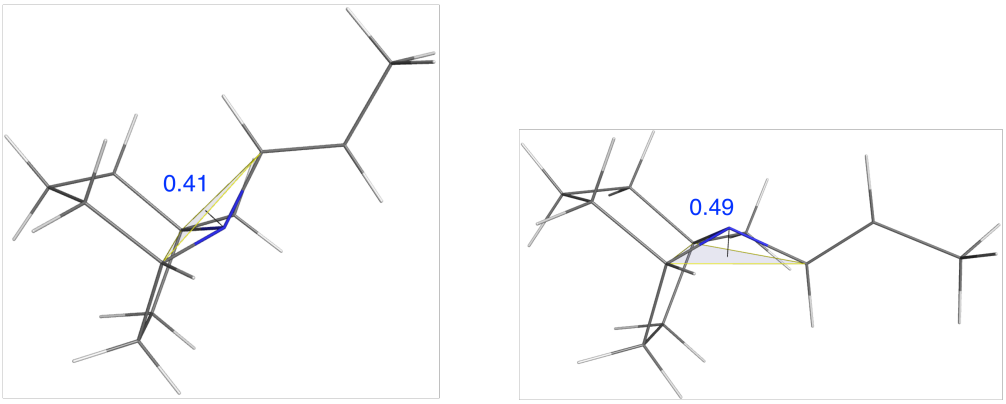

(a) $\Delta G^{\ddagger} = 23.6$ **(b)** $\Delta G^{\ddagger} = 24.6$

Figure 4.16: TSs for tropane enamine **4.13a** rotation about the enamine with their computed $\Delta G^{\ddagger}$ in kJ/mol at 65°C; structures were optimised with B3LYP-D3 and a 6-31G(d) basis set with CPCM solvation in acetonitrile; pyramidalisation distances (blue) are in Å.

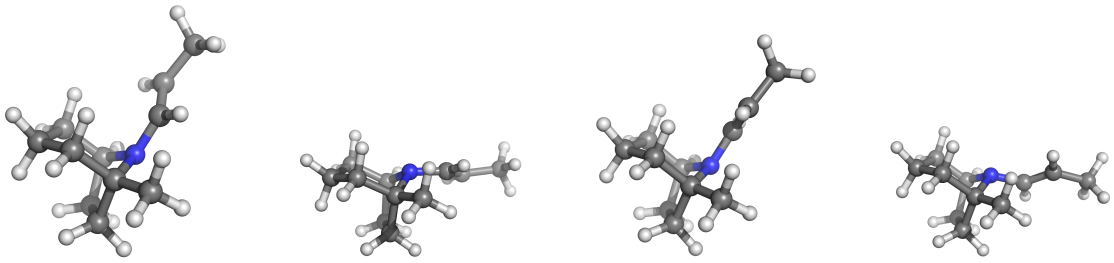

s-*trans*; 0.0 s-*trans*; +10.9 s-*cis*; +10.1 s-*cis*; +20.4

Figure 4.17: Four tropane enamine conformers with their ΔG_{rel} in kJ/mol; structures were optimised with B3LYP-D3 and a 6-31G(d) basis set with CPCM solvation in acetonitrile.

In our previous study of tropane enamine alkylation, we computed all six s-*trans* enamine alkylation TSs to obtain our predicted ee (three conformers for both *Si*-

Table 4.8: ΔG values for TSs of all six conformers on both *Re*- and *Si*-faces for each tropane-type system investigated in kJ/mol; values are relative to the separated starting materials. Calculations were performed at the B3LYP-D3/6-31G(d) level of theory (LANL2DZ for I) in CPCM acetonitrile solvation.

Face	Geometry	Conformer ΔG		
		a	b	c
Si	s-*trans*	72.2	71.8	77.6
	s-*cis*	84.9	90.4	76.9
Re	s-*trans*	74.4	70.5	63.1
	s-*cis*	83.1	88.4	85.3

and *Re*-face addition); in this followup study, we needed to calculate alkylation TSs for the analogous six TSs for the s-*cis* enamine geometry. The results are summarised in **Table 4.8**; the majority of s-*cis* conformers are high enough in energy relative to the s-*trans* conformers that they contribute little to the Boltzmann calculated ee. The exception is the *Si*-face s-*cis* conformer 'c' TS, which is comparable in stability to some s-*trans* conformers; upon closer inspection of this TS, it becomes clear that there is a similar H-bonding type interaction between the ethyl group and the N, analogous to that seen in the *Re*-face s-*trans* conformer 'c' TS which is discussed earlier (see section 4.7). Inclusion of this TS in the calculation of the Boltzmann weighted ee has little effect, with the predicted ee staying the same as before at 84%. Calculating all twelve possible TSs for each system poses a significantly larger computational hurdle and, since the influence of the additional six s-*cis* TSs is so minute, we must consider whether this approach is necessary in subsequent investigations.

4.8 Experimental results

Ongoing work in the Hodgson Group has generated new experimental results for us to compare our previously computed predictions with. Both tropane **4.13a** and the tropane enamine with geminal methyl groups, **4.13b**, have been synthesised

and drs from alkylation with ethyl iodide have been determined (**Figure 4.2**). Interestingly, in the alkylation of **4.13a**, it was observed that a single diastereomer of a quaternary enamonium species was generated in the reaction mixture; this meant that either a [1,3] alkyl shift was happening, or that ethyl iodide was alkylating directly to N. No N-alkylation product was observed in the tropane enamine with geminal methyl groups, **4.13b**.

Although the antarafacial [1,3] alkyl shift is thermally allowed by the Woodward-Hoffman rules, we were unable to locate a TS for this process; however, even if such a TS were to exist, it is unlikely to be energetically accessible under the reaction conditions.[160] This assumption was backed up by the experimental observation that there was no interconversion of the N-alkylated product to the C-alkylated species when the reaction mixture was heated for two days. In our previous C-alkylation study of the tropane enamine motif, we needed to consider three conformers for addition to each face of the sp^2 hybridised systems; fortunately, in the case of N-alkylation, we only needed to consider a single conformer for attack on each face of the tertiary N, as steric congestion dictates that the ethyl group point away from the methylated bridgehead, and also away from the heterocycle. We were able to locate two TSs for N-alkylation of the tropane enamine (**Figure 4.18**), leading to separate diastereomeric products. **TS 4.18a** is stable enough to be competitive with C-alkylation upon the *Si*-face (see **Table 4.8**) but **TS 4.18b** is high enough in energy that we can assume it does not contribute towards the products of this reaction. This computational observation is in keeping with experimental results, where only a single diastereomer is observed. The reason for the discrepancy in the stabilities of these two TSs is once again likely to be sterics, with the six membered ring of the tropane posing a greater hinderance to N-alkylation. Since the N-alkylation is irreversible, it will not impact our predictions made towards the selectivity of C-alkylation.

We were also able to locate a single TS for the formation of the N-alkylated product of tropane system **4.13b** in which N-alkylation occurs on the same face as the five membered ring (analogous to **TS 4.18a**), the relative free energy of which was computed to be > 25 kJ/mol when compared to the most stable C-alkylation TS of the same system. Of the two possible TSs for N-alkylation of **4.13b**, the one

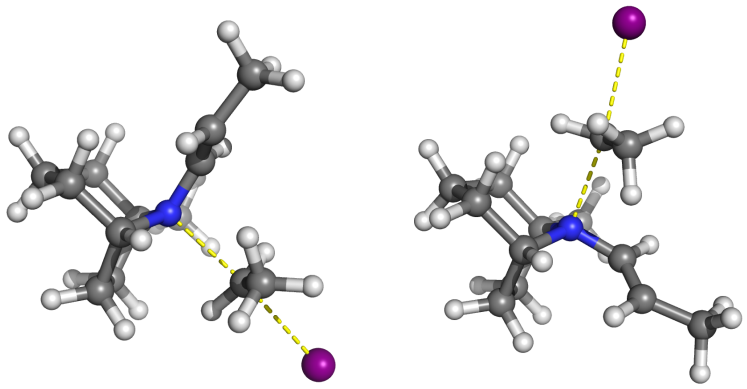

(a) $\Delta G^{\ddagger} = 71.9$ **(b)** $\Delta G^{\ddagger} = 85.2$

Figure 4.18: Two TSs for N-alkylation of the basic tropane system, **4.13a**.

we were able to locate is likely to be the more stable of the two, by analogy to the N-alkylation TSs found for **4.13a**; we can therefore assert that the observed experimental absence of N-alkylated product in system **4.13b** is due to the TS being uncompetitive relative to those for C-alkylation.

The latest experimentally determined drs for alkylation of **4.13a** and **4.13b** (**Figure 4.2**) match the sense of selectivity predicted through our calculations. For the basic tropane system, **4.13a**, the dr was 64:36, leading to an ee of 28%. Although this value is significantly lower than our computed ee of 84%, our predicted major enantiomer is the same. In the geminally methylated tropane enamine, **4.13b**, the dr was 88:12, giving an ee of 76%. Our computed ee of 96% (**Table 4.9**) predicts the same sense of selectivity shown in experiment, but is once again higher than the experimental value. However, converting these selectivity ratios to free energy differences reveals that these apparently large values equate to relatively small stability differences between the TSs; 28% and 84% for system **4.13a** equate to free energy differences of 1.6 kJ/mol and 6.8 kJ/mol at 65°C respectively, with a difference of 5.2 kJ/mol, and 76%, and 76% and 96% for system **4.13b** equate to free energy differences of 5.6 kJ/mol and 10.9 kJ/mol at 65°C respectively, with a difference of 5.3 kJ/mol; both these differences are well within the error range of other dispersion corrected functionals.[101]

Table 4.9: ΔG values for TSs of all six conformers on both *Re*- and *Si*-faces for each tropane-type system investigated in kJ/mol; values are relative to the separated starting materials. Calculations were performed at the B3LYP-D3/6-31G(d) level of theory (LANL2DZ for I) in CPCM acetonitrile solvation.

Face	Geometry	Conformer ΔG		
		a	b	c
Si	s-*trans*	71.0*	70.2*	77.5
	s-*cis*	80.1	78.9	68.4
Re	s-*trans*	60.1	62.3	56.1
	s-*cis*	78.7	79.0	79.3

* Structures were optimised with non-default conversion criteria, "maxstep=10".

4.9 Conclusions

Through the course of our investigation we were able to develop, improve, and implement a new methodology for explaining the stereoselective alkylation of tropane-type enamine systems. Starting with the simplistic four TS model, we used chemical intuition to expand the model to incorporate six, and eventually twelve TSs; by doing so, we were able to more accurately describe the alkylation reaction we were investigating. Through the use of various techniques, we probed the influence of varying the sterics and electronics of the system, on the predicted selectivity of the alkylation reaction; we successfully showed the relationship between the relative steric volume of the tropane enamine auxiliary and the level of enantioinduction imparted upon alkylation. Additionally, we were able to account for the diastereoselective formation of the N-alkylated side product in the basic tropane system, **4.13a**, through TS analysis, along with the absence of any such side product in the geminally methylated system, **4.13b**.

Our computationally derived selectivity predictions made for systems **4.13a** and **4.13b** were subsequently given credence by experimental results; the agreement between computational and experimental results was within ∼5 kJ/mol, with our computational predictions implicating higher selectivity in both cases.

5 Thermochemical kinetics of azetidine conformational behaviour

5.1 Background

The azetidine functional motif is found in many drug leads and bioactive natural products, and it is a common pharmaceutical tool;[161] azetidines have also shown to be useful as ligands in metal-catalysed transformations and as chiral auxiliaries.[162] There exist numerous ways to assemble α-branched amines, including: reductive amination, alkene hydroamination, C-H insertion by a nitrogen source, carbanion addition to imines, and the reaction of an α-C-H bond of a suitably N-protected/activated amine.[163] The latter method has proven to be a successful means of substituting α to N in an abundance of compounds,[164] but has only recently proven useful in the functionalization of azetidine containing compounds. Recently, Prof. Hodgson and coworkers have investigated the protecting group dependence of α-functionalization of azetidine systems. **Figure 5.1** shows the general outline of this reaction with MeI acting as the electrophile functionalizing the azetidine following α-lithiation-electrophile trapping, however, this reaction has shown much scope with incorporation of a number of different electrophiles.[165]

The regioselective second alkylation to form products **5.1.03** and **5.1.06** in the reactions shown in **Figure 5.1** was unexpected and the origins of regiodivergence were not immediately obvious, particularly in the thiopivaloyl system where the second lithiation is directed at the already substituted and unactivated 2-position (**5.1.02** $\rightarrow$ **5.1.03**). However, through collaboration with Prof. Claridge and Prof. Hodgson, we were able to provide insight into this unexpected bias through our in depth computational investigation of the structures preceding the dimethylated products, and the TSs by which they interconvert. Additionally, we computed and accounted for the differing stabilities of other protected/functionalised azetidine systems for which rotational barriers had been obtained experimentally. Ground state conformational studies could not be carried out on **5.2.01** to **5.2.04** because of the symmetric nature of the unfunctionalised azetidine moiety, however, we cal-

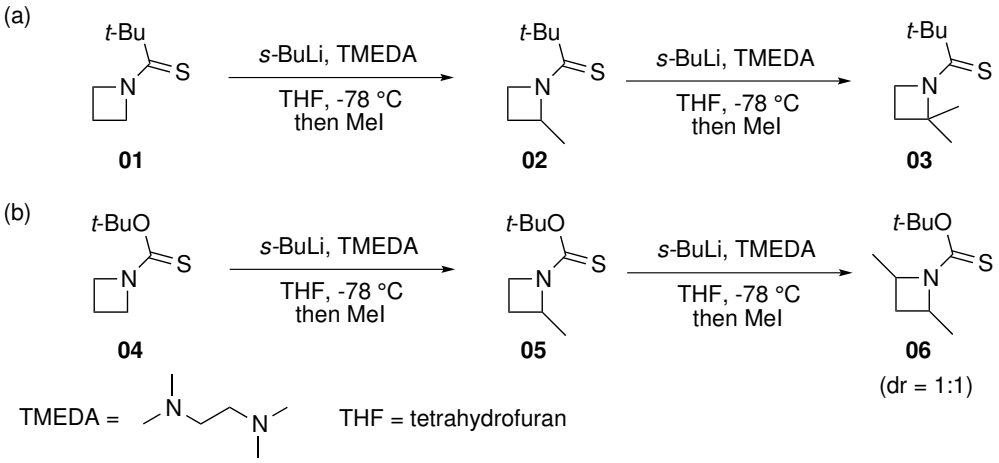

Figure 5.1: α-Lithiation-electrophile trapping with: (a) thiopivaloyl (t-BuC=S = tPiv) and (b) *tert*-butoxythiocarbonyl (t-BuOC=S = Botc) protected azetidines.

culated their TSs for rotation in the interest of benchmarking through comparison with NMR derived barriers for the same compounds.

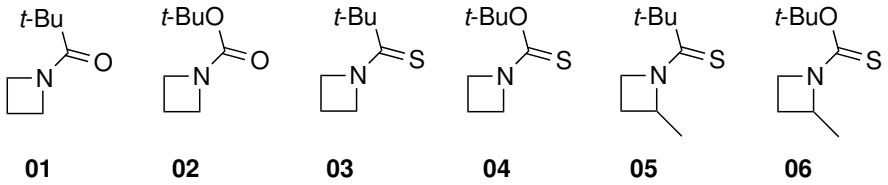

Figure 5.2: Range of protected/functionalised azetidine systems studied in our investigation; rotational barriers were established experimentally for all molecules.

5.2 Computational methods

Our calculations were performed using the Gaussian 09 software,[5] primarily using the M06-2X functional,[24] a hybrid meta-generalised gradient approximation (GGA) density functional. Through the inclusion of a local spin kinetic energy density term in the exchange-correlation functional, this method has proved to be effective at modelling thermochemical and kinetic parameters of organic/organocatalytic transformations, particularly where non-local dispersion interactions play a role.[166,167] The other density functionals used for benchmarking were wB97XD[110] and B3LYP,[19,20,23,168] both of which gave similar results to

M06-2X (**Table 5.1** and **Table 5.2**). We used a valence triple-ζ polarised 6-311++G(d,p) basis set[80,81] for all geometry optimisations. An implicit simulation of the reaction medium, toluene, was used in all optimisations through the use of a conductor-like polarisable continuum solvation model (CPCM),[35,36] with the United Atom Topological Model (UAKS), which defines the solute cavity in terms of radii for functional groups (i.e. terminal methyl groups and intermediate methylene units are classed as single particles);[83,169] while a UFF cavity definition (as is the default in recent versions of the Gaussian) gave comparable results in most cases, it also showed pathological failures for structures with close nonbonded contacts between neighbouring groups. In addition to DFT methods, we also used the composite *ab initio* calculations CBS-QB3 for comparative purposes.[170,171] Gibbs free energies were evaluated at 298 K with vibrational entropy contributions computed using a free-rotor approximation for low frequency modes.[149,172] A smooth damping function centred about a frequency of 100 cm^{-1} was used to switch between the harmonic approximation for vibrations above this value and the free-rotor approximation below.[84,85] All processes studied are unimolecular and therefore free energy changes are independent of the choice of standard state. Vibrational frequencies were computed for all stationary points to confirm them as either minima or TSs, possessing zero or a single imaginary frequency, respectively. TSs were found using dihedral scans and were confirmed with the use of intrinsic reaction coordinate (IRC) calculations,[86,87] which connected each TS to the appropriate species on either side of the rotation barrier on the potential energy surface (PES). Molecular graphics have been produced with Pymol[173] and illustrations showing the planes and distances associated with pyramidalization were generated using our in-house Compiled Graphics Objects (CGO) generating software, written in OpenGL,[174] a graphics programming language (see section 6.2). Analysis of non-covalent interactions was carried out using NCIPLOT,[175,176] NBO[102] and AIMALL[177] software.

5.3 Benchmarking

We optimised both *cis* and *trans* ground state conformers of the *N*-thiopivaloyl and *N*-Botc systems using a range of different functionals and solvent models, all with the large 6-311++G(d,p) basis set. Our DFT results were corroborated using the composite *ab initio* CBS-QB3 method. We ran calculations on the *N*-thiopivaloyl system with the knowledge that the major ground state stereoisomer (determined by low-temperature NOESY studies) adopted the *cis* geometry across the thioamide, and that the observed conformer ratio (determined by ^{1}H NMR in [D_8]toluene at 25 °C) was 12.5:1, which amounts to a free energy difference of 5.7 kJ/mol.

Using the experimental data from the *N*-thiopivaloyl system, we were able to quantitatively assess the effectiveness with which these various techniques describe the relative energies of the two conformers of this system (**Table 5.1**). We saw that the wB97XD and B3LYP functionals consistently under- and overestimated the difference in conformer stabilities respectively. Conversely, the M06-2X functional consistently predicted conformational free energy differences within 0.6 kJ/mol of experimental result. Interestingly, the second highest free energy deviation from experiment was for the CBS-QB3 computed free energy difference, with a value of 8.4 kJ/mol (2.7 kJ/mol higher than experiment); this is perhaps due to the absence of a solvation model in this calculation - we see that for the wB97XD functional, the calculation performed in the gas-phase results in a stability difference that is higher than that for the three calculations incorporating implicit solvation. Encouragingly, all levels of theory showed the *cis* stereoisomer of the *N*-thiopivaloyl system to be the most stable.

Initially, the identity of the major stereoisomer for the *N*-Botc system was unknown as low-temperature NOESY studies of the system had failed to determine the conformational geometry definitively. The ratio between the two conformers was determined by ^{1}H NMR in [D_8]toluene at 25 °C to be 2.2:1, giving a free energy difference between the conformers of 2.0 kJ/mol. Once again, we computed the stability differences between the two conformers with a range of computational techniques and pleasingly, all methods used predicted the same major *trans*

Table 5.1: *N*-thiopivaloyl-2-methylazetidine conformer ΔE and ΔG differences obtained at different levels of theory (with the 6-311++G(d,p) basis set) and solvent models. The *cis*-form is universally favoured.

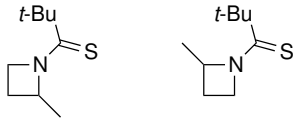

major *cis* minor *trans*

Level of theory	Solvent model	ΔE/kJ/mol	ΔG/kJ/mol
wB97XD	gas-phase	4.7	6.5
	CPCM(UFF)	3.7	5.0
	CPCM(UAKS)	4.0	5.2
	SMD	3.6	3.2
M06-2X	CPCM(UFF)	4.7	6.2
	CPCM(UAKS)	5.0	6.3
	SMD	4.6	5.9
B3LYP	CPCM(UFF)	5.8	8.7
	CPCM(UAKS)	6.0	8.2
	SMD	5.6	7.6
CBS-QB3	-	6.3	8.4
Experiment	-	-	5.7

stereoisomer of the *N*-Botc system. For this system, we saw that the wB97XD and B3LYP functionals consistently over- and underestimated the difference in conformer stabilities respectively, in contrast to the *N*-thiopivaloyl system in which the opposite trend was seen. The M06-2X functional again produced relative stabilities in the middle of the range of those obtained using DFT which were close to the experimentally observed value. Interestingly, the CBS-QB3 conformational free energy difference was this time smaller, as was the unsolvated wB97XD computed result; this suggests that lack of solvation in this system instead lowers the difference in stability between conformers.

Table 5.2: *N-tert*-butoxythiocarbonyl-2-methylazetidine conformational ΔE and ΔG differences obtained at different levels of theory (with the 6-311++G(d,p) basis set) and solvent models. The *trans*-form is universally favoured.

major *trans* minor *cis*

Level of theory	Solvent model	ΔE/kJ/mol	ΔG/kJ/mol
wB97XD	gas-phase	1.3	1.9
	CPCM(UFF)	-	-
	CPCM(UAKS)	2.2	4.1
	SMD	2.2	2.8
M06-2X	CPCM(UFF)	-	-
	CPCM(UAKS)	1.5	1.6
	SMD	1.6	1.3
B3LYP	CPCM(UFF)	-	-
	CPCM(UAKS)	1.2	1.5
	SMD	1.3	1.0
CBS-QB3	-	0.7	1.1
Experiment	-	-	2.0

Following our benchmarking study, we were able to select the most appropriate level of theory with which to proceed in this investigation: the M06-2X functional with CPCM implicit solvation and UAKS for the definitions of solute cavities in terms radii of functional groups. M06-2X was clearly the most effective functional at describing this system, and it out performed wB97XD and B3LYP across all solvent models. The use of the CPCM solvation with a UFF definition of the solute cavities was ruled out because of its incompatibility with the *N-tert*-butoxythiocarbonyl-2-methylazetidine system, with calculations across all functional failing to terminate without error, for reasons we attribute to poor

handling of the methylated azetidine moiety (our calculations on the unmethylated systems ran to completion without error). The use of the M06-2X functional with SMD solvation was a close contender for use in this investigation, but we opted for CPCM with UAKS defined solute cavities because of its lower percentage deviation from experiment across the two systems. Unless stated otherwise, calculations in this investigation were performed using the same level of theory: M06-2X with a 6-311++G(d,p) basis set and CPCM solvation with UAKS defined solute cavities.

5.4 Ground state conformer analysis

5.4.1 *N*-thiopivaloyl-2-methylazetidine

Figure 5.3 shows close non-bonded contacts between the tertiary butyl group and the *cis* oriented α-position of the azetidine, which lead to the rotamer where the CHMe group is oriented *cis* to the thiocarbonyl group being favoured. In the higher energy trans rotamer, increased unfavourable steric interactions are found between the α-methyl and the *t*-Bu groups, with non-bonded H-H distances as close as 2.08 Å(cf, sum of van der Waals' radii = 2.4 Å).[178] Greater repulsion in the trans-conformer is also evident from the more severely distorted exocyclic C-N-C bond angles shown in **Figure 5.3**, and also illustrated graphically by the noncovalent interaction index (NCI) isosurface:[175,176] the region in between the tertiary butyl group and the azetidine is the largest in area, indicative that this interaction is a major conformational discriminant.

This steric argument is also evident from space-filling models shown in **Figure 5.4**. Despite the N atom being part of a 4-membered ring, conjugation between the nitrogen lone pair and the thiocarbonyl π-system results in a high degree of planarity at nitrogen,[179,180] and only a single very slightly pyramidalised stereoisomer of each ground state rotamer exists; the pyramidalization, as judged by the vertical distance of the N atom from the plane defined by the three connected atoms, is 0.08 and 0.03 Å for the favoured and disfavoured rotamers, respectively.

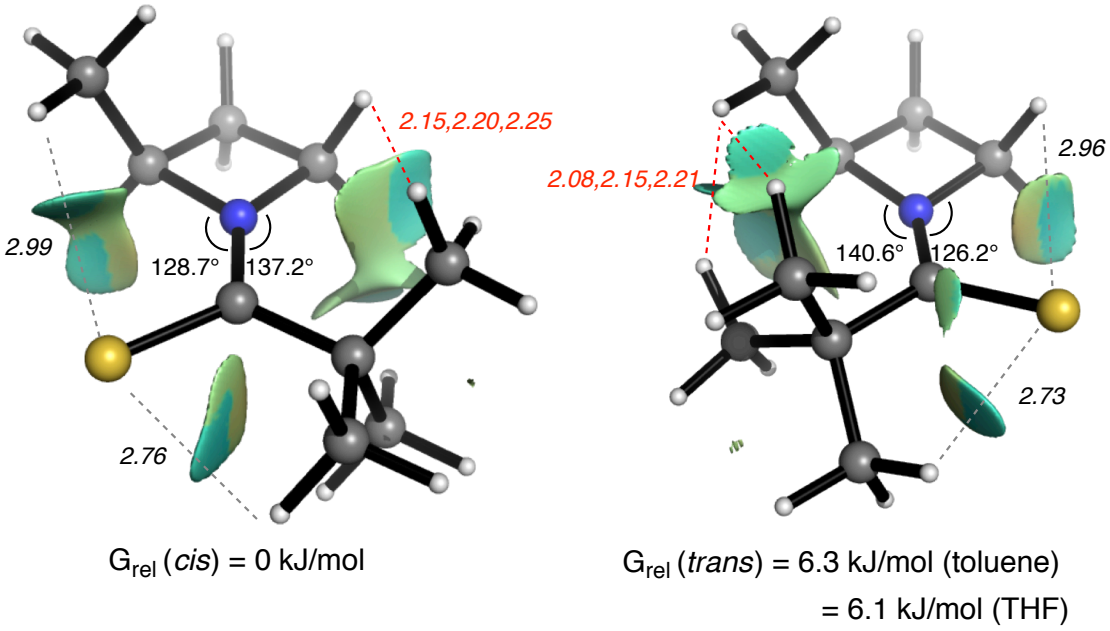

Figure 5.3: Optimised *cis* and *trans* ground state rotamers for *N*-thiopivaloyl-2-methylazetidine; distances shown in Å and steric contacts (< 2.5 Å) highlighted in red. The NCI isosurface indicates the existence of nonbonding interactions.

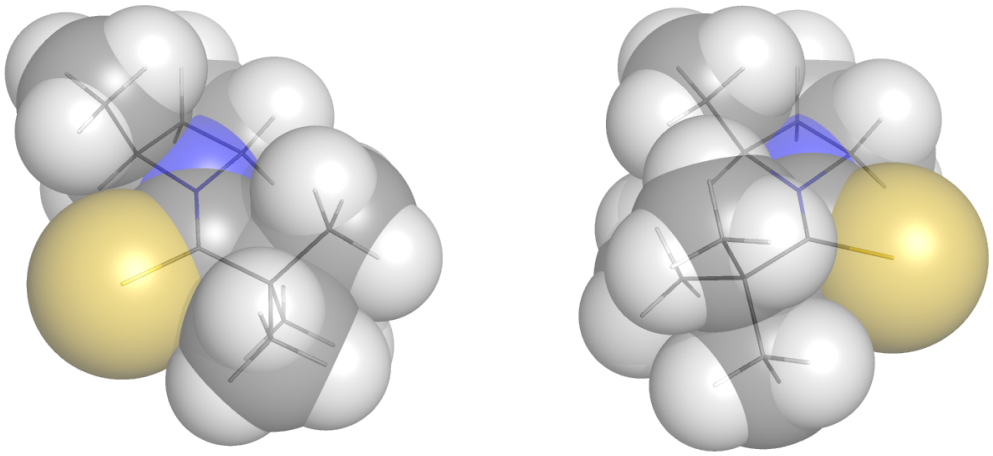

Figure 5.4: Optimised *cis* (left) and *trans* (right) space filling models for *N*-thiopivaloyl-2-methylazetidine conformers.

5.4.2 *N-tert*-butoxythiocarbonyl-2-methylazetidine

Unlike the dominant effect of the *t*-Bu group on the conformation of *N*-thiopivaloyl-2-methylazetidine, the presence of the oxygen atom spacer in *N-tert*-butoxythiocarbonyl-2-methylazetidine now results in the *t*-Bu group being effectively remote from the azetidine, such that steric interactions between these groups do not significantly influence the conformation; corresponding nonbonding interactions are absent from the NCI isosurface (**Figure 5.5**) and space filling models (**Figure 5.6**) show these groups to be sufficiently distant to negate such effects. **Figure 5.5** shows our computed ground state rotamers for this system; both have S-C-O-CMe_3 dihedral angles of 6°, with bias of the *t*-Bu group toward the azetidine face bearing the methyl group. Exocyclic C-N-C angles are similar and distances between S and the *t*-Bu group are almost identical. There is no appreciable difference in either the C-N or C-S bonds of the thioamide, indicating little difference in π-conjugation between the two rotamers. A nonbonded interaction exists between the *t*-Bu group and the thiocarbonyl, although this feature is common to both structures.

Unsurprisingly, only a small conformational preference results: the ΔG ranges from 1.0 to 4.1 kJ/mol depending on the computational method, with the CPCM-M06-2X/6-311++G(d,p) level of theory, which describes the thiopivaloyl system well, (see section 5.3) giving a value of 1.6 kJ/mol (for a full comparison of all methods examined, **Table 5.2**). The calculated rotamer free energy difference is close to 2.0 kJ/mol, determined from the 2.2:1 rotamer ratio seen by ^{1}H NMR in [D_8]toluene at 25 °C. A small energy difference makes bold prediction on the identity of the major rotamer difficult; however, all DFT and *ab initio* methods consistently favour the same rotamer, in which the thiocarbonyl lies *trans* to the azetidine-Me group, opposite to that preferred for the thiopivaloyl protecting group but consistent with the NOEs noted earlier for the thiopivaloyl system. This small conformational preference results from the alleviation of steric interactions between thiocarbonyl and methyl groups: Natural Bonding Orbital (NBO) contributions to the steric exchange energy (Pauli repulsion) between occupied orbitals are more unfavourable by 3.8 kJ/mol when the thiocarbonyl is *cis* to the methyl group. The presence of

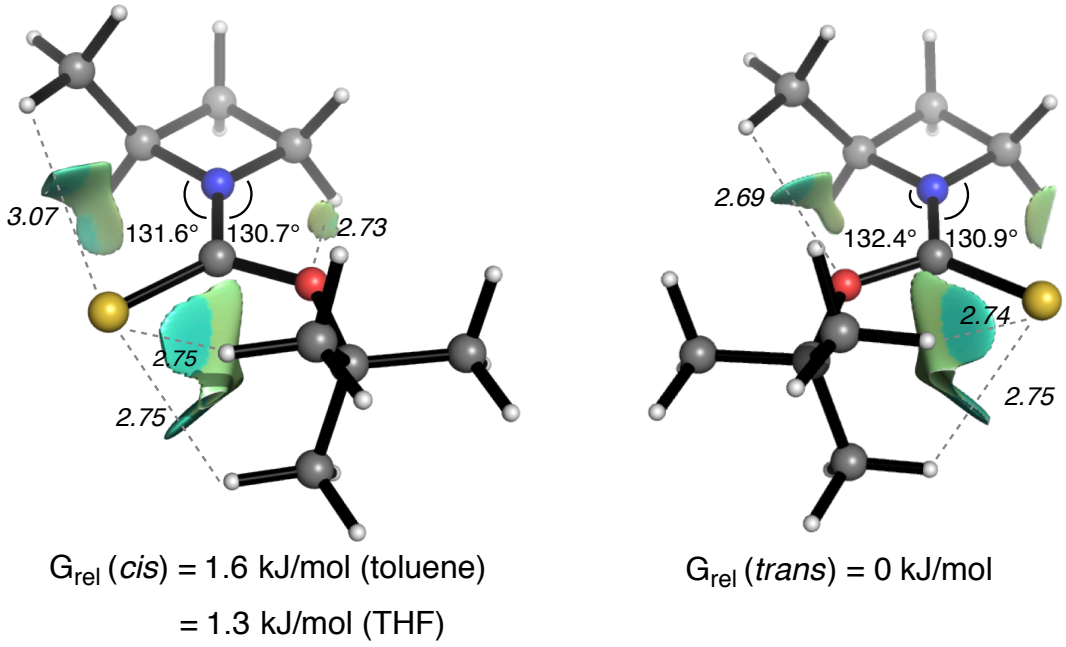

Figure 5.5: Optimised *cis* and *trans* ground state rotamers for *N*-thiopivaloyl-2-methylazetidine; distances shown in Å. The NCI isosurface indicates the existence of nonbonding interactions.

a weak stabilising CH-O interaction (2.69 Å) involving the C-2 methyl group may be detected in the favoured conformation, although its magnitude (0.4 kJ/mol by second-order perturbative estimates in the NBO basis) is insufficient to account for the overall conformational energy difference. As with the thiopivaloyl system above, conjugation between the N lone pair and the thiocarbonyl π-system yields essentially planar structures (pyramidalisation of 0.09 and 0.13 Å for the favoured and disfavoured rotamers, respectively) without isomerism at nitrogen.

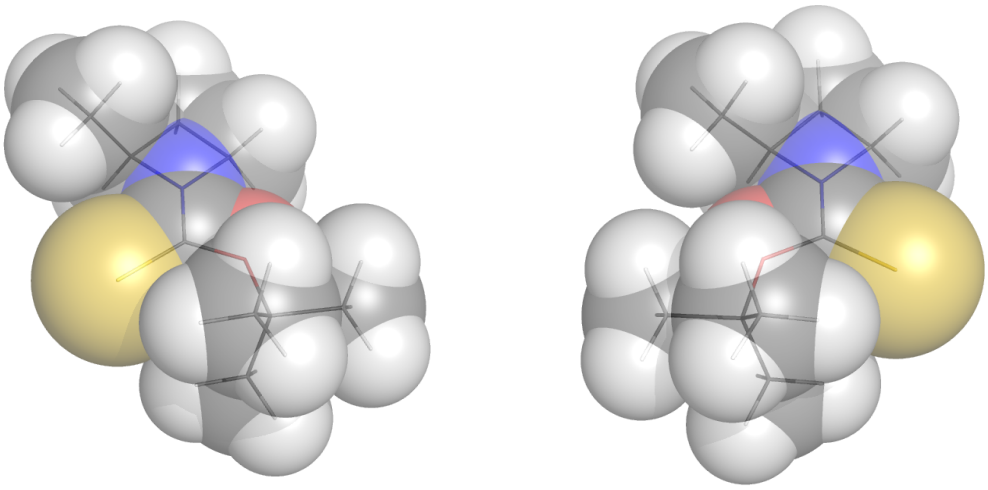

Figure 5.6: Optimised *cis* (left) and *trans* (right) space filling models for *N*-*tert*-butoxythiocarbonyl-2-methylazetidine conformers.

5.5 Potential energy surface

In order to locate the TSs for interconversion between asymmetric 2-methylated azetidine ground states *via* rotation about the N-C bond, we ran dihedral angle scans, both in clockwise and anticlockwise directions, in order to develop an understanding of the potential energy surface (PES) for these systems. As a result of the C_s symmetric nature of the unmethylated systems, their rotational TSs could be located by performing fixed geometry optimisations with dihedral angles across the N(LP)-N-C-O/S set to either -90° or 90° (see key in **Figure 5.7**).

Due to the high computational throughput required for PES calculations, we decided to focus our attention on the *N*-*tert*-butoxythiocarbonyl-2-methylazetidine system; knowledge of this system would then provide insights towards isolation of TSs in the other 2-methylated system of interest (*N*-thiopivaloyl-2-methylazetidine). **Figure 5.7** shows the clockwise and anticlockwise PES dihedral scans of the aforementioned system. The C(Me)-N-C-S dihedral angles of the TSs found (using geometries taken from the PES) are highlighted to show the importance of this method for locating such rotational TSs. Chronologically, we conducted this section of our investigation before the ground state benchmarking of functionals and solvation models; therefore, the wB97XD/6-311++G(d,p) level

of theory was used in the absence of a solvation model for this study. It is worth noting that little geometric variation occurs when switching between functionals and solvation models.

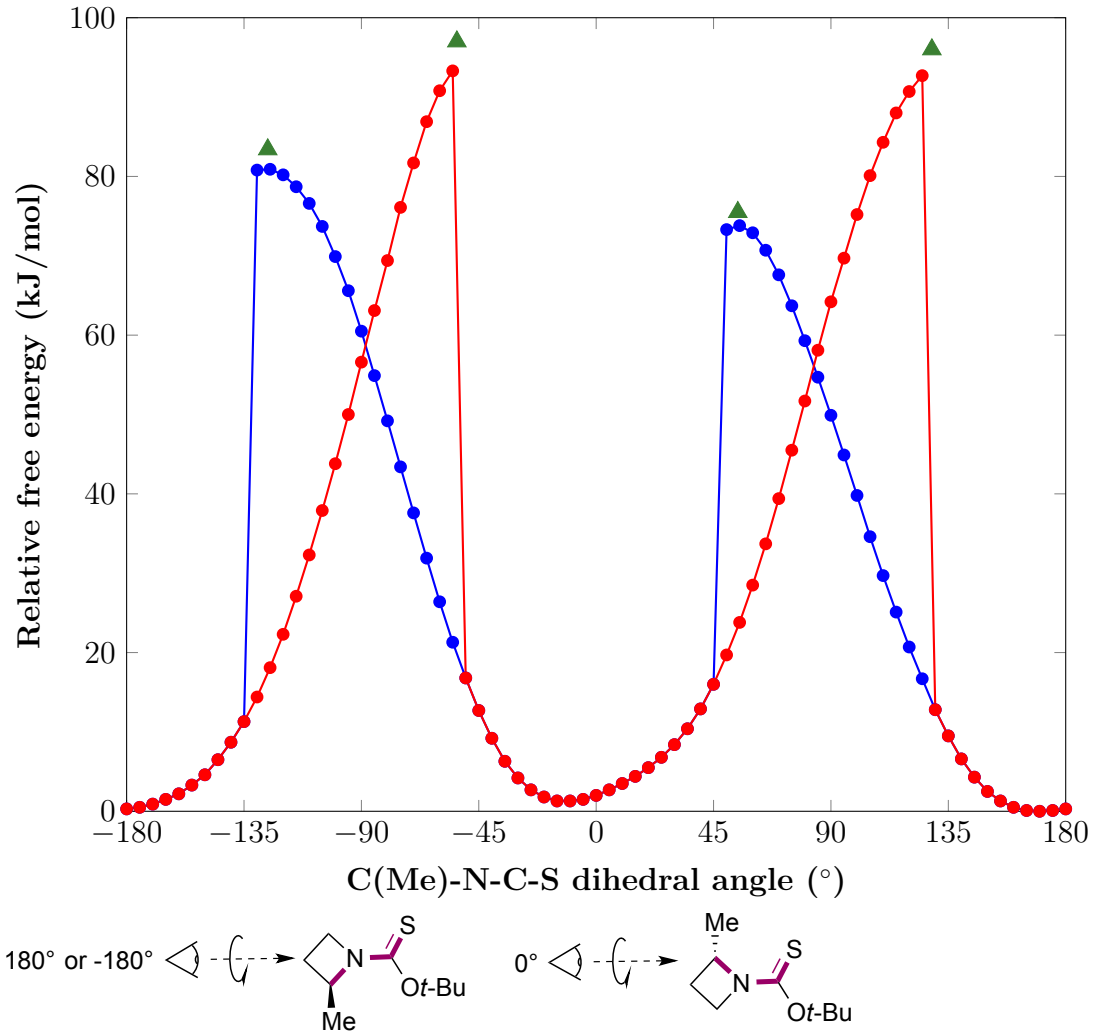

Figure 5.7: Fixed geometry PES scans clockwise (red) and anticlockwise (blue) about the C(Me)-N-C=S bond of *N-tert*-butoxythiocarbonyl-2-methylazetidine at the wB97XD/6-311++G(d,p) level of theory. Green triangles represent the location of fully optimised rotational TSs at the same level of theory.

5.6 Rotational TS analysis

For the exocyclic rotation of an unsubstituted azetidine ring about its C-N bond to its adjacent to a C_s symmetric functional group, there are two possible TSs for rotation. The lone pair on N may be synperiplanar or antiperiplanar across the rotating bond, resulting in two distinct TSs. When the azetidine is functionalised (methylated) α to N, the number of TSs doubles as the conformers in which the added functionality sits either axial or equatorial to the azetidine ring must also be taken into account in each of the two previous conformers. In the interest of completeness, we investigated all possible rotational TSs for each of the systems where possible, to ensure that the lowest energy TS was selected for comparison with experimental results in each case.

5.6.1 *N*-pivaloyl-azetidine

In this simple amide containing system, shown in **Figure 5.8**, we found the two expected TSs for the rotation of the azetidine ring about the C-N bond of the amide. The lowest energy of the two TSs is **TS 5.8a**, shown in **Figure 5.8**, and it has a free energy barrier to rotation of 57.2 kJ/mol at 25 °C, in excellent agreement with the experimentally obtained barrier of 57.6 kJ/mol at the same temperature (within 0.4 kJ/mol). The less stable **TS 5.8b** was significantly higher in energy with a relative free energy of 97.2 kJ/mol. The origin of the large free energy difference between the two TSs can be explained using a combination of steric and electronic effects.

It is expected that the C-O σ^* will be a better acceptor when compared to the C-C σ^* of the carbonyl bond to the tertiary butyl group, and this is reflected in NBO analysis of the TSs which showed a larger amount of conjugation of the lone pair of N into the σ^* of the carbonyl in the lower energy TS in **Figure 5.8a** (6.3 kJ/mol more than in the higher energy TS in **Figure 5.8b**). Interestingly, this measured electronic interaction is not reflected in the geometries of the two amide TS. Instead, the higher energy TS has a lower degree of pyramidalization and the N-C bond length is shorter, both indicative of greater N lone pair delocalisation.

This observation can be explained by steric clashing between the axial C-H bonds on the azetidine ring against the tertiary butyl group, in the higher energy TS - this interaction forces a more planar N, resulting in greater sp^2 character, and a more developed N-C bond in the amide.

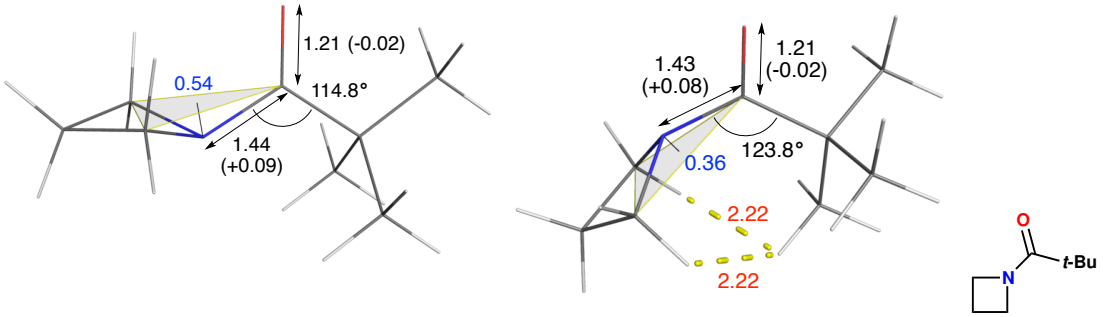

(a) Major TS; $\Delta G^{\ddagger} = 57.2$ kJ/mol **(b)** Minor TS; $\Delta G^{\ddagger} = 97.2$ kJ/mol

Figure 5.8: Optimised rotation TSs for *N*-pivaloyl-azetidine with G computed at 25 °C. Interatomic distances (black), pyramidalisation (blue), and steric interactions (red), are all shown in Å. Parentheses indicate changes relative to the ground state.

5.6.2 *N-tert*-butoxycarbonyl-azetidine

We only found a single TS conformer for the carbamate containing *N-tert*-butoxycarbonyl-azetidine system shown in **Figure 5.9**, out of the two expected TSs for rotation. In the methyl-substituted analogue of this system (methyl group α to N on the azetidine, section **5.6.6**), all four expected TSs were found and the most stable two conformers for pyramidalisation in each direction differed by 3.9 kJ/mol, with the most stable TS having the N lone pair antiperiplanar to the C=O (N lone pair $\rightarrow$ C-O σ^* of the carbonyl). The energy difference between the two lowest energy conformers in the methylated system is small, but this still suggests that there is a missing lower energy conformer for the unmethylated system. Despite this, the agreement between our calculated barrier to rotation of 62.1 kJ/mol is in agreement with the experimentally determined 58.5 kJ/mol at 25 °C (within 3.6 kJ/mol).

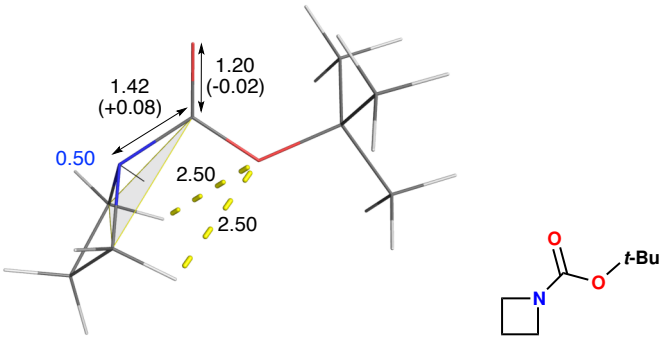

TS; $\Delta G^{\ddagger} = 62.1$ kJ/mol

Figure 5.9: Optimised rotation TS for *N*-*tert*-butoxycarbonyl-azetidine with G computed at 25 °C. Interatomic distances (black), pyramidalisation (blue), and steric interactions (red), are all shown in Å. Parentheses indicate changes relative to the ground state.

5.6.3 *N*-thiopivaloyl-azetidine

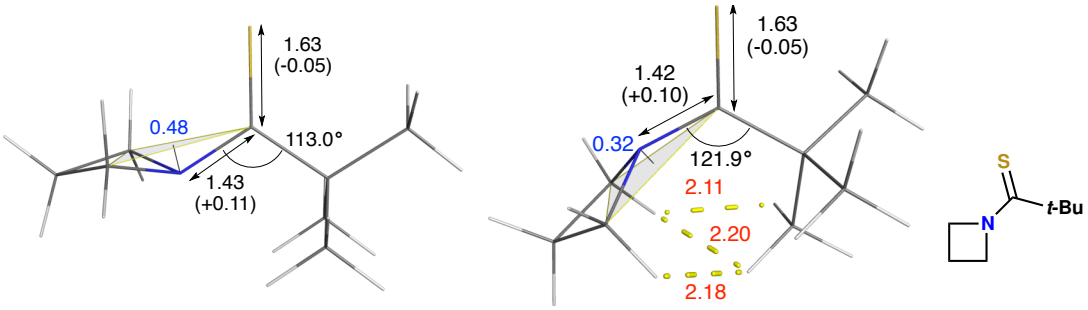

(a) Major TS; $\Delta G^{\ddagger} = 80.2$ kJ/mol **(b)** Minor TS; $\Delta G^{\ddagger} = 122.9$ kJ/mol

Figure 5.10: Optimised rotation TSs for *N*-thiopivaloyl-azetidine with G computed at 25 °C. Interatomic distances (black), pyramidalisation (blue), and steric interactions (red), are all shown in Å. Parentheses indicate changes relative to the ground state.

We were able to find both expected TSs for N-CS rotation for the *N*-thiopivaloyl-azetidine system. In the higher energy **TS 5.10b**, pyramidalisation at N puts the lone pair synperiplanar to the thiocarbonyl resulting in greater steric clashing between C-H bonds on the azetidine and the tertiary butyl group; the degree of pyramidalisation is reduced in order to alleviate this repulsive steric interaction and this is evidenced in the N to plane distance, the C-N bond length and the increased N-C-C bond angle. In the favoured **TS 5.10a** there is no steric interaction between

methylene groups on azetidine and the tertiary butyl group. In addition, having the lone pair on N antiperiplanar to the thiocarbonyl should lead to a stabilising N lone pair → C-S σ^* electronic interaction. The free energy of the most stable rotational barrier of 80.2 kJ/mol was in good agreement with the experimentally determined value of 76.9 kJ/mol at 25 °C (within 3.3 kJ/mol).

5.6.4 *N-tert*-butoxythiocarbonyl-azetidine

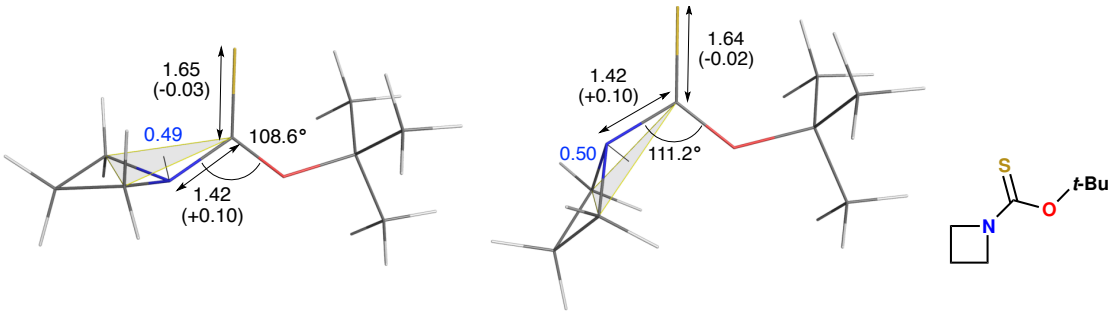

(a) Major TS; $\Delta G^{\ddagger}$ = 81.6 kJ/mol **(b)** Minor TS; $\Delta G^{\ddagger}$ = 86.7 kJ/mol

Figure 5.11: Optimised rotation TSs for *N-tert*-butoxythiocarbonyl-azetidine with G computed at 25 °C. Interatomic distances (black), pyramidalisation (blue), and steric interactions (red), are all shown in Å. Parentheses indicate changes relative to the ground state.

Similar arguments to those used in the carbamate containing *N-tert*-butoxycarbonyl-azetidine system (**Figure 5.9**) can be used to explain the similarity between the TSs for *N-tert*-butoxythiocarbonyl-azetidine shown in **Figure 5.11**. There is no steric penalty to the N lone pair being synperiplanar to the thiocarbonyl (unlike in the thiopivaloyl and pivaloyl systems) and the absence of methyl substitution on the azetidine means there are no issues with 1,3-diaxial clashing. The difference in energies is down to electronics, specifically the σ^* acceptor abilities of the C-S or C-O bonds, with the thiocarbonyl being better able to accept N lone pair electron density. Our lowest calculated barrier for rotation in this system of 81.6 kJ/mol at 25 °C agreed well with the experimentally derived barrier of 75.0 kJ/mol at the same temperature (within 6.6 kJ/mol).

5.6.5 *N*-thiopivaloyl-2-methylazetidine

We were able to locate two of the four predicted TSs for the *N*-thiopivaloyl-2-methylazetidine system, shown in **Figure 5.12**. In both of these TSs, the N lone pair sits antiperiplanar to the thiocarbonyl, thus alleviating the azetidine methylene on tertiary butyl steric penalty seen in both the previously discussed *N*-pivaloyl-azetidine and *N*-thiopivaloyl-azetidine systems (**Figure 5.8** and **Figure 5.10**). This alignment also allows for overlap between the N lone pair and the σ^* of the C-S bond. Neither of the TSs with the N lone pair antiperiplanar to the tertiary butyl group could be found, since these would have extremely unfavourable steric interactions and the degree of hyperconjugation would be reduced. The energetic cost for the analogous optimised TS in the **Figure 5.10** system resulted in a $\Delta\Delta G^{\ddagger}$ of 42.7 kJ/mol. Therefore, we can be confident that the missing TSs do not contribute significantly to the rate of rotation for the *N*-thiopivaloyl-2-methylazetidine system.

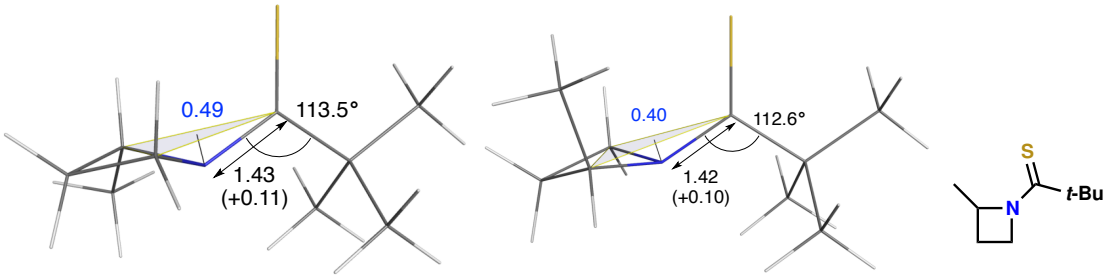

(a) Major TS; $\Delta G^{\ddagger}$ = 71.3 kJ/mol **(b)** Minor TS; $\Delta G^{\ddagger}$ = 92.6 kJ/mol

Figure 5.12: Optimised rotation TSs for *N*-thiopivaloyl-2-methylazetidine with G computed at 25 °C. Interatomic distances (black), pyramidalisation (blue), and steric interactions (red), are all shown in Å. Parentheses indicate changes relative to the ground state.

In the more stable **TS 5.12a**, the 2-methyl adopts an equatorial position on the puckered azetidine ring, while it is axially oriented in the less favourable structure. The equatorial positioning of the 2-methyl significantly reduces 1,3-diaxial steric interactions with the opposite methylene group on the azetidine ring which largely accounts for the $\Delta\Delta G^{\ddagger}$ of 21.3 kJ/mol between the two TSs. Additionally, the

1,3-diaxial steric interaction in **TS 5.12b** forces planarity on the azetidine ring, reducing the extent of pyramidalisation at N - this is quantified by the reduction in N to plane distance between the major and minor TSs shown in **Figure 5.12**. A reduction in planarity results in decreased availability of the N lone pair for a hyperconjugative interaction with the σ^* of the C-S, thus further reducing the stability of **TS 5.12b** relative to **TS 5.12a**. Our computed lowest energy rotation barrier for this system of 71.3 kJ/mol is in excellent agreement with the NMR value of 70.7 kJ/mol (within 0.6 kJ/mol).

5.6.6 *N-tert*-butoxythiocarbonyl-2-methylazetidine

We were able to compute all four possible TSs for C-N rotation in the *N-tert*-butoxythiocarbonyl-2-methylazetidine system and their relative stabilities can be rationalised with a combination of steric and electronic arguments. Conformations in which the methly group is axially oriented with respect to the puckered azetidine ring (**TS 5.13a** and **TS 5.13b**) experience 1,3-diaxial strain, similar to in **TS 5.12a**, raising the energy of these TSs by ∼20 kJ/mol relative to the other two, in which the methyl sits equatorial. The tertiary butyl group exerts little steric effect upon the conformational preference. Therefore, the most stable TS (with an equatorial methyl group) is **TS 5.13c**, in which pyramidalisation at N is such that the lone pair is oriented antiperiplanar to C-O σ^*. As in previous cases, our rotational barrier computed for the most stable TS (75.8 kJ/mol) lies in excellent agreement with the experimental value of 75.0 kJ/mol at 25 °C (within 0.8 kJ/mol), lending further credence to computation. The lower rotational barrier for this system found computationally, relative to the unmethylated case, may be attributable to greater steric strain present in the planar ground state, and its relief in the rotational TS.

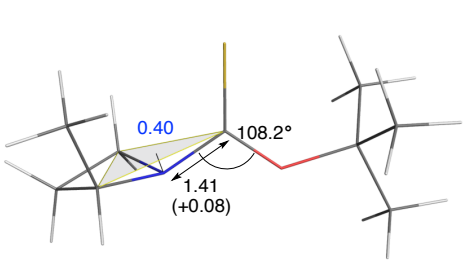

(a) Minor TS; $\Delta G^{\ddagger} = 97.9$ kJ/mol

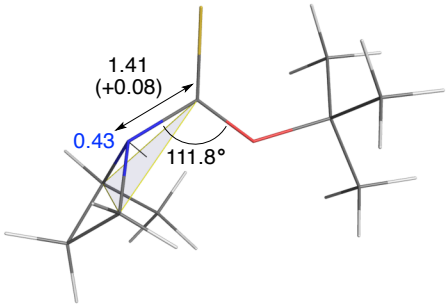

(b) Minor TS; $\Delta G^{\ddagger} = 97.2$ kJ/mol

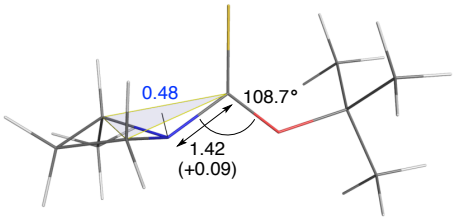

(c) Major TS; $\Delta G^{\ddagger} = 75.8$ kJ/mol

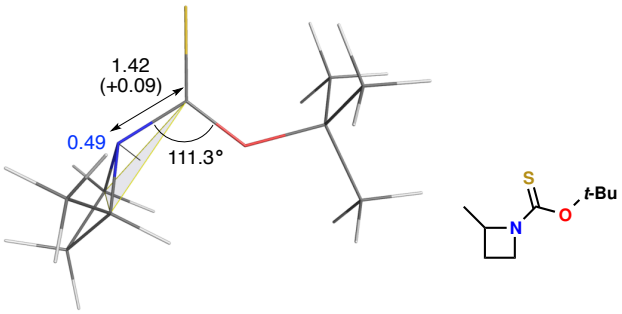

(d) Minor TS; $\Delta G^{\ddagger} = 81.9$ kJ/mol

Figure 5.13: Optimised rotation TSs for *N-tert*-butoxythiocarbonyl-2-methylazetidine with G computed at 25 °C. Interatomic distances (black), pyramidalisation (blue), and steric interactions (red), are all shown in Å. Parentheses indicate changes relative to the ground state.

5.6.7 Summary and analysis of trends in rotational barriers

We were able to show good agreement between NMR and computationally derived rotation barriers for all systems investigated. In general, our computationally derived rotational barriers were marginally higher than those derived from the NMR study. In the case of the asymmetric compounds (**Table 5.3: 05** and **06**) this could in part be due to the fact that we have calculated our TS barriers relative only to the most stable ground state conformer. However, in the NMR investigation, there is naturally a Boltzmann distribution of major and minor ground state conformers to which the derived TS barrier is relative.

Rotations in N-C=O systems proceeded with a lower barrier in the N-C=S systems; this reflects the expected trend as thioamides are known to have higher barriers

to rotation than amides due to the greater polarisability of S, allowing a greater charge transfer from N to S.[181,182] The slight decrease in rotational barriers upon methylation of azetidine in the N-C=S systems (**Table 5.3: 03** to **05**; **04** to **06**) is presumably a result of the greater extent of ground state pyramidalisation in these structures, leaving these systems geometrically closer to their most stable TS for rotation; the unmethylated ground states are effectively planar whilst their methylated counterparts have degrees of pyramidalisation ranging from 0.08 to 0.09 Å in the major conformers (measured as the vertical distance of the N atom from the plane defined by the three connected atoms).

Table 5.3: Comparison of experimental and M06-2X/6-311++G(d,p) computed rotational barriers for various azetidines; NBO Wiberg bond orders and populations are shown.

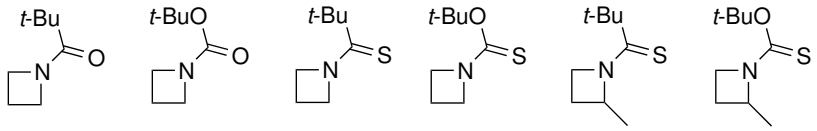

01 **02** **03** **04** **05** **06**

N-substituted azetidine	NMR $\Delta G^{\ddagger}$ kJ/mol[a]	DFT $\Delta G^{\ddagger}$ kJ/mol[b]	DFT-NMR $\Delta\Delta G^{\ddagger}$ kJ/mol	$r_{C\text{-}N}$ (Å)[c]	B.O.[d]	n_N occupancy[e]
01	57.6	57.2	-0.4	1.34	1.18	1.70e
02	58.5	62.1	3.6	1.34	1.15	1.72e
03	76.9	80.2	3.3	1.32	1.28	1.61e
04	75.0	81.6	6.6	1.32	1.24	1.65e
05	70.7	71.3	0.6	1.32	1.29	1.61e
06	75.0	75.8	0.8	1.33	1.23	1.65e

[a] Obtained from VT NMR study, value computed at 25 °C with errors estimated to be +/− 1.5 kJ/mol. [b] DFT optimisations using CPCM-M06-2X/6-311++G(d,p) at 25 °C. [c] Ground state C-N bond distances. [d] Calculated C-N Wiberg bond order. [e] NBO computed occupancy of the N lone pair in the planar ground state.

We see the expected trend in ground state C-N bond lengths across the structures we investigated; systems with N adjacent to carbonyl functionality had longer C-

N bonds relative to those with N adjacent to thiocarbonyl groups. The origin of this lies in the lesser extent to which the N lone pair can delocalise into the C=O π^* orbital, compared to the C=S π^*. This trend is more quantitatively reflected in the Wiberg bond order values for the C-N bonds, which also allow for further distinction to be made between (thio)amide and (thio)carbamate groups. With the two carbonyl containing systems (**Table 5.3: 01** and **02**) we see a reduction in bond order upon replacement of a tertiary butyl group with a tertiary butoxy. This is because the additional O in the system competes with the N as a lone pair donor into the carbonyl C=O π^*. An analogous trend is observed in the thiocarbonyl systems, with introduction of an O spacer also resulting in reduced C-N bond order (**Table 5.3: 03** and **04**; **05** and **06**).

The general trend in NBO computed occupancy of the N lone pair in the ground state values (n_N) pleasingly correlates inversely with the bond order magnitudes. For these systems this is the expected trend as the greater the C-N bond order, the greater the amount of electron density on N which has delocalised into the (thio)carbonyl π^*, therefore resulting in lower N lone pair occupancy.

A scatterplot of activation barriers to rotation against the change in NBO energy of the N lone pair from the ground state to TS (**Figure 5.14**) reveals a strong correlation, with an R^2 value of 0.898. This trend is expected as in the less favourable TSs, we expect less stabilisation of the N lone pair *via* electronic delocalisation into the σ^* of the adjacent antiperiplanar functional group.

5.7 Conclusions

The ability to selectively substitute different C-H bonds in a substrate, through different removable activating groups attached at a common position on the substrate, contributes to flexibility in molecule construction (diversity-orientated synthesis). Our work in this chapter shows how computations on chemical systems can shed light the origins of substituted azetidine synthesis, an area of considerable current interest. We were able to provide insights into the factors influencing rotamer preference and, more generally, the magnitude of rotational barriers of a range of (thio)carbonyl-substituted azetidines, corroborating results obtained

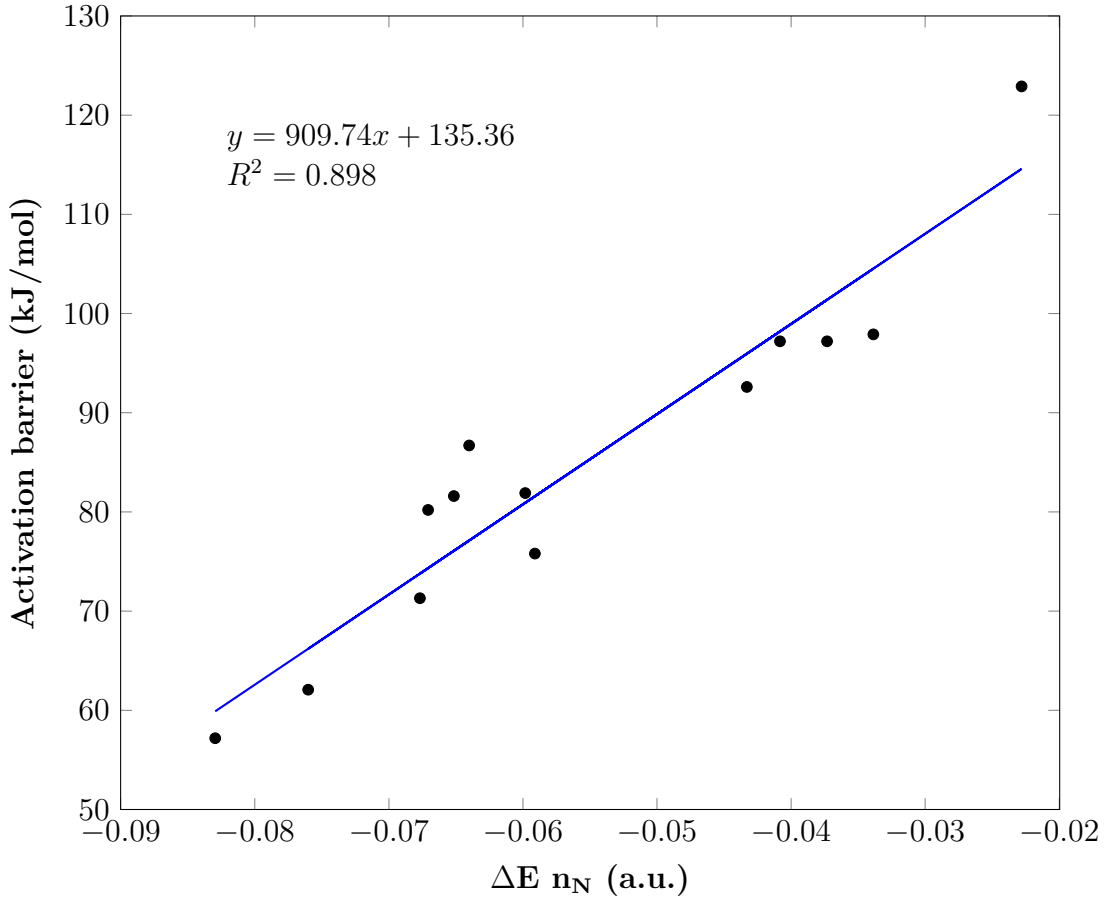

Figure 5.14: Linear correlation between M06-2X/6-311++G(d,p) activation barrier for rotation for all fourteen TSs and the change in NBO energy of the nitrogen lone pair.

through NMR studies. Isolation of the various factors influencing the stabilities of both ground states and TSs was achieved through the use of a wide range of computational techniques.

In the *N*-thiopivaloyl-2-methylazetidine system, we showed that the origin of our computed difference in stabilities between ground state conformers of 6.3 kJ/mol (5.7 kJ/mol from the 12.5:1 ratio by ^{1}H NMR in [D_8]toluene at 25 °C) was largely due to the steric interaction between the 2-methyl on the azetidine and the tertiary butyl group. We were also able to locate the lowest energy TS for rotation and could rationalise its greater stability relative to the other TSs found for this

system.

The origin of the stability difference between the *N-tert*-butoxythiocarbonyl-2-methylazetidine ground states proved more difficult to rationalise; this was largely down to the small computed stability difference between the two structures of 1.6 kJ/mol (2 kJ/mol from the 2.2:1 ratio by ^{1}H NMR in [D_8]toluene at 25 °C). We were, however, able to unequivocally determine which conformer was dominant by using a range of functionals, solvent models, DFT, and *ab initio* techniques, all of which indicated conformational bias towards the same structure. Elucidating the chemical interactions behind this small stability difference in this system required the use of a range of analytical computational methods; we were eventually able to show that the observed result was down to a weak repulsive interaction between the thiocarbonyl and the 2-methyl on azetidine when the two groups are *cis* in the less stable conformer. We located all four possible TSs for rotation in this system; using a combination of chemical intuition and analytical computational techniques, we were able to rationalise the cause of their varied stability.

6 Computational methods development

Throughout the course of the investigations described in this thesis, we wrote a number of programs using Python and OpenGL programming languages, with the express purpose of solving some of the challenges presented to us. In this chapter, we discuss how two of these programs work and look at their potential future applications in the field of Computational Chemistry.

6.1 Magnetic sampling: centroids, vectors and planes

NICS analysis can provide valuable insight into the magnetic environment in and around chemical systems.[46] Previously, studies have been conducted where multiple NICS values have been calculated along vectors for systems with planar symmetry.[50] Information pertaining to the aromatic, antiaromatic and non-aromatic nature of ground state and transition structures can be determined through such studies. Herein, we describe our own method for the automated generation of these vectors and discuss what information we can extract relating to the electronic structure of various systems.

6.1.1 Theory

Our program for the automated plotting of "ghost atom" probes relies on being able to locate the centroid of any given ring system, calculating the plane of that ring, and then generating a vector perpendicular to the aforementioned plane which passes through the previously located centroid. Raw NICS values give us isotropic chemical shift data, which is contaminated by orbital shielding in all directions; if we are looking to uncover useful information about the aromatic properties of systems, we must take the anisotropic component of these calculated values which is perpendicular to the plane of the ring system of interest. We refer to this as the out-of-plane component or $NICS_{zz}$.

The position of the centroid can be determined with the x, y and z coordinates of

all the atoms in the ring of interest, using the equations,

$$\bar{x} = \frac{\sum_{i=1}^{n} x_i}{n}$$

$$\bar{y} = \frac{\sum_{i=1}^{n} y_i}{n}$$

$$\bar{z} = \frac{\sum_{i=1}^{n} z_i}{n}$$

In order to obtain the plane of best fit for the ring systems, we applied three dimensional least squares fitting by implementing the matrix,

$$\begin{bmatrix} \sum_{i=1}^{n} x_i^2 & \sum_{i=1}^{n} x_i y_i & \sum_{i=1}^{n} x_i \\ \sum_{i=1}^{n} x_i y_i & \sum_{i=1}^{n} y_i^2 & \sum_{i=1}^{n} y_i \\ \sum_{i=1}^{n} x_i & \sum_{i=1}^{n} y_i & \sum_{i=1}^{n} 1 \end{bmatrix} \begin{bmatrix} A \\ B \\ C \end{bmatrix} = \begin{bmatrix} \sum_{i=1}^{n} x_i z_i \\ \sum_{i=1}^{n} y_i z_i \\ \sum_{i=1}^{n} z_i \end{bmatrix}$$

The solution provides the least squares solution, $f(x, y, z) = ax + by + cz + d = 0$, which defines the plane of best fit. We can now find the normal $\vec{n}$, to the plane which passes through the centroid, which is given by,

$$\vec{n} = \nabla f = \begin{bmatrix} i \\ j \\ k \end{bmatrix}$$

which is then normalised with the following to yield the unit normal vector $\hat{n}$,

$$\hat{n} = \frac{\vec{n}}{|\vec{n}|}$$

From this we can construct our vector along which we place our "ghost atoms" for use in NICS analysis (**Figure 6.1**). The scaling of the x, y and z components of the isotropic NICS values is done using the coefficients of the calculated unit normal vector to ensure we are dealing with the anisotropic σ_{zz}, out-of-the-plane NICS values; this is done by taking the scalar product of the unit normal and the isotropic σ:

$$\sigma_{zz} = \sigma \cdot \hat{n}$$

Taking the negative of these results yields values in ppm, and are representative of nuclear shielding in these positions. We incorporated all of these techniques into a program written in Python which aided us in our investigation in section 3.3.

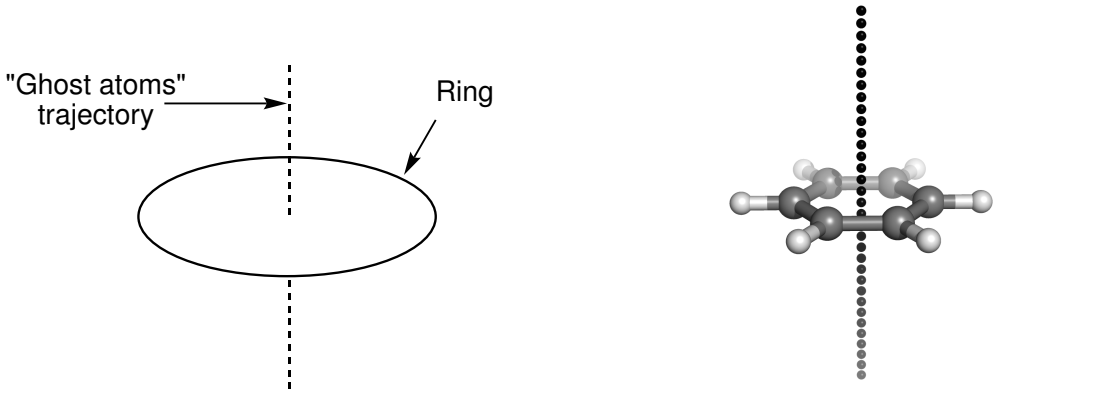

(a) Hypothetical ring system with "Ghost atom" trajectory shown.

(b) Benzene with 4 Å of "Ghost atoms" passing through its ring plane.

Figure 6.1: Illustrations of ring systems with "Ghost atoms" passing through the centroid, perpendicular to the plane of the ring.

6.1.2 Aromatic, antiaromatic and non-aromatic systems

In a proof of concept study, we used our program to assess the magnetic character, and subsequently the orbital topology, of a range of systems known to be either aromatic, antiaromatic, or non-aromatic. The results from some of these calculations are shown in **Table 6.1**, **Table 6.2** and **Table 6.3**.

In the Hückel aromatic systems shown in **Table 6.1**, we see that plots of the nuclear shielding in ppm, derived from anisotropic NICS values, reveal the expected topology of aromatic systems, generating the characteristic "w" shaped plot; this indicates a maximum in nuclear shielding about 1 Å to 1.5 Å above and below the plane of the ring, and a local minimum in electron shielding at the centroid,

revealing the π-system surrounding aromatic rings. The plots for systems **01** to **03** are similar in both magnitude and shape, typical of purely aromatic species. The plot for one of the aromatic rings of biphenylene, **04**, reveals contamination by the antiaromatic system adjacent to it, causing shielding around the centroid to be lower than in the other aromatic systems, and a decrease in overall shielding across the vector.

The antiaromatic systems shown in **Table 6.2** show significant deshielding in close proximity to the centroid of these ring systems, indicative of low electron density. This deshielding effect remains strong until $\sim$2 Å away from the centroid. In the non-aromatic systems (**Table 6.3**), there is a similar deshielding effect around the centroid but the magnitude of this is much lower. It is difficult to define a characteristic non-aromatic shape for these plots as the diversity of non-aromatic structures is vast.

The range of systems examined in this section can hopefully shed light upon future investigations into the electronic nature of other cyclic structures and cyclic TSs. In future, we hope that our program may be used in the determination of such properties, and help to elucidate the nature of ring forming mechanisms, in a similar way to in section 3.3.

Table 6.1: Computed GIAO $NICS_{zz}$ values for a range of aromatic systems at the B3LYP/6-311++G(d,p) level of theory. Where there are two or more non-equivalent ring systems in a structure, the cycle of interest is highlighted in bold.

	System	-$NICS_{zz}$ plot (ppm)
01	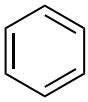	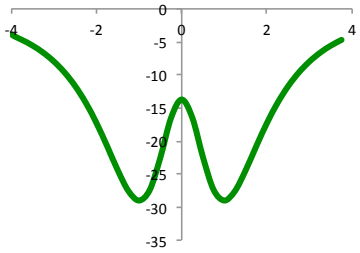
02	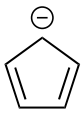	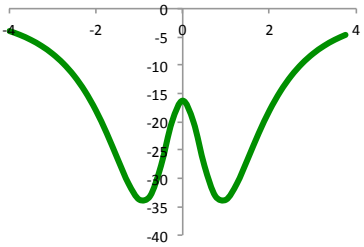
03	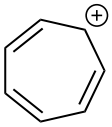	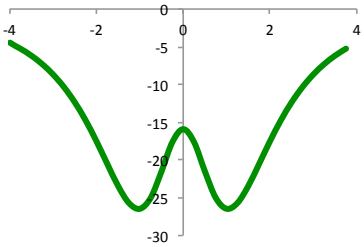
04	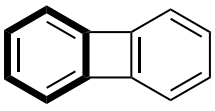	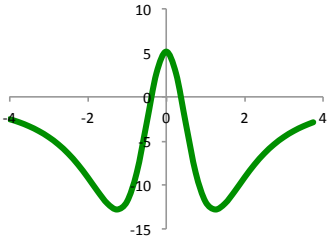

Table 6.2: Computed GIAO $NICS_{zz}$ values for a range of antiaromatic systems at the B3LYP/6-311++G(d,p) level of theory. Where there are two or more non-equivalent ring systems in a structure, the cycle of interest is highlighted in bold.

	System	-$NICS_{zz}$ plot (ppm)
05	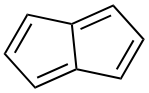	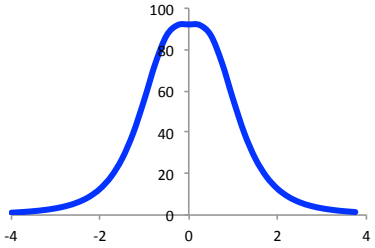
06	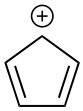	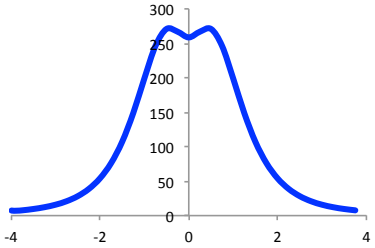
07		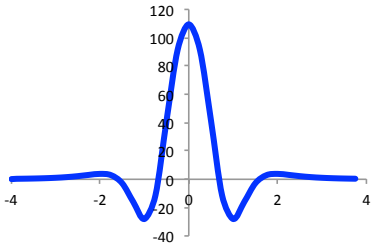
08	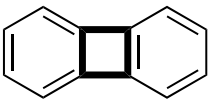	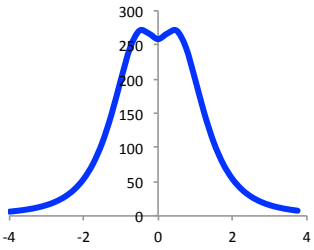

Table 6.3: Computed GIAO $NICS_{zz}$ values for a range of non-aromatic systems at the B3LYP/6-311++G(d,p) level of theory. Where there are two or more non-equivalent ring systems in a structure, the cycle of interest is highlighted in bold.

System		-$NICS_{zz}$ plot (ppm)
09	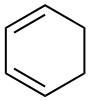	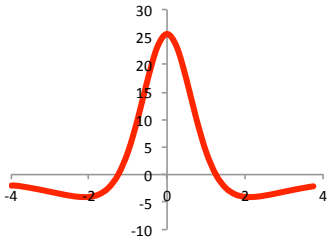
10	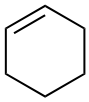	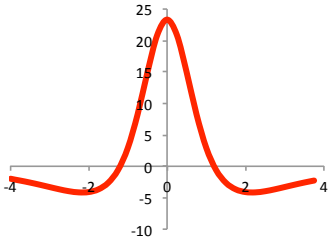
11	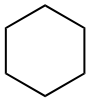	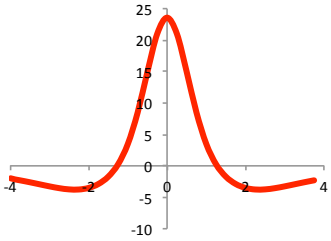
12	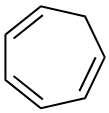	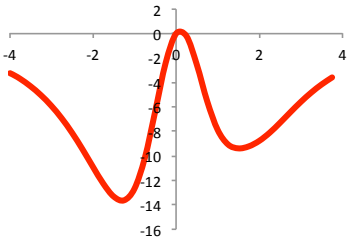

In Chapter 3, we looked at two TSs for the 5-*endo-trig* cyclisation of ester and malonate substrates in the formation of the indane motif. Comparing the results for these systems shown in **Figure 3.13** to the results in **Table 6.1** to **Table 6.3** reveals that the plot for the computationally and experimentally disfavoured cyclisation in the ester system bares a close resemblance to the plots for aromatic systems while the favoured cyclisation of the malonate looks most similar to the non-aromatic plots. This observation is in agreement with our conclusions in section 3.3 about the nature of these cyclisation and why regiodivergence upon cyclisation is seen between the two systems.

6.2 Visualising pyramidalization

In our computational analysis of into the regiodivergent α- and α'-lithiation-electrophile trapping of *N*-thiopivaloyl- and *N*-(*tert*-butoxythiocarbonyl)-α-alkylazetidines in Chapter 5, pyramidal isomerism played an important role in altering the stability of the numerous rotational TSs we calculated. Being able to visualise the extent of this pyramidalisation using a plane provided us with a valuable tool to assess these conformers.

6.2.1 Theory and implementation

In much the same way as was outlined in section 6.1.1, we used least squares fitting to find the plane of best fit for the three atoms across which we wish to generate a plane. Using Python and the graphics programming language, OpenGL, we were able to write a module for Pymol which enables us to select the four atoms of interest in each system by simply clicking on them (**Figure 6.2**), before the program generates the plane of interest, and a vector perpendicular to that plane from the nitrogen (or other pyramidal atom), together with the length of the vector. The plane defined by three non-collinear points, A, B and C, can be calculated by taking the cross product of two vectors joining these points, for example, $\vec{AB}$ and $\vec{AC}$, which results in the normal to this plane, $\vec{n}$, from which an equation for the plane can be extrapolated. Normalising $\vec{n}$ gives us the unit normal $\hat{n}$, which may

then be used to calculate the perpendicular distance d, from Nitrogen, N, to the ABC plane:

$$d = \vec{AN} \cdot \hat{n} = \vec{BN} \cdot \hat{n} = \vec{CN} \cdot \hat{n}$$

In our investigation into azetidine rotation, we used the length of this vector as a metric for the extent of pyramidalisation in these systems.

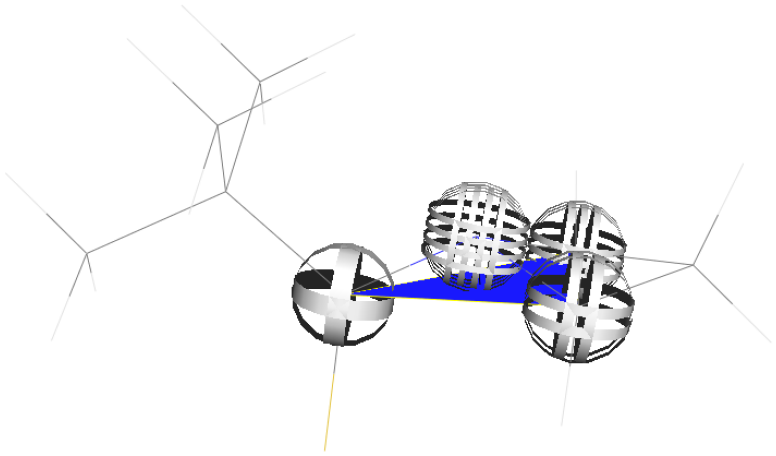

Figure 6.2: Screenshot from Pymol running our custom module, with atoms relevant to our determination of pyramidalisation selected and the generated plane shown in blue.

Figure 6.3 shows how pyramidalisation at nitrogen can be more clearly highlighted in an example system of thiopivaloyl protected azetidine. This methodology is not limited to use on azetidine, or even nitrogen, containing systems; it has scope for applications in a number of areas of Organic and Inorganic Chemistry, where the extent of pyramidalisation is important in determining the behaviour of different systems.

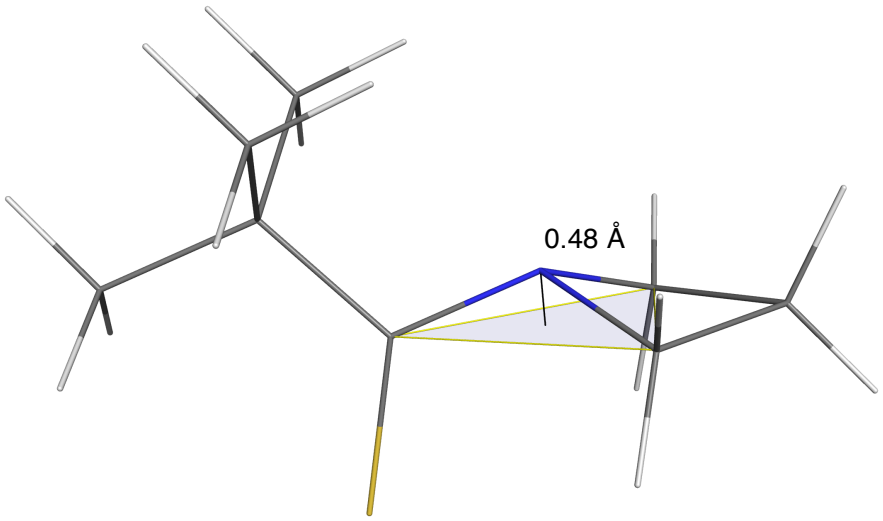

Figure 6.3: Pymol generated image of the rotational TS for thiopivaloyl protected azetidine with pyramidalisation highlighted through the use of a plane and vector.

References

[1] http://www.nobelprize.org/nobel_prizes/chemistry/laureates/1998/press.html.

[2] http://www.nobelprize.org/nobel_prizes/chemistry/laureates/2013/.

[3] Karo, A. M.; Allen, L. C. *Journal of the American Chemical Society* **1958**, *80*, 4496–4499.

[4] Streitwieser, A.; Brauman, J. I.; Coulson, C. A. *Supplemental tables of molecular orbital calculations*, 1st ed.; Pergamon Press, 1965.

[5] Frisch, M. J.; et al.; *Gaussian 09 Revision D.01*; Gaussian Inc. Wallingford CT 2009.

[6] Atkins, P. W. *Molecular Quantum Mechanics*, 4th ed.; Oxford University Press, 2005.

[7] P. W. Atkins, J. D. P. *Atkins' Physical Chemistry*, 8th ed.; Oxford University Press, 2006.

[8] Max Born, J. R. O. *Annalen der Physik* **1927**, *84*, 457–484.

[9] Jensen, J. H. *Molecular Modeling Basics*, 1st ed.; CRC Press, 2010.

[10] D. Marx, J. H. *Ab Initio Molecular Dynamics*, 1st ed.; Cambridge University Press, 2009.

[11] Slater, J. C. *Physical Review* **1930**, *36*.

[12] Yatsimirskii, K. B. *Theoretical and Experimental Chemistry* **1995**, *31*, 153–168.

[13] Einstein, A. *Relativity: The Special and General Theory*; Methuen and Co Ltd, 1916.

[14] Hay, P. J.; Wadt, W. R. *The Journal of Chemical Physics* **1985**, *82*, 299.

[15] Koch, W. *Chemist's Guide to Density Functional Theory*; Wiley-VCH, 2002.

[16] P. Hohenberg, W. K. *Physical Review* **1964**, *155*, 864–871.

[17] Levy, M. *Proceedings of the National Academy of Science* **1979**, *76*, 6062–6065.

[18] W. Kohn, L. J. S. *Physical Review* **1965**, *140*, 1133–1138.

[19] Becke, A. D. *The Journal of Chemical Physics* **1993**, *98*, 5648.

[20] Lee, C.; Yang, W.; Parr, R. G. *Physical Review B* **1988**, *37*, 785–789.

[21] Grimme, S.; Antony, J.; Ehrlich, S.; Krieg, H. *The Journal of Chemical Physics* **2010**, *132*, 154104.

[22] Becke, A. D. *Physical Review A* **1988**, *38*, 3098–3100.

[23] Vosko, S. H.; Wilk, L.; Nusair, M. *Canadian Journal of Physics* **1980**, *58*, 1200–1211.

[24] Zhao, Y.; Truhlar, D. G. *Theoretical Chemistry Accounts* **2008**, *120*, 215–241.

[25] Ehrlich, S.; Moellmann, J.; Grimme, S. *Accounts of Chemical Research* **2013**, *46*, 916–926.

[26] Grimme, S. *Wiley Interdisciplinary Reviews: Computational Molecular Science* **2011**, *1*, 211–228.

[27] Marom, N.; Tkatchenko, A.; Rossi, M.; Gobre, V. V.; Hod, O.; Sche, M.; Kronik, L. *Journal of Chemical Theory and Computation* **2011**, 3944–3951.

[28] Hehre, W. J.; *A Guide to Molecular Mechanics and Quantum Chemical Calculations*; 2003.

[29] Pople, J. A.; Beveridge, D. L. *Approximate Molecular Orbital Theory*; McGraw Hill HIgher Education, 1970.

[30] Stewart, J. J. P. *Journal of Molecular Modeling* **2007**, *13*, 1173–1213.

[31] Korth, M.; Pitonak, M.; Rezac, J.; Hobza, P. *Journal of Chemical Theory and Computation* **2010**, *6*, 344–352.

[32] Leach, A. R. *Molecular Modelling Principles and Applications*; Prentice Hall, 2001.

[33] Bartlett, R. J. *The Journal of Physical Chemistry* **1989**, *93*, 1697–1708.

[34] Pal, S.; Durga Prasad, M.; Mukherjee, D. *Theoretica Chimica Acta* **1984**, *66*, 311–332.

[35] Barone, V.; Cossi, M. *Journal of Physical Chemistry* **1998**, *102*, 1995–2001.

[36] Cossi, M.; Rega, N.; Scalmani, G.; Barone, V. *Journal of Computational Chemistry* **2003**, *24*, 669–681.

[37] Marenich, A. V.; Cramer, C. J.; Truhlar, D. G. *The Journal of Physical Chemistry B* **2009**, *113*, 6378–6396.

[38] Schlegel, H. B. *Theoretica Chimica Acta* **1984**, 333–340.

[39] Hunter, J. D. *Computing In Science & Engineering* **2007**, *9*, 90–95.

[40] Chang, G.; Guida, W. C.; Still, W. C. *Journal of the American Chemical Society* **1989**, *111*, 4379–4386.

[41] Kim, S.; Chmely, S. C.; Nimlos, M. R.; Bomble, Y. J.; Foust, T. D.; Paton, R. S.; Beckham, G. T. *The Journal of Physical Chemistry Letters* **2011**, *2*, 2846–2852.

[42] *Python Language Reference by Python Software Foundation, version 3.3.2.*; **2015**. `https://www.python.org/`.

[43] Tantillo, D. J.; Chen, J.; Houk, K. N. *Current Opinion in Structural Biology* **1998**, *2*, 743–750.

[44] Peng, C.; Ayala, P. Y.; Schlegel, H. B.; Frisch, M. J. *Journal of Computational Chemistry* **1996**, *17*, 49–56.

[45] Ditchfield, R. *Molecular Physics* **1974**, *27*, 789–807.

[46] von Ragué Schleyer, P.; Maerker, C.; Dransfeld, A.; Jiao, H.; van Eikema Hommes, N. J. R. *Journal of the American Chemical Society* **1996**, *118*, 6317–6318.

[47] Chen, Z.; Wannere, C. S.; Corminboeuf, C.; Puchta, R.; von Ragué Schleyer, P. *Chemical Reviews* **2005**, *105*, 3842–3888.

[48] Johnston, C. P.; Kothari, A.; Sergeieva, T.; Okovytyy, S. I.; Jackson, K. E.; Paton, R. S.; Smith, M. D. *Nature Chemistry* **2015**, *7*, 171–177.

[49] Jiménez-Halla, J. O. C.; Matito, E.; Robles, J.; Solà, M. *Journal of Organometallic Chemistry* **2006**, *691*, 4359–4366.

[50] Stanger, A. *The Journal of Organic Chemistry* **2006**, *71*, 883–893.

[51] Matito, E.; Poater, J.; Duran, M.; Solà, M. *Journal of Molecular Structure* **2005**, *727*, 165 – 171.

[52] Morao, I.; Lecea, B.; Cossío, F. P. *The Journal of Organic Chemistry* **1997**, *62*, 7033–7036.

[53] Marcus, R. A. *Reviews of Modern Physics* **1993**, *65*, 599–610.

[54] Gilmore, K.; Manoharan, M.; Wu, J. I.-C.; Schleyer, P. V. R.; Alabugin, I. V. *Journal of the American Chemical Society* **2012**, *134*, 10584–94.

[55] Cannon, J. S.; Overman, L. E. *Angewandte Chemie International Edition* **2012**, *51*, 4288–311.

[56] Ballette, R.; Pérez, M.; Proto, S.; Amat, M.; Bosch, J. *Angewandte Chemie International Edition* **2014**, *126*, 6316–6319.

[57] Lu, Z.; Li, Y.; Deng, J.; Li, A. *Nature chemistry* **2013**, *5*, 679–84.

[58] Bonjoch, J.; Diaba, F.; Bradshaw, B. *Synthesis* **2011**, *7*, 993–1018.

[59] Quirante, J.; Vila, X.; Escolano, C.; Bonjoch, J. *The Journal of Organic Chemistry* **2002**, *67*, 2323–2328.

[60] Diaba, F.; Bonjoch, J. *Organic & Biomolecular Chemistry* **2009**, *7*, 2517–9.

[61] MacMillan, D. W. C. *Nature* **2008**, *455*, 304–8.

[62] Houk, K. N.; Cheong, P. H.-Y. *Nature* **2008**, *455*, 309–13.

[63] Moran, A.; Hamilton, A.; Bo, C.; Melchiorre, P. *Journal of the American Chemical Society* **2013**, *135*, 9091–8.

[64] Jackson, K.; Jaffar, S. K.; Paton, R. S. *Annual Reports Section "B" (Organic Chemistry)* **2013**, *109*, 235.

[65] Mitsumori, S.; Zhang, H.; Ha-Yeon Cheong, P.; Houk, K. N.; Tanaka, F.; Barbas, C. F. *Journal of the American Chemical Society* **2006**, *128*, 1040–1.

[66] Cramer, C. J. *Essentails of Computational Chemistry*; Wiley-VHC, 2002.

[67] Eder, B. U.; Sauer, G.; Wiechert, R. *Angewandte Chemie International Edition* **1971**, *10*, 496–497.

[68] Hajos, Z. G.; Parrish, D. R. *Journal of Organic Chemistry* **1974**, *39*, 1615–1621.

[69] List, B.; Lerner, R. A.; Iii, C. F. B.; Torrey, N.; Road, P.; Jolla, L.; December, R. V. *Journal of the American Chemical Society* **2000**, *122*, 2395–2396.

[70] Clemente, F. R.; Houk, K. N. *Angewandte Chemie International Edition* **2004**, *116*, 5890–5892.

[71] Sharma, A. K.; Sunoj, R. B. *Angewandte Chemie International Edition* **2010**, *49*, 6373–7.

[72] Puchot, C.; Agami, C.; Sevestre, H. *Tetrahedron Letters* **1986**, *27*, 1501–1504.

[73] Wittkopp, A.; Schreiner, P. R. *Chemistry - A European Journal* **2003**, *9*, 407–414.

[74] Kotke, M.; Schreiner, P. R. *Tetrahedron* **2006**, *62*, 434–439.

[75] Roca-López, D.; Marqués-López, E.; Alcaine, A.; Merino, P.; Herrera, R. P. *Organic & Biomolecular Chemistry* **2014**, *12*, 4503–10.

[76] Hamza, A.; Schubert, G.; Soós, T.; Pápai, I. *Journal of the American Chemical Society* **2006**, *128*, 13151–13160.

[77] Schreiner, P. R.; Wittkopp, A. *Organic Letters* **2002**, *4*, 217–220.

[78] Clayden, J. P.; Greeves, N.; Warren, S.; Worthers, P. D. *Organic Chemistry*, 1st ed.; Oxford University Press, 2001.

[79] Xu, L.-W.; Luo, J.; Lu, Y. *Chemical Communications* **2009**, 1807–21.

[80] McLean, A. D.; Chandler, G. S. *The Journal of Chemical Physics* **1980**, *72*, 5639.

[81] Krishnan, R.; Binkley, J. S.; Seeger, R.; Pople, J. A. *The Journal of Chemical Physics* **1980**, *72*, 650.

[82] Cossi, M.; Barone, V.; Cammi, R.; Tomasi, J. *Chemical Physics Letters* **1996**, *255*, 327–335.

[83] Takano, Y.; Houk, K. N. *Journal of Chemical Theory and Computation* **2005**, *1*, 70–77.

[84] Grimme, S. *Chemistry - A European Journal* **2012**, *18*, 9955–64.

[85] Ribeiro, R. F.; Marenich, A. V.; Cramer, C. J.; Truhlar, D. G. *The Journal of Physical Chemistry B* **2011**, *115*, 14556–14562.

[86] Hratchian, H. P.; Schlegel, H. B. *The Journal of Chemical Physics* **2004**, *120*, 9918–24.

[87] Hratchian, H. P.; Schlegel, H. B. *Journal of Chemical Theory and Computation* **2005**, *30*, 61–69.

[88] Stewart, J. J. P.; *MOPAC2012*. `http://OpenMOPAC.net`.

[89] Lam, Y.-H.; Houk, K. N.; Scheffler, U.; Mahrwald, R. *Journal of the American Chemical Society* **2012**, *134*, 6286–6295.

[90] Grayson, M. N.; Pellegrinet, S. C.; Goodman, J. M. *Journal of the American Chemical Society* **2012**, 2716–2722.

[91] Sahoo, G.; Rahaman, H.; Madarász, A.; Pápai, I.; Melarto, M.; Valkonen, A.; Pihko, P. M. *Angewandte Chemie International Edition* **2012**, *51*, 13144–8.

[92] Patil, M. P.; Sunoj, R. B. *The Journal of Organic Chemistry* **2007**, *72*, 8202–8215.

[93] Seeman, J. I. *Chemical Reviews* **1983**, *83*, 83–134.

[94] Woodward, R. B.; Hoffmann, R. *Journal of the American Chemical Society* **1965**, *87*, 2511–2513.

[95] Duschmalé, J.; Wiest, J.; Wiesner, M.; Wennemers, H. *Chemical Science* **2013**, *4*, 1312.

[96] Patora-Komisarska, K.; Benohoud, M.; Ishikawa, H.; Seebach, D.; Hayashi, Y. *Helvetica Chimica Acta* **2011**, *94*, 719–745.

[97] Burés, J.; Armstrong, A.; Blackmond, D. G. *Journal of the American Chemical Society* **2012**, *134*, 6741–50.

[98] Seebach, D.; Sun, X.; Ebert, M.-O.; Schweizer, W. B.; Purkayastha, N.; Beck, A. K.; Duschmalé, J.; Wennemers, H.; Mukaiyama, T.; Benohoud, M.; Hayashi, Y.; Reiher, M. *Helvetica Chimica Acta* **2013**, *96*, 799–852.

[99] Gammack Yamagata, A. D.; Datta, S.; Jackson, K. E.; Stegbauer, L.; Paton, R. S.; Dixon, D. J. *Angewandte Chemie International Edition* **2015**, *54*, 4899–4903.

[100] Řezáč, J.; Fanfrlík, J.; Salahub, D.; Hobza, P. *Journal of Chemical Theory and Computation* **2009**, *5*, 1749–1760.

[101] Zhao, Y.; Truhlar, D. G. *Theoretical Chemistry Accounts* **2007**, *120*, 215–241.

[102] Glendening, E. D.; Landis, C. R.; Weinhold, F. *Journal of Computational Chemistry* **2013**, *34*, 1429–37.

[103] Baldwin, B. J. E. *Journal of the Chemical Society, Chemical Communications* **1976**, 734–736.

[104] Baldwin, J. E.; Cutting, J.; Kruse, L.; Silberman, L.; Thomas, R. C. *Journal of the Chemical Society, Chemical Communications* **1976**, 736–738.

[105] Baldwin, J. E.; Thomas, R. C.; Kruse, L. I.; Silberman, L. *Journal of Organic Chemistry* **1977**, *42*, 3846–3852.

[106] Baldwin, J. E.; Kruse, L. I. *Journal of the Chemical Society, Chemical Communications* **1977**, *8*, 233–235.

[107] Hotta, K.; Chen, X.; Paton, R. S.; Minami, A.; Li, H.; Swaminathan, K.; Mathews, I. I.; Watanabe, K.; Oikawa, H.; Houk, K. N.; Kim, C.-Y. *Nature* **2012**, *483*, 355–8.

[108] Baldwin, J. E. *Tetrahedron* **1982**, *38*, 2939–2947.

[109] Walden, P. *Berichte der deutschen chemischen Gesellschaft* **1896**, *29*, 133–138.

[110] Chai, J.-D.; Head-Gordon, M. *Physical Chemistry Chemical Physics* **2008**, *10*, 6615–20.

[111] Pieniazek, S. N.; Clemente, F. R.; Houk, K. N. *Angewandte Chemie International Edition* **2008**, *47*, 7746–7749.

[112] Osuna, S.; Dermenci, A.; Miller, S. J.; Houk, K. N. *Chemistry – A European Journal* **2013**, *19*, 14245–14253.

[113] Karthikeyan, S.; Ramanathan, V.; Mishra, B. K. *The Journal of Physical Chemistry A* **2013**, *117*, 6687–6694.

[114] *Chemical Physics Letters* **1995**, *247*, 63 – 68.

[115] London, F. *Journal de Physique et le Radium* **1937**, *8*, 397.

[116] Ditchfield, R. *The Journal of Chemical Physics* **1972**, *56*, 5688.

[117] Wolinski, K.; Hinton, J. F.; Pulay, P. *Journal of the American Chemical Society* **1990**, *112*, 8251–8260.

[118] Corminboeuf, C.; Heine, T.; Seifert, G.; Schleyer, P. v. R.; Weber, J. *Phys. Chem. Chem. Phys.* **2004**, *6*, 273–276.

[119] Benson, R. C.; Flygare, W. H. *Journal of the American Chemical Society* **1970**, *92*, 7523–7529.

[120] Watson, M. P.; Jacobsen, E. N. *Journal of the American Chemical Society* **2008**, *130*, 12594–12595.

[121] Arp, F. O.; Fu, G. C. *Journal of the American Chemical Society* **2005**, *127*, 10482–10483.

[122] Albicker, M.; Cramer, N. *Angewandte Chemie International Edition* **2009**, *48*, 9139–9142.

[123] Martin, N.; Pierre, C.; Davi, M.; Jazzar, R.; Baudoin, O. *Chemistry – A European Journal* **2012**, *18*, 4480–4484.

[124] Yang, J. W.; Fonseca, M. T. H.; List, B. *Journal of the American Chemical Society* **2005**, *127*, 15036–15037.

[125] Belmessieri, D.; Morrill, L. C.; Simal, C.; Slawin, A. M. Z.; Smith, A. D. *Journal of the American Chemical Society* **2011**, *133*, 2714–2720.

[126] Phillips, E.; Wadamoto, M.; Chan, A.; Scheidt, K. *Angewandte Chemie International Edition* **2007**, *46*, 3107–3110.

[127] Li, Y.; Wang, X.-Q.; Zheng, C.; You, S.-L. *Chemical Communications* **2009**, 5823–5825.

[128] Biswas, A.; Sarkar, S. D.; Fröhlich, R.; Studer, A. *Organic Letters* **2011**, *13*, 4966–4969.

[129] Chua, P. J.; Tan, B.; Yang, L.; Zeng, X.; Zhu, D.; Zhong, G. *Chemical Communications* **2010**, *46*, 7611–7613.

[130] Ross, J. A.; Seiders, R. P.; Lemal, D. M. *Journal of the American Chemical Society* **1976**, *98*, 4325–4327.

[131] Birney, D. M.; Wagenseller, P. E. *Journal of the American Chemical Society* **1994**, *116*, 6262–6270.

[132] Matito, E.; Poater, J.; Duran, M.; Solà, M. *ChemPhysChem* **2006**, *7*, 111–113.

[133] Paton, R. S.; Steinhardt, S. E.; Vanderwal, C. D.; Houk, K. N. *Journal of the American Chemical Society* **2011**, *133*, 3895–3905.

[134] de Lera, A. R.; Alvarez, R.; Lecea, B.; Torrado, A.; Cossío, F. P. *Angewandte Chemie International Edition* **2001**, *40*, 557–561.

[135] Duncan, J. A.; Calkins, D. E. G.; Chavarha, M. *Journal of the American Chemical Society* **2008**, *130*, 6740–6748.

[136] Fabian, W. M. F.; Kappe, C. O.; Bakulev, V. A. *The Journal of Organic Chemistry* **2000**, *65*, 47–53.

[137] Fabian, W. M. F.; Bakulev, V. A.; Kappe, C. O. *The Journal of Organic Chemistry* **1998**, *63*, 5801–5805.

[138] Zhou, C.; Birney, D. M. *Journal of the American Chemical Society* **2002**, *124*, 5231–5241.

[139] Huisgen, R. *Angewandte Chemie International Edition* **1980**, *19*, 947–973.

[140] Breugst, M.; Zipse, H.; Guthrie, J.; Mayr, H. *Angewandte Chemie International Edition* **2010**, *49*, 5165–5169.

[141] Marti, C.; Carreira, E. M. *Journal of the American Chemical Society* **2005**, *127*, 11505–11515.

[142] Enders, D.; Demir, A. S.; Rendenbach, B. E. M. *Chemische Berichte* **1987**, *120*, 1731–1735.

[143] Enders, D.; Wortmann, L.; Peters, R. *Accounts of Chemical Research* **2000**, *33*, 157–69.

[144] Evans, D. A.; Tedrow, J. S.; Shaw, J. T.; Downey, C. W. *Journal of the American Chemical Society* **2002**, *124*, 392–393.

[145] Myers, A. G.; Yang, B. H.; Chen, H.; McKinstry, L.; Kopecky, D. J.; Gleason, J. L. *Journal of the American Chemical Society* **1997**, *119*, 6496–6511.

[146] Job, A.; Janeck, C. F.; Bettray, W.; Peters, R.; Enders, D. *Tetrahedron* **2002**, *58*, 2253–2329.

[147] Vesely, J.; Rios, R. *ChemCatChem* **2012**, *4*, 942–953.

[148] Nicewicz, D. a.; MacMillan, D. W. C. *Science* **2008**, *322*, 77–80.

[149] Hodgson, D. M.; Charlton, A.; Paton, R. S.; Thompson, A. L. *The Journal of Organic Chemistry* **2013**, *78*, 1508–1518.

[150] Um, J. M.; Kaka, N. S.; Hodgson, D. M.; Houk, K. N. *Chemistry - A European Journal* **2010**, *16*, 6310–6316.

[151] Neve-Foster, B. L. *Part II Thesis: Towards the Development of Direct Methodology to Enantioenriched α-Alkylated Aldehydes*; University of Oxford, **2015**.

[152] R. Harrison, J.; O'Brien, P.; W. Porter, D.; M. Smith, N. *Journal of the Chemical Society, Perkin Transactions 1* **1999**, 3623–3631.

[153] Naylor, A.; Howarth, N.; Malpass, J. R. *Tetrahedron* **1993**, *49*, 451–468.

[154] Blum, Z.; Nyberg, K. *Acta Chemica Scandinavica* **1981**, *35b*, 739–741.

[155] Hansson, C.; Wickberg, B. *The Journal of Organic Chemistry* **1973**, *38*, 3074–3076.

[156] de Meijere, A. *Angewandte Chemie International Edition* **1979**, *18*, 809–826.

[157] Armstrong, A.; Boto, R. a.; Dingwall, P.; Contreras-García, J.; Harvey, M. J.; Mason, N. J.; Rzepa, H. S. *Chemical Science* **2014**, *5*, 2057.

[158] Jindal, G.; Sunoj, R. B. *Angewandte Chemie International Edition* **2014**, *126*, 4521–4525.

[159] Jackson, K. E.; Mortimer, C. L.; Odell, B.; McKenna, J. M.; Claridge, T. D. W.; Paton, R. S.; Hodgson, D. M. *The Journal of Organic Chemistry* **2015**, *80*, 9838–46.

[160] Fleming, I. *Pericyclic Reactions*; Oxford University Press, 2015.

[161] G. S. Singh, D. K., M. D'hooghe *Comprehensive Heterocyclic Chemistry III*; Stevens, C. V., Ed.; Elsevier: Oxford, 2008; Vol. 2.

[162] Brandi, A.; Cicchi, S.; Cordero, F. M. *Chemical Reviews* **2008**, *108*, 3988–4035.

[163] Hodgson, D. M.; Pearson, C. I.; Kazmi, M. *Organic Letters* **2014**, *16*, 856–859.

[164] Beak, P.; Zajdel, W. J.; Reitz, D. B. *Chemical Reviews* **1984**, *84*, 471–523.

[165] Hodgson, D. M.; Mortimer, C. L.; McKenna, J. M. *Organic Letters* **2015**, *17*, 330–333.

[166] Paton, R. S.; Steinhardt, S. E.; Vanderwal, C. D.; Houk, K. N. *Journal of the American Chemical Society* **2011**, *133*, 3895–905.

[167] Fogueri, U. R.; Kozuch, S.; Karton, A.; Martin, J. M. *The Journal of Physical Chemistry A* **2013**, *117*, 2269–2277.

[168] Stephens, P. J.; Devlin, F. J.; Chabalowski, C. F.; Frisch, M. J. *The Journal of Physical Chemistry* **1994**, *98*, 11623–11627.

[169] Barone, V.; Cossi, M.; Tomasi, J. *The Journal of Chemical Physics* **1997**, *107*, 3210–3221.

[170] Montgomery, J. A.; Frisch, M. J.; Ochterski, J. W.; Petersson, G. A. *The Journal of Chemical Physics* **1999**, *110*, 2822–2827.

[171] Montgomery, J. A.; Frisch, M. J.; Ochterski, J. W.; Petersson, G. A. *The Journal of Chemical Physics* **2000**, *112*, 6532–6542.

[172] Simón, L.; Paton, R. S. *The Journal of Organic Chemistry* **2015**, *80*, 2756–2766.

[173] *The PyMOL Molecular Graphics System, Version 1.3, Schrödinger LLC*; **2010**.

[174] `https://www.opengl.org/`.

[175] Johnson, E. R.; Keinan, S.; Mori-sa, P.; Contreras-garcía, J.; Cohen, A. J.; Yang, W. *Journal of the American Chemical Society* **2010**, *132*, 6498–6506.

[176] Contreras-garcía, J.; Johnson, E. R.; Keinan, S.; Chaudret, R.; Piquemal, P.; Beratan, D. N.; Yang, W. *Journal of Chemical Theory and Computation* **2011**, *7*, 625–632.

[177] *AIMAll (Version 15.05.18), Todd A. Keith, TK Gristmill Software, Overland Park KS, USA, (aim.tkgristmill.com)*; **2015**.

[178] Bondi, A. *The Journal of Physical Chemistry* **1964**, *68*, 441–451.

[179] Hodgson, D. M.; Kloesges, J. *Angewandte Chemie International Edition* **2010**, *49*, 2900–2903.

[180] Hodgson, D. M.; Pearson, C. I.; Thompson, A. L. *Journal of Organic Chemistry* **2013**, *1*, 2–10.

[181] Wiberg, K. B.; Rablen, P. R. *Journal of the American Chemical Society* **1995**, *117*, 2201–2209.

[182] Wiberg, K. B.; Rush, D. J. *Journal of the American Chemical Society* **2001**, *123*, 2038–2046.

Appendix

Basis sets

6-31G	Pople split valence basis set with six primitive Gaussians for the contracted core functions
6-311G	Pople triple-ζ basis set
6-31+G	Indicates augmentation of the basis set with an additional s and one set of p functions with small exponents on heavy atoms to describe spatially diffuse MOs
6-31++G	As above with additional diffuse s functions on hydrogens
6-31G(d)	Indicates inclusion of a set of d functions on heavy atoms to increase flexibility of atom centred AOs to adequately describe MOs
6-31G(d,p)	As above with the inclusion of p functions on hydrogens
6-311G(d,p)	As above but with a triple-ζ basis set
6-311+G(d,p)	As above with an additional s and one set of p functions with small exponents on heavy atoms to describe spatially diffuse MOs
6-311++G(d,p)	As above with additional diffuse s functions on hydrogens

LANL2DZ	LANL basis set for which fourth row elements are handled using a nonrelativistic [Ar] 18-electron core and a relativistic [Kr] 36-electron core with double-ζ split valence function for fifth row elements

Density functionals

B3LYP — Becke's three parameter functional with Lee-Yang-parr correlation.

B3LYP-D3 — Same as above with Grimme's D3 dispersion correction.

M06-2X — Minnesota 06 meta exchange-correlation functional by Truhlar which contains twice the amount of nonlocal exchange (2X) as M06; it is parameterised for nonmetals only and has 54% HF exchange. It is a hybrid meta-generalised gradient approximation (GGA) exchange functional.

wB97XD — Functional by Head-Gordon which includes dispersion correction using Grimme's D2 dispersion correction.

Solvation models

PCM — The polarisable continuum model is an implicit solvation model in which solute charge distribution is described as being inside a cavity that displaces an otherwise homogeneous dielectric medium. The Poisson equation is valid for situations where a polarisable medium responds linearly to an embedded charge and expresses the electrostatic potential as a function of charge density and dielectric constant. The molecular cavity is described by the molecular surface and the solute charge it distributed onto the grin points on this surface.

CPCM — The conductor-like polarisable continuum model is a more recent implementation of the model in the framework of the polarisable continuum model. In this extension of PCM, the solvent is treated as a conductor and therefore impacts the polarisation charge of accessible surface area between the solute and solvent.

SMD This density based implicit solvation model separates the observable solvation free energy into two main components: the bulk electrostatic contribution, which arises from a self-consistent reaction field treatment that involves the solution of the non-homogeneous Poisson equation for electrostatics in terms of the integral equations formalism PCM and the cavity dispersion solvent structure term, which is the contribution arising from short-range interactions between the solute and solvent molecules in the first solvation shell.

Computational data

All energies and Gibbs free energies in this section are given in Hartrees (H); imaginary frequencies are given in cm^{-1}; NICS values are given in ppm.

Appendix to Chapter 2

Figure 2.5

Structure	Energy	Gibbs Free Energy	Imaginary Frequency
H2O	-76.42717	-76.42073	
Methylamine	-95.83859	-95.79564	
01	-749.02529	-748.76557	
02	-768.43425	-768.13664	
03	-768.43316	-768.13552	
04	-768.42945	-768.13098	
05	-768.43049	-768.12655	
06	-768.42547	-768.12245	
07	-768.42394	-768.11573	
08	-768.44511	-768.13897	
09	-768.46699	-768.16332	
10	-768.47078	-768.16545	
11	-749.05691	-748.79208	
12	-768.38191	-768.08335	-845.8
13	-768.40604	-768.10470	-486.5
14	-768.40812	-768.10755	-411.9
15	-768.41442	-768.11206	-142.0
16	-768.38822	-768.08898	-966.7
17	-768.41390	-768.10825	-161.0
18	-768.41316	-768.10944	-283.9
19	-768.46090	-768.15822	
20	-749.05365	-748.78819	
21	-768.46748	-768.16322	

Figure 2.7

Structure	Energy	Gibbs Free Energy	Imaginary Frequency
H2O	-76.46559355	-76.45948644	
Methylamine	-95.89943721	-95.85713633	
01	-749.3845958	-749.1289178	
02	-768.8129463	-768.5196779	
03	-768.8102982	-768.516035	
04	-768.8068009	-768.5125555	
05	-768.7994317	-768.4997433	
06	-768.7942072	-768.4957461	
07	-768.795685	-768.4921396	
08	-768.8123071	-768.5096898	
09	-768.8374088	-768.5376515	
10	-768.8398406	-768.5385607	
11	-749.4081789	-749.1465022	
12	-768.7578464	-768.4634269	-831.8
13	-768.7847352	-768.4879827	-439.8
14	-768.7875286	-768.4909802	-400.6
15	-768.7839209	-768.4863137	-152.5
16	-768.7644171	-768.4694049	-827.8
17	-768.7884301	-768.4872369	-68.4
18	-768.7879681	-768.4882318	-134.8
19	-768.8316525	-768.5329868	
20	-749.4053405	-749.1441147	
21	-768.836129	-768.5360368	

Figure 2.11

Structure	Energy	Gibbs Free Energy	Imaginary Frequency
1	-1550.08109	-1549.59702	
2	-1550.0836	-1549.59969	
3	-1550.0854	-1549.60258	
4	-1550.0822	-1549.60033	
5	-1550.070657	-1549.58536	-397.1
6	-1550.0857	-1549.59802	
7	-1550.065607	-1549.58041	-1152.5
8	-1550.095245	-1549.60649	
9	-1550.1192	-1549.63158	
10	-1550.062525	-1549.57813	-411.6
11	-1550.0789	-1549.58993	
12	-1550.061117	-1549.57656	-1248.1
13	-1550.089069	-1549.60025	
14	-1550.12	-1549.63269	

Figure 2.11

Structure	Energy	Gibbs Free Energy	Imaginary Frequency
1	-1550.08109	-1549.59702	
2	-1550.0836	-1549.59969	
3	-1550.0854	-1549.60258	
4	-1550.0822	-1549.60033	
5	-1550.070657	-1549.58536	-397.1
6	-1550.0857	-1549.59802	
7	-1550.065607	-1549.58041	-1152.5
8	-1550.095245	-1549.60649	
9	-1550.1192	-1549.63158	
10	-1550.062525	-1549.57813	-411.6
11	-1550.0789	-1549.58993	
12	-1550.061117	-1549.57656	-1248.1

13	-1550.089069	-1549.60025	
14	-1550.12	-1549.63269	

Figure 2.12

Structure	Energy	Gibbs Free Energy	Imaginary Frequency
1	-1549.708358	-1549.217789	
2	-1549.707894	-1549.21576	
3	-1549.707217	-1549.216259	
4	-1549.698107	-1549.202503	
5	-1549.690863	-1549.193316	
6	-1549.694476	-1549.197864	
7	-1549.699134	-1549.204412	
8	-1549.685337	-1549.190977	-409.7
9	-1549.676124	-1549.182814	-1195.5
10	-1549.678587	-1549.185287	-379.5
11	-1549.660975	-1549.169718	-986.7

Figure 2.19

Structure	Energy	Gibbs Free Energy	Imaginary Frequency
01	-1192.369615	-1191.921149	
02	-1192.366151	-1191.919296	
03	-1192.366841	-1191.921699	
04	-1192.373522	-1191.926625	
05	-1192.346788	-1191.89938	-500.7
06	-1192.361425	-1191.911707	
07	-1192.343997	-1191.894415	-511.0
08	-1192.359874	-1191.90856	

Figure 2.20

Structure	Energy	Gibbs Free Energy	Imaginary Frequency

01	-1192.366151	-1191.919296	
02	-1192.369615	-1191.921149	
03	-1192.366841	-1191.921699	
04	-1192.373522	-1191.926625	
05	-1192.350446	-1191.902073	-411.5
06	-1192.370951	-1191.920179	
07	-1192.357122	-1191.907514	-76.6
08	-1192.408389	-1191.957428	
09	-1192.348977	-1191.899791	-418.5
10	-1192.37169	-1191.920364	
11	-1192.359253	-1191.907944	-56.6
12	-1192.40513	-1191.954189	

Appendix to Chapter 3

Figure 3.8

Structure	Energy	Gibbs Free Energy	Imaginary Frequency
1	-1035.10798	-1034.84211	
2	-1035.09054	-1034.82300	-256.6
3	-1035.09872	-1034.83045	
4	-1035.10479	-1034.83892	
5	-1035.07826	-1034.81191	-151
6	-1035.13521	-1035.13521	

Figure 3.9

Structure	Energy	Gibbs Free Energy	Imaginary Frequency
1	-1262.97844	-1262.67456	
2	-1262.95631	-1262.65056	-103.2
3	-1262.95668	-1262.65256	
4	-1262.97318	-1262.66930	
5	-1262.95686	-1262.65400	-148.7

6	-1262.99611	-1262.69057

Figure 3.10 and Figure 3.11

Distance (Å)	TS 01 (ppm)	TS 02 (ppm)	TS 03 (ppm)
-4	-3.32	-3.02	-4.39
-3.75	-3.85	-3.54	-5.02
-3.5	-4.48	-4.18	-5.78
-3.25	-5.24	-4.98	-6.69
-3	-6.15	-5.98	-7.80
-2.75	-7.22	-7.26	-9.17
-2.5	-8.49	-8.88	-10.88
-2.25	-9.98	-10.97	-13.03
-2	-11.74	-13.64	-15.74
-1.75	-13.84	-17.01	-19.13
-1.5	-16.34	-21.12	-23.25
-1.25	-19.26	-25.77	-27.90
-1	-22.37	-30.23	-32.33
-0.75	-25.04	-32.97	-34.85
-0.5	-26.32	-31.89	-33.17
-0.25	-25.77	-26.02	-26.34
0	-24.22	-17.66	-17.26
0.25	-22.89	-11.52	-11.17
0.5	-21.83	-10.08	-10.27
0.75	-20.37	-11.67	-12.33
1	-18.31	-13.48	-14.35
1.25	-16.05	-14.16	-15.06
1.5	-13.97	-13.69	-14.58
1.75	-12.19	-12.52	-13.40
2	-10.64	-11.07	-11.92
2.25	-9.25	-9.59	-10.43
2.5	-7.99	-8.21	-9.03
2.75	-6.87	-7.00	-7.80

3	-5.88	-5.95	-6.73
3.25	-5.04	-5.07	-5.82
3.5	-4.33	-4.33	-5.05
3.75	-3.72	-3.71	-4.40
4	-3.21	-3.20	-3.85

Figure 3.12 and Figure 3.13

Distance (Å)	TS 01 (ppm)	TS 02 (ppm)
-4	-2.07	-3.89
-3.75	-2.24	-4.35
-3.5	-2.40	-4.87
-3.25	-2.52	-5.45
-3	-2.59	-6.10
-2.75	-2.56	-6.80
-2.5	-2.40	-7.54
-2.25	-2.08	-8.29
-2	-1.58	-8.96
-1.75	-0.87	-9.43
-1.5	0.18	-9.49
-1.25	1.82	-8.77
-1	4.35	-6.83
-0.75	7.81	-3.46
-0.5	11.43	0.67
-0.25	13.57	3.56
0	12.82	3.07
0.25	9.38	-0.74
0.5	4.68	-5.48
0.75	0.12	-8.76
1	-3.71	-9.84
1.25	-6.89	-9.27
1.5	-9.81	-7.92
1.75	-12.63	-6.43

2	-15.03	-5.15
2.25	-16.23	-4.19
2.5	-15.64	-3.54
2.75	-13.84	-3.16
3	-12.30	-2.96
3.25	-11.89	-2.86
3.5	-12.48	-2.80
3.75	-13.24	-2.74
4	-12.85	-2.67

Table 3.1

Structure	**Energy**	**Gibbs Free Energy**	**Imaginary Frequency**
01 *endo*	-1034.76862	-1034.50263	-151
01 *exo*	-1034.78505	-1034.51593	-256.6
02 *endo*	-1074.07343	-1073.78056	-339.6
02 *exo*	-1074.08312	-1073.78713	-238.2
03 *endo*	-1191.94651	-1191.57112	-232.4
03 *exo*	-1191.95449	-1191.57812	-172.5
04 *endo*	-1443.34995	-1442.98923	-247.8
04 *exo*	-1443.36081	-1442.99938	-242.3
05 *endo*	-1127.00336	-1126.73954	-314.7
05 *exo*	-1127.01129	-1126.74627	-247
06 *endo*	-1219.23156	-1218.96975	-364.9
06 *exo*	-1219.23794	-1218.97663	-255.8
07 *endo*	-1127.00494	-1126.74006	-314.6
07 *exo*	-1127.01645	-1126.75192	-269.6
08 *endo*	-1262.57235	-1262.26645	-297.9
08 *exo*	-1262.58544	-1262.27847	-232.2
09 *endo*	-1148.06236	-1147.78701	-331.5
09 *exo*	-1148.07141	-1147.79571	-240.1
10 *endo*	-1239.21737	-1238.94969	-324.4
10 *exo*	-1239.22670	-1238.95786	-232.6

11 *endo*	-1443.66358	-1443.39633	-403.3
11 *exo*	-1443.67190	-1443.40463	-266.5
12 *endo*	-1239.22468	-1238.95693	-343.3
12 *exo*	-1239.23635	-1238.96831	-261.2

Figure 3.18, **Figure 3.19** and **Figure 3.20**; X = C

Structure	**Energy**	**Gibbs Free Energy**	**Imaginary Frequency**
4-*endo* TS	-384.46469	-384.36259	-583
4-*endo* closed	-384.54406	-384.43944	
4-*endo* ring	-384.49969	-384.39750	
4-*exo* TS	-384.49366	-384.39093	-270.7
4-*exo* closed	-384.52766	-384.42161	
4-*exo* open	-384.49805	-384.39510	
5-*endo* TS	-423.80273	-423.67329	-218.3
5-*endo* closed	-423.88909	-423.75443	
5-*endo* ring	-423.80951	-423.67945	
5-*exo* TS	-423.80484	-423.67384	-150.7
5-*exo* closed	-423.86647	-423.73211	
5-*exo* open	-423.80952	-423.67897	
6-*endo* TS	-463.11004	-462.95246	-282.9
6-*endo* closed	-463.20850	-463.04583	
6-*endo* ring	-463.12072	-462.96559	
6-*exo* TS	-463.11511	-462.95786	-29.7
6-*exo* closed	-463.18527	-463.02204	
6-*exo* open	-463.11740	-462.95896	
7-*endo* TS	-502.42116	-502.23632	-206
7-*endo* closed	-502.51505	-502.32503	
7-*endo* ring	-502.42962	-502.24599	
7-*exo* TS	-502.42226	-502.23652	-166.1
7-*exo* closed	-502.48857	-502.29730	
7-*exo* open	-502.43019	-502.24774	
Conjugate TS	-425.00917	-424.86433	-172.9

Conjugate closed	-425.09973	-424.94777	
Conjugate open	-425.01173	-424.86644	
Direct TS	-425.00656	-424.86031	-208.7
Direct closed	-425.07364	-424.92096	
Direct open	-425.01226	-424.86711	

Figure 3.18, **Figure 3.19** and **Figure 3.20**; X = N

Structure	**Energy**	**Gibbs Free Energy**	**Imaginary Frequency**
4-*endo* TS	-400.51917	-400.42700	-609
4-*endo* closed	-400.57740	-400.48308	
4-*endo* ring	-400.56837	-400.47560	
4-*exo* TS	-400.55845	-400.46484	-277.9
4-*exo* closed	-400.57460	-400.47994	
4-*exo* open	-400.56669	-400.47434	
5-*endo* TS	-439.86849	-439.74814	-304.4
5-*endo* closed	-439.92175	-439.79782	
5-*endo* ring	-439.87786	-439.75856	
5-*exo* TS	-439.87301	-439.75267	-140.7
5-*exo* closed	-439.91273	-439.78939	
5-*exo* open	-439.87798	-439.75991	
6-*endo* TS	-479.17726	-479.02996	-219.8
6-*endo* closed	-479.24019	-479.08887	
6-*endo* ring	-479.18845	-479.04234	
6-*exo* TS	-479.18845	-479.04234	-42.4
6-*exo* closed	-479.22672	-479.07406	
6-*exo* open	-479.18845	-479.04234	
7-*endo* TS	-518.49101	-518.31515	-325
7-*endo* closed	-518.54725	-518.36784	
7-*endo* ring	-518.49776	-518.32570	
7-*exo* TS	-518.49305	-518.31819	-122.9
7-*exo* closed	-518.53098	-518.35228	
7-*exo* open	-518.49734	-518.32356	

Conjugate TS	-441.07735	-440.94106	-56.9
Conjugate closed	-441.13184	-440.99005	
Conjugate open	-441.07844	-440.94448	
Direct TS	-441.07701	-440.93965	-92.5
Direct closed	-441.11463	-440.97125	
Direct open	-441.07802	-440.94298	

Figure 3.18, **Figure 3.19** and **Figure 3.20**; X = O

Structure	**Energy**	**Gibbs Free Energy**	**Imaginary Frequency**
4-*endo* TS	-420.40908	-420.32805	-660.8
4-*endo* closed	-420.44592	-420.36311	
4-*endo* ring	-420.47354	-420.39337	
4-*exo* TS	-420.45248	-420.37113	-291.8
4-*exo* closed	-420.45409	-420.37226	
4-*exo* open	-420.47131	-420.38999	
5-*endo* TS	-459.76295	-459.65362	-405.6
5-*endo* closed	-459.78897	-459.68113	
5-*endo* ring	-459.78292	-459.67476	
5-*exo* TS	-459.77587	-459.66670	-154.2
5-*exo* closed	-459.78864	-459.67813	
5-*exo* open	-459.78297	-459.67495	
6-*endo* TS	-499.07849	-498.94239	-288.8
6-*endo* closed	-499.10787	-498.96858	
6-*endo* ring	-499.09142	-498.95572	
6-*exo* TS	-499.09283	-498.95585	-106.2
6-*exo* closed	-499.10371	-498.96407	
6-*exo* open	-499.09305	-498.95779	
7-*endo* TS	-538.39002	-538.22637	-190.5
7-*endo* closed	-538.41648	-538.24963	
7-*endo* ring	-538.40433	-538.24234	
7-*exo* TS	-538.39923	-538.23357	-98.6
7-*exo* closed	-538.40979	-538.24359	

7-*exo* open	-538.40291	-538.24141	
Conjugate TS	-460.97720	-460.85213	-220
Conjugate closed	-460.99842	-460.86966	
Conjugate open	-460.98067	-460.85884	
Direct TS	-460.97868	-460.85238	-181.1
Direct closed	-460.99009	-460.86075	
Direct open	-460.98031	-460.85537	

Table 3.2

Structure	**Energy**	**Gibbs Free Energy**	**Imaginary Frequency**
01 *endo* TS	-423.80273	-423.67329	-218.3
01 *endo* closed	-423.88909	-423.75443	
01 *endo* open	-423.80951	-423.67945	
01 *exo* TS	-423.80484	-423.67384	-150.7
01 *exo* closed	-423.86647	-423.73211	
01 *exo* open	-423.80952	-423.67897	
02 *endo* TS	-439.86849	-439.74814	-304.4
02 *endo* closed	-439.92175	-439.79782	
02 *endo* open	-439.87786	-439.75856	
02 *exo* TS	-439.87300	-439.75267	-140.7
02 *exo* closed	-439.91273	-439.78939	
02 *exo* open	-439.87798	-439.75991	
03 *endo* TS	-459.76295	-459.65362	-405.6
03 *endo* closed	-459.78897	-459.68113	
03 *endo* open	-459.78292	-459.67476	
03 *exo* TS	-459.77587	-459.66670	-154.2
03 *exo* closed	-459.78864	-459.67813	
03 *exo* open	-459.78297	-459.67495	
04 *endo* TS	-753.87537	-753.70668	-348.7
04 *endo* closed	-753.93885	-753.76578	
04 *endo* open	-753.89194	-753.72236	
04 *exo* TS	-753.88238	-753.71278	-283.6

04 *exo* closed	-753.92133	-753.74644	
04 *exo* open	-753.89121	-753.72412	
05 *endo* TS	-789.86807	-789.71747	
05 *endo* closed	-789.88589	-789.73566	
05 *endo* open	-789.90401	-789.75425	
05 *exo* TS	-789.88459	-789.73452	
05 *exo* closed	-789.88685	-789.73615	
05 *exo* open	-789.90372	-789.75451	
06 *endo* TS	-782.72226	-782.62010	-153.2
06 *endo* closed	-782.78468	-782.67734	
06 *endo* open	-782.72421	-782.62264	
06 *exo* TS	-782.71452	-782.61213	-103.8
06 *exo* closed	-782.75895	-782.65135	
06 *exo* open	-782.71565	-782.61480	
07 *endo* TS	-502.42621	-502.24347	-125.9
07 *endo* closed	-502.52020	-502.33327	
07 *endo* open	-502.42959	-502.24717	
07 *exo* TS	-502.43047	-502.24802	-78.8
07 *exo* closed	-502.49358	-502.30607	
07 *exo* open	-502.42968	-502.24712	
08 *endo* TS	-538.39708	-538.23567	-384.7
08 *endo* closed	-538.42567	-538.26284	
08 *endo* open	-538.41626	-538.25514	
08 *exo* TS	-538.41651	-538.25368	-207.6
08 *exo* closed	-538.42447	-538.26069	
08 *exo* open	-538.41633	-538.25510	
09 *endo* TS	-608.34246	-608.21640	-464.3
09 *endo* closed	-608.35966	-608.23191	
09 *endo* open	-608.37386	-608.25110	
09 *exo* TS	-608.34373	-608.21756	-159.3
09 *exo* closed	-608.34377	-608.21770	
09 *exo* open	-608.37386	-608.25111	
10 *endo* TS	-608.28526	-608.16294	-293.7

10 *endo* closed	-608.35941	-608.23282	
10 *endo* open	-608.29078	-608.16884	
10 *exo* TS	-608.29220	-608.16833	-225.7
10 *exo* closed	-608.32944	-608.20259	
10 *exo* open	-608.29233	-608.17008	
11 *endo* TS	-792.79264	-792.67438	-456.4
11 *endo* closed	-792.80353	-792.68569	
11 *endo* open	-792.82680	-792.70962	
11 *exo* closed	-792.82386	-792.70644	
11 *exo* open	-792.82695	-792.70991	
12 *endo* TS	-622.31782	-622.20420	-246.4
12 *endo* closed	-622.40013	-622.28393	
12 *endo* open	-622.33322	-622.22129	
12 *exo* TS	-622.32677	-622.21310	-138.9
12 *exo* closed	-622.37232	-622.25682	
12 *exo* open	-622.33323	-622.22079	
13 *endo* TS	-516.05220	-515.92608	-298.1
13 *endo* closed	-516.13240	-516.00152	
13 *endo* open	-516.06089	-515.93510	
13 *exo* TS	-516.05974	-515.93191	-201.5
13 *exo* closed	-516.10783	-515.97813	
13 *exo* open	-516.06079	-515.93434	
14 *endo* TS	-832.88051	-832.74818	-509.0
14 *endo* closed	-832.89620	-832.76440	
14 *endo* open	-832.92393	-832.79239	
14 *exo* TS	-832.87611	-832.74433	-226.0
14 *exo* closed	-832.87675	-832.74506	
14 *exo* open	-832.92391	-832.79270	
15 *endo* TS	-644.24545	-644.14127	-406.3
15 *endo* closed	-644.25149	-644.14895	
15 *endo* open	-644.27005	-644.17047	
15 *exo* open	-644.27032	-644.17126	
16 *endo* TS	-552.02414	-551.91849	-381.7

16 *endo* closed	-552.02695	-551.92078	
16 *endo* open	-552.03462	-551.93037	
16 *exo* TS	-552.02073	-551.91645	-236.6
16 *exo* closed	-552.02265	-551.91683	
16 *exo* open	-552.03482	-551.93177	
17 *endo* TS	-654.83550	-654.63044	-211.2
17 *endo* closed	-654.92057	-654.71128	
17 *endo* open	-654.84061	-654.63649	
17 *exo* TS	-654.84064	-654.63524	-185.2
17 *exo* closed	-654.89596	-654.68787	
17 *exo* open	-654.84176	-654.63588	
18 *endo* TS	-885.86220	-885.58079	-153.7
18 *endo* closed	-885.94456	-882.75033	
18 *endo* open	-885.86804	-885.58497	
18 *exo* closed	-885.92036	-885.63402	
18 *exo* open	-885.86909	-885.58679	
19 *endo* TS	-690.79764	-690.61450	-384.4
19 *endo* closed	-690.82122	-690.63753	
19 *endo* open	-690.81793	-690.63638	
19 *exo* closed	-690.81765	-690.92266	
19 *exo* open	-690.81826	-690.63541	
20 *endo* TS	-497.85912	-497.74718	-570.3
20 *endo* closed	-497.91401	-497.80076	
20 *endo* open	-497.89681	-497.78523	
20 *exo* TS	-497.86630	-497.75419	-438.3
20 *exo* closed	-497.89123	-497.77802	
20 *exo* open	-497.89644	-497.78552	
21 *endo* TS	-497.86604	-497.75331	-416.4
21 *endo* closed	-497.88044	-497.76696	
21 *endo* open	-497.89614	-497.78552	
21 *exo* open	-497.89619	-497.78462	
22 *endo* TS	-725.75168	-725.60170	-531.3
22 *endo* closed	-725.78909	-725.63846	

22 *endo* open	-725.79549	-725.64618	
22 *exo* TS	-725.75673	-725.60685	-363.6
22 *exo* closed	-725.76760	-725.61702	
22 *exo* open	-725.79543	-725.64744	
23 *endo* TS	-725.75938	-725.60883	-402.7
23 *endo* closed	-725.76639	-725.61496	
23 *endo* open	-725.79484	-725.64726	

Appendix to Chapter 4

Figure 4.12 blue

Structure	**Energy**	**Gibbs Free Energy**	**Imaginary Frequency**
Ethyl iodide	-90.61592	-90.58005	
5,6 *Si* A	-575.93948	-575.63874	-381.2
5,6 *Si* B	-575.93976	-575.63891	-378.8
5,6 *Si* C	-575.93996	-575.63852	-350.1
5,6 *Re* A	-575.94042	-575.63944	-396.6
5,6 *Re* B	-575.94068	-575.63987	-393.1
5,6 *Re* C	-575.94356	-575.64202	-343.6
5,6 Auxiliary C.1	-485.34473	-485.09983	
5,6 Auxiliary C.2	-485.34105	-485.10041	
5,7 *Si* A	-615.24765	-614.9183	-384.6
5,7 *Si* B	-615.24766	-614.91904	-390.6
5,7 *Si* C	-615.24576	-614.91657	-364.7
5,7 *Re* A	-615.24954	-614.9217	-390.3
5,7 *Re* B	-615.24972	-614.92191	-379
5,7 *Re* C	-615.25198	-614.92386	-344.4
5,7 *Si** A	-615.24692	-614.91764	-385.4
5,7 *Si** B	-615.24705	-614.91884	-389
5,7 *Si** C	-615.24501	-614.91638	-367.3
5,7 *Re** A	-615.24894	-614.92146	-392.3
5,7 *Re** B	-615.24924	-614.92061	-384.4

5,7 *Re** C	-615.25154	-614.92296	-346.2
5,7 Auxiliary C.1	-524.65277	-524.38064	
5,7 Auxiliary C.2	-524.65241	-524.38028	
5,8 *Si* A	-654.55431	-654.19757	-389.9
5,8 *Si* B	-654.5545	-654.19811	-389.1
5,8 *Si* C	-654.55108	-654.19463	-372.1
5,8 *Re* A	-654.55745	-654.20132	-384.7
5,8 *Re* B	-654.55754	-654.20156	-371.8
5,8 *Re* C	-654.55858	-654.20255	-356.1
5,8 Auxiliary	-563.95478	-563.65425	

Figure 4.12 red

Structure	**Energy**	**Gibbs Free Energy**	**Imaginary Frequency**
Ethyl iodide	-90.61592	-90.58005	
5,5 *Si* A	-615.24122	-614.91649	-412.3885
5,5 *Si* B	-615.24141	-614.91720	-406.6099
5,5 *Si* C	-615.24217	-614.91699	-352.7905
5,5 *Re* A	-615.24127	-614.91714	-385.4285
5,5 *Re* B	-615.24157	-614.91786	-382.5698
5,5 *Re* C	-615.24344	-614.91863	-348.9987
5,5 Auxiliary	-524.64787	-524.37904	
5,6 *Si* A	-654.56140	-654.20680	-395.5831
5,6 *Si* B	-654.56134	-654.20744	-392.8554
5,6 *Si* C	-654.56015	-654.20627	-362.1959
5,6 *Re* A	-654.56378	-654.21053	-381.5382
5,6 *Re* B	-654.56392	-654.21057	-376.6476
5,6 *Re* C	-654.56533	-654.21131	-341.881
5,6 Auxiliary	-563.96504	-563.66744	
5,7 *Si* A	-693.86453	-693.48230	-389.6371
5,7 *Si* B	-693.86465	-693.48178	-385.7049
5,7 *Si* C	-693.86483	-693.48213	-357.5369
5,7 *Re* A	-693.86475	-693.48277	-395.8735

5,7 *Re* B	-693.86456	-693.48110	-379.6786
5,7 *Re* C	-693.86391	-693.48115	-365.4663
5,7 *Si** A	-693.86803	-693.48624	-375.589
5,7 *Si** B	-693.86800	-693.48657	-379.1553
5,7 *Si** C	-693.86882	-693.48699	-351.5294
5,7 *Re** A	-693.86854	-693.48633	-377.1979
5,7 *Re** B	-693.86854	-693.48719	-379.4875
5,7 *Re** C	-693.86949	-693.48776	-350.787
5,7 Auxiliary	-603.27054	-602.94450	
5,8 *Si* A	-733.16940	-732.75965	-398.0635
5,8 *Si* B	-733.16922	-732.75878	-384.8387
5,8 *Si* C	-733.16806	-732.75722	-371.6358
5,8 *Re* A	-733.17460	-732.76438	-380.6126
5,8 *Re* B	-733.17458	-732.76503	-377.3559
5,8 *Re* C	-733.17450	-732.76469	-366.2124
5,8 Auxiliary	-642.57796	-642.22507	

Table 4.4

Structure	**Energy**	**Gibbs Free Energy**	**Imaginary Frequency**
O; *Si* A	-611.8377493	-611.5605256	-381.6213
O; *Si* B	-611.8381968	-611.5606338	-379.2483
O; *Si* C	-611.8367704	-611.5594913	-365.8382
O; *Re* A	-611.8349898	-611.557766	-409.2919
O; *Re* B	-611.8354728	-611.5581457	-400.1312
O; *Re* C	-611.8382081	-611.5608651	-352.7754
O; enamine	-521.2434973	-521.0224441	
S; *Si* A	-934.8120691	-934.5387261	-382.3141
S; *Si* B	-934.8122009	-934.5397704	-382.9926
S; *Si* C	-934.8094982	-934.5368782	-368.7468
S; *Re* A	-934.8116415	-934.5390312	-411.6512
S; *Re* B	-934.8119506	-934.5395347	-402.6898
S; *Re* C	-934.8143982	-934.5409737	-359.7341

S; enamine	-844.2197953	-844.0033902	
SiH_2; *Si* A	-827.3182265	-827.0286973	-116.1411
SiH_2; *Si* B	-827.3180162	-827.0320701	-389.9532
SiH_2; *Si* C	-827.3171425	-827.0293418	-358.0495
SiH_2; *Re* A	-827.319766	-827.0335742	-395.004
SiH_2; *Re* B	-827.3199171	-827.0334769	-388.7091
SiH_2; *Re* C	-827.3223143	-827.0337862	-346.8136
SiH_2; enamine	-736.7232837	-736.4931942	
NH; *Si* A	-591.9702378	-591.6801249	-381.7878
NH; *Si* B	-591.9706578	-591.6803036	-379.5612
NH; *Si* C	-591.9685543	-591.6787677	-366.463
NH; *Re* A	-591.9670413	-591.6773877	-416.3462
NH; *Re* B	-591.9674633	-591.677808	-409.2893
NH; *Re* C	-591.9702717	-591.6801825	-360.3968
NH; enamine	-501.3727624	-501.1392053	
CH_2; *Si* A	-575.9394765	-575.6387413	-416.3462
CH_2; *Si* B	-575.9397591	-575.6389118	-409.2893
CH_2; *Si* C	-575.9399597	-575.6385163	-360.3968
CH_2; *Re* A	-575.9404249	-575.6394435	-396.6424
CH_2; *Re* B	-575.9406826	-575.6398708	-393.1459
CH_2; *Re* C	-575.943556	-575.6420243	-343.6133
CH_2; enamine	-485.3447276	-485.0998254	
CMe_2; *Si* A	-654.5614026	-654.2067967	-395.5831
CMe_2; *Si* B	-654.5613414	-654.2074377	-392.8554
CMe_2; *Si* C	-654.5601518	-654.2062699	-362.1959
CMe_2; *Re* A	-654.5637753	-654.2105271	-381.5382
CMe_2; *Re* B	-654.5639202	-654.2105674	-376.6476
CMe_2; *Re* C	-654.5653317	-654.2113055	-341.881
CMe_2; enamine	-563.965035	-563.6674371	
$C(CF_3)_2$; *Si* A	-1249.994023	-1249.692436	-397.7819
$C(CF_3)_2$; *Si* B	-1249.993517	-1249.692361	-398.4474
$C(CF_3)_2$; *Re* A	-1249.994499	-1249.693581	-387.6793
$C(CF_3)_2$; *Re* B	-1249.994716	-1249.694035	-384.3631

$C(CF_3)_2$; *Re* C	-1249.995132	-1249.693622	-351.332
$C(CF_3)_2$; enamine	-1159.399514	-1159.156003	
CF_2; *Si* A	-774.4209171	-774.1381191	-376.0892
CF_2; *Si* B	-774.421257	-774.1389614	-369.2075
CF_2; *Si* C	-774.4197227	-774.1370662	-337.4208
CF_2; *Re* A	-774.4197768	-774.1373222	-391.1183
CF_2; *Re* B	-774.4199687	-774.1377392	-387.5258
CF_2; *Re* C	-774.4221389	-774.1396229	-325.5093
CF_2; enamine	-683.8254416	-683.5994861	
CCl_2; *Si* A	-1495.117528	-1494.839968	-397.2308
CCl_2; *Si* B	-1495.117803	-1494.840028	-390.2702
CCl_2; *Si* C	-1495.116313	-1494.839105	-365.2716
CCl_2; *Re* A	-1495.11939	-1494.841825	-390.6714
CCl_2; *Re* B	-1495.119603	-1494.842411	-385.0494
CCl_2; *Re* C	-1495.120572	-1494.842572	-356.5256
CCl_2; enamine	-1404.524968	-1404.304049	
CBr_2; *Si* A	-5717.538238	-5717.263128	-399.5441
CBr_2; *Si* B	-5717.538373	-5717.264245	-391.5566
CBr_2; *Si* C	-5717.536555	-5717.262313	-363.0923
CBr_2; *Re* A	-5717.539819	-5717.265655	-392.121
CBr_2; *Re* B	-5717.540124	-5717.265839	-385.8887
CBr_2; *Re* C	-5717.541058	-5717.266473	-356.5917
CBr_2; enamine	-5626.945577	-5626.728424	
$C(SiH_3)_2$; *Si* A	-1157.305187	-1156.981099	-404.4643
$C(SiH_3)_2$; *Si* B	-1157.305285	-1156.981395	-400.9448
$C(SiH_3)_2$; *Si* C	-1157.304513	-1156.979928	-363.7795
$C(SiH_3)_2$; *Re* A	-1157.308803	-1156.98553	-384.3252
$C(SiH_3)_2$; *Re* B	-1157.308928	-1156.985899	-385.0194
$C(SiH_3)_2$; *Re* C	-1157.310418	-1156.98687	-354.4804
$C(SiH_3)_2$; enamine	-1066.711705	-1066.445369	
$C(C_2H_4)$; *Si* A	-653.3227701	-652.9903526	-382.5379
$C(C_2H_4)$; *Si* B	-653.3227957	-652.9903067	-371.2823
$C(C_2H_4)$; *Si* C	-653.3233544	-652.9906735	-342.7738

$C(C_2H_4)$; *Re* A	-653.3234786	-652.991744	-387.7953
$C(C_2H_4)$; *Re* B	-653.3236529	-652.9917867	-385.985
$C(C_2H_4)$; *Re* C	-653.323707	-652.9914325	-344.014
$C(C_2H_4)$; enamine	-562.7262497	-562.4507961	

Table 4.7 B3LYP-D3

Structure	**Energy**	**Gibbs Free Energy**	**Imaginary Frequency**
5,6 *Si* A	-576.02010	-575.71654	-387.2
5,6 *Si* B	-576.02072	-575.71670	-374.1
5,6 *Si* C	-576.02024	-575.71449	-110.6
5,6 *Re* A	-576.02017	-575.71569	-394.3
5,6 *Re* B	-576.02092	-575.71718	-391.5
5,6 *Re* C	-576.02457	-575.71999	-323.8
Quart. TS C.1	-576.02236	-575.71667	-315.1
Quart. TS C.2	-576.01702	-575.71157	-322.6
Quart. Prod. C.1	-576.06721	-575.75526	
Quart. React. C.1	-576.03955	-575.73675	
Quart. Prod. C.2	-576.03516	-575.73194	
Quart. React. C.2	-576.06663	-575.75605	

Table 4.7 wB97XD

Structure	**Energy**	**Gibbs Free Energy**	**Imaginary Frequency**
5,6 *Si* A	-575.7917958	-575.4828869	-516.7332
5,6 *Si* B	-575.7928539	-575.4834552	-494.1
5,6 *Si* C	-575.7916586	-575.4830731	-461.3397
5,6 *Re* A	-575.7920746	-575.4844521	-520.7183
5,6 *Re* B	-575.7929478	-575.4850754	-521.8107
5,6 *Re* C	-575.7960557	-575.4881291	-449.5722
Enamine	-485.2148119	-484.9652103	
Quart. TS C.1	-575.7960234	-575.4853288	-445.9035
Quart. TS C.2	-575.7907102	-575.4807572	-439.8534

Table 4.7 M062X

Structure	Energy	Gibbs Free Energy	Imaginary Frequency
5,6 *Si* A	-575.6126036	-575.3056504	-545.1608
5,6 *Si* B	-575.6137631	-575.305557	-527.8861
5,6 *Si* C	-575.6122999	-575.3048194	-517.8565
5,6 *Re* A	-575.6131903	-575.3061755	-554.4026
5,6 *Re* B	-575.6143666	-575.3072212	-547.7115
5,6 *Re* C	-575.616686	-575.3092044	-515.0883
Enamine	-485.1206919	-484.8714838	
Quart. TS C.1	-575.6178048	-575.3086357	-479.7503
Quart. TS C.2	-575.6126421	-575.303777	-479.3238

Table 4.8

Structure	Energy	Gibbs Free Energy	Imaginary Frequency
s-*trans Si* A	-576.02010	-575.71654	-387.2
s-*trans Si* B	-576.02072	-575.71670	-374.1
s-*trans Si* C	-576.02024	-575.71449	-110.6
s-*cis Si* A	-576.01589	-575.71168	-389.1
s-*cis Si* B	-576.01498	-575.70959	-400.0
s-*cis Si* C	-576.01927	-575.71474	-320.6
s-*trans Re* A	-576.02017	-575.71569	-394.3
s-*trans Re* B	-576.02092	-575.71718	-391.5
s-*trans Re* C	-576.02457	-575.71999	-323.8
s-*cis Re* A	-576.01641	-575.71237	-386.0
s-*cis Re* B	-576.01584	-575.71038	-382.3
s-*cis Re* C	-576.01631	-575.71153	-340.5

Table 4.9

Structure	Energy	Gibbs Free Energy	Imaginary Frequency
s-*trans Si* A	-654.65729	-654.30022	-400.9

s-*trans Si* B	-654.65769	-654.30053	-392.4
s-*trans Si* C	-654.65695	-654.29777	-346.8
s-*cis Si* A	-654.65531	-654.29677	-381.0
s-*cis Si* B	-654.65449	-654.29722	-393.4
s-*cis Si* C	-654.65808	-654.30120	-325.8
s-*trans Re* A	-654.66040	-654.30439	-375.6
s-*trans Re* B	-654.66063	-654.30355	-381.7
s-*trans Re* C	-654.66285	-654.30589	-326.4
s-*cis Re* A	-654.65537	-654.29730	-397.3
s-*cis Re* B	-654.65473	-654.29717	-387.7
s-*cis Re* C	-654.65474	-654.29708	-375.3

Appendix to Chapter 5

Table 5.1

Structure	**Energy**	**Gibbs Free Energy**
B3LYP SMD *cis*	-881.52495	-881.31124
B3LYP SMD *trans*	-881.52543	-881.31161
M062X SMD *cis*	-881.26999	-881.05395
M062X SMD *trans*	-881.27060	-881.05443
wB97XD SMD *cis*	-881.35646	-881.13949
wB97XD SMD *trans*	-881.35730	-881.14055
B3LYP UAKS *cis*	-881.52476	-881.31413
B3LYP UAKS *trans*	-881.52521	-881.31470
M062X UAKS *cis*	-881.27021	-881.05707
M062X UAKS *trans*	-881.27078	-881.05767
wB97XD UAKS *cis*	-881.35649	-881.14259
wB97XD UAKS *trans*	-881.35734	-881.14414
No solvation *cis*	-881.34330	-881.12624
No solvation *trans*	-881.34378	-881.12698

Table 5.2

Structure	Energy	Gibbs Free Energy
B3LYP SMD *cis*	-881.52495	-881.31124
B3LYP SMD *trans*	-881.52543	-881.31161
M062X SMD *cis*	-881.26999	-881.05395
M062X SMD *trans*	-881.27060	-881.05443
wB97XD SMD *cis*	-881.35646	-881.13949
wB97XD SMD *trans*	-881.35730	-881.14055
B3LYP UAKS *cis*	-881.52476	-881.31413
B3LYP UAKS *trans*	-881.52521	-881.31470
M062X UAKS *cis*	-881.27021	-881.05707
M062X UAKS *trans*	-881.27078	-881.05767
wB97XD UAKS *cis*	-881.35649	-881.14259
wB97XD UAKS *trans*	-881.35734	-881.14414
No solvation *cis*	-881.34330	-881.12624
No solvation *trans*	-881.34378	-881.12698

Table 5.3

Structure	Energy	Gibbs Free Energy	Imaginary Frequency
TS **01**	-443.75950	-443.57134	-86.6
TS **02**	-518.99439	-518.80324	-85.5
TS **03**	-766.70229	-766.51633	-87.8
TS **04**	-841.93157	-841.74341	-81.2
TS **05**	-806.01323	-805.80216	-55.6
TS **06**	-881.24264	-881.02880	-56.9

Appendix to Chapter 6

Table 5.3

Distance (Å)	01 (ppm)	02 (ppm)	03 (ppm)	04 (ppm)
-4	-3.99	-3.93	-4.49	-2.52
-3.75	-4.69	-4.63	-5.25	-2.89
-3.5	-5.56	-5.51	-6.17	-3.33
-3.25	-6.63	-6.60	-7.28	-3.88
-3	-7.96	-7.97	-8.65	-4.56
-2.75	-9.62	-9.70	-10.31	-5.40
-2.5	-11.68	-11.87	-12.33	-6.44
-2.25	-14.22	-14.60	-14.73	-7.69
-2	-17.28	-17.98	-17.49	-9.15
-1.75	-20.78	-22.01	-20.50	-10.72
-1.5	-24.43	-26.52	-23.43	-12.12
-1.25	-27.56	-30.88	-25.69	-12.80
-1	-29.00	-33.74	-26.46	-11.90
-0.75	-27.40	-33.09	-25.01	-8.59
-0.5	-22.47	-27.74	-21.51	-3.02
-0.25	-16.49	-20.06	-17.63	2.67
0	-13.72	-16.25	-15.91	5.14
0.25	-16.49	-20.06	-17.62	2.67
0.5	-22.47	-27.74	-21.50	-3.02
0.75	-27.40	-33.09	-25.01	-8.59
1	-29.00	-33.74	-26.45	-11.90
1.25	-27.56	-30.88	-25.69	-12.80
1.5	-24.43	-26.52	-23.43	-12.12

1.75	-20.78	-22.01	-20.50	-10.72
2	-17.28	-17.98	-17.49	-9.15
2.25	-14.22	-14.60	-14.73	-7.69
2.5	-11.68	-11.87	-12.33	-6.44
2.75	-9.62	-9.70	-10.31	-5.40
3	-7.96	-7.97	-8.65	-4.56
3.25	-6.63	-6.60	-7.28	-3.88
3.5	-5.56	-5.51	-6.17	-3.33
3.75	-4.69	-4.63	-5.25	-2.89
4	-3.99	-3.93	-4.49	-2.52

Table 5.3

Distance (Å)	**05 (ppm)**	**06 (ppm)**	**07 (ppm)**	**08 (ppm)**
-4	1.14	6.20	0.31	6.20
-3.75	1.45	7.65	0.41	7.65
-3.5	1.87	9.58	0.55	9.58
-3.25	2.44	12.20	0.76	12.20
-3	3.25	15.82	1.07	15.82
-2.75	4.42	20.91	1.54	20.91
-2.5	6.15	28.19	2.22	28.19
-2.25	8.74	38.72	3.11	38.72
-2	12.65	54.00	3.82	54.00
-1.75	18.55	76.00	2.92	76.00
-1.5	27.29	107.05	-2.78	107.05
-1.25	39.71	148.81	-15.97	148.81
-1	55.91	198.99	-28.06	198.99
-0.75	73.49	246.14	-11.33	246.14
-0.5	86.84	270.89	41.61	270.89
-0.25	91.89	266.83	91.55	266.83
0	92.18	258.58	109.46	258.58
0.25	91.87	266.83	91.55	266.83
0.5	86.81	270.89	41.61	270.89

0.75	73.47	246.14	-11.33	246.14
1	55.90	198.99	-28.06	198.99
1.25	39.70	148.81	-15.97	148.81
1.5	27.28	107.05	-2.78	107.05
1.75	18.55	76.00	2.92	76.00
2	12.65	54.00	3.82	54.00
2.25	8.73	38.72	3.11	38.72
2.5	6.14	28.19	2.22	28.19
2.75	4.42	20.91	1.54	20.91
3	3.25	15.82	1.07	15.82
3.25	2.44	12.20	0.76	12.20
3.5	1.86	9.58	0.55	9.58
3.75	1.45	7.65	0.41	7.65
4	1.14	6.20	0.31	6.20

Table 5.3

Distance (Å)	**09 (ppm)**	**10 (ppm)**	**11 (ppm)**	**12 (ppm)**
-4	-1.86	-1.99	-2.03	-3.18
-3.75	-2.12	-2.27	-2.30	-3.69
-3.5	-2.42	-2.58	-2.61	-4.30
-3.25	-2.76	-2.93	-2.94	-5.02
-3	-3.12	-3.30	-3.26	-5.89
-2.75	-3.49	-3.66	-3.55	-6.92
-2.5	-3.82	-3.97	-3.74	-8.11
-2.25	-4.05	-4.15	-3.76	-9.45
-2	-4.05	-4.10	-3.51	-10.88
-1.75	-3.61	-3.67	-2.88	-12.26
-1.5	-2.41	-2.62	-1.73	-13.32
-1.25	0.02	-0.59	0.24	-13.63
-1	4.15	2.93	3.48	-12.69
-0.75	10.16	8.29	8.48	-10.16
-0.5	17.21	14.94	14.96	-6.34

-0.25	23.18	20.89	21.01	-2.39
0	25.56	23.32	23.56	0.00
0.25	23.18	20.89	21.01	-0.20
0.5	17.21	14.94	14.96	-2.55
0.75	10.16	8.29	8.48	-5.55
1	4.16	2.93	3.48	-7.87
1.25	0.02	-0.59	0.24	-9.07
1.5	-2.41	-2.62	-1.73	-9.38
1.75	-3.61	-3.67	-2.88	-9.22
2	-4.05	-4.10	-3.51	-8.77
2.25	-4.05	-4.15	-3.76	-8.10
2.5	-3.82	-3.97	-3.74	-7.29
2.75	-3.49	-3.66	-3.55	-6.42
3	-3.12	-3.30	-3.26	-5.58
3.25	-2.76	-2.93	-2.94	-4.82
3.5	-2.42	-2.58	-2.61	-4.15
3.75	-2.12	-2.27	-2.30	-3.58
4	-1.86	-1.99	-2.03	-3.09